Sondes à impédance mutuelle pour plateformes nanosatellite

Luca Bucciantini

UNIVERSITÉ D'ORLÉANS

ÉCOLE DOCTORALE ÉNERGIE, MATÉRIAUX, SCIENCES DE LA TERRE ET DE L'UNIVERS

[LPC2E, OSUC, CNRS]

THÈSE présentée par :

Luca BUCCIANTINI

soutenue le : **30 mars 2023**

pour obtenir le grade de : **Docteur de l'Université d'Orléans**

Discipline/ Spécialité : **Sciences de l'Univers**

SONDES À IMPÉDANCE MUTUELLE POUR PLATEFORMES NANOSATELLITE

THÈSE dirigée par :

HENRI Pierre	Chargé de Recherche, LPC2E, Lagrange, CNRS

RAPPORTEURS :

ANDRÉ Nicolas	Chargé de Recherche, IRAP, CNRS
ISSAUTIER Karine	Directrice de Recherche, LESIA, Observatoire de Paris, CNRS

JURY :

CELESTIN Sebastien	Professeur, LPC2E, CNRS, Président du jury
ANDRÉ Nicolas	Chargé de Recherche, IRAP, CNRS
ISSAUTIER Karine	Directrice de Recherche, LESIA, Observatoire de Paris, CNRS
BERTHOMIER Matthieu	Chargé de Recherche, LPP, CNRS
SAHRAOUI Fouad	Directeur de Recherche, LPP, CNRS
HENRI Pierre	Chargé de Recherche, LPC2E & Lagrange, CNRS
AMSIF Kader	Thématicien CNES

Acknowledgments

In this section, I thank all the people that contributed to this PhD work.

I thank the jury for their review of this PhD document. Their insights and overall contributions are essential to the finalization of this PhD work.

Thank you, Pierre and Xavier, not only for the help you provided directly to my PhD work, but also for everything that you did for me. Some years ago, despite knowing little to nothing of me, you gave me the chance to come to France. You believed in me, and you taught me so much about so many topics. You made me improve on all aspects. You made me grow from a master student to what I am now. You have been the reference for me during these years, and I will keep using you as a role-model in the future. Thanks for teaching me.

Thank you, Nicolas, Germain, Ousmane, Manuel, Gaëtane, Andrea, Chloi, Federico, Pietro and Pacio for the support that you provided during my PhD work. The interactions that we had, both work and not-work related, have always been both useful and very pleasant. With you, I also thank all those LPC2E colleagues that helped me during different aspects of my PhD. In particular, I thank Jean-Yves, Olivier, Thomas, Matthieu, Clemence, Stéphane, Gilles, Manuel, Thierry, Ted, Fabrice, Guillaume, Aude-Lyse, Isabelle, Catherine, Tiphaine, Dominique, Dominique, Gaëtan and Jérémie. My time at LPC2E has been really fun thanks to you all.

I thank different members of my family for the support that they provided during these years. Thank you, Rutilio, Fiammetta, Andrea, Nonna Anna, Nonno Graziano and Nonna Solange. In particular, I thank my sister and brother, Elena and Marco, for always being there. Despite the long distance that separates us, our connection has always been strong and I am sure it will always be.

Two people, above most, have always believed in me and given everything they had to ensure that I could become whatever I wanted. It has not been always easy, but despite the difficulties they always managed to be there and provide all the emotional and practical support I needed. Thank you, mamma Stefania and babbo Rudy, for all the sacrifices that you have done for me. Each of your efforts, from the small to the big ones, has made a significant difference. I promise that I will keep doing whatever I can to show you that your efforts did not go to waste.

They say that behind every great achievement there is always a great woman. That is definitely the case for this PhD work, which has received never-ending support from my wife. Thank you, Valentina, for the strong and unyielding help that you gave me during all the difficult moments that have come, the many late-night discussions that you encouraged and the several working weekends that you have endured. You are and always will be a fixed point in my life. I wouldn't have reached my current achievements without you.

Contents

List of Figures

List of Tables

List of Acronyms

AM2P: Active Measurement of Mercury's Plasma.

CNES: Centre National d'Études Spatiales.

COMIX: COmpact Mutual Impedance eXperiment.

COMPLIMENT: COMetary Plasma Light InstruMENT.

DFP: Dust-Field-Plasma.

DFT: Discrete Fourier Transform.

ESA: European Space Agency.

FFT: Fast Fourier Transform.

IAW: Ion Acoustic Wave.

JAXA: Japan Aerospace Exploration Agency.

LAP: LAngmuir Probe.

LP: Langmuir Probe.

LPC2E: Laboratoire de Physique et Chimie de l'Environnement et de l'Espace.

MI: Mutual Impedance.

MIME: Mutual Impedance MEasurement.

MIP: Mutual Impedance Probe.

PWI: Plasma Waves Investigation.

QTN: Quasi-Thermal Noise.

RPC: Rosetta Plasma Consortium.

RPWI: Radio & Plasma Wave Investigation.

RS: Relaxation Sounder.

R&D: Research and Development.

SNR: Signal-to-Noise Ratio.

Chapter 1

Introduction

1.1 Single-Point Large Spacecraft vs Multi-Point Nanosatellite Missions for Space Exploration

Space missions push forward our understanding of the solar system by sending into space satellites equipped with a variety of diagnostic instruments to explore target environments, observe their characteristics by collecting in situ data. Such data fuels scientific investigations and, as new regions are explored and more data is collected, our comprehension of the solar system improves.

Both the satellite's platform and the scientific instruments carried into space are chosen depending on the goals of the mission. For instance, when a region is explored for the first time, the goal is typically to grasp the overall characteristics of the environment. In such case, the satellite could carry a variety of instruments to monitor the environment from different perspectives. When a region has been explored several times, instead, the satellite carries particular instruments to target specific questions regarding specific domains.

If a certain space mission requires the simultaneous monitoring of several different characteristics of the probed environment, then the satellite needs to carry into space multiple instruments. Large quantities of instruments correspond to a significant mass, large occupied volume and considerable power consumption. However, volume, mass and power are very constrained onboard certain types of platforms, such as small satellites. Large satellites have less constraints and, as a consequence, they are usually the preferred type of platform chosen for missions exploring space regions for the first times.

However, the significant mass, the complex architecture and the diversified set of instruments carried into space make large satellites very expensive platforms. Hence, they are mostly selected for single-point missions, where a single satellite is sent into space to observe the local properties of a specific space region. This is typically the case for planetary and solar wind missions. But one cannot distinguish between spatial and temporal variations of the monitored properties if only single-point measurements are used [Paschmann and Daly, 1998]. In particular, if the satellite moves relatively to the observed environment, the modifications of the measurements captured by the instruments can either depend on the spatial or on the temporal variation of the characteristics of the probed region. To make the distinction, multi-point measurements are needed. Multi-point missions (e.g. the ESA/NASA Cluster mission [Escoubet et al., 2001] and the NASA THEMIS [Angelopoulos, 2008] and MMS missions [Burch et al., 2016]) investigate physical phenomena perturbing the environment over different spatial scales (i.e. electron, ion or fluid scales) [Retinò et al., 2021] by sending into space multiple identical satellites. Therefore, their cost is significantly larger than a single-point mission investigating the same environment but with only one satellite. For this reason, few multi-point large satellite missions have been selected in the past.

Recently, small satellite platforms (e.g. nanosatellites) have lighted the interest of the scientific community [Camps, 2019]. Thanks to their limited costs, nanosatellites are seen as the mean to cut down the

price of multi-point missions and to speed-up the development process of specific single-point missions.[1] But their very strong requirements in terms of mass, volume and power consumption, limit both the quantity and type of scientific instruments they can carry. Therefore, small-satellite missions are likely to focus on the observation of specific properties, while large-satellites should provide a much broader monitoring of the explored environment. Advantageously, as multiple small satellites are used, the same (few) properties are monitored simultaneously from different positions. This means that the distinction between time and spatial variations of given properties could be made by comparing the measurements obtained simultaneously by different small satellites located at different positions [Paschmann and Daly, 1998]. This goes beyond the understanding that past and recent single-point measurements can provide. For this reason, more and more multi-point projects (e.g. the Helioswarm mission [Spence, 2019]) are recently being designed as they are considered the next step in space exploration. In all, small satellites significantly enhance the investigation of physical phenomena affecting space over different spatial scales.[2] Consequently, as they provide observations of specific properties of the probed environment, they will complement the understanding provided by large satellite single-point missions.

The use of nanosatellites for multi-point space missions has only recently begun. For instance, the future ESA F-Class Comet Interceptor mission, consisting of a large (mother) satellite supported by two (daughter) nanosatellites, will explore a pristine comet entering for the first time the solar system [Snodgrass and Jones, 2019]. With the increasing interest on multi-point measurements, more and more nanosatellite missions are expected in the future. Industries are already launching constellation missions, that involve the simultaneous use of hundreds of nanosatellites (e.g. Starlink or Galileo [Mortara, 2015.]). Public space exploration will also take part in constellation missions in the future [Sandau et al., 2010, Curzi et al., 2020]. In this context, scientific payload instruments need to be ready to embark nanosatellites.

For the preparation of future multi-point nanosatellite missions, instruments built in the past for large satellite applications need to ensure they comply with the volume, mass and power requirements of nanosatellites. Among others, payload instruments such as plasma diagnostic instruments need to ensure they respect the requirements of small platforms. Plasma diagnostic instruments are the main subject of this work. In the following section, I describe different types of plasma diagnostic instruments used for in situ space exploration.

1.2 Plasma Diagnostic Instruments for Space Exploration

In situ plasma diagnostic instruments measure the properties of plasma environments encountered by the satellite, such as the solar wind, planets' ionospheres and magnetospheres. Depending on the type of instrument, they monitor parameters such as density, temperature, distribution functions or drifting velocity of charged particles composing the plasma as well as the local electro-magnetic field. Hereby, I provide a non-exhaustive list of instruments for in situ plasma monitoring, by focusing on those instrument that measure the characteristics of the electron and ion populations composing the plasma.

- Mass spectrometers (e.g. the mass-spectrometer part of MPPE-MSA instrument [Delcourt et al., 2009, 2016] included in the BepiColombo mission [Benkhoff et al., 2021]) determine the chemical composition of space plasmas. They typically consist of a time of flight chamber [Managadze, 1986] that performs a *mass/charge* analysis to count and identify the ions composing the plasma. This is done by measuring the time of flight the particles require for crossing the chamber's length. Practically, a first sensor [Allegrini et al., 2003] detects the particles entering the instrument and a second sensor detects when they arrive at the bottom of the chamber. The time of flight required to reach the second sensor from the first is directly correlated to the type of particle measured by the instrument [Möbius et al., 1990]. Therefore, the instrument discriminates the particles

[1] Thanks to their limited costs and fast mission profiles, nanosatellites have been repeatedly selected for student missions in the past decade.

[2] Note that nanosatellite missions with significant numbers of platforms might even monitor parameters over different spatial scales simultaneously.

depending on their time of flight and, by doing so, it identifies which types of ions compose the plasma.

- Plasma analyzers [Vaisberg et al., 2005, Morel et al., 2017] determine the distribution function of the plasma particles. They are separated into electron analyzers (e.g. MPPE-MEA [Sauvaud et al., 2010] instrument included in the BepiColombo mission) or ion analyzers (e.g. the plasma analyzer part of MPPE-MSA), depending on the particles they investigate. In both cases, they consist of an electrostatic analyzer, which is typically composed of a filter [Collinson and Kataria, 2010] and a collector [Fraser, 2002]. The filter is an electromagnetic component that modifies the particles' trajectories depending on their energy. As plasma particles enter the instrument with a given direction, the filter deflects them. The collector is an electric sensor that registers the deflection of the particles. The instrument measures the distribution function by counting the particles undergoing the same deflections. Note that the resolution of the distribution function depends on the selection mechanism of the filter and the resolution of the detector.

- Langmuir probes (e.g. RPC-LAP [Eriksson et al., 2007] onboard the orbiter of the Rosetta mission [Taylor et al., 2017]) determine the local plasma density [Johansson et al., 2021], the electron temperature [Odelstad et al., 2018] the ion temperature (or ion drift velocity [Vigren et al., 2017]) and other parameters [Odelstad et al., 2017]. They consist of an electric sensor embedded in the plasma to be diagnosed [Mott-Smith and Langmuir, 1926]. While the sensor is polarized to given electric potentials, the instrument measures simultaneously the current required to maintain such potentials. By repeating the measure for different potentials, the so-called I-V curve is built. Such curve is also called Langmuir Probe sweep. From particular signatures of the I-V curve, Plasma parameters such as the electron temperature, the (local) plasma density, the ion temperature or drift velocity [Odelstad et al., 2018] are identified.

- Relaxation sounder (RS) experiments (e.g. WHISPER included in the CLUSTER mission [Béghin et al., 2005, Trotignon et al., 2003, 2010]) are electric instruments composed of emitting and receiving sensors. The emitting sensors perturb the plasma with strong signals, characterized by large emission amplitudes and different emission frequencies. The receiving sensors measure, after the emission, the electric fluctuations that have been triggered in the plasma by the emission. Such retrieved fluctuations are, then, used for building relaxation sounder spectra, from which the plasma density is derived [Harvey et al., 1979, Trotignon et al., 1986, Décréau et al., 1987, Osherovich et al., 1993].

- Quasi-Thermal noise instruments (e.g. RFS/FIELDS instrument included in the Parker Solar Probe mission)[Pulupa et al., 2017, Moncuquet et al., 2020] is a passive plasma technique using a radio receiver connected to a set of dipolar antennas. They are used to both measure the local electric field oscillations and determine the (absolute) plasma density and electron temperature. The sensors monitor the electric fluctuations generated by the thermal motion of plasma particles passing close to the sensors' surfaces [Meyer-Vernet and Perche, 1989, Issautier et al., 1999, Meyer-Vernet et al., 2017]. Plasma density and electron temperature are obtained from the quasi-thermal noise spectra built from the electric fluctuations measured by the instrument. The QTN technique is currently implemented on Parker Solar Probe, Solar Orbiter and BepiColombo.

- Mutual impedance instruments [Storey et al., 1969] (e.g. RPC-MIP [Trotignon et al., 2007] included in the Rosetta mission) are active plasma wave instruments that measure the electric field oscillations of the plasma and also determine the (absolute) plasma density and electron temperature, similarly to quasi-thermal noise instruments. Mutual Impedance instruments use a set of emitting and receiving sensors to measure the plasma response to given electric excitation signals. From the plasma response, mutual impedance spectra are built. Then, the plasma density

and electron temperature are identified from the spectrum analysis. Section 1.3 focuses on this instrumental technique.

Different versions of the above-mentioned instruments were designed to respect the constraints of large platforms. However, the recent rise of interest in small platforms is pushing towards the miniaturization of plasma diagnostic instruments (e.g. Berthomier et al. [2022]) to ensure the respect of the strong constraints of nanosatellites. For instance, the R&D project COMIX developed at LPC2E aims at defining new smaller versions of mutual impedance instruments that respect the strong limitations of nanosatellites. In this document, to support the instrumental development of the R&D COMIX, I focus on the effects that the miniaturisation of mutual impedance (MI) experiments have on MI plasma diagnostic.

First, I describe in detail how the MI instrumental method works (section 1.3). Second, I discuss how nanosatellite platforms might perturb MI measurements and how COMIX plans to answer such perturbations (section 1.4). Third, I discuss the specific objectives of my instrumental study (section 1.5), which aims at supporting COMIX into miniaturizing the MI instrument without loss of plasma diagnostic performances.

1.3 Mutual Impedance Experiments: Plasma Density and Electron Temperature Diagnostic

Mutual impedance (MI) experiments are in situ plasma diagnostic techniques for the identification of the plasma density and the electron temperature.
Figure 1.1 shows RPC-MIP, which is the MI instrument part of the ESA mission Rosetta that characterized the coma of comet 67P-CG. MI instruments, such as RPC-MIP, are composed of one or two

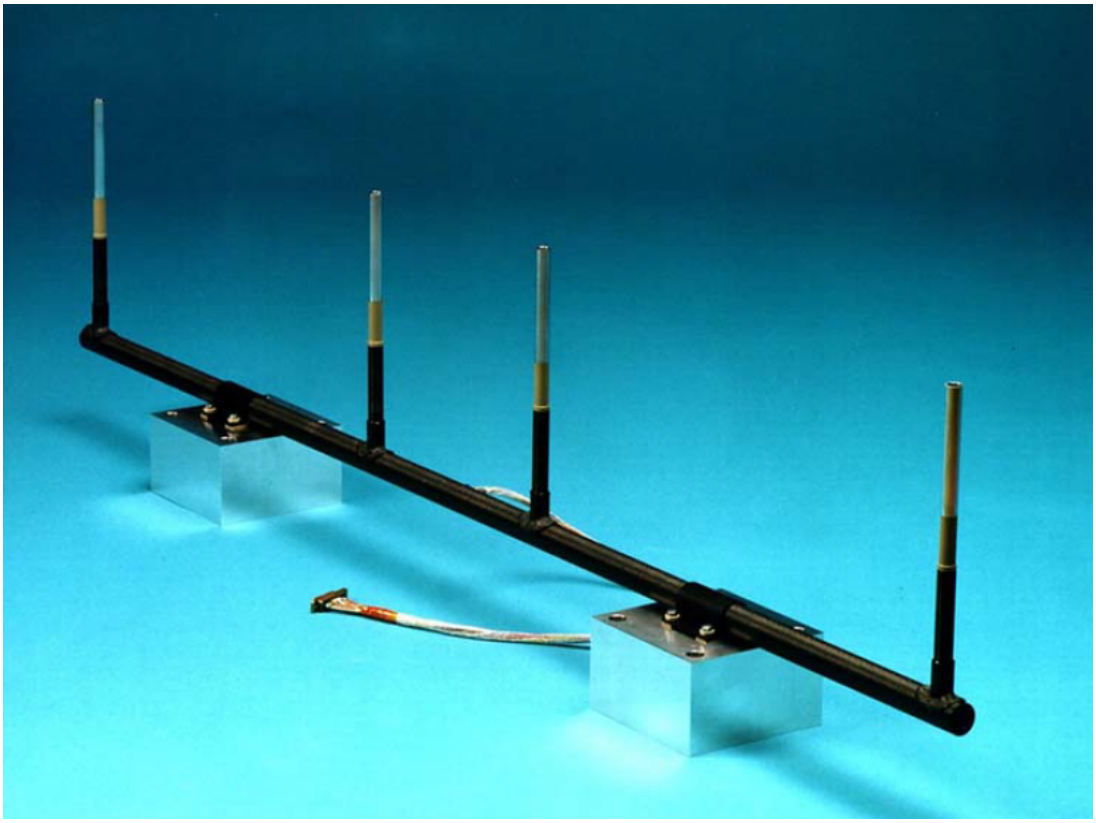

Figure 1.1: RPC-MIP onboard the Rosetta spacecraft. Credits: Trotignon et al. [2007].

emitting electrodes and two receiving sensors. The emitting electrodes inject a succession of electric signals in the plasma. Such signals oscillate at specific frequencies selected over a given frequency range. Simultaneously, the receiving sensors measure the plasma fluctuations triggered by the emission. The received signals are used for identifying the amplitude of those fluctuations that oscillate at the emission frequency. Such amplitudes are used for building MI measurements, the so-called MI spectra. The MI spectra present different resonant frequencies (eigenfrequencies) depending on the properties of the probed plasma. In the case of an unmagnetized plasma and Maxwellian electrons, they have only one resonance for frequencies of the order of the plasma frequency [Storey et al., 1969]. The analysis of the resonant signature enables the identification of the plasma density and electron temperature. MI experiments are described in detail in Chapter 2. Note that, as discussed in section 5.5, MI spectra in magnetized plasmas might present multiple resonant signatures. Since multiple resonances complexify the analysis, magnetized plasmas are avoided in this PhD work and they will be adressed in future studies.

Different versions of MI experiments were included in past and present space exploration missions (e.g. RPC-MIP onboard the ESA mission Rosetta, Figure 1.1) [Storey et al., 1969, Béghin and Debrie, 1972, Pottelette et al., 1975, Décréau et al., 1978, Pottelette and Storey, 1981, Bahnsen et al., 1988, Grard, 1997, Trotignon et al., 2007]. Among others, I recall the ongoing ESA-JAXA mission BepiColombo carrying the PWI [Kasaba et al., 2020] - AM2P [Trotignon et al., 2006] experiment, the ESA mission JUICE [Vallat et al., 2018] that will carry the RPWI [Bergman et al., 2017] - MIME [Rauch et al., 2017] experiment and the ESA mission Comet Interceptor that will carry the DFP-COMPLIMENT instrument [Rothkaehl et al., 2021]. Recently, in preparation of future multi-point nanosatellite space missions, the R&D project COMIX is defining new versions of MI instruments compatible with the strong constraints of small satellite platforms. This PhD work focuses on COMIX and the impact that small platforms such as nanosatellites have on MI measurements.

1.4 The R&D Project COMIX: Towards Mutual Impedance Experiments for Multi-Point Nanosatellite Missions

COmpact Mutual Impedance eXperiment (COMIX) is an ongoing R&D project developed at LPC2E laboratory (Orléans, France) and funded by the french Centre National d'Études Spatiales (CNES). Its objective is the definition of new versions of MI instruments for multi-point nanosatellite missions. To achieve such objective, COMIX is miniaturizing the MI instrument to ensure it respects the mass and volume requirements of nanosatellites. In this context, one of the challenges of the COMIX project is to identify and mitigate the repercussions that the miniaturization has on MI measurements. Hereafter, (i) I discuss the typical configuration of MI instruments onboard large satellites and (ii) I highlight how switching to smaller platforms perturbs the measurements. For each perturbation, I describe COMIX's mitigation strategies for reducing its impact.

(i) Onboard large satellites, the electric sensors of MI instruments are typically installed on long deployable mechanisms (booms) that position them far from the satellite platform. Such configuration minimizes the platform electromagnetic perturbations captured by the instrument, as spurious electric signals generated onboard the platform have to cover long distances to reach the instrument's sensors.
The length of the booms typically amounts to a few meters, depending on both the attitude stabilization strategy of the satellite and the size of the platform. For 3-axis stabilized satellites, the deployable booms are typically as long as some multiples of the side-length of the platform. This is the case for both RPC-MIP instrument installed on a 1.5 m long boom [Carr et al., 2007] deployed by the 3-axis stabilized Rosetta spacecraft (Figure 1.2) and RPWI-MIME sensors installed on 3 m and 8 m long booms attached to the stabilized JUICE spacecraft. For spinning satellites, the deployable length considerably exceeds the size of the satellite. In such case, the booms are replaced by wires that deploy the sensors using the centrifugal force of the rotating platform.
This is the case for PWI-AM2P instrument installed on 15 m long wires attached to the spinning Mio spacecraft of the BepiColombo mission [Karlsson et al., 2020].

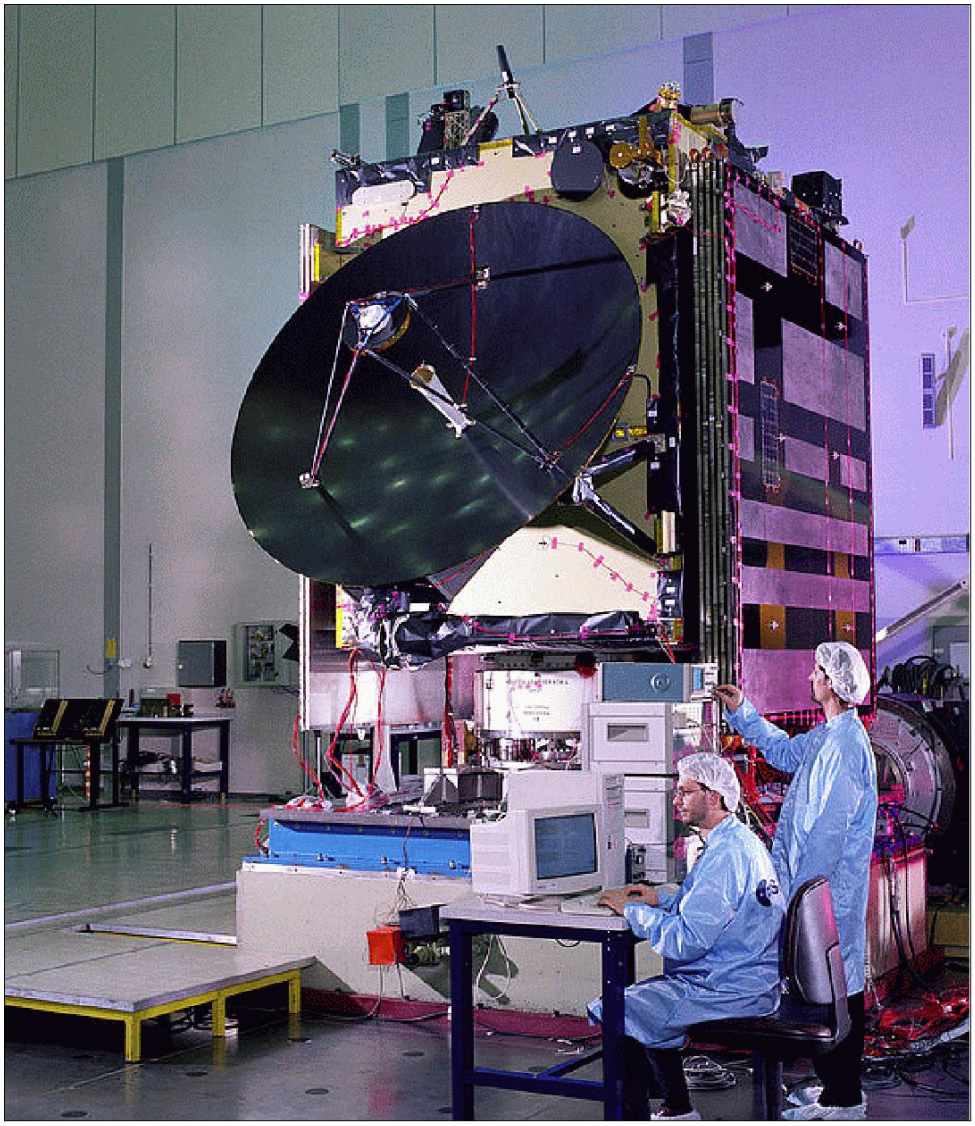

Figure 1.2: The Rosetta spacecraft. The size of the body of the satellite was equivalent to that of a cube of 2 m x 2 m x 3 m. The RPC-MIP instrument is installed on a 1.5 m long boom. [Credits: ESA.]

(ii) Onboard small satellites, instead, long deployable mechanisms are difficult to implement. Nanosatellites have side-lengths of about 0.1 to 0.3 m, which results in typical deployable lengths of about 1 m for 3-axis stabilized nanosatellites [West et al., 2015] [3]. Spinning nanosatellites could deploy long wires, but spinning is typically avoided due to the complexity that it introduces in the mission [Neilsen et al., 2014] [4]. Therefore, COMIX assumes MI sensors to be deployed at a distance of 1 m from the platform. Such distance is however not considered sufficient to neglect the spurious electric perturbations generated from the nanosatellite. Even stronger perturbations of the measurements are expected if the booms are short with respect to the Debye length of the plasma explored by the nanosatellite (see following section).
On top of that, nanosatellites can only integrate a limited amount of deployable booms. Therefore, if the sensors of different instruments need to be deployed, then they might be required to share the same boom [de Keyser et al., 2021]. In some cases, for the sake of mass minimization, different instruments are even required to share the same electric sensors. This has consequences on the antenna occupation time and, therefore, on the time resolution of the instrument.
All in all, different problematics are expected to arise when adapting MI instruments to nanosatellite platforms. In the following paragraphs, I describe one by one such problematics and, in some cases, the solutions proposed by COMIX.

1.4.1 Spurious Electric Signals Perturb Mutual Impedance Measurements

Electronic devices onboard the satellite emit electric signals that propagate in the surrounding plasma. After covering the short distance between the nanosatellite platform and the instrument, such signals reach MI antennas and perturb the measurements by reducing their Signal-to-Noise Ratio (SNR). Lower SNRs impact the analysis of the spectra and the plasma diagnostic performances of the instrument. Note that this type of perturbation of the measurements is typically referred to as ElectroMagnetic Compatibility (EMC) [Youssef, 1996]. Onboard large platforms, some typical EMC mitigation procedures consist of, e.g., of shielding of the electronic boards from electro-magnetic perturbations and distancing of the electric sensors from perturbing devices. The mass and volume constraints of nanosatellites prevent us from efficiently implementing such types of procedures. It follows that EMC is an acknowledged problematic for nanosatellites [Korepanov et al., 2001, Pronenko et al., 2015].

In order to limit the loss of diagnostic performance of MI experiments, COMIX plans to mitigate EMC issues by increasing the MI emission amplitude (section 4.1). This will increase the amplitude of the oscillations in the plasma and, consequently, the amplitude of the received signals. As a result, the SNR should be improved. Note however that stronger MI emissions might result in perturbations of the measurements performed by nearby plasma instruments. The extent of such perturbations shall be investigated case by case, as it depends on the specific instruments included in the space missions, on the specific investigated plasma and on the specific MI emission amplitude. This is the first problematic investigated by this PhD work.

1.4.2 Small-Scale Plasma Inhomogeneities Perturb Mutual Impedance Measurements

Satellites and their appendices (e.g. booms carrying instruments) interact with the plasma by collecting charge currents at their surface. The currents charge the satellites, that therefore acquire a given electric potential [Grard et al., 1983, Lai, 2012]. This electric potential perturbs, in turn, the plasma that, in turn, forms a small-scale (i.e. of the order of the Debye length λ_D) inhomogeneous region around the surface of the satellite and its instruments. Such region is called plasma sheath [Tonks and Langmuir, 1929, Riemann, 2008, Allen, 2008]. The plasma sheath is known to perturb different types of plasma measurements.
First, the trajectories of the plasma particles are modified as the particles are accelerated/decelerated due

[3] New technologies are being developed for increasing the deployable length onboard small satellites [Fernandez, 2017]. Hence, while still limited by the mass and volume constraints of nanosatellites, longer deployable lengths might be achieved in the future.

[4] This is not the case for larger satellites, e.g. THEMIS micro-satellites [Auslander et al., 2008].

to the electric potential gradient within the plasma sheath. Hence, measurements of both particles counts (i.e. mass-spectrometer measurements) and particles velocities (i.e. plasma analyzer measurements) are perturbed by the plasma sheath [Bergman et al., 2020].
Second, the electric field of the plasma is modified by the electric potential gradient of the plasma sheath. Hence, electric-field measurements (i.e. electric field measurements of quasi-thermal noise and MI measurements) are perturbed by the plasma sheath [Marchand et al., 2010].
Third, the plasma sheath is inhomogeneous and, therefore, it perturbs the plasma density diagnostic of some monitoring techniques that correspond to very local measurements (e.g. Langmuir Probe measurements) [Johansson et al., 2020, 2021].
To minimize the perturbations that the plasma sheath introduces on the measurements, plasma diagnostic instruments are typically placed far from the satellite platform. In the case of nanosatellites, this is not possible. Despite being installed on booms, the instruments remain close to the platform. In this context, I need to quantify the impact that plasma inhomogeneities such as the plasma sheath have on MI measurements. In the case of a significant impact, I need to devise a proper counter strategy to the perturbations. This is the second problematic investigated by this PhD work.

1.4.3 Antenna Sharing Reduces Measurements Time Resolution

The mass and volume constraints of nanosatellites limit not only the size of the booms, but also the number of booms carried by nanosatellites. This means that, if multiple plasma instruments are carried, each boom might need to deploy multiple instruments. Depending on the volume of the sensors, accommodating multiple instruments on the same boom is not always a simple task. Recently, for the sake of payload mass minimization, different plasma diagnostic instruments are even required to share their sensors. Despite the optimization of the mass of the platform, experiments that share their sensors need to schedule their antenna occupation time. As a result, the time resolution of MI measurements onboard nanosatellites would be affected. Lower time resolutions can impact the scientific analysis of the measurements, as the fast variations of the plasma cannot be observed.
To counteract the reduced time resolution, I need to identify new faster MI instrumental modes. This is the third problematic investigated by this PhD work.

1.5 Objectives of This Study

MI experiments onboard nanosatellites are perturbed by different problematics (section 1.4), related to EMC issues, to the plasma sheath enveloping the nanosatellite and to antenna sharing between different experiments. To answer such problematics, COMIX plans to (i) improve the SNR of the measurements by increasing the instrument's emission amplitude, (ii) assess how the plasma sheath affects the measurements, (iii) define new fast MI instrumental modes.
To support COMIX in achieving its goals, the objectives of this PhD work are:

- To quantify the impact of strong antenna emission amplitudes on the diagnostic performance of MI experiments and identify the maximum amplitude for which such performances are acceptable according to past and present MI space applications;
- To quantify the effects of plasma inhomogeneities on the diagnostic performance of MI experiments;
- To design, test and validate two new fast MI instrumental modes.

Hereafter, I describe in detail how this PhD work has enabled to achieve each objective.

Note that this PhD work focuses on MI experiments performed in unmagnetized plasmas that correspond to a simplified analysis of MI measurements. As discussed in section 5.5, the impact of the magnetic field on MI measurements will be addressed by future studies.

1.5.1 Consequence of Strong Antenna Emission Amplitudes on the Diagnostic Performance of Mutual Impedance Experiments

Spurious electric signals reduce the SNR of MI measurements. In response, COMIX plans to counter the perturbation by increasing the MI antenna emission amplitude. On the one hand, if the plasma response to MI emissions is linear, stronger emissions correspond to stronger received signals. If the noise of the measurements is uncorrelated, then the SNR of MI measurements improves by increasing the emission amplitude. On the other hand, if the MI emission is too strong, then the energy injected in the plasma can be significant w.r.t. the electron thermal energy (i.e. significant electric-to-thermal energy ratios). In such case, the large amplitude of the waves injected in the plasma triggers different types of non-linear plasma interaction, such as wave-particle and wave-wave interactions.
Wave-particle interactions modify the electron distribution function [O'Neil, 1965]. Large amplitude plasma waves are emitted and propagate in the plasma with given group and phase velocity. Electrons that move in phase with the plasma waves perceive a constant electric field that accelerates/decelerates them. If the emission is sufficiently strong, then such electrons get trapped in the potential wells of the large amplitude waves. Signatures of trapped electrons are visible in phase-space domain as vortices of the electron distribution function. Such vortices are located in phase-space at velocities near the phase velocities of the emitted plasma waves. Figure 1.3 illustrates the signature of trapped electrons in phase space.

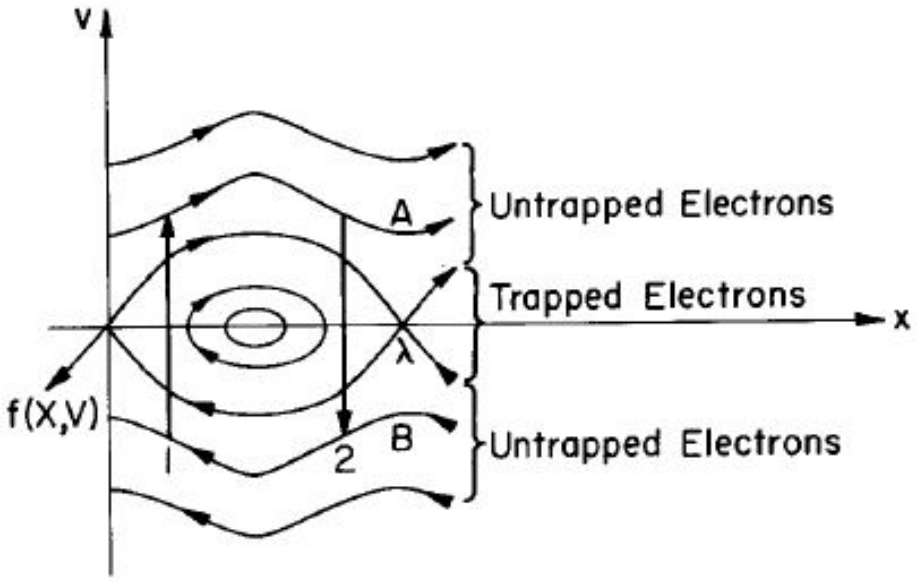

Figure 1.3: Trapped electrons form vortices in phase space. [Credits: Berk and Roberts [1967].]

Wave-wave interactions, such as parametric excitation processes [**?**], trigger plasma waves by draining the energy of the strong plasma oscillations generated by the instrument towards other modes. For instance, in the case of these electrostatic parametric excitation processes, the emitted strong amplitude plasma wave $(k,\, \omega)$ excites two waves, $(k_1,\, \omega_1)$ and $(k_2,\, \omega_2)$ that respect the resonant relation [Sagdeev and Galeev, 1969]:

$$\begin{cases} k = k_1 + k_2 \\ \omega = \omega_1 + \omega_2 \end{cases} . \tag{1.1}$$

Note that the plasma waves $(k_1,\, \omega_1)$ and $(k_2,\, \omega_2)$ are excited only if they are eigenmodes of the system. Since my work assumes an unmagnetized plasma, this means that each of the two waves needs to be

solution of either the Langmuir waves dispersion relation [Krall and Trivelpiece, 1973]:

$$\frac{\omega_L^2}{\omega_p^2} = 1 + 3k_L^2\lambda_D^2 \tag{1.2}$$

or solution of the Ion Acoustic Waves dispersion relation [Krall and Trivelpiece, 1973]:

$$\omega_{IAW}^2 = (k_{IAW}^2 C_s^2)/(1 + k_{IAW}^2\lambda_D^2) \tag{1.3}$$

with $\lambda_D = \sqrt{(\varepsilon_0 k_B T_e)\,/\,(e^2 n_e)}$ the Debye length and $C_s = \sqrt{(k_B T_e)/m_i}$ the ion sound-speed, where ε_0 is the vacuum permittivity, e is the electron charge, k_B is the Boltzmann constant, T_e is the electron temperature and m_i is the ion mass.

In all, plasma waves emitted by the MI instrument are perturbed by wave-particle interactions, that modify the distribution function of electrons, and by wave-wave interactions, that drain the energy of the strong plasma waves towards other oscillations. But the typical procedures used for the analysis of MI measurements (section 2.2) assume that the plasma is characterized by specific distribution functions and that the energy injected by the emitting antennas excites plasma oscillations only at the emitted frequencies. Hence, non-linear plasma interactions are expected to perturb the diagnostic performance of MI experiments.

In this context, my first objective is to investigate the plasma perturbations generated by strong MI antenna emission amplitudes and quantify the largest amplitude for which MI diagnostic performances are acceptable (i.e. similar to typical performances, according to recent MI space applications).

In practice, I use a numerical model to simulate MI measurements for different antenna emission amplitudes. I build MI spectra from the numerical measurements. I retrieve the apparent plasma density and electron temperature from the numerical spectra. Then, I repeat the process for different emission amplitudes to identify for which amplitude range the plasma diagnostic performances are not perturbed by the emission amplitude. The numerical model is described in section 3.1, while the numerical experiments and their analysis are described in section 4.1.

Note that strong emission signals might trigger EMC issues with nearby instruments, whose measurements might be perturbed by the large-amplitude MI signals. This issue needs to be adressed case by case, considering the specific mission and associated payload instruments.

This first investigation has been the subject of the publication shown in section 6.1.

1.5.2 Significance of Plasma Sheath on Mutual Impedance Plasma Diagnostic Performances

The nanosatellite's plasma sheath is expected to surround MI electric sensors due to the short deployable booms that nanosatellites can carry into space. Therefore, COMIX needs to quantify the impact that plasma inhomogeneities have on the diagnostic performance of MI measurements. Although the impact of medium to large scale inhomogeneities on propagating plasma waves is known, at the state-of-the-art no analytic model for the propagation of MI emission signals through the plasma sheath exists.

Medium to large scale (i.e. of scale much larger than the wavelength of the emitted waves) plasma inhomogeneities are known to significantly impact the propagation of plasma waves (WKB solutions) [Wentzel, 1926, Kramers, 1926, Brillouin, 1926]. Their medium to large scale variations of the plasma density correspond to medium to large scale variations of the local plasma frequency. As plasma waves oscillating at a given frequency propagate through the inhomogeneity, the variations of local plasma frequency modify the Landau damping of the waves. This results in vanishing (resp. reflecting) plasma waves for strong reductions (resp. increase) in the local density (e.g. [Westcott, 1962, Krasnoselskikh et al., 2019]).

If small-scale and medium to large scale plasma inhomogeneities have similar impact on propagating plasma waves, then MI experiments are expected to be significantly impacted.

To support COMIX, the second objective of this PhD is to quantify for the first time what is the impact that small-scale plasma inhomogeneities such as the plasma sheath have on the MI plasma diagnostic performance. On top of that, I verify if small-scale (such as those generated by spacecraft charging) and medium to large scale plasma inhomogeneities (such as those generated by plasma compressible fluctuations) have the same effects on MI measurements.
To do so, I use numerical simulations (Vlasov-Poisson model described in section 3.1) to investigate MI measurements performed in the presence of specific plasma inhomogeneities, associated to specific density profiles. In function of the inhomogeneity, I identify the plasma density and electron temperature diagnostic performances derived from the corresponding MI spectra. The details and results of this second investigation are discussed in section 4.2.

This second investigation shall be the subject of a future publication, which submitted manuscript is shown in section 6.2.

1.5.3 Test and Validation of Two New (Fast) Mutual Impedance Instrumental Modes

Onboard nanosatellites, the time resolution of MI experiments is limited by the sharing of the antennas with other experiments. COMIX plans to answer such perturbation by defining new (faster) experimental procedures (instrumental modes) that will enable higher time resolution measurements. To support COMIX, my third objective is to test and validate the new MI instrumental modes.
Practically, I use numerical simulations (Vlasov-Poisson model from section 3.1) and experimental tests (LPC2E testing facility described in section 3.2) of MI experiments. The numerical simulations reproduce the response of the new instrumental modes. Such response is compared to that of the reference MI instrumental mode typically used for space applications. The experimental tests validate the two new modes in a plasma representative of Earth's ionospheric plasma by comparing the new fast instrumental responses to that of the reference MI instrumental mode. The results of this numerical and experimental investigation are discussed in section 4.3.

This third investigation has been the subject of the publication shown in section 6.3.

1.6 Contents

This PhD manuscript is organized as follows. In Chapter 2, I describe the experimental procedure of MI experiments. In Chapter 3, I describe the numerical model (section 3.1) and the plasma chamber (section 3.2) used for my investigation. In Chapter 4, I discuss the results of my investigation. In Chapter 6, I show the accepted and submitted papers related to my investigation. In Chapter 5, I discuss the conclusions of this PhD work. In Appendix B, I indicate all the necessary information required to repeat the investigation. In Appendix C, I describe the parallelization of the numerical implementation of the Vlasov-Poisson model.

Chapter 2

Mutual Impedance Experiments

Mutual Impedance (MI) experiments are a type of plasma diagnostic technique used for monitoring in situ the plasma density and electron temperature of space plasmas. In this chapter, I focus on the description of MI instruments. In particular, I detail the typical experimental procedure used for performing MI measurements and I describe the analysis technique used for deriving from such measurements the plasma density and electron temperature. The procedures described hereafter are used in the following chapters for simulating MI experiments and their diagnostic performance both by means of complementary numerical and experimental investigations.

2.1 Mutual Impedance Experimental Procedure: the Frequency Sweep Mode

MI instruments, such as RPC-MIP onboard the orbiter of the Rosetta mission, are composed of one or two emitting electrodes and two receiving sensors, as shown in Figure 2.1. Using MI experiments, the plasma density and electron temperature are derived following five steps. (i) The emitting antennas perturb the plasma with given electric signals. (ii) The receiving antennas simultaneously measure the electric fluctuations of the plasma that are triggered by the emission. (iii) The received electric fluctuations are treated by the onboard software to build MI spectra that present resonant signatures in correspondence to characteristic frequencies (eigenfrequencies) of the probed plasma. In the simplified case of an unmagnetized plasma characterized by Maxwellian electrons, the spectra present only one resonance for frequencies of the order of the plasma frequency [Storey et al., 1969]. The analysis of the resonant signature found in the MI spectra enables the identification of the (iv) plasma density and (v) electron temperature.

Note that the experimental procedure discussed in the following sections is the same procedure that I use in the following chapters to perform MI measurements.

2.2 Instrumental Mode: the Frequency Sweep Mode

In this section, I describe in detail the state-of-the-art procedure used for performing MI experiments, the so-called *frequency sweep* instrumental mode following the five steps introduced previously. In particular, I describe (i) the emission process, (ii) the reception process and (iii) the analysis used for building MI measurements from the received signals.

(i) During the emission process, the emitting antennas inject in the plasma a succession of j sinusoidal electric signals, with j the number of emitted frequencies. The signals excite the plasma over the frequency range (f_{min}, f_{max}) embedding the plasma frequency f_p, with f_{min} (resp. f_{max}) the lowest (resp. largest) scanned frequency. The $i-th$ emitted electric signal $V_{sw,i}$, associated to the emitted frequency f_i, reads:

$$V_{sw,i} = A\sin(2\pi f_i t) \quad t_{i-1} < t < t_i \tag{2.1}$$

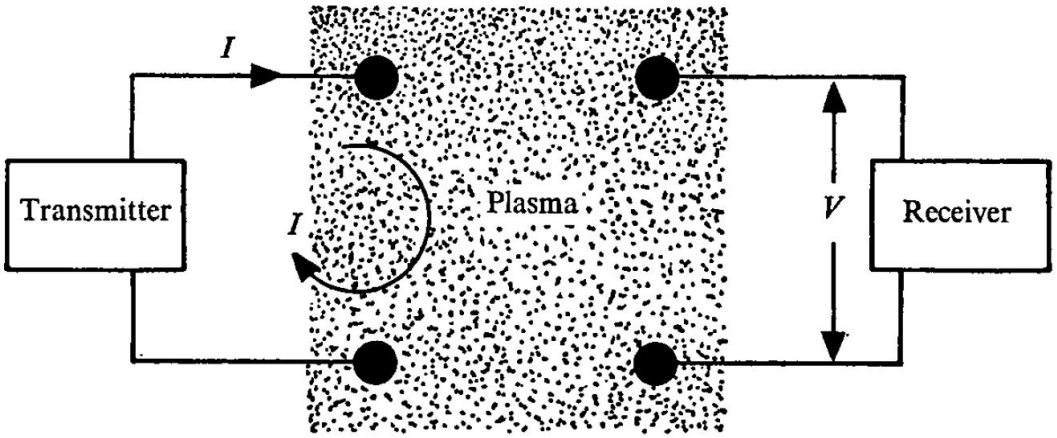

Figure 2.1: Schematics of Mutual Impedance Instruments. Credit: Chassériaux et al. [1972].

with A the amplitude, $f_i = f_{min}\,(1+\Delta)^i\,, i = 0, ..., j-1$ the frequency, $t_i = t_{i-1} + T_i$ the ending time of the emission of the $i-th$ frequency, $T_i = N/f_i$ the emission duration of $V_{sw,i}$, Δ the relative frequency resolution of the measurement and N the amount of repetitions of the oscillation period of f_i. In this document, I fix $\Delta = 0.05$, which corresponds to a plasma density resolution of $|n_e|/n_e = 10\%$, with n_e the plasma density. A relative plasma density resolution of 10% is typically consistent with the scientific needs of space exploration missions.

(ii) During the reception process, the electric oscillations triggered in the plasma by the emission are retrieved by measuring simultaneously the electric potential difference between two receiving sensors embedded in the plasma. In particular, for each $i-th$ emission, a simultaneous $i-th$ reception of about [1] the same duration T_i is performed. Therefore, the duration of one frequency sweep measurement corresponds to the total duration of the emission, which is $T_{sw} = N\sum_{i=0}^{j-1} 1/f_i$.

(iii) MI spectra are built from the received signals as follows. For each $i-th$ emission, a Discrete Fourier Transform (DFT) at frequency f_i is computed on the $i-th$ received signal. By doing so, a spectral energy component is obtained for each frequency and a MI spectrum is built. Then, to account for the instrument transfer function and highlight the plasma response, the spectra are normalized to the vacuum response of the instrument (i.e. MI spectra measured in vacuum). The spectra obtained for an unmagnetized plasma composed of a single electron population exhibit only a resonance, at the plasma frequency.
Figure 2.2 shows an example of normalized MI spectra obtained from measurements of the ISOPROBE experiment onboard the ARCAD3 satellite [Béghin et al., 1982], for the frequency range (4.4 MHz, 6.4 MHz).

In the following sections, I describe the reference procedures used for identifying the plasma density and electron temperature from MI spectra.

2.3 Plasma Diagnostic: the Plasma Density

(iv) In this section, I describe the procedure that I use in the following sections to identify the plasma density from MI measurements.

The plasma frequency f_p is identified from the position of the MI spectra resonant peak [Storey et al., 1969, Béghin and Debrie, 1972, Rooy et al., 1972, Pottelette et al., 1975, Décréau et al., 1978, Pottelette

[1] The reception might be shorter than the emission for the purpose of discarding initial transients related to the beginning of the emission.

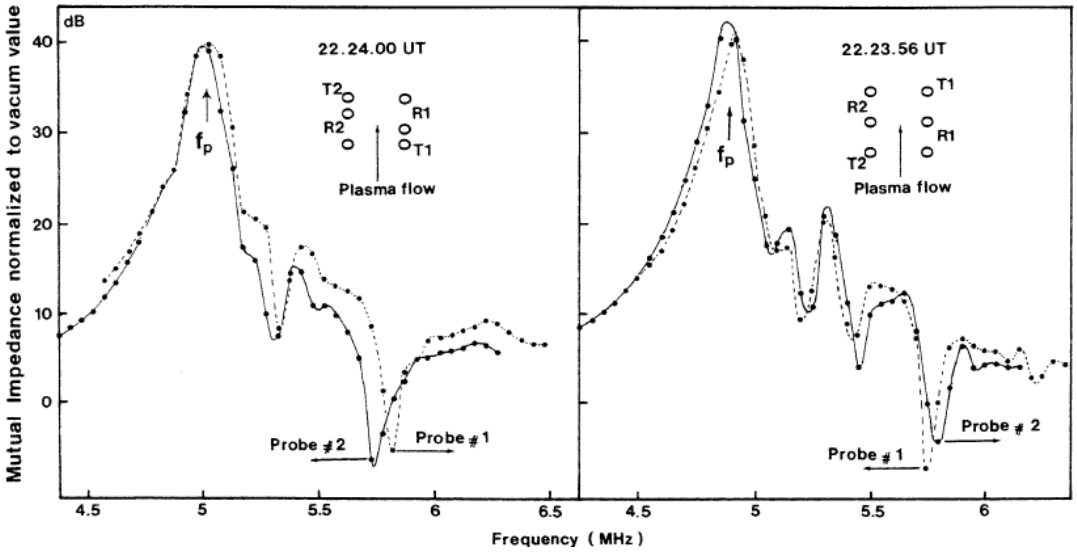

Figure 2.2: Mutual impedance spectra measured by the ISOPROBE experiment onboard ARCAD3. For both left and right panels, the amplitude (dB) of the spectra is represented in function of the investigated frequencies (MHz). Image adapted from Béghin et al. [1982].

and Storey, 1981, Bahnsen et al., 1988, Grard, 1997, Geiswiller et al., 2001, Gilet et al., 2017]. For instance, in the case of ISOPROBE measurements shown in Figure 2.2, the resonant peak of the spectra (f_p) is found at about 5 MHz (both for left and right panels). The density n_e is computed from the definition of the plasma frequency:

$$n_e = \frac{\varepsilon_0 m_e (2\pi f_p)^2}{e^2} \tag{2.2}$$

with ε_0 the vacuum permittivity, m_e the electron mass and e the electron charge.

Note that the frequency corresponding to the position of the resonance of the spectra might differ from the actual plasma frequency of the probed medium, according to the frequency resolution Δ of MI measurements. In particular, MI measurements injects in the plasma a series of discrete frequencies, according to the investigated frequency range and according to the freqeuncy resolution Δ. The plasma frequency might not correspond to one of the frequencies emitted by the MI instrument despite being embedded in the investigated frequency range. In such a case, the MI spectrum has a resonant signature that peaks at the frequency closest to the plasma frequency. If the apparent plasma frequency is identified as the position of the maximum of the spectra, then there could be discrepancies between the apparent and the actual plasma frequencies up to Δ. In my investigation, I have found that such discrepancies are significantly reduced if the plasma frequency is identified after applying a polynomial interpolation of second order to the spectra. In this PhD work, I therefore derive the plasma density after interpolating the MI spectra. In the next chapters, the apparent plasma density indicates the density derived from the MI spectra. The actual plasma density is the density that I aim to measure with MI experiments.

2.4 Plasma Diagnostic: the Electron Temperature

(v) In this section, I describe the procedure used in the following chapters for identifying the electron temperature from MI measurements. The electron temperature is identified from the shape of the resonant peak. Different techniques are or can be used for this aim.
The first technique identifies the position of local minima, the so-called anti-resonances, for frequencies larger than f_p (e.g. the local minima at $f = 5.3\ MHz$ and $f = 5.7\ MHz$ in the left panel of Figure 2.2) [Geiswiller et al., 2001]. A local minimum at a certain frequency f_i indicates that the distance between

the emitting and receiving antennas is a multiple of the wavelength of the plasma wave triggered by the corresponding $i-th$ emission. The wavelength normalized to the Debye length is known after the identification of the plasma frequency, considering the dispersion relation of Langmuir waves. The actual distance between the sensors is a known parameter, given by the geometric configuration of the instrument's antennas. Hence, by comparing the wavelength and the distance between sensors, one can derive the Debye length, from which the electron temperature can be computed, knowing the density.
The second technique consists of analyzing the amplitude sharpness of the resonant peak [Chassériaux et al., 1972, Décréau et al., 1978]. The sharpness is related to the spatial Landau damping of the plasma waves propagating from the emitting to the receiving antennas. In practice, for each Langmuir wave triggered in the plasma by the emission [Béghin, 1995], the amplitude scales with the distance x from the emitting antennas as $\exp(-k_i\ x)$ [Podesta, 2005], with k_i the complex part of the waves' wavenumbers (spatial Landau damping). Note that k_i is known in function of the Debye length for each frequency above the plasma frequency ($f_i > f_p$), once the plasma frequency has been computed. Since the distance between the sensors is also known, the Debye length is identified from the damping of the different emitted waves. From the Debye length, knowing the plasma density, the electron temperature is computed.
The third technique consists of comparing the investigated experimental spectrum to a series of synthetic reference spectra [Wattieaux et al., 2020]. Each reference spectrum is computed numerically, for a given distance (in amounts of Debye length) from the emitting antennas, in function of the plasma frequency. The comparison consists of computing the root mean squared error:

$$\xi = \sqrt{\sum (x_i - y_i)^2 / L} \tag{2.3}$$

with L the amount of emitted frequencies, x_i and y_i the Fourier components corresponding to the $i-th$ emitted frequency for the investigated and reference spectra, respectively. From the comparison, a matching reference spectrum is identified as the one corresponding to the minimum root mean squared error. The distance d_{app} for which the matching spectrum was computed is, then, associated to the investigated spectrum. Note that d_{app} is known in function of the Debye length. Hence, by comparing d_{app} to the actual distance d_{ph} between the sensors, the Debye length is identified. From the Debye length, knowing the plasma density, the electron temperature is computed.
In my investigation, I use this third technique to compute the electron temperature associated to each investigated spectrum. Note that the comparison is not always performed using the full spectrum (green and blue lines of Figure 2.3). Sometimes, depending on the application, only subparts of the spectra (gray region of the spectra from Figure 2.3) are actually necessary and therefore used for the analysis. In my analysis, for each application of this technique, I will give the details on the portion of the spectra used for the comparison.

In the next chapters, the apparent electron temperature indicates the temperature derived from the MI spectra. The actual electron temperature is the temperature that I aim to measure with MI experiments.

2.5 Models Describing the Mutual Impedance Instrumental Response

In this section, I briefly describe the two reference models typically used for investigating the instrumental response of MI experiments.

- The DSCD model developed by Geiswiller et al. [2001] is used for quantifying the plasma response of MI experiments by taking into account the shape of both MI emitting and receiving sensors and the shape of the satellite on which such sensors are installed. In particular, the DSCD model is based on the solution of the linearized Vlasov-Poisson equations computed in a homogeneous plasma. The model is used for computing the electric charges and the electric potential that specific emitted electric signals induce on the nearby conductive surfaces. Hence, it is used for building MI spectra by taking into account the particular geometry of the instrument, of its electrodes and of the satellite on which the instrument is mounted. The DSCD model assumes

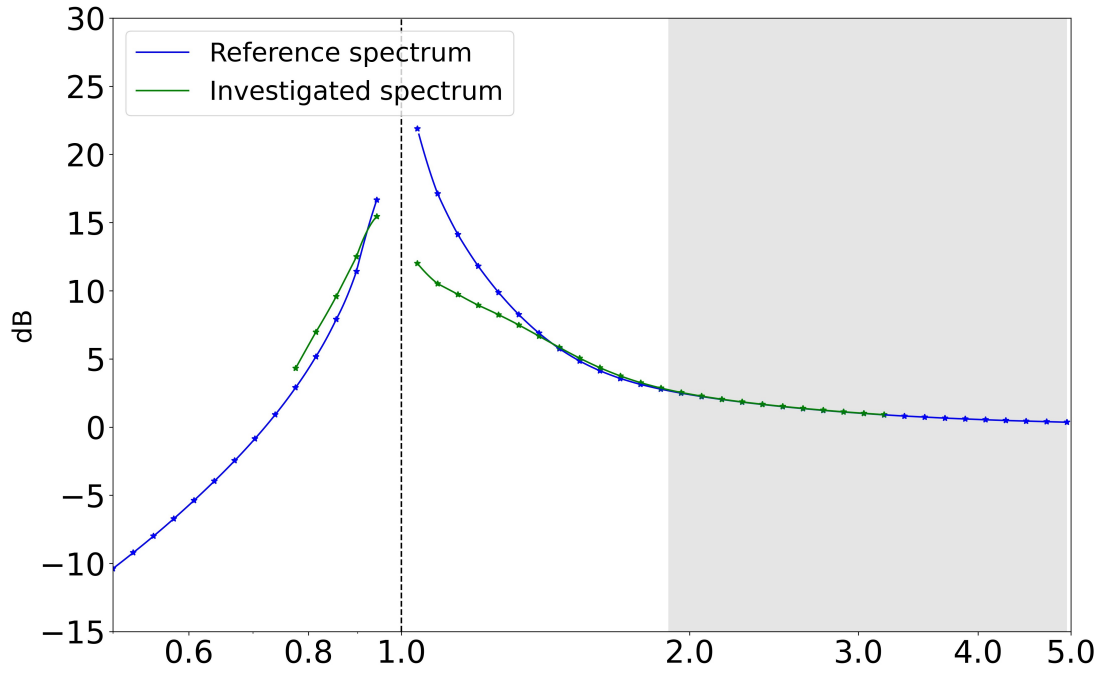

Figure 2.3: Example of comparison of Mutual Impedance spectra. The investigated spectrum (green line) is compared to a reference synthetic spectrum (blue line).

long emission durations perturbing a homogeneous unmagnetized plasma and triggering negligible perturbations of the plasma dielectric. Such model is the reference for the investigation of MI measurements. It was used in the past [Wattieaux et al., 2019, 2020] for investigating RPC-MIP measurements performed onboard the Rosetta spacecraft to investigate the coma of comet 67P-CG.

- The model developed by Gilet et al. [2017] is used for assessing the impact that different particles distribution functions have on 3D MI experiments. Basically, such model derives the plasma response to MI emissions of long duration (i.e. neglecting all types of transient effects) by solving the Vlasov-Poisson system of equations in the case of small perturbations of the plasma dielectric, an unmagnetized homogeneous plasma, isotropic particles distribution functions and MI emitting sensors of negligible size with respect to the Debye length of the plasma. This model was used for the analysis of RPC-MIP measurements (Rosetta mission) performed in the presence of multiple electron populations that correspond to double peaks in the resonant signature of MI spectra.

Note that both models described above assume an unmagnetized homogeneous plasma perturbed by MI emissions of long duration and associated to negligible perturbations of the plasma dielectric, as expected for a linear plasma response. In this PhD work I investigate for the first time the impact that strong emissions, inhomogeneous plasmas and fast MI measurements have on the diagnostic performance of MI experiments. Such topics cannot be investigated using past MI models. Hence, a new model is required. In the following chapter, I describe the tools (numerical model and experimental facility) which I use to reach the objectives described in section 1.5.

Chapter 3

Tools: the Numerical Model and the Plasma Chamber Testing Facility

In this chapter, I describe the tools that enable my investigation. First, a full kinetic Vlasov-Poisson 1D-1V model that I use to simulate numerically MI experiments (section 3.1). Second, the testing facility of the space laboratory LPC2E (section 3.2), which I use to perform MI experiments in a plasma medium that is representative of space. In chapter 4, I use these tools to (i) quantify the impact on the MI diagnostic performance of non-linear plasma interactions triggered by strong emission amplitudes (section 4.1), (ii) assess the effects of the nanosatellite's plasma sheath on MI measurements (section 4.2) and (iii) test and validate the performances of the new fast MI instrumental modes (section 4.3) against those of the reference frequency sweep mode described in chapter 2.

3.1 The 1D-1V Full Kinetic Vlasov Poisson Numerical Model

I simulate numerically MI measurements using a full kinetic Vlasov-Poisson model in cartesian geometry. Such model solves the Vlasov-Poisson system of equations that evolves in time a numerical plasma box perturbed by MI emission signals. The model that I use is a 1D-1V unmagnetized version of the model developed by Mangeney et al. [2002]. In particular, it is the same version that was used in the past by Henri et al. [2010] to study Langmuir Electrostatic Decay processes observed in the presence of solar type-III radio emissions during the STEREO mission.

Equations describing the Vlasov-Poisson model

The model evolves in time a numerical plasma box by solving the Vlasov equation for both the electron and the ion distribution functions ($f_e\left(t,x,v_e\right)$ and $f_{ion}\left(t,x,v_{ion}\right)$, respectively, where t is the time, x is the position and v is the velocity):

$$\frac{\partial f_\gamma\left(x,t,v_\gamma\right)}{\partial t}+v_\gamma\frac{\partial}{\partial x}f_\gamma\left(x,t,v_\gamma\right)-\frac{q_\gamma}{m_\gamma}E\frac{\partial}{\partial v_\gamma}f_\gamma\left(x,t,v_\gamma\right)=0 \tag{3.1}$$

where $\gamma=e,ion$ is the particle species, q_γ and m_γ are the electric charge and mass of the particles, E is the electric field. Such electric field is computed self-consistently from the particles density profiles using the Poisson equation:

$$\frac{\partial E}{\partial x}=e\frac{n_{ion}-n_e\left(x,t\right)}{\varepsilon_0}+\frac{\rho_{ext}\left(x,t\right)}{\varepsilon_0} \tag{3.2}$$

where n_e (resp. n_{ion}) is the electron (resp. ion) density and ρ_{ext} is the external charge density that I use for modeling MI emitting electric antennas. Such external term is an addition that I made to the already implemented code in order to simulate MI measurements. It enables external perturbations of the box which are consistent with MI emissions. The validation of this external source term is discussed in

section 3.1.3. The oscillating electric charge that I impose to the external localized MI emitting antennas reads:

$$\rho_{ext}(x,t) = \sigma\delta(x)\ \sin(\omega t) \tag{3.3}$$

where σ is the amplitude of the electric charge and $\omega = 2\pi f$ is the emitted angular frequency. This external oscillating charge is consistent with the MI emission signals described in chapter 2 (EQ. 2.1). Note that a localized external charge density term in 1D cartesian frame corresponds in 3D space to an infinite, uniformly charged plane [Podesta, 2005]. For simplicity, I model such plane as a transparent grid such as a fine metallic grid and, thus, I neglect the currents that the antennas collect from the plasma. The actual antenna configuration of the numerical model is discussed in detail in section 3.1.2.

Normalization of the numerical model

The model is normalized using electron characteristic quantities: the elementary charge e, the electron mass m_e, the Debye length λ_D, the time ω_p^{-1}, where $\omega_p = 2\pi f_p$ is the angular plasma frequency, and n_0 is the mean density. Consequently, the velocities are normalized to the electron thermal speed $v_{th,e} = \lambda_D\omega_p$, the electric field to $E = (m_e v_{th,e}\omega_p)/e$, the electric potential to $V_0 = (k_B T_e)/e$ and the electric charge at the antenna to $\bar{\sigma} = en_0\lambda_D$.

Boundary condition

The boundary conditions are periodic in physical space. In velocity space, I assume vanishing distribution functions for velocities outside a given velocity range (e.g. $f_\gamma(x, |v_\gamma| > v_{\gamma,max}, t) = 0$ with $v_{\gamma,max}$ up to 40

The numerical model is initialized by imposing at $t = 0$ both the Poisson equation and the Ampère equation. In particular, (i) the electric field generated by the emitting antennas is imposed consistent with the net charge density profile and (ii) the net currents in the plasma are imposed consistent with the current injected in the box by the emitting antennas. Note that, by imposing the Poisson and Ampère equations at initialization, I ensure that such equations are respected also at later stages of the numerical simulations [Besse, 2009].

Poisson equation at initialization

The profiles that I use to initialize the net charge density depend on the objectives of the simulation. In the case of the assessment of the perturbations that strong emission amplitudes introduce on MI measurements (section 4.1) and for the investigation of the new fast MI instrumental modes (section 4.3), I impose in the numerical box an initially homogeneous plasma (i.e. $n_e = n_i = n_0$). For the investigation of the impact of the nanosatellite's plasma sheath on MI measurements, I impose at $t = 0$ density profiles corresponding to the plasma inhomogeneity of interest. The derivation of such inhomogeneous profiles is described in section 4.2.

The oscillating charge σ at the emitting antennas is initialized to zero (i.e. $\sigma(t = 0) = 0$). Hence, according to the Poisson equation, the self-consistent initial electric field for homogeneous plasmas is initialized to zero everywhere inside the numerical box ($E(x, t = 0) = 0$).

The Ampère equation

The Ampère equation imposes the consistency between the electric field and the currents in the numerical box. The analytic expression of the electric field generated by each emitting antenna is composed of a far-field and a close-field component [Podesta, 2005] (the nature of such components is discussed in detail in section 3.1.2). The close-field ($E_b(x,t)$, where x is the position in the box) is the wave-component and it propagates from the emitting antennas to the surrounding plasma. Its contribution at $t = 0$ is equivalent to zero everywhere ($E_b(x, t = 0) = 0$). The far-field term ($E_a(x,t)$) is the component of the

electric field that corresponds to the cold-plasma response. In the 1D case, it reads:

$$E_a(x,t) = \frac{\sigma \sin(t\omega)}{2\varepsilon_0(1-\frac{\omega_p^2}{\omega^2})} sgn(x) \tag{3.4}$$

where $sgn(x)$ is the sign function. According to the Ampère equation, such electric field is actually generated in the box only if the current at each position ($j_{tot}(x,t)$) corresponds to:

$$j_{tot}\,(x, t=0) = -\varepsilon_0 \frac{\partial E_a}{\partial t}(x, t=0). \tag{3.5}$$

If the current inside the box is different from j_{tot}, then transient effects are triggered and the electric field differs from E_a.

The currents in the box at $t = 0$ are composed of the plasma's and the emitting antennas' contributions. If electrons and ions are initialized with Maxwellian distribution functions and the plasma is homogeneous, then the plasma's contribution is zero at each position in the box. The antennas' contribution is computed from the currents that they inject in the plasma at $t = 0$, that reads:

$$j_{ext}\,(t=0) = \sigma\omega. \tag{3.6}$$

But the antennas' contribution differs from the current j_{tot}. Hence, if the particles are initialized as Maxwellian, then transient effects are triggered in the box and the generated electric field differs from EQ. 3.4. Note that this phenomenon actually takes place in the case of MI space applications. Consider a MI instrument embedded in a homogeneous Maxwellian plasma. Before beginning the measurement, MI electrodes are polarized to a zero electric potential. When the emission begins, according to the Ampère equation, the electric field emitted by the MI instrument is compatible with that from EQ. 3.4 only if the current contribution from the plasma and from the antennas matches j_{tot}. But there is no reason for the plasma to provide the exact required contribution before the emission begins. This means that, according to the Ampère equation, MI instruments in space trigger transient effects with their emission, as expected [Derfler and Simonen, 1969]. Thus, when the emission begins, the electric field generated by the instrument is modified by such transients. However, in the case of my numerical simulations, one can modify the initial distribution functions to ensure that transient effects related to the beginning of the emission can be neglected. Considering that the impact of such transient effects on MI measurements is beyond the scope of my analysis, I modify as follows the initial electron distribution functions to impose that the current provided by the plasma at $t = 0$ is the one consistent with j_{tot} and j_{ext}.

Instead of using Maxwellian distributions to initialize the electron population I use shifted Maxwellian distributions in order to control the initial current. The shift (v_{offset}) of the distributions is computed for each position in the box from the difference between the current expected analytically j_{tot} and the current injected at that same position by the emitting antennas j_{ext}. This velocity offset reads:

$$\frac{v_{offset}}{v_{the}} = \frac{\sigma}{2}\frac{\omega/\omega_p}{\omega^2/\omega_p^2 - 1}. \tag{3.7}$$

In the following section, I describe how the external emitting antennas are arranged inside the numerical box.

3.1.2 Modeling of Mutual Impedance Emitting Sensors

In this section, I describe the MI emitting antennas and their configuration in the box.

Each 1D emitting antenna is equivalent, in 3D, to an infinite planar grid electrically charged with a given uniform oscillating charge distribution. The grid is assumed to be so thin that the currents collected at its surface are negligible [Buckley, 1968]. Practically, this means that the grid does not collect plasma particles from the numerical box. This assumption is similar to the point-like emission assumption made in previous works investigating MI measurements [Béghin, 1995, Gilet et al., 2017].

The electric field generated by the emitting antennas is composed of a uniform term (the so-called far-field) and a spatially damped term that propagates from the antennas (the so-called close-field) [Podesta,

2005]. The far-field term is equivalent to the electric field expected in the cold plasma limit (i.e. $\omega >> \omega_p$) [Chassériaux et al., 1972]. Such 1D far-field term is the equivalent to the 3D electric field component generated by a point charge and decreasing in $1/d_{ph}^2$, where d_{ph} is the distance from the emitting antenna. The close-field term is the wave-component of the emitted electric field. In 3D, its equivalent is the radial electric field that would propagate from the emitting antennas to the surrounding plasma.

Due to the periodic boundary conditions of the numerical box, the electric field and the potential generated by the emitting antennas need to be spatially periodic. But the 1D far-field component generated by a charged infinite planar grid assumes different values depending on the position (EQ. 3.4). In particular, on the two sides of the 1D electric sensor the far-field component assumes opposite values. Hence, a single 1D emitting antenna does not ensure the periodicity of the electric field and potential in the box. Periodic fields are obtained by using at least two different 1D sensors with opposite electric charge.

A succession of two sensors with opposite charge corresponds to a capacitor of parallel infinite planar electrodes. Such electrodes are embedded in the plasma box which they perturb by means of their polarization charges. The total electric field they generate is equivalent to the sum of the contributions of the two sensors (i.e. far-fields and close-field terms). Hence, similarly to a plate capacitor, the two electrodes generate a total far-field that is doubled (resp. cancels out) in-between (resp. on the sides of) the two electrodes. Considering that the numerical box is periodic, one capacitor is not sufficient to have positions where the far-field is neutralized. That is achieved by placing two sensors polarized with the same electric charge next to each other. Thus, I choose to perturb the numerical box using two capacitors in series, which correspond to a succession of four electrodes polarized with negative-positive-positive-negative electric charges. For such configuration, each electrode is placed next to a different electrode carrying the same charge and, in-between the two, the far-field component of the electric field is neutralized. Note that by using such model one has the possibility to investigate the contribution of the close-field term separately from that of the total electric field (far-field + close-field). Such investigation cannot be performed using 2D or 3D models because the far-field component that they would generate is not constant with the distance from the antennas.

In all, I identified two different geometric antennas configurations called Model A and Model B. Such configurations are illustrated in top and bottom panel of Figure 3.1, where σ is the external charge imposed at the antennas and L is the spatial size of the numerical plasma box.
Model A only enables the simulation of MI experiments with the contribution of the total electric field. It is composed of four emitting antennas arranged in sets of two emitting capacitors. The positions of the electrodes are chosen in order to maximize the distance between any two antennas with opposite charge, as shown in Figure 3.1 top panel.
Model B enables the simultaneous simulation of MI experiments with and without the contribution of the far-field component, depending on the position in the plasma box. This is achieved by building MI spectra from the plasma oscillations retrieved between two electrodes with opposite (resp. same) electric charge, where the amplitude of the far-field component is doubled (resp. cancels out). The positions of the electrodes are chosen to maximize the distance between any two antennas, as shown in Figure 3.1 bottom panel.

The numerical results shown in the following chapters are obtained using the Model B configuration. In order to mimic 3D experimental MI measurements where close-field and far-field term concurr to the total electric field, I present in this PhD work only results that include the contribution of the far-field term. If, in the future, the contribution of only the close-field term is of interest, then one will be able to replicate my analysis using the same outputs from which I derived my results. The datasets used for performing my investigation are available online. The links are given in Appendix B.1. If future studies will investigate MI experiments using the same 1D-1V Cartesian Vlasov-Poisson model that I used for this PhD work, then I suggest the selection of the Model A configuration unless one is interested in the plasma perturbations triggered by only the close-field component of the electric field. In such case, one

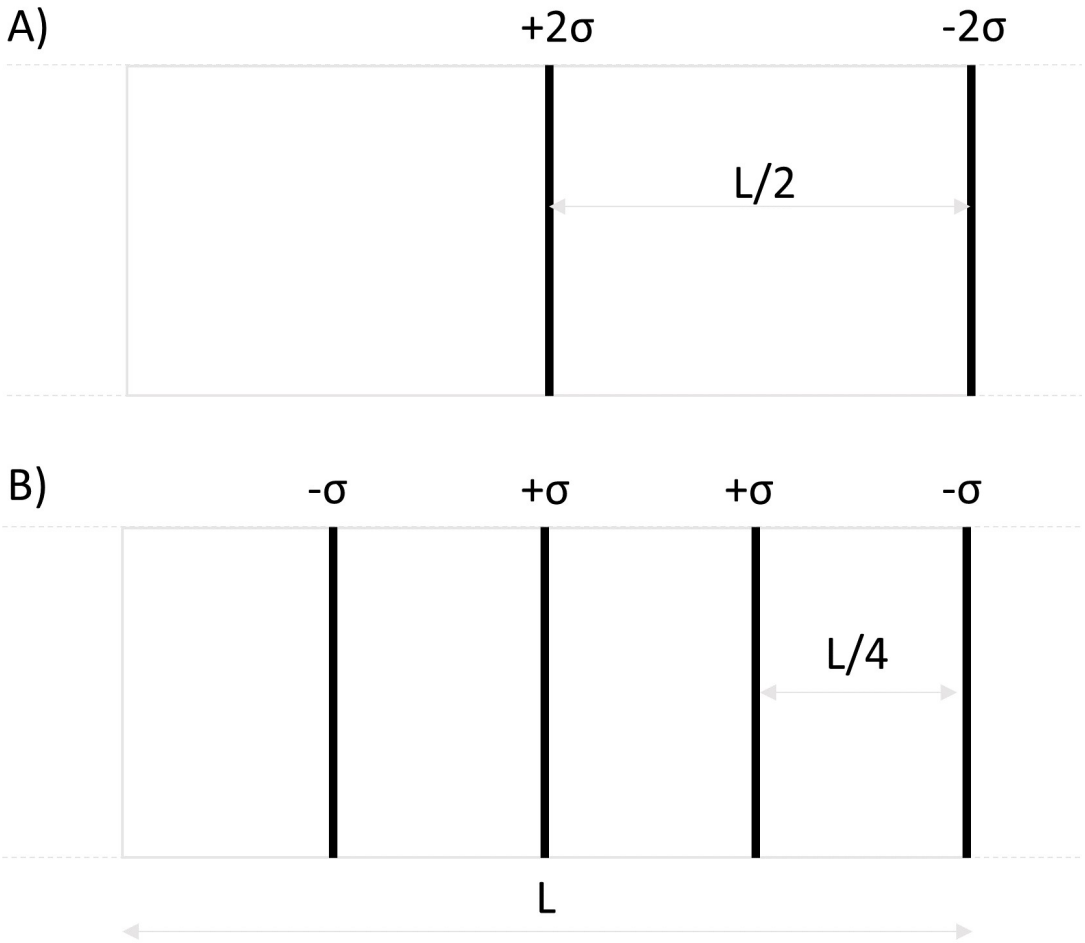

Figure 3.1: Representation of the emitting antennas configuration in the periodic simulation box. The top (resp. bottom) panel represents the model A (resp. B), characterized by two (resp. four) emitting antennas. σ is the oscillating charge used for polarizing the emitting antennas and L is the spatial size of the numerical box.

should use the Model B configuration.

3.1.3 Validation of the Emitting Sensors

I introduced in the Poisson equation of the model an external source term to enable the simulation of MI measurements. Such term was not present in the past version of the model [Henri et al., 2010]. Hence, it needs to be validated.

Hereby, I describe the two different approaches that I used for validating the model.

Validation 1: Comparison with Theoretical Electric Field Waveforms

I compare the theoretical electric field computed analytically to the numerical electric field generated in the plasma box. Such analytic solution is known for specific limits. To ensure the robustness of the validation, I repeat the process for different polarization charges of the emitting electrodes. The theoretical electric field is obtained by solving the 1D-1V Vlasov-Poisson coupled equations as described in Krall and Trivelpiece [1973] and by limiting the analysis to real frequencies and complex wavenumbers, as done in the past by Podesta [2005]. In the following, I compute the actual theoretical electric field curves using the frequency-wavenumber couples that I obtained with the linear Vlasov-Maxwell solver WHAMP [Roennmark, 1982], in the limit of an unmagnetized plasma. Note that the two models are not expected to match at positions where the wave packet has not yet travelled.

Figure 3.2 illustrates an example of the comparison between the numerical (red line) and the analytic (black line) electric fields for the validation of Model A (Panel a) and Model B (Panel b) geometric configurations. In the figure, I indicate with a green shaded area the distance covered by the emitted plasma waves, according to their group velocity.

Along the distance covered by the emitted wave, I find that the oscillations triggered in the plasma box agree with the theoretical oscillations that I computed. Some differences between the numerical and analytical curves are acceptable because my analytic computations only take into account the contribution of the dominant pole of the plasma dielectric [Krall and Trivelpiece, 1973]. In particular, they neglect the contribution of higher-order poles [Derfler and Simonen, 1969] associated to strong damping. Note that the discrepancies shown in Figure 3.2 are representative of the differences between numerical and theoretic electric fields that I found throughout the validation process. Additional extensive validation tests include the comparison between theoretical and numerical curves for different emission durations, different distances from the emitting antennas and different emission frequencies.

Validation 2: Comparison with DSCD Reference Mutual Impedance Spectra

Using a second approach, I validate the modeling of the emitting antennas indirectly, by comparing the numerical MI measurements I obtained with my model to reference spectra obtained using the DSCD model [Béghin and Kolesnikova, 1998, Geiswiller et al., 2001, Wattieaux et al., 2019, 2020]. Note that the DSCD is the reference tool for the modelling of the MI instrumental response.

The DSCD model (section 2.5) takes into account the contribution of nearby conductive surfaces – such as the satellite's metallic surfaces – when simulating the instrumental response of the instrument. Therefore, it is frequently used to better understand the measurements performed by MI instruments in space. But the DSCD model assumes electrostatic linear perturbations of a homogeneous plasma and very long emission durations. Thus, it cannot be used to accomplish the objectives of my study because they involve a non-linear plasma (section 4.1), an inhomogeneous plasma (section 4.2) and fast MI measurements (section 4.3). Hence, I use DSCD simulations of MI measurements only to validate my model. Note that, in contrast to my 1D model, the DSCD neglects all transient effects, such as the delay required by the emitted waves to propagate from the emitting sensors to the surrounding plasma.

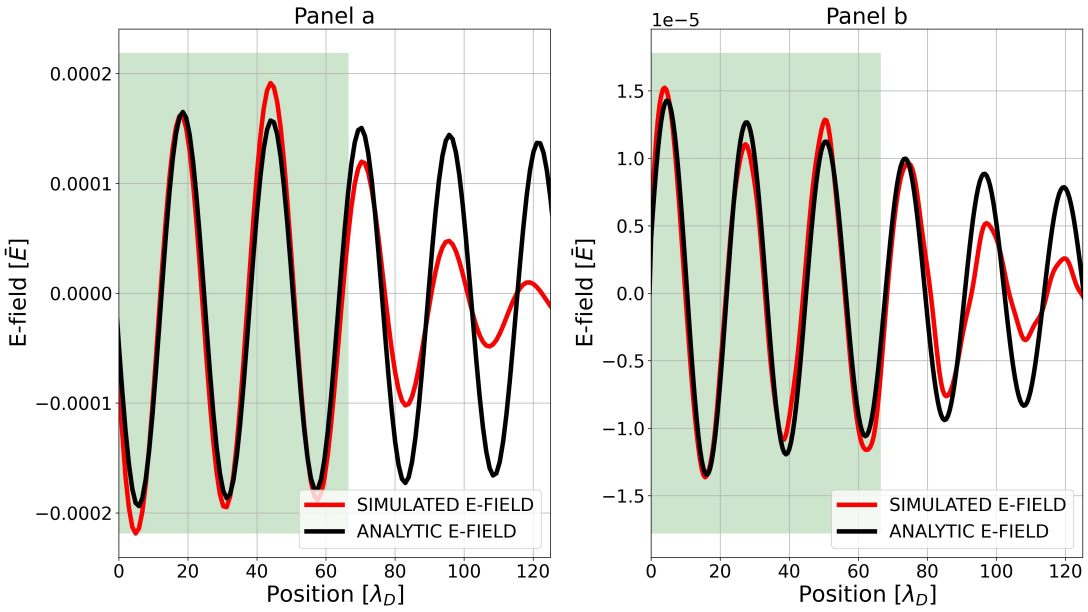

Figure 3.2: Validation of model A (panel A) and model B (panel b). Comparison between the electric fluctuations obtained numerically (red line) and those computed analytically (black line), in function of the emitting-receiving antennas distance, for the emission frequency $\omega = 1.1\omega_p$ and at time $t = 100\omega_p^{-1}$. At such time the emitted wave packet, propagating at group velocity $v_g = 0.67v_{the}$, has covered the distance $d = 67\lambda_D$ (green shaded area).

The DSCD spectra are obtained by recreating in 3D the geometry simulated by the 1D-1V Vlasov-Poisson model. Practically, this means that the emission is performed by infinite planar plates disposed along a specific direction, which is perpendicular to the plates themselves. The reception is performed along that direction, using the same dipolar configuration used in the Vlasov-Poisson model (i.e. antennas at $d_1 = d$ and $d_2 = 2d$).

Figure 3.3 shows the comparison between MI spectra obtained from the Vlasov-Poisson model (blue points) and from the DSCD model (black line) for the distances $d = 0.5\ \lambda_D$, $d = 5\ \lambda_D$, $d = 20\ \lambda_D$, $d = 40\ \lambda_D$ from the emitting antennas (increasing distance from top to bottom panels). Such spectra are obtained following the frequency sweep procedure described in chapter 2, for the frequency range ($0.5\ \omega_p$, $2.0\ \omega_p$) and with the frequency resolution $\Delta = 0.05$. I find that the spectra disagree for d smaller than $5\lambda_D$. This is due to differences in the way the emitting antennas are simulated in the two models. For d larger than $5\lambda_D$, instead, the spectra agree. Therefore, in my investigations I always focus on distances larger than $5\lambda_D$ and neglect the MI spectra obtained for smaller distances from the emitting antennas. Note that a Vlasov description is invalid for distances below $1\lambda_D$. Thus, neither my 1D-1V cartesian Vlasov-Poisson model nor the DSCD model are expected to provide reliable results there.

Note also that the resonant signature in Vlasov-Poisson spectra do not present the same anti-resonant signatures (i.e. local minima) that are found instead in the DSCD spectra. Anti-resonances are found at frequencies where the corresponding wavelength of the emitted waves is a multiple of the distance between the dipolar receiving sensors. Hence, the discrepancy between the spectra is attributed to the duration of the measurements compared by the two models. While, on the one hand, DSCD measurements assume long emissions that begin at $t = -\infty$, on the other hand, Vlasov-Poisson measurements take into account the propagation time of the plasma waves from the emitting to the receiving antennas and, therefore, the finite time of MI experiments.

The model described in this section is used in the next chapter for investigating numerically the diagnostic performance of MI measurements. In the next section, I describe the testing facility used for investigating experimentally MI measurements.

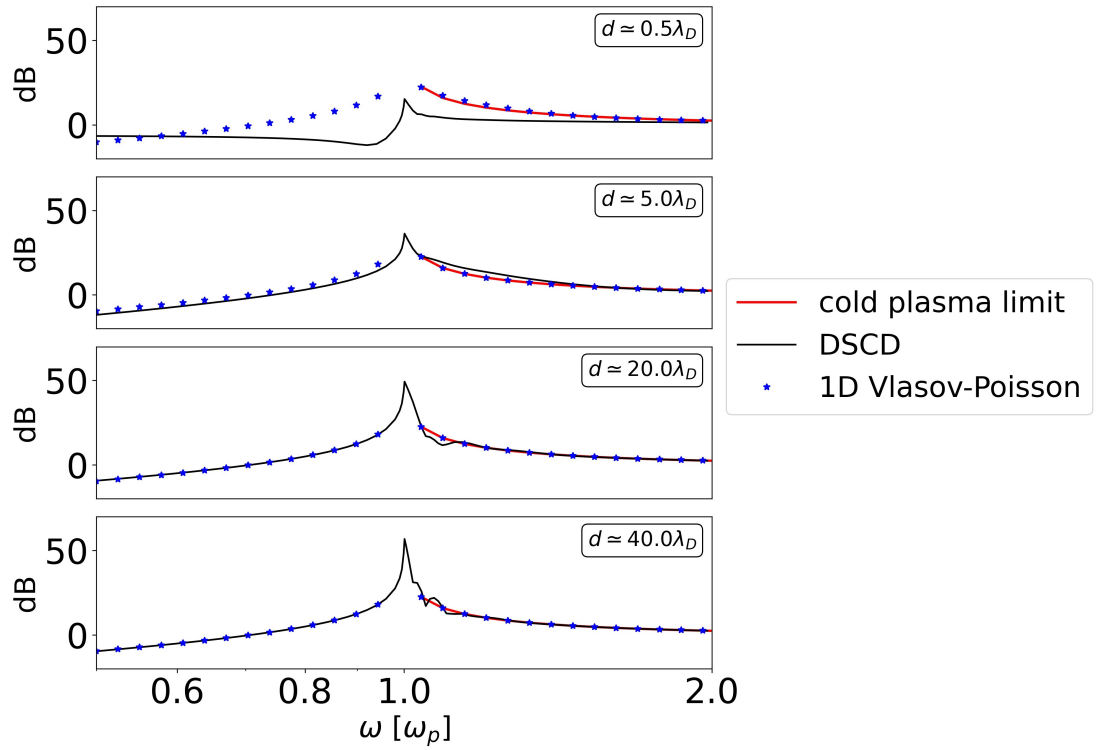

Figure 3.3: Validation of the 1D-1V Vlasov-Poisson model (blue points) using the mutual impedance spectra obtained with the DSCD model (black line). The red line represents the cold plasma response, valid for $\frac{\omega}{\omega_p} >> 1$. Top to bottom panel: the spectra are obtained for the distances $d = 0.5\lambda_D$, $d = 5\lambda_D$, $d = 20\lambda_D$, $d = 40\lambda_D$.

3.2 The PEPSO Testing Facility of LPC2E: the Vacuum Chamber and the Plasma Source

LPC2E (Laboratoire de Physique et Chimie de l'Environnement et de l'Espace, CNRS, Université d'Orléans, CNES, Orléans, France) is a French space laboratory that, among other topics, specializes on MI instruments for in situ space plasma diagnostic. LPC2E owns a testing facility that I developed in the framework of the PEPSO project (Plasma Environment Platform for Satellite tests in Orléans) to enhance instrument validation and prototyping at LPC2E. I have purchased this chamber as a solution to the strong need of the COMIX project of a vacuum chamber designed for testing small MI instruments. In particular, (i) I have purchased the chamber, the pumping system and different equipment devices (e.g. a commercial Langmuir Probe), (ii) I have installed at LPC2E the system and (iii) I have performed a partial characterization of the chamber. Such characterization has been extended by students that I supervised or helped supervising. Figure 3.4 shows the testing facility, that is composed of a plasma chamber, a pumping system and a plasma source.

For the purpose of my investigation, I use the facility to test and validate COMIX instrumental modes in a representative plasma environment (section 4.3). In the following sections, I describe both the facility and the geometric configuration that I use for my experimental tests.

3.2.1 The Plasma Chamber

The principal components of LPC2E's testing facility are the plasma chamber, the pumping system and the plasma source.

The plasma chamber is a metallic chamber fabricated in ALSI304L alloy and shaped as a cylinder with a diameter of 1 m and a length of 1.8 m. Thanks to its size, the chamber can accommodate multiple instruments and small nanosatellites simultaneously. In the case of MI investigations, I only use it for testing MI instruments. In the future, COMIX will use the chamber to test specific MI antennas configurations in the presence of small nanosatellites. Note that the chamber also contributes to the development of other space projects, that are not necessarily related to nanosatellite applications. For instance, I have used the chamber to perform the first plasma chamber tests of COMPLIMENT's merged sensor [de Keyser et al., 2021], in preparation of the Comet Interceptor mission. Such merged sensor is composed of a spherical electric sensor, used for MI and Langmuir Probe measurements, carrying inside a magnetic sensor for local magnetic field monitoring. The tests that I performed, together with LPC2E Comet Interceptor team, aimed at quantifying the impact that magnetic field measurements have on simultaneous MI measurements.

The pumping system is composed of a set of pumps, a primary pump and a secondary pump, that are used for reducing the ambient pressure inside the chamber. First, low pressures are required for turning on the plasma source: if the pressure is above 10^{-3} $mbar$ (10^{-1} Pa) then the plasma source would break due to excessive convective heat exchanges. Second, low pressures reduce the collision rate of neutral particles and make the simulated environment in the chamber more similar to that encounter in space. The primary pump (Pfeiffer/ACP40) removes the neutral gas from the chamber and, by doing so, it brings down the chamber pressure from the ambient pressure of 1 bar ($\simeq 10^5$ Pa) to $10^{-2} mbar$ ($\simeq 1$ Pa). The secondary turbo-molecular pump (Pfeiffer/ATH3204M) is used to further reduce the neutral gas pressure in the chamber, from primary vacuum down to $10^{-6} mbar$ ($\simeq 10^{-4}$ Pa).

The plasma source (Figure 3.5 and Figure 3.6) is a Kaufman type [Kaufman et al., 1982] electric source used for the generation of plasma in the chamber. It consists of a small cylindrical ionization chamber (anode), a cathode (tungsten filament) placed inside the ionization chamber, a solenoid rolled around the source, a filtering grid placed at the exit of the ionization chamber and a neutralizer (tungsten filament, identical to the cathode) placed at the exit of the source. Its working principle is the following. After the ambient pressure of the plasma chamber has been reduced to 5 x $10^{-5} mbar$ or less, a strong

Figure 3.4: The testing facility of LPC2E. The cylindrical vacuum chamber is held by a metallic support frame. The pumping system is installed below the chamber, while the plasma source is attached to the middle of the chamber's door.

electric potential difference is imposed between the ionization chamber and the cathode. A current is sent to heat the cathode. When sufficiently hot[1], the cathode emits electrons by means of thermionic emissions. Such electrons move towards the anode, due to its positive electric potential. Simultaneously, neutral gas particles (Argon $> 99.999\%$) are injected in the ionization chamber. Such neutral particles cross the path of electrons and, as a result, they are ionized by electron-neutral collisions. The electrons produced by the collisions join the ionization process and trigger an electron avalanche. The filtering grid placed at the exit of the ionization chamber is polarized to a strong negative potential. By doing so, electrons are maintained inside and positive Argon ions (Ar^+) are extracted from the source. Hence, a flow of positive ions escapes the ionization chamber and reaches the exit of the plasma source. At that position a neutralizer filament is heated and, similarly to the cathode, it produces electrons by means of thermionic emissions. Such electrons are attracted by the positive ion flow and follow the ions outside the source and along the plasma chamber. As a result, the plasma source injects in the plasma chamber a drifting quasi-neutral plasma flow that I used for the testing of plasma diagnostic instruments. The solenoid coiled around the axis of the plasma source is used for increasing the ionization rate of the neutral gas and, as a consequence, the density of the plasma generated by the source. As a current flows into the solenoid, a magnetic field is generated inside the plasma source. Such magnetic field magnetizes the electrons, which then gyrate in the ionization chamber. This process efficiently increases the path of electrons. It follows that electrons cover longer distances before being collected by the anode, so that more electron-neutral collisions take place and higher ionization rates are reached[2]. Figure 3.5 shows an image of the plasma source. Figure 3.6 shows, instead, a schematic illustration of the source where (1) represents the filament, (2) and (6) the ionization chamber, (3) the filtering grid, (4) the neutralizing filament, (5) the external solenoid and (7) the access port for the inlet neutral gas.

The characteristics of the plasma generated in the chamber are given in section 3.2.3. Such characteristics depend on the settings of the plasma source. For instance, one can modify the plasma density by changing either the Argon gas flow rate or the amplitude of the electric current used for heating the cathode filament.

3.2.2 The Equipment of the Plasma Chamber

The characteristics of the environment generated inside the plasma chamber are monitored using different devices.
First, the neutral pressure inside the chamber is monitored using a multi-range probe (not shown here) that covers the pressure range from 1 bar down to 10^{-10} bar. In the case of my investigation, experiments are performed at about 10^{-8} bar.
Second, the characteristics of the plasma in the chamber are measured using two commercial Langmuir Probes (LPs, described in section 1.2) that I acquired from the IMPEDANS company with the objective of improving the equipment of the facility. The LPs perform I-V curve measurements. Such curves are used by the LPs' software to identify the plasma density and electron temperature at specific positions in the chamber. Such independent densities and temperatures are the parameters used as a reference for my experimental tests. Both probes have a spherical electric sensor of 0.05 m in diameter. One probe (Figure 3.7), LP1, is a fixed type of probe. It is used for measuring the plasma characteristics on the axis of the chamber, at a distance of about 1.35 m from the source. The other probe, LP2, is instead a flexible type that can be moved to different positions (Figure 3.8). It is installed on a moving support (Figure 3.9) placed at 0.9 m from the source. The moving support enables one to rotate and translate the flexible probe in the chamber without modifying the characteristics of its environment.

Third, the magnetic field in the chamber is monitored using a three-axis magnetic sensor piloted by an Arduino electronic card and placed at the position of MI electrodes. The Earth's magnetic field

[1] In the case of a tungsten filament of 2.5 x 10^{-4} m in diameter and 8.0 x 10^{-2} m in length, the necessary emission temperature is reached for a current of about 6.0 A.

[2] The electron gyration inside the ionization chamber has been part of the topic of student experiments which I supervised. The objective of such guided experiments (TP/TD) was to observe the plasma density of the flow injected in the chamber increases when the magnetic field gets to values for which the electron gyration radius becomes smaller than the radius of the ionization chamber.

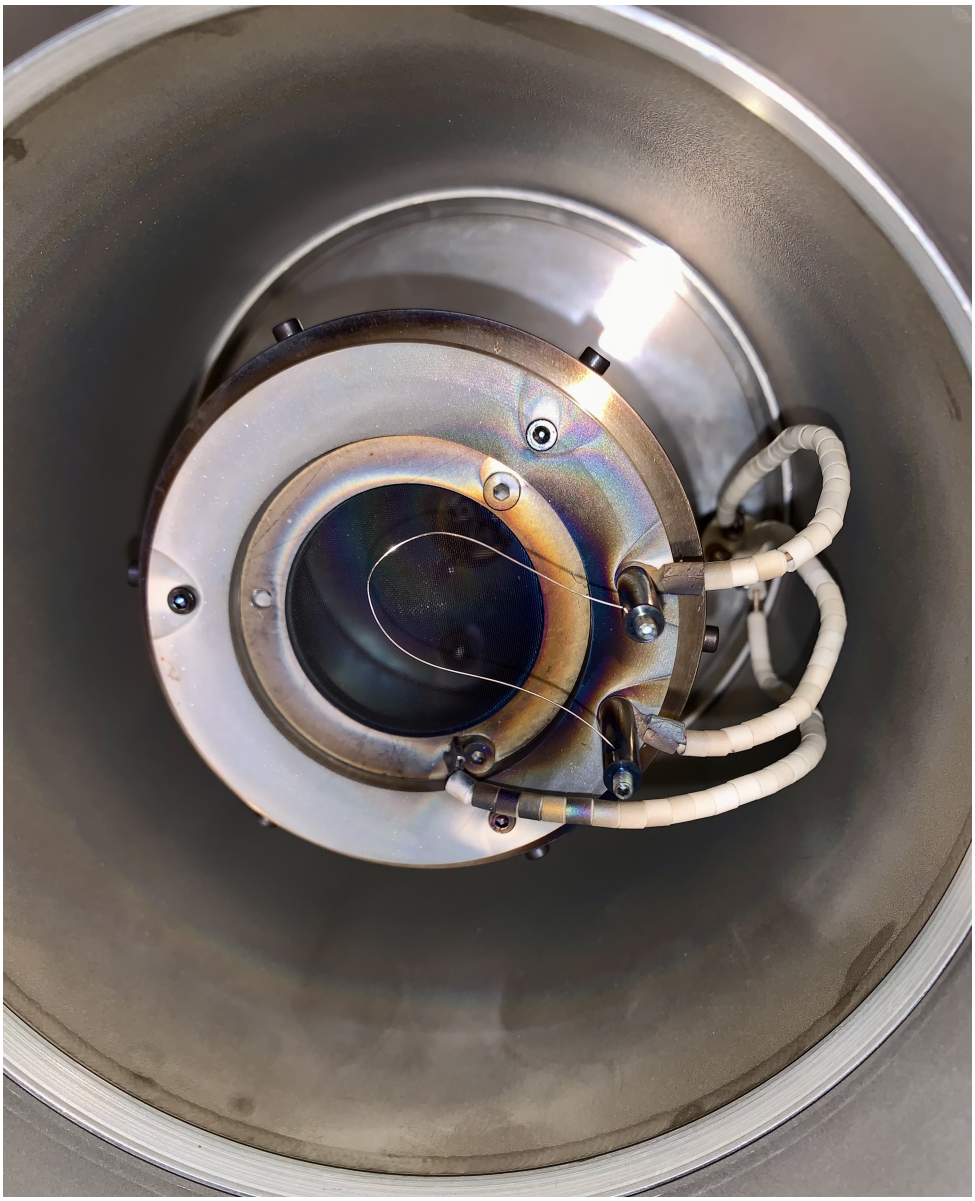

Figure 3.5: Plasma source, frontal view. Electric scheme of the source represented in Figure 3.6

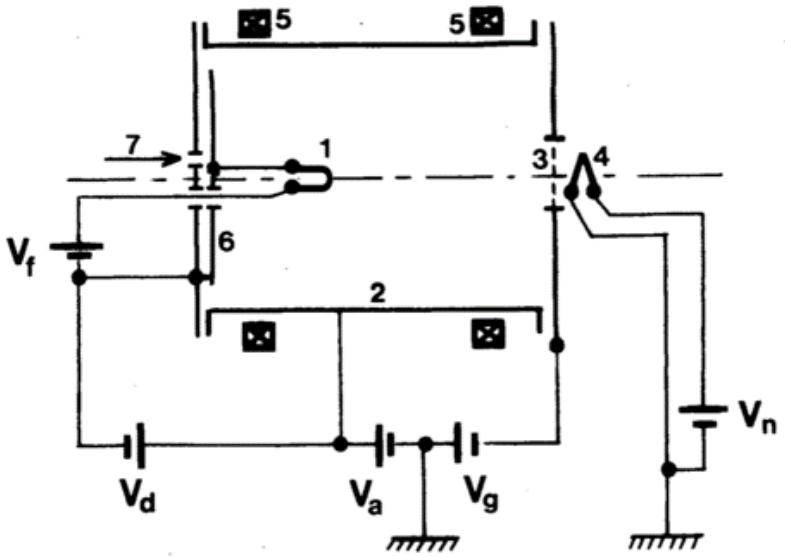

Figure 3.6: Plasma source schematics. 1: filament (cathode). 2,6: ionization chamber (anode). 3: filtering grid. 4: neutralizing filament. 5: solenoid. 7: inlet neutral gas.

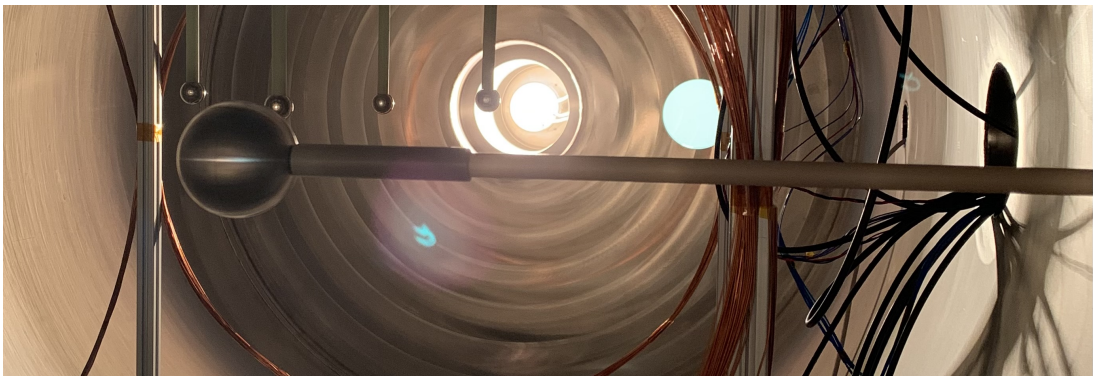

Figure 3.7: Fixed Langmuir Probe (LP1) as seen inside the plasma chamber during measurements.

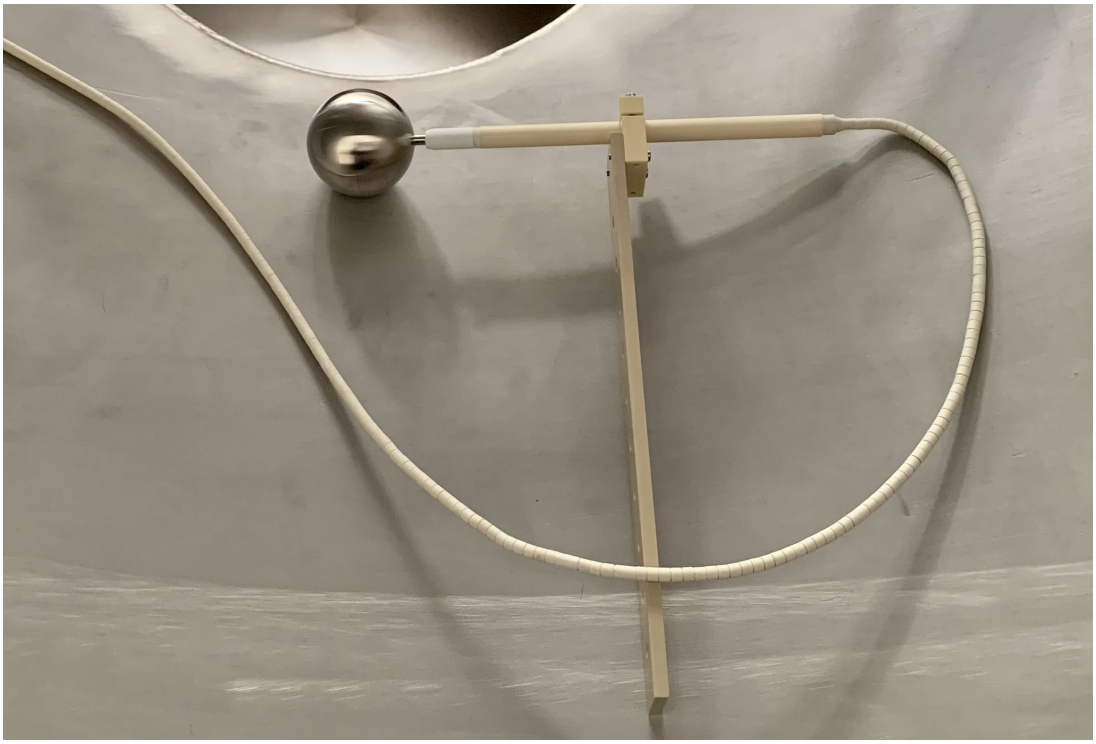

Figure 3.8: Flexible Langmuir Probe (LP2).

Figure 3.9: Translating and rotating support.

amplitude, at the position of the compensation system, amounts to $3.8\ x\ 10^4\ nT$ (i.e. $0.38G$) and the associated plasma cyclotron frequency is $f_{ce} = 1.1\ MHz$. As described in the following sections, such cyclotron frequency is of the same order as the plasma frequency f_p in the chamber and, as a consequence, the Larmor radius is of the same order as the Debye length. In such conditions, the contribution of the Earth's geomagnetic field to MI experimental tests cannot be neglected. However, for my numerical investigation (section 3.1) the plasma is assumed unmagnetized. Note that this is also the case for different space plasmas, such as the solar wind plasma [Meyer-Vernet, 2007], cometary plasma (both in the comet's ionosphere and induced magnetosphere) [Henri et al., 2017] and the plasma found surrounding unmagnetized planets [Luhmann and Brace, 1991, Luhmann, 1995]. Hence, to make my experiments consistent with my numerical tests, I couple the use of the magnetic sensor with that of a magnetic field compensation system that modifies the magnetic field amplitude at the position of MI antennas. Such magnetic field compensation system has been developed during my PhD, by a student which I co-supervised. As shown in Figure 3.10, the compensation system is composed of three perpendicular pairs of wire coils, where each coil is wrapped along a different direction to enable the modification of the three components of the magnetic field. The diameter of the coils corresponds to the side-length of the cubic structure that supports them. By sending currents into the coils, one modifies the magnetic field near the MI antennas. Using the feedback of the magnetic sensor, the currents sent into the coils are adjusted so that the magnetic field at the MI antennas is reduced down to at most 6% of its ambient value. For such magnetic field amplitude, the unmagnetized plasma approximation is valid ($\omega_p/\omega_{ce} \gg 1$).

3.2.3 Characteristics of the Plasma Generated by the Plasma Source

In this section, I describe the properties of the plasma inside the chamber, as obtained from LP measurements. In particular, I discuss the stability over time and the homogeneity of the plasma parameters (i.e. density and temperature) and I quantify the drift velocity of the plasma flow.

The properties of the generated plasma depend on the electric settings of the plasma source. Thus, when the settings are modified, also the plasma in the chamber is modified. To investigate the stability of the plasma parameters over time, I have focused on two different aspects: (i) the time required by the plasma parameters to settle after the source's settings have been modified and (ii) the amplitude of the time-variations of the plasma parameters as the source's settings are maintained constant. Both aspects have been investigated by performing rapid successions of the fixed LP1 measurements. (i) The measurements show that the plasma settles about 30 s after the source's settings have been modified. After the settling time, the plasma density and electron temperature remain stable, with (ii) time-variations of the order of 2% of their average value. Such variations are significantly lower than the density resolution $|\Delta n_e|/n_e = 10\%$ of the MI experiments I performed (section 4.3), therefore they are considered negligible.

The homogeneity of the plasma is investigated by performing LP2 measurements at different positions in the chamber for a fixed plasma and by identifying the dependency of the retrieved plasma parameters to the position of the LP2 instrument. Practically, it consists of performing several LP2 measurements for the same plasma but at different positions in the chamber. This is achieved by rotating ($0 - 360$ deg with a radius of 0.25 m) and translating (from $h_{min} = -0.08$ m up to $h_{max} = 0.20$ m with respect to the axis of the chamber) the flexible LP2 using the moving support, after the settling time of the plasma has passed.

LP2 measurements show that the plasma density varies from $4\ x\ 10^5$ to $4.5\ x\ 10^4$ along $46\,cm$ with a decrease of a factor 9 with the distance from the source. Over the same range of distances, I find a Debye length ranging between $\lambda_D = 0.008$ m and $\lambda_D = 0.023$ m. The plasma density, the electron temperature and their associated Debye length at the position of the MI electric sensors during the experimental tests discussed in section 4.3 are listed in Table 3.1. The plasma density and electron temperature uncertainties are parameters automatically provided by the Impedans Langmuir Probe software and computed as the standard deviation from a repetition of multiple Langmuir Probe sweeps.

The Kaufman type plasma source injects in the chamber a plasma that drifts with a certain drift velocity. I use two different approaches to quantify such drift velocity.

First, I compute the theoretic drift velocity of the Argon ions according to the electrostatic acceleration provided by the source. I find that the positive Argon ions (Ar^+ with mass $m_{Ar} = 3.01\ x\ 10^{-26}$ kg)

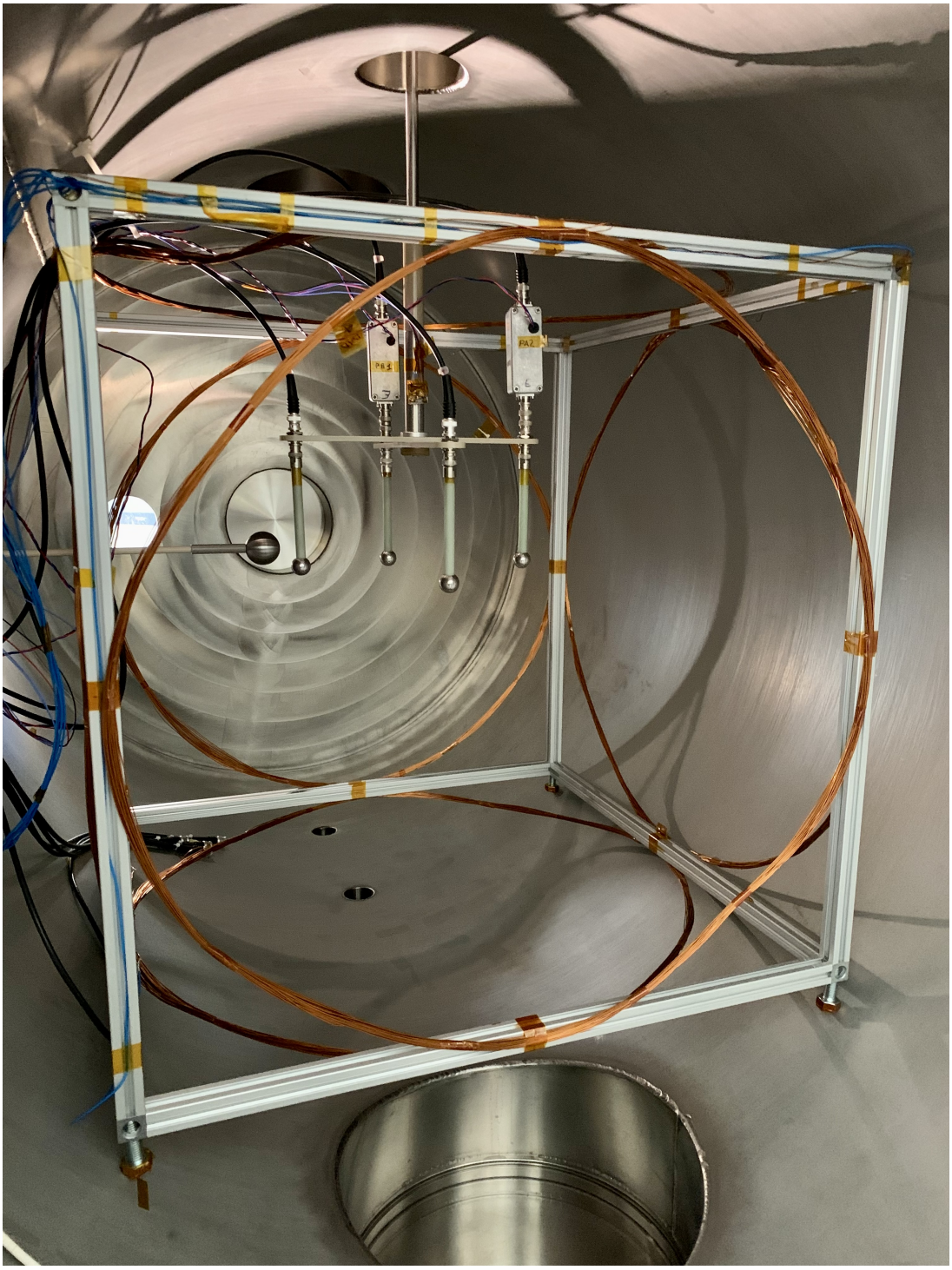

Figure 3.10: Mutual impedance spherical electric sensors inside the plasma chamber, surrounded by the magnetic field compensation system.

Table 3.1: List of plasma density and electron temperature parameters characterizing the two experimental tests discussed in chapter 4.

Test	n_e [cm^{-3}]	T_e [eV]	λ_D [m]
T_01	53156 ± 3195	0.47 ± 0.20	0.22
T_02	67970 ± 3485	0.49 ± 0.03	0.20

are accelerated by the electrostatic potential $V_A = 20\ V$, resulting in the drift velocity $v_{D,1} \simeq 15$ km/s. Note that this first estimate can only be used as a maximum theoretical value for the drift velocity in the chamber. Inside the chamber I expect lower drifting velocities because of acceleration efficiencies below 100% for the source and because of energy losses of the plasma flow along the chamber.
Second, I derive the drift velocity directly from LP2 measurements, by analyzing the ion saturation part of the I-V curves obtained at different positions in the chamber. In the analysis, I assume that the ion thermal velocity is negligible with respect to the drift velocity (i.e. supersonic ions) and that the plasma is quasi-neutral (i.e. $n_i = n_e$, with n_e measured by LP2). Then, to compute the drift velocity, I follow the procedure described in Odelstad et al. [2018] (equation 7) and use the relation:

$$\frac{\partial I}{\partial V} = \frac{Aq^2 n_i}{2m_i} \frac{\sqrt{(8k_B T_{ion})/(\pi m_i) + v_D^2}}{(2k_B T_{ion})/(m_i) + v_D^2} \tag{3.8}$$

where I and V are the electric currents and potentials from the I-V curve, $A = 4\pi r^2$ is the surface of the LP2, $q = e$ and $m_i = m_{Ar}$ are the charge and mass of the Ar^+ and T_{ion} is the ion temperature. By fitting the equation above to different LP2 I-V curves, I find drift velocities in the range $v_{D,2} = 1 - 12.5$ km/s. All in all, the two independent estimates agree and, as expected, the first estimate is the theoretic upper limit of the drift velocity of the plasma generated in the chamber.

3.2.4 MI Antennas Configuration Inside the Plasma Chamber

In this section, I describe the sensors configuration that I use for testing the new MI instrumental modes.

I perform MI experiments using one emitting and two receiving electric sensors. Such configuration is similar to that used by RPC-MIP onboard Rosetta when performing measurements in LDL mode [Trotignon et al., 2007] and also it is similar to the configuration of COMPLIMENT onboard Coment Interceptor [Rothkaehl et al., 2021]. Each sensor consists of an aluminum sphere (radius of 0.01 m) placed near the axis of the chamber at a distance of 0.9 m from the plasma source. The distance between the antennas is about 0.15 m, which is larger than the Debye length of the plasma generated in the chamber during the tests (Table 3.1). The actual configuration of the antennas is shown in Figure 3.10, where the spherical electrodes are placed inside the magnetic field compensation system.

MI experiments are performed using the electronic evaluation board Eclypse that integrates a Zynq7000 processor (Xilinx), equipped with Digital-to-Analog and Analog-to-Digital converters. The electronic board has been coded so that it could perform MI emissions, MI receptions and it could also build MI spectra from the received signals, according to the procedure associated to the MI instrumental mode of interest. For instance, in the case of frequency sweep measurements, MI spectra are obtained by the Eclypse board by following the procedure described in chapter 2.
To boost the received signals and improve the SNR of the measurements, I use two amplifiers (the two metallic boxes on top of the receiving sensors, as shown in Figure 3.10) that increase the received signal's amplitude by a factor 8.7 (i.e. 18.79 dB).

In the following chapter, I focus on the results of this PhD work which I obtained using both the Vlasov-Poisson numerical model and LPC2E testing facility.

Chapter 4

Results

In this section, I describe the results of this PhD work, that aims at supporting COMIX's adaptation of MI instruments to nanosatellite platforms by reaching the objectives described in section 1.5. Such objectives consist on (i) assessing the impact on MI experiments of strong antenna emissions that trigger non-linear plasma interactions (section 4.1), (ii) quantifying the effects of the plasma sheath on MI experiments (section 4.2) and (iii) validating new fast MI instrumental modes (section 4.3). This investigation is based on the Vlasov-Poisson numerical model (section 3.1) and the testing facility of LPC2E (section 3.2) described in the previous chapter.

Note that the settings parameters defining the numerical runs discussed in this PhD work are all listed in Appendix B.2. The datasets derived from such numerical runs and used for computing the MI spectra shown in the following sections are all available online, as described in Appendix B.1.

4.1 Mutual Impedance Plasma Diagnostic Performance To Finite Antenna Emission Amplitudes

Electric devices carried by the satellite generate spurious electric signals that perturb the surrounding environment. The amplitude of such signals is strong near the device and it decreases as they propagate far from their source. If the source is near the MI electric sensors, the Signal-to-Noise Ratio (SNR) of MI measurements can be affected. To make such perturbations negligible, MI instruments are typically deployed far from the satellite platform [Trotignon et al., 2007, 2006], where the amplitude of the spurious electric signals is smaller. But onboard nanosatellites the deployable booms are short due to the mass and volume limitations of small platforms. Therefore, MI instruments should be deployed near the nanosatellite and the SNR of their measurements is likely to be impacted. In this context, COMIX plans to mitigate the non-negligible spurious perturbations of the measurements by increasing the MI emission amplitude. The drawback to the emission of strong amplitude signals is that, above a certain threshold, it modifies significantly the plasma dielectric by triggering non-linear plasma interactions. Non-linear interactions affect the plasma response to MI emissions and, consequently, perturb the diagnostic performance of MI measurements. I aim here at quantifying for the first time such perturbation on plasma diagnostic. For this purpose, I quantify the maximum MI antenna emission amplitude for which the perturbations of MI performances due to non-linear plasma interactions are negligible, according to typical, recent, MI performances (e.g. DFP-COMPLIMENT onboard Comet Interceptor). This topic is the subject of the accepted publication showed in section 6.1.

I achieve such objective by means of 1D-1V Vlasov-Poisson numerical simulations focusing on the MI instrumental response to strong emission amplitudes. To do so, I use the model described in section 3.1, modified to enable the simulation of MI measurements. Practically, I achieve the objective as follows. I perturb a numerical plasma box with MI emissions, using the Model B antenna configuration (section 3.1.2). The emitted electric signals are consistent with the signals associated to the frequency sweep

procedure described in chapter 2. I retrieve the electric potential fluctuations of the plasma from different positions of the numerical box and I use them to build MI spectra. I follow the typical diagnostic procedures described in section 2.3 and section 2.4 to derive from the spectra the apparent plasma density and the apparent electron temperature, respectively. Then, I compute density and temperature relative errors by comparing such apparent parameters which I derived from the measurements to the actual plasma density and electron temperature characterizing my numerical simulations. Such relative errors define the diagnostic performance of the experiment. I repeat the process for different emission amplitudes and, in this way, I find the largest amplitude for which the MI plasma diagnostic performances do not exceed specific threshold uncertainties. Mimicking typical MI space applications (e.g. DFP-COMPLIMENT onboard Comet Interceptor), I set as maximum accepted plasma density (resp. electron temperature) relative error the value $|n_e|/n_e \sim 10\%$ (resp. $|T_e|/T_e \sim 20\%$ [Décréau et al., 1978]).

This investigation is focused on the frequency range (0.5 ω_p, 5 ω_p) that embeds the angular plasma frequency $\omega_p = 2\pi f_p$. Each investigated frequency is emitted for the same amount of repetitions $N = 15$, corresponding to the emission duration $T_i = 15/f_i$. Such duration is of the same order as that used by the DFP-COMPLIMENT instrument included in the Comet Interceptor mission.

Note that I use a monopolar emission and a dipolar reception to simulate MI experiments. This means that I consider only the perturbations of the plasma box due to one emitting antenna and I build MI spectra from the differential electric potential measured between two receiving antennas. Hence, in the following sections, a reception at distance d from the emitting antenna means that the two receiving antennas are positioned at distance $d_1 = d$ and $d_2 = 2d$, respectively.

I set the numerical runs with the ion-to-electron mass ratio $m_i/m_e = 100$ to enable faster numerical runs and the ion-to-electron temperature ratio $T_{ion}/T_e = 0.1$ to ensure that Ion Acoustic Waves (IAWs) are triggered by MI emissions. The reason behind this choice is discussed in the following sections.

Effect of strong emission amplitudes on mutual impedance measurements

MI experiments perturb the numerical plasma box by generating plasma oscillations that propagate from the MI emitting electrodes to the surrounding plasma. The frequency of such oscillations is the emission frequency, while the amplitude corresponds to the emission amplitude modified by the plasma. MI instruments use the receiving electrodes to measure such oscillations and, in particular, to retrieve the amplitude of the plasma fluctuations that oscillate at the emission frequency. By repeating the process for different frequencies, MI instruments retrieve a set of amplitudes, which is used to build MI spectra. Hence, the MI spectra indicate how the plasma modifies the emitted signals in function of their frequency. If the amplitude of the fluctuations in the plasma is sufficiently small with respect to the electron thermal energy, then the plasma response to the MI emission is linear and the energy emitted by the instrument at the emission frequency remains at that frequency. This means that a MI instrument emitting signals at frequency f_0 associated to the wavenumber k_0 triggers fluctuations in the plasma at those same frequency and wavenumber. If the amplitude of the fluctuations is significant, then non-linear plasma interactions like parametric excitation processes are triggered. In such case, the energy injected in the plasma by MI sensors flows from the emitted fluctuations to the excitation of plasma waves respecting the resonant relation of EQ. 1.1, according to parametric excitation processes [**?**]. This means that the energy injected in the plasma by MI emissions flows from the plasma wave (f_0, k_0) to the excitation of resonant modes of the system (f_1, k_1) and (f_2, k_2). As a result, the amplitude of the plasma oscillations at frequency f_0 decreases while that of the oscillations at frequency f_1 and f_2 increases. But MI spectra are built from the amplitude of the plasma oscillations retrieved at frequency f_0. Hence, parametric excitation processes modify the plasma response to MI emissions and, consequently, they perturb the diagnostic performance of MI measurements. This effect is illustrated in Figure 4.1, where the large amplitude *pump* electron plasma wave (indicated with label 1) triggers two resonant modes of the system: a forward ion acoustic wave (indicated with label 3) and a backward plasma wave (indicated with label 2).

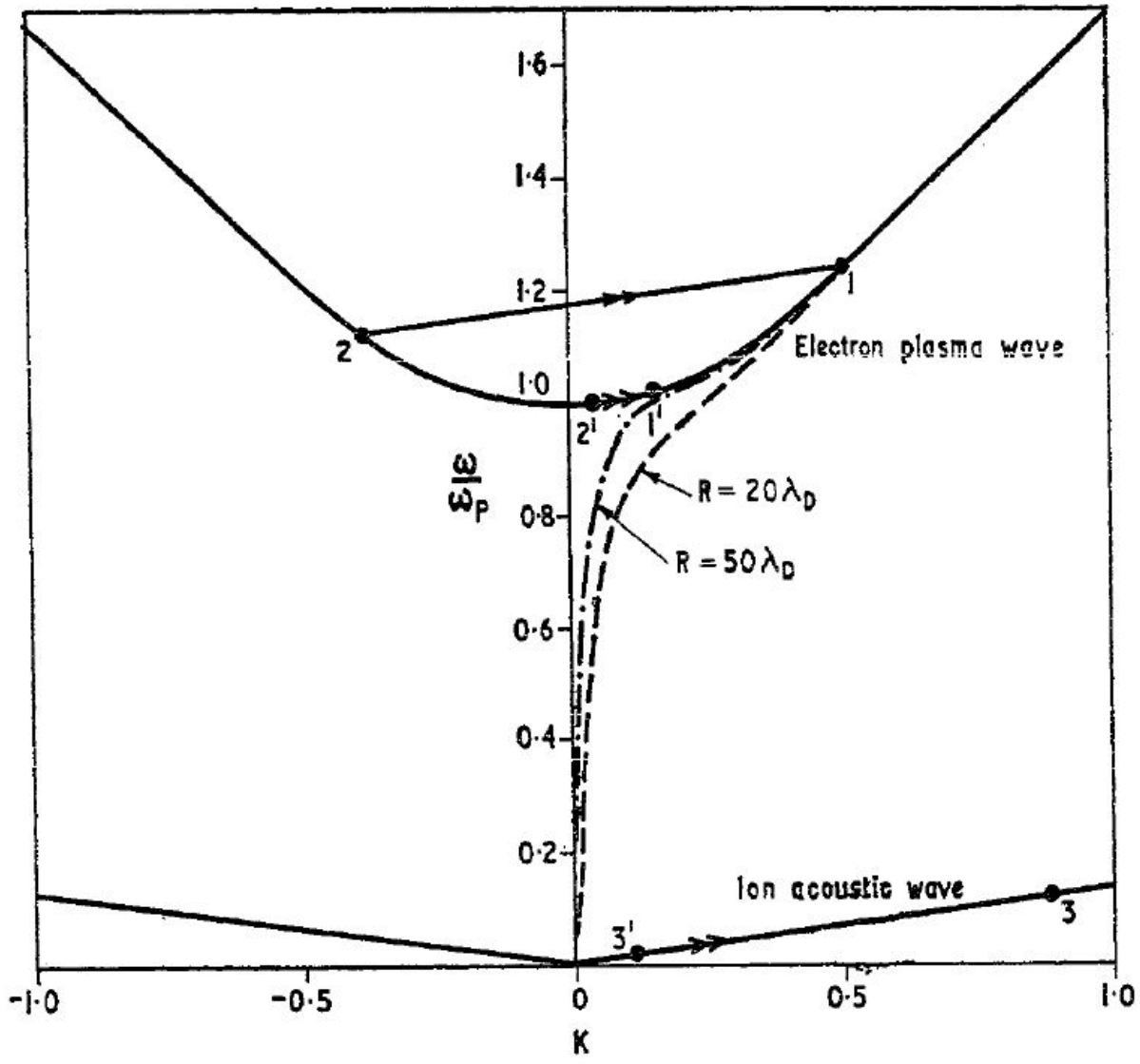

Figure 4.1: Non-linear excitation of resonant modes of the system. Credits: Dysthe and Franklin [1970].

Level of non-linearity triggered by mutual impedance emissions

Non-linear plasma interactions are triggered if the electric energy of the oscillations generated by the MI emission is significant with respect to the thermal energy of electrons. I identify the level of non-linearity of MI emissions as the ratio of the electric energy of the generated plasma waves to the electron thermal energy $\alpha = (E^2\varepsilon_0)/(n_0 k_b T_e)$. Large (resp. small) α correspond to strong (resp. negligible) perturbations of the plasma dielectric and a non-linear (resp. linear) plasma response. In the following sections, I focus my investigation on the range of electric-to-thermal energy ratios that goes from (the linear) $\alpha = 10^{-10}$ up to (the non-linear) $\alpha = 1$. I avoid larger ratios ($\alpha > 1$) because I found that they generate strong plasma fluctuations that make the numerical runs unstable and because a Vlasov description of a plasma fails for $\alpha > 1$ [Krall and Trivelpiece, 1973].

Dependency of the non-linear plasma perturbations on the duration and frequency of the emitted signal

For a given emission amplitude, the non-linear plasma perturbations that are triggered in the numerical box depend on the (i) duration and (ii) the frequency of the MI emitted signal.
(i) The duration modifies the amount of energy that flows from the emitted plasma waves to the excitation of non-linear modes of the system. Longer durations correspond to stronger non-linear perturbations. In the case of my investigation I impose emission durations of $N = 15$ periods. This means that all non-linear effects that would develop over larger time-scales are neglected.
(ii) For each MI measurement, all frequencies are emitted using the same amplitude at the MI sensors. However, the plasma resonates for MI emitted signals that oscillate at frequencies close to the plasma frequency. In particular, the amplitude of the plasma oscillations scales in $1/(1-\omega_p^2/\omega)$. This means that for a specific emission amplitude at the MI sensors the amplitude of the plasma oscillations is larger for frequencies near the plasma frequency. It follows that the non-linear perturbations of MI measurements are expected to be significant near the resonance of the spectra. It is important to remind that MI measurements perturb the plasma by polarizing the emitting sensors with electric signals that oscillate with the same amplitude but with different frequencies. Hence, despite the same emission amplitude at the MI sensors, different levels of non-linear plasma interactions are actually triggered during the same MI measurement due to the dependency on the frequency. For consistency, in the following sections, I sistematically identify the electric-to-thermal energy ratio α of MI measurements as the α related to the emission at frequency $\omega = 5\ \omega_p$ for that same measurement.

4.1.1 Efficient use of High-Power-Computing (HPC) resources: reduction of the required computation time

As described in section 3.1.2, I focus on MI measurements performed using one emitting sensor and two receiving sensors. But, according to the Model B antennas configuration, the plasma box is perturbed using multiple external emitting sources. By taking the antennas configuration into account, the numerical investigation of non-linear plasma interactions triggered by MI experiments requires very large and refined boxes both in space and in velocity domain:

- A large spatial domain (i.e. 4000 λ_D) ensures that the plasma perturbations generated by different MI antennas do not interact. This means that the distance covered by the emitted plasma waves, as they propagate from MI sensors, is smaller than half the distance between two emitting antennas. The distance covered by the propagating plasma waves is given by their group velocity ($v_{g,i}$) multiplied by the duration of the emission ($T_i = N/f_i$). Hence, by scaling the size of the spatial domain with N, I ensure that I observe non-linear effects triggered by only one emitting sensor.

- A refined spatial domain (i.e. $dx \simeq 0.5\ \lambda_D$) enables the investigation of small-scale plasma perturbations, which is compatible with the type of perturbations triggered by non-linear wave-wave

interactions (see following sections).

- A large velocity domain (i.e. v_e between $-40\ v_{th,e}$ and $40\ v_{th,e}$, v_i between $-25\ v_{th,i}$ and $25\ v_{th,i}$) enables the modeling of particles trapping and acceleration effects, associated to vortices in phase space domain (details in the next section). If the velocity domain is not sufficiently large, the numerical run cannot ensure the conservation of mass as particles would be accelerated outside the modeled velocity range.

- A refined velocity domain (i.e. down to $dv_e, \simeq 0.08\ v_{th,e}$ and $dv_i \simeq 0.08\ v_{th,i}$) ensures a detailed modeling of particles trapping effects.

Note that imposing both very large and refined spatial and velocity domains imply that a significant amount of data needs to be evolved in time during the numerical runs. On top of that, refined spatial and velocity resolutions limit the time-step advancement of the numerical runs (i.e. down to $dt = 5\ x\ 10^{-4}\ \omega_p^{-1}$), according to the Courant–Friedrichs–Lewy (CFL) stability condition [Birdsall and Langdon, 2004]. As a consequence, the numerical runs I require might be very time consuming. For this reason, I parallelized the numerical implementation of the model using an OpenMP architecture (Appendix C). Nevertheless, simulations investigating non-linear plasma interactions triggered by MI measurements are very expensive in terms of computing resources. To overcome this, I attempted to reduce such computational cost by (i) reducing the size of the spatial numerical box, by (ii) neglecting the contribution of the ion dynamics to MI spectra, so that only the Vlasov equation for electrons needed to be evolved in time, and (iii) by imposing a reduced ion-to-electron mass ratio.

Reduction of the size of the numerical box

The numerical box's size is reduced by shortening the distance covered by the emitted plasma waves. I do so by reducing the total duration of each numerical run. As described hereafter, this is achieved without changing the emission duration of MI signals.

MI experiments perturb the plasma by emitting a succession of j sinusoidal signals (chapter 2). Such signals oscillate at different frequencies and, in particular, the $i-th$ emitted signal oscillates at frequency f_i, with $i = 0, ..., j-1$. For each $i-th$ emission, the experiment performs a simultaneous $i-th$ reception that measures the electric fluctuations that have been triggered in the plasma. Hence, MI experiments have a synchronous architecture, where the j emissions correspond to j simultaneous receptions. I exploit this characteristic and split MI measurements into j sub-parts, each one investigating a different emission frequency. I simulate such sub-parts separately, so that the $i-th$ numerical run investigates the $i-th$ emission. This means that the box does not need to contain the perturbations generated by the succession of j emissions, i.e. the whole MI measurement. It needs to contain only the perturbations of each $i-th$ emission, separately. Note that, on top of reducing the size of the box, such strategy also enables the parallel computation of the numerical runs composing each MI measurement. In particular, one can exploit modern supercomputers to perform simultaneously different $i-th$ numerical runs.

The drawback to faster simulations and lower computing resources is that I neglect the coupling between plasma perturbations triggered by different emitted frequencies. Thus, I assessed the significance of such coupling by performing a separate investigation (not shown here). I selected three MI emission frequencies and I simulated their emission both using a single numerical run and using multiple runs. I retrieved from the numerical runs the electric fluctuations of the box and I used such fluctuations to build MI spectra. By comparing the spectra, I quantified the impact of the coupling between perturbations due to successive MI emissions. Practically, I investigated the emission of the frequencies $\omega_1 = 1.1\ \omega_p$, $\omega_2 = 1.32\ \omega_p$ and $\omega_3 = 1.584\ \omega_p$, for antenna emission amplitudes corresponding to electric-to-thermal energy ratio $\alpha \simeq 10^{-1}$. I chose these frequencies because they discretize the MI resonant peak signature

that corresponds to enhanced non-linear plasma interactions. I find that the spectra differ at most by 2 dB, which is of the same order as the typical instrumental noise of MI measurements (i.e. 1 dB). Therefore, the effect of the coupling is negligible in my analysis. Such negligible coupling might be due to the short emission durations associated to MI measurements.

Contribution of the ion dynamics to mutual impedance spectra

The numerical model used in this analysis evolves a numerical plasma box by evolving in time the distribution function for both electron and ion populations (section 3.1). If the contribution of the massive ions to the measurements is negligible, then I can model ions as immobile and evolve in time only the electron distribution. As a result, the required computing resources would be halved. I performed a separate test to verify if the ions contribution to MI measurements is, indeed, negligible. In particular, I performed MI measurements either neglecting or modeling the motion of ions, in the case of strong MI emission amplitudes. From the measurements, I build MI spectra and, by comparing the spectra, I identified the impact of the ion motion. To do so, I used the ion-to-electron temperature ratio $T_{ion}/T_e = 0.1$ for which IAWs can be excited in the plasma.
Such impact is shown to be significant, as illustrated in Figure 4.2, where I show two MI spectra obtained including (violet line) and neglecting (blue line) the contribution of the motion of ions. Both spectra are obtained for $\alpha = 0.6$ and with MI receiving sensors at distance $d = 5\lambda_D$ (i.e. one antenna at $d_1 = 5\lambda_D$ and one antenna at $d_2 = 10\lambda_D$) from the emitting antennas. Each MI spectrum is built following the procedure described in chapter 2. In particular, they are built by computing DFTs at the emitted frequencies on the retrieved plasma fluctuations and by normalizing the DFTs to the vacuum instrumental response (i.e. MI spectrum measured in vacuum). I find significant discrepancies, up to 7 dB near the plasma frequency, between spectra obtained neglecting or modeling the motion of ions. This was expected, since mobile ions enable the energy transfer from the emitted plasma waves to the non-linear excitation of both Ion Acoustic Waves (IAW) and other plasma waves (e.g. via parametric excitation processes) [**?**].

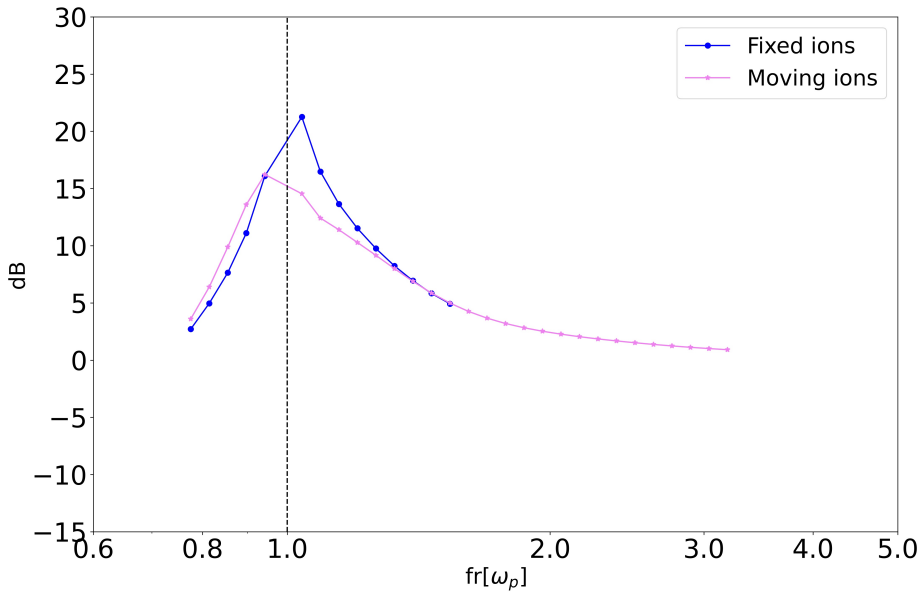

Figure 4.2: Example of Mutual impedance spectra obtained for $\alpha = 0.6$ when considering (violet line) or neglecting (blue line) the contribution of the ions' dynamic. Both numerical spectra are obtained at distance $d = 5\lambda_D$ from the emitting antenna.

In all, I find that the contribution of the ion motion to the investigation is significant. Therefore, the motion of ions needs to be modeled when investigating the impact that non-linear plasma interactions have on MI measurements, especially at frequencies close to the plasma frequency. According to this result, I investigate the impact of strong emission amplitudes by also modeling the ion kinetic dynamics through the Vlasov equation for the evolution of the ion distribution function. In the next section, I investigate what non-linear plasma interactions are triggered by MI emissions.

Reduced ion-to-electron mass ratio

As discussed above, the impact of strong emission amplitudes on MI measurements is investigated by fixing the amount of emitted repetitions to $N = 15$ for each investigated frequency. Such parameter N is consistent with the DFP-COMPLIMENT experiment onboard Comet Interceptor, but it does not agree with the parameters used for other MI experiments. For instance, for recent MI space applications such as Rosetta/RPC-MIP and BepiColombo/RPWI/AM2P, the amount of repetitions N depends on the emitted frequencies. In the case of Rosetta/RPC-MIP, it varies between $N = 8$ and $N = 1000$ within the same measurement. In the case of BepiColombo/RPWI/AM2P, it varies between $N = 10$ and $N = 150$. While the dependency of the non-linear perturbations of MI spectra on the parameter N is outside the objective of this investigation, longer emission durations correspond to stronger non-linear perturbations of the plasma. Hence, hereby I enhance the ion acoustic frequency so that short emission durations (i.e. fast numerical runs) trigger in the numerical box non-linear interactions that are expected for longer durations in actual space experiments. To do so, I use a reduced mass ratio $m_i/m_e = 100$ instead of the proton-to-electron mass ratio $m_i/m_e \simeq 1836$. Thus, I enhance the ion acoustic frequency by a factor ≥ 4. Consequently, the investigated perturbations of the diagnostic performance are stronger than those expected for DFP-COMPLIMENT and the maximum emission amplitude identified by this study is a lower conservative.

4.1.2 Non-Linear Plasma Interactions and Their Impact On Mutual Impedance Spectra

In this section, I investigate what non-linear perturbations of the plasma dielectric trigger the strong modifications of MI spectra shown in Figure 4.2. In particular, I investigate which non-linear plasma perturbations are triggered by strong MI emissions in function of the frequency. As shown in Figure 4.2, stronger non-linear plasma interactions are expected for frequencies close to the plasma frequency. To investigate this, I perform three numerical runs, each of which simulate the MI emission at a different frequency: a first one below the plasma frequency where linear Langmuir waves do not propagate (at $\omega_1 = 0.5\ \omega_p$), a second one close to the plasma frequency where linear Langmuir waves are expected to propagate (at $\omega_2 = 1.1\ \omega_p$) and, finally, a third one above the plasma frequency where linear Langmuir waves are expected to be strongly damped ($\omega_3 = 2.0\ \omega_p$). The amplitude of the emission signals is set to $\sigma = 0.1\ \bar{\sigma}$, for which non-linear plasma interactions are expected at frequencies near the plasma frequency. Such emission amplitude at MI sensors corresponds to $\alpha_1 = 0.01$, $\alpha_2 = 0.33$ and $\alpha_3 = 0.01$ due to the dependency on the oscillation frequency for the amplitude of the plasma fluctuations. Note that Figure 4.2 shows that I should expect non-linear plasma interactions to be excited only in the case of ω_2.

For the three runs, I find that the emission triggers plasma fluctuations that oscillate at the frequency of the emitted signals. In the case of ω_1 and ω_3, only the plasma at positions near the emitting antennas is perturbed. This is due to the generation of either evanescent waves that do not propagate in the plasma (ω_1) or to Langmuir waves associated to strong Landau damping effects (ω_3) [Brunetti et al., 2000]. All in all, for both emitted frequencies, I do not observe signatures of non-linear plasma interactions in the plasma box.

In the case of $\omega_2 = 1.1\ \omega_p$, the emission generates Langmuir waves (k_L =-0.244 λ_D^{-1}, $\omega_L = \omega_2$) that propagate from the emitting antennas to the surrounding plasma. The strong oscillations of such Langmuir waves trigger both (i) wave-particle and (ii) wave-wave non-linear plasma interactions.

Signatures of wave-particle interaction

My numerical simulations show signatures of wave-particle interactions in phase-space domain for the electron distribution function (Figure 4.3 top panel). In particular, vortices are found near the phase velocity of the emitted Langmuir wave $v_\phi \simeq 4.5\ v_{th,e}$ (light blue line), between $v_e = 2\ v_{th,e}$ and $v_e = 7\ v_{th,e}$. This means that electrons moving with velocities close to the phase velocity of the wave get trapped in-between the electric potential peaks of the sinusoidal propagating wave (Figure 4.3 bottom panel). Their oscillation period in-between the peaks is the bouncing time $T_B = \sqrt{m_e/(eEk)}$ [Zakharov and Karpman, 1963, O'Neil, 1965].

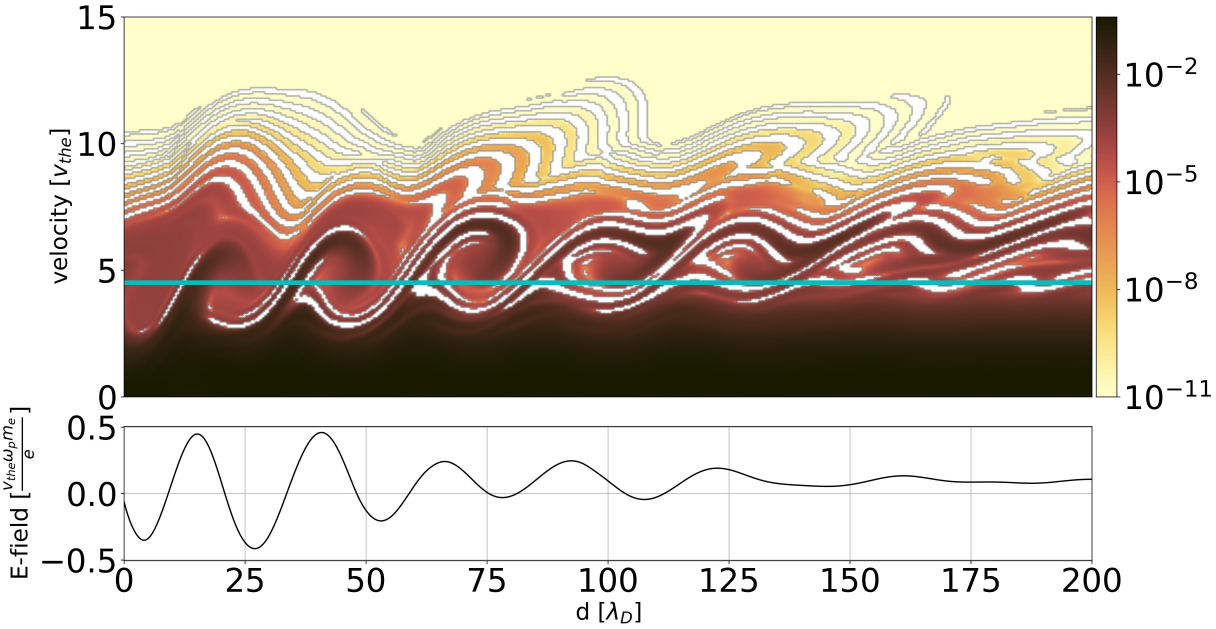

Figure 4.3: Signatures of particles trapping in phase space. Top panel: electron velocity distribution function in phase space domain, for $\omega = 1.1\ \omega_p$ at time $t \simeq 120\ \omega_p^{-1}$. The phase velocity of the emitted wave is represented as a blue line. Bottom panel: electric field associated to top panel, as a function of distance d from the emitting antenna.

Trapped electrons move at velocities close to the phase velocity of the emitted wave. During the bouncing time T_B, the trapped particles cover the distance $L_v \simeq T_B v_\phi$. The emitted plasma wave propagates through the plasma at group velocity v_g. It follows that the wave covers such distance L_v at time $t_{trap} \simeq L_v/v_g$. Hence, electrons are trapped only after an efficient trapping time $t_{trap} \simeq L_v/v_g = T_B v_\phi/v_g = T_B(1-\omega_p^2/\omega^2)^{-1} >> T_B$. In the case of ω_2, I find $T_B \simeq 17\ \omega_p^{-1}$, corresponding to a distance $L_v \simeq 75\ \lambda_D$ and to an efficient trapping time $t_{trap} \geq 113\ \omega_p^{-1}$. This is consistent with my numerical runs, where I find that particles are fully trapped only after the trapping time t_{trap} (e.g. Figure 4.3).

The vortices significantly modify the electron distribution function that gets flattened near v_ϕ when averaged over physical space. This reduces the Landau damping of the emitted waves.

Signatures of wave-wave interactions

My numerical simulations also show signatures of wave-wave interactions in the Fourier spectrum of both the net charge density and the ion density, as shown in Figure 4.4. Note that the emitted Langmuir wave

corresponds to the signature at the frequency-wavenumber ($\omega_L = 1.1\ \omega_p$, $k_L = -0.244\ \lambda_D^{-1}$).

- From net charge oscillations (top panel), a signature of the so-called virtual wave represented as charge density localized at ($2\ \omega_L = 2.2\ \omega_p$, $2\ k_L = -0.488\lambda_D^{-1}$) [?] is observed on top of the emitted Langmuir wave.

- From ion density oscillations (bottom panel), my simulations show at (ω_{IAW}, $\pm k_L$) the signatures of IAWs, with ω_{IAW} obtained from the IAW dispersion relation $\omega_{IAW}^2 = (k_L^2 C_s^2)/(1 + k_L^2\lambda_D^2)$ where C_s is the ion sound-speed. Such waves do not form a resonant triads with the emitted Langmuir wave. In particular, they do not respect the resonant relation from EQ. 1.1. Hence, they are not triggered by parametric excitation processes. I have performed separate dedicated simulations to understand the origin of these IAWs by modifying the ion-to-electron temperature ratio. In particular, I have increased the temperature ratio to increase the damping of the IAWs, thus enabling the identification of the position at which the IAWs are triggered. I find that the IAWs are triggered at the wave-front of the propagating Langmuir wave, where the electric energy gradient is significant. Such gradient, according to the ponderomotive force [Califano and Lontano, 1999, Henri et al., 2011], acts as a pressure force on the ions and triggers their oscillation.

- Signatures of backward Langmuir waves are observed in the net charge density (top panel) at ($\omega_L = 1.1\ \omega_p$, $k_L = 0.244\ \lambda_D^{-1}$). Such backward fluctuations occur where ion density oscillations exceed $\Delta n_i/n_i > 0.2$, as expected. This process is similar to the reflection of radio waves observed in Earth's ionosphere due to the electron inhomogeneity corresponding to a density increase with the altitude [Tkachenko et al., 2021]. Note that the propagation of plasma waves through inhomogeneities is discussed in detail in section 4.2.

- Parametric excitation processes related to non-linear beats of the wave ($\pm k_L = \pm 0.244\lambda_D^{-1}$, $\omega_{IAW} = 0.025\omega_p$) trigger ion oscillations at the harmonic ($\pm 2k_L = \pm 0.488\lambda_D^{-1}$, $2\omega_{IAW} = 0.05\omega_p$). Such harmonics are observed among the ion density oscillations as localized charge density.

- Due to similar parametric excitation processes, IAWs are observed at the second harmonic ($3k_L$, $3\omega_{IAW}$).

Note that the wave-wave interactions described above have been verified in three steps. First, I identified from Figure 4.4 which modes of the system have been excited by the MI emission. Second, I investigated which modes verified the resonant relations from EQ. 1.1. Third, I isolated each mode from the frequency-wavenumber Fourier space and I converted them back to the physical space. By doing so, I verified that the interacting waves indeed are found at the same location. Note that I only took into account three-waves interactions and neglected quadratic interactions.

Summary on the impact of wave-particle and wave-wave interactions

As expected, I find that non-linear perturbations are enhanced for frequencies near the plasma frequency. In particular, for such frequencies, I find that both wave-particle and wave-wave interactions perturb significantly the characteristics of the plasma by modifying the electron distribution function and by exciting different modes of the system. However, wave-wave and wave-particle interactions trigger two counteracting effects. On the one hand, wave-wave interactions enable the non-linear energy transfer between the emitted waves and different non-linear modes of the system. As a consequence, they reduce the amplitude of the plasma waves emitted by the MI experiments. On the other hand, wave-particle interactions flatten the electron distribution function near the phase velocity of the emitted wave and,

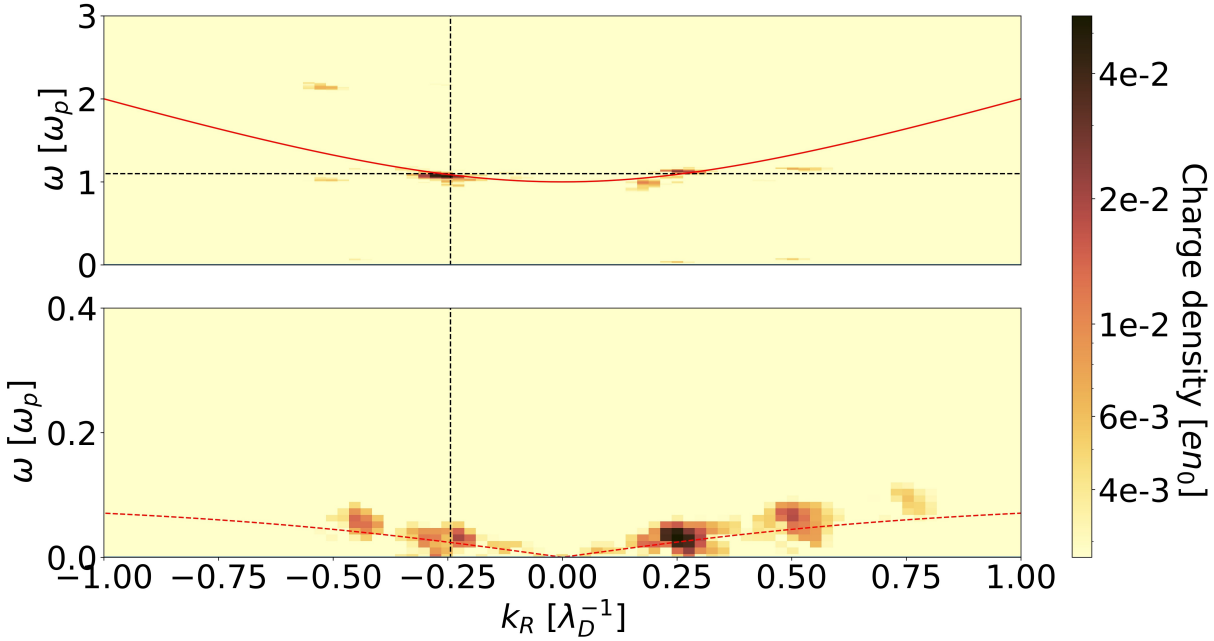

Figure 4.4: Net charge density and ion density Fourier spectra (top and bottom panels, respectively) obtained for the emission frequency $\omega_2 = 1.1\ \omega_p$. Both panels are obtained at time 550 ω_p^{-1} after the beginning of the emission. Top panel: 2D Fourier transform of the net charge density. The red line represents the Langmuir waves dispersion relation. The black dotted lines represent the frequency ω_L and wavenumber k_L of the emitted Langmuir wave. Bottom panel: 2D Fourier transform of the ion density. The red dotted line represents the IAW dispersion relation. The black dotted line represents k_L.

consequently, they reduce the Landau damping of the emitted Langmuir wave. In the next section, I show that these two counteracting effects do not balance out.

Mutual impedance spectra perturbed by strong emission amplitudes

In this section, I show the impact that the wave-particle and wave-wave interactions, described in the previous section, have on MI spectra. To do so, I compare MI spectra obtained over the same frequency range (i.e. from 0.5 ω_p up to 5.0 ω_p, with the frequency resolution $\Delta = 0.05$) and for different emission amplitudes (i.e. associated to electric-to-thermal energy ratios varying from $\alpha = 10^{-10}$ up to $\alpha = 1$).

Figure 4.5 shows the MI spectra obtained following the frequency sweep experimental procedure (chapter 2), for different emission amplitudes (increasing α from top to bottom panel), in function of the distance d from the emitting antenna. These are the spectra that I use in the following section to quantify the diagnostic performance of MI measurements for strong emission amplitudes. To highlight the impact

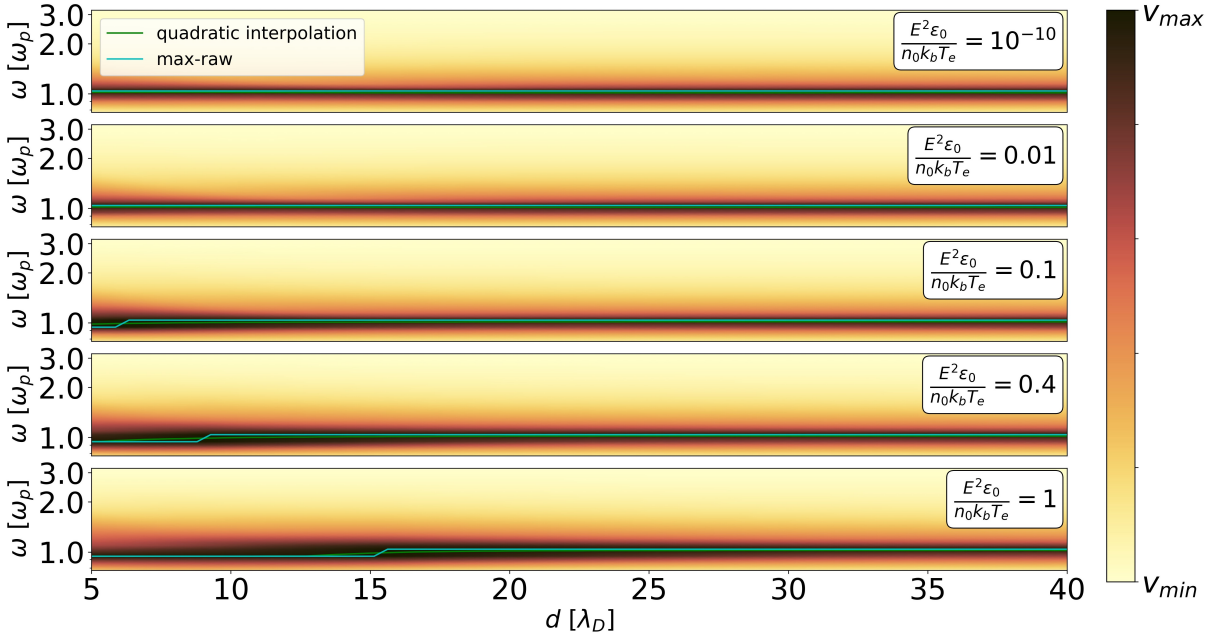

Figure 4.5: MI spectrograms in function of the emitting-receiving antennas distance d. Each spectrum, normalized for the corresponding spectrum in vacuum, is represented between its minimum and maximum amplitudes. The plasma frequency is identified as the frequency of (i) the maximum of each spectrum (light blue line), (ii) the maximum of the quadratic interpolation of each spectrum (green line).

that strong emission amplitudes have on MI measurements, in Figure 4.6, I compare MI spectra obtained for emitting-receiving antennas distances $d = 5\ \lambda_D$, $d = 10\ \lambda_D$, $d = 20\ \lambda_D$ (top, middle and bottom panel, respectively) and for different α. The spectra obtained for $\alpha = 10^{-10}$ (blue line) are associated to a linear plasma response to MI emissions. Therefore, the spectra associated to $\alpha = 10^{-10}$ are used as reference for the comparison to highlight the perturbations that non-linear plasma interactions induce on MI measurements. I find significant discrepancies between (non-linear) spectra and the reference (linear) spectra, with differences up to 10 dB at the resonant peak of the spectra for $\alpha = 1$. This means that non-linear plasma interactions significantly modify the shape of MI spectra.

All things considered, from an instrumental point of view, strong emission amplitudes trigger significant modifications of the resonant signature of MI spectra. Such signature is used for the identification of the plasma density and electron temperature. Hence, strong amplitudes are expected to have signif-

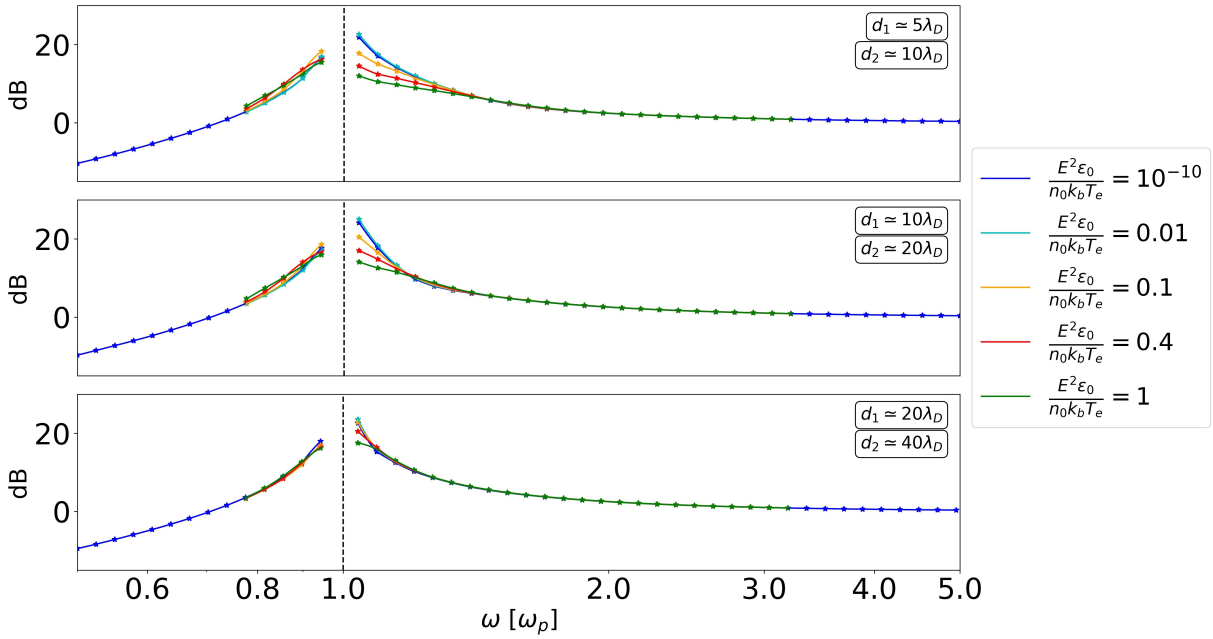

Figure 4.6: Mutual impedance spectra. The distances of the two receiving antennas from the emitting antenna are represented as d_1 and $d_2 = 2d_1$. From top to bottom panel, mutual impedance spectra are obtained for $d_1 \simeq 5\lambda_D$, $d_1 \simeq 10\lambda_D$, $d_1 \simeq 20\lambda_D$, for different antenna emission amplitudes (solid lines).

icant repercussions on the MI plasma diagnostic performance. In the following section, I quantify such performances using the spectra shown in Figure 4.5.

4.1.3 Plasma Density and Electron Temperature Diagnostic Performance

Hereafter, I use the techniques described in chapter 2 to identify the apparent plasma density and the apparent electron temperature from the MI spectra illustrated in Figure 4.5. Then, I use such apparent parameters to compute the diagnostic performance of MI measurements in function of the emission amplitude associated to different α and in function of the distance from the emitting antennas d.

Plasma Density Diagnostic Performance

The plasma density diagnostic performance is computed as the relative error between the apparent ($n_{e,app}$) plasma density derived from MI spectra and the actual plasma density ($n_e = n_0$). The apparent plasma densities are obtained from the apparent plasma frequency ($\omega_{p,app}$) which, in turn, corresponds to the position of the resonant peak of the spectra. Consequently, the plasma density relative error reads:

$$\frac{\Delta n_{e,app}}{n_e} = \frac{|n_{e,app} - n_e|}{n_e} = 2\frac{\Delta\omega_{p,app}}{\omega_p}. \tag{4.1}$$

The density relative errors obtained for different α (colored lines) in function of the distance d is shown in Figure 4.7 (top panel). Such errors are compared to the plasma density uncertainty of 10% (gray shaded area) associated to the frequency resolution of the measurements (i.e. $\Delta = 0.05$).

Significant result. A first significant result of my investigation is that I find plasma density diagnostic errors below 5% (resp. 12%) for $\alpha < 0.1$ (resp. $\alpha = 1$). Such errors are smaller than (resp. of the order of) the plasma density resolution of the measurement. This means that, for the

investigated range of α, the strong emission amplitudes implemented by COMIX to improve the SNR of MI measurements is expected to have negligible repercussions on the plasma density diagnostic performance of the experiment.

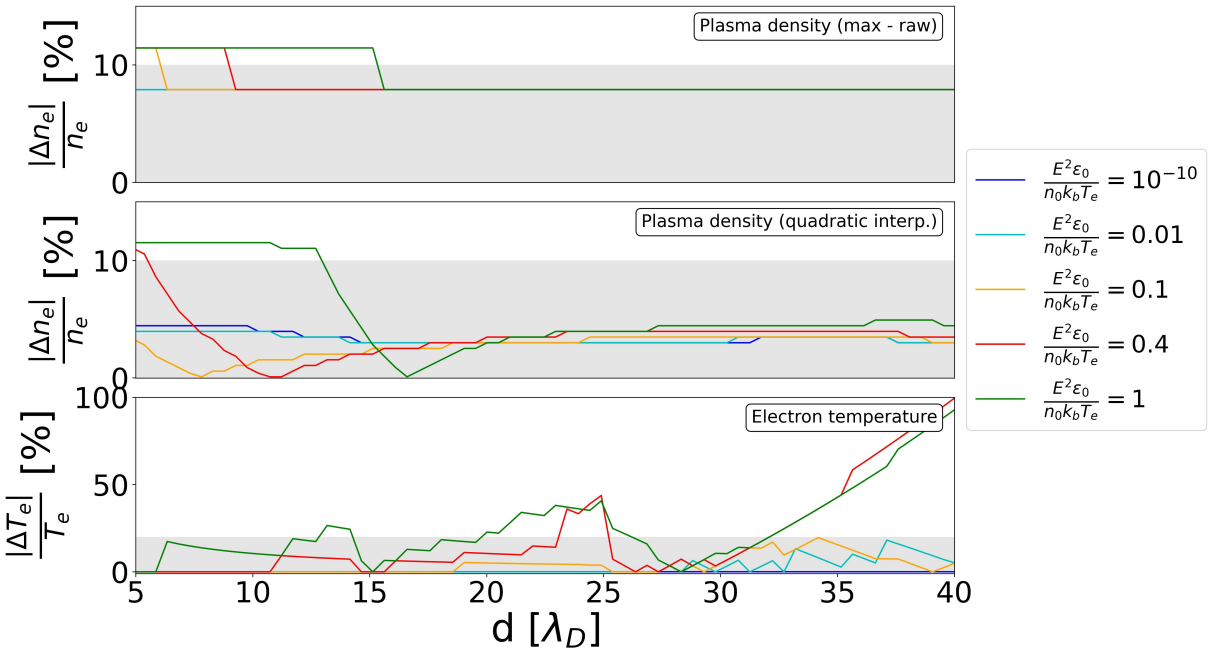

Figure 4.7: MI plasma density and electron temperature diagnostic performance (top and bottom panels, respectively) in function of the emitting-receiving antennas distance d, for α between 10^{-10} and 1. Plasma density resolution of 10% and electron temperature uncertainty of 20% are represented as gray shaded areas.

Electron Temperature Diagnostic Performance

The electron temperature diagnostic performance is computed by comparing the apparent electron temperature $T_{e,app}$ derived from the measurements to the actual electron temperature T_e of the simulations. In particular, it is identified by the electron temperature relative error, that reads:

$$\frac{|\Delta T_{e,app}|}{T_e} = \frac{|T_e - T_{e,app}|}{T_e} = |1 - \frac{T_{e,app}}{T_e}|. \tag{4.2}$$

The apparent electron temperature is obtained following the technique described in chapter 2. Such technique is based on the comparison between the observed (non-linear) spectra and all reference (linear) spectra. I use as reference spectra the MI measurements that I obtained for $\alpha = 10^{-10}$ (i.e. top panel of Figure 4.5). Note that the analysis described hereafter supposes that the observed and the reference spectra have similar shapes. This means that I analyse the observed spectra as if they were associated to linear perturbations of the plasma. By doing so, I mimic the error that one would make when analysing MI space measurements without knowing *a priori* that non-linear plasma interactions have been triggered by the experiment. The comparison consists of computing for each observed spectrum the root-mean-squared error with respect to the reference spectra. The comparison is performed by focusing on portions of the spectra corresponding to frequencies larger than 1.9 ω_p. This allows one to discard from the analysis most of the resonant signature of the spectra, which is strongly modified by non-linear plasma interactions.

The reference spectrum associated to the minimum root-mean-squared error is the matching spectrum. The matching spectrum is identified as the linear equivalent of the non-linear observed spectrum. Practically, I assume that matching and reference spectrum are obtained for the same distance d_{app} from the emitting antennas. The relation between the apparent d_{app} and the actual distance d associated to the observed spectrum reads:

$$d_{ph} = d_{app}\lambda_{D,app} = d\lambda_D \tag{4.3}$$

where d_{ph} is the physical distance between the receiving sensors, λ_D is the actual Debye length of the simulation and the apparent Debye length is:

$$\lambda_{D,app} = \sqrt{(\varepsilon_0 k_B T_{e,app}) \,/\, (e^2 n_{e,app})}. \tag{4.4}$$

The squared ratio of d to d_{app} corresponds to the ratio of apparent to actual electron temperatures. This means that the electron temperature relative error reads:

$$\frac{|\Delta T_{e,app}|}{T_e} = |1 - \frac{n_{e,app}}{n_e}\left(\frac{d}{d_{app}}\right)^2| = |1 - \left(\frac{d}{d_{app}}\right)^2|. \tag{4.5}$$

Note that, to mimic typical experimental applications [Wattieaux et al., 2020], the (known) actual plasma density of the reference spectra is imposed equal to the apparent plasma density of the observed spectra (e.g. $n_{e,app} = n_e$). This means that the plasma density used for producing the reference spectra is imposed equal to the density identified from the observed spectra.

Figure 4.7 (bottom panel) represents the electron temperature relative errors obtained in function of the distance d, for different antenna emission amplitudes. I find that small (resp. large) values of α are associated to negligible (resp. significant) electron temperature relative errors. I find errors within the typical electron temperature performances (i.e. gray shaded area) for MI antenna emission amplitudes up to $\alpha = 0.1$. For larger emission amplitudes (e.g. $\alpha = 1$) I find significant non-linear perturbations of the spectra that would result in major reductions of the electron temperature diagnostic performance.

Significant result. A second significant result of my investigation is that COMIX can choose to increase the MI emission amplitudes to have electric-to-thermal energy ratios up to $\alpha = 0.1$, for which the perturbations of the electron temperature diagnostic performance are also found negligible.

4.2 Impact of Small-Scale Plasma Inhomogeneities like the Nanosatellite's Plasma Sheath on Mutual Impedance Diagnostic

A satellite in space interacts with the plasma it aims to explore. From such interaction, the satellite platform collects currents at its surface, it gets charged and, consequently, it acquires a floating electric potential [Lai, 2012]. Such electric potential perturbs the plasma, that reacts by enveloping the satellite with an inhomogeneous region called plasma sheath [Tonks and Langmuir, 1929]. The satellite's plasma sheath is known to perturb in situ plasma diagnostic measurements [Marchand et al., 2010, Bergman et al., 2020, Johansson et al., 2020, 2021]. Such perturbations are typically reduced by installing the plasma instruments on long booms that deploy them far from the platform and the platform's plasma sheath (e.g. RPC-MIP and RPC-LAP onboard Rosetta [Carr et al., 2007]). But, in the case of nanosatellites, the booms are short due to the mass and volume constraints of small platforms. Thus, for nanosatellite applications the contribution of plasma inhomogeneities to in situ plasma measurements is expected to be significant and it cannot be neglected. In this context, for the purpose of including MI instruments in future nanosatellite multi-point missions, COMIX needs to quantify the impact that small-scale plasma inhomogeneities like the plasma sheath have on the diagnostic performance of MI experiments. This topic is the subject of the submitted draft publication showed in section 6.2. The underlying foundamental question of this investigation, from a science of measurement point of view, is the spatial spread of MI

measurements. In other words: how local are in situ MI measurements ?

To answer this question and support COMIX, I use Vlasov-Poisson numerical simulations (section 3.1) to model for the first time the impact of plasma inhomogeneities, such as the plasma sheath, on MI measurements. For this purpose, I initialize a numerical plasma box with plasma inhomogeneities compatible with the density gradients of the satellite's plasma sheath. Then, I perturb the plasma box with MI measurements. I simulate MI measurements following the frequency sweep procedure described in section 2.2. Such procedure consists of perturbing the plasma box with MI emissions and of retrieving simultaneously the electric fluctuations within the plasma. The plasma oscillations are used for building MI spectra, from which the plasma density and electron temperature diagnostic performances are derived. Such performances are compared to reference performances which are compatible with the performances typically accepted for MI space applications. In particular, similarly to the analysis of MI spectra in the case of strong emission amplitudes (section 4.1), I set a maximum acceptable plasma density error of $\Delta n_e/n_e = 10\%$, consistent with the resolution of MI measurements, and a maximum electron temperature error of 20%, consistent with typical expected temperature uncertainties. I arrange MI emitting antennas in the numerical box according to the Model B configuration described in section 3.1.2. I concentrate in this study on two typical plasma density inhomogeneity scale lengths: at small scale (few Debye lengths) to adress the impact of the spacecraft plasma sheath on MI measurements; at medium to large scale (some 10s of Debye length) to address the typical density structures expected in space plasmas. Note that hereafter I focus on the impact that plasma inhomogeneities have on the diagnostic performance of MI experiments rather than the structure of the plasma sheath for nanosatellites. This means that I investigate MI experiments performed in the presence of specific plasma inhomogeneities and I avoid the research of the solution of the 1D plasma sheath, as discussed in section 4.2.1.

I focus on MI emissions that perturb the plasma box over the frequency range (0.5 ω_p, 3.2 ω_p) using small emission amplitudes ($\alpha = 10^{-10}$) that are associated to a linear plasma response to MI emissions, according to section 4.1. This means that I investigate linear perturbations of the plasma and avoid all non-linear plasma interactions discussed in section 4.1. The duration of each emission is set equal to $N = 20$ repetitions of the oscillation period for each emitted frequency. It follows that the contribution of the ion dynamics to MI measurements is negligible due to the small emission amplitudes and to the short MI emission durations, as discussed in section 4.1.1. Hence, in this section, I neglect the ion dynamics and I evolve in time only the electron distribution function.

4.2.1 Numerical Simulation of Plasma Inhomogeneities: the Density and Electric Potential Profiles

The plasma inhomogeneity is simulated by initializing the numerical box with specific density and electric potential profiles. In this section, I describe such profiles.
Electrons are modeled as Boltzmanian:

$$\frac{n_e(x, t = 0)}{n_0} = \exp\left(\frac{eV(x, t = 0)}{k_B T_e}\right) \tag{4.6}$$

where $n_e(x, t)$ is the electron density, n_0 is the normalization density of the numerical model, T_e is the normalization electron temperature and $V(x, t = 0)$ is the electric potential associated to the inhomogeneity. Such electric potential is initialized as:

$$V(x, t = 0) = A_{in}\ \exp\left[-\left(\frac{x - x_0}{L\lambda_D}\right)^2\right] \tag{4.7}$$

where A_{in} is the amplitude, x_0 is the center of the inhomogeneity with respect to the MI emitting antenna, L is the spatial scale of the inhomomogeneity. Note that A_{in} represents the electric potential of the satellite generating the formation of the inhomogeneity in the surrounding plasma. Hence, positive (resp. negative) A_{in} correspond to a satellite which is charged to a positive (resp. negative) electric potential. It follows that for a positive (resp. negative) A_{in} I simulate a plasma inhomogeneity with an

Table 4.1: Parameters defining the simulated plasma inhomogeneities: location (x_0/λ_D), width (L^2) and depth (A_{in}/V_0) of the inhomogeneity.

Simulation	x_0/λ_D	L^2	A_{in}/V_0
S_00	0	1.95	±0.5
S_01	1	1.95	±0.5
S_02	2	1.95	±0.5
S_04	4	1.95	±0.5
S_08	8	1.95	±0.5
S_16	16	1.95	±0.5
L_50	50	4000	±0.5

excess (resp. a depletion) of electrons. The ion density profile n_p is computed self-consistently from the Poisson equation:

$$\nabla^2 V(x, t=0) = -e\frac{n_p(x, t=0) - n_e(x, t=0)}{\varepsilon_0}. \tag{4.8}$$

Note that $n_p(x,t) = n_p(x, t=0)$ is fixed throughout the numerical simulations because the motion of ions is neglected, as discussed in the previous section.

The numerical plasma box is perturbed by multiple emitting antennas, according to the Model B configuration of the antennas. In order to maintain the symmetry of the numerical box (section 3.1.2), I initialize the model with multiple plasma inhomogeneities, one near each emitting antenna. Such inhomogeneities are all placed at distance x_0 from their corresponding emitting antenna. This enables the investigation of the impact that localized space charges have on only the wave-like (close-field) component of the electric field by using the same numerical runs that I computed and by focusing on regions of the perturbed plasma box where the cold-plasma (far-field) component cancels out [1]. While such investigation is avoided because out of the scope of this PhD work, it might be of interest in future studies.

Hereby, I quantify the impact that localized space charges have on MI measurements by performing numerical simulations that target MI experiments performed near small scale plasma inhomogeneities compatible with the density profiles of the plasma sheath. In particular, I place the inhomogeneity at different distances from the emitting antennas (i.e. from $x_0 = 0$ up to $x_0 = 16\lambda_D$). I perturb the inhomogeneous plasma box with MI measurements, according to the frequency sweep procedure described in section 2.2. Then, I analyse the derived spectra to identify the impact that the plasma inhomogeneity has on MI measurements. To do so, I initialize the model using the inhomogeneities defined by the parameters lised in Table 4.1.

The density profiles I use to initialize the model are different from the 1D solution of the plasma sheath problem [Riemann, 1991]. Such solutions have been discarded because they correspond to non-smooth density profiles at the position of the antenna, which is a property required by my 1D numerical model. Therefore, instead of investigating the effects that the actual plasma sheath has on MI measurements, I hereby investigate the impact of a smoothed version of such plasma sheath and discard the refined density profiles from Riemann [1991].

4.2.2 Impact of Small-Scale Plasma Inhomogeneities on Mutual Impedance Plasma Diagnostic

In this section, I quantify the impact that small-scale plasma inhomogeneities have on MI spectra. To do so, I simulate MI measurements following the same approach described in section 4.1. In particular, I perturb the numerical plasma box with a succession of MI signals, each one oscillating at a different

[1] The Model B configuration that I use to perturb the plasma box enables the investigation of the close-field term separately from the far-field term. The distinction between such two components of the electric field is discussed in section 3.1.2

frequency. I retrieve from the box the plasma fluctuations generated by the emission and I use such fluctuations to build MI spectra. Then, I follow the techniques described in chapter 2 to analyze the spectra and derive the apparent plasma density and the apparent electron temperature from the measurements. Finally, I quantify the diagnostic performances of MI experiments by comparing the apparent plasma parameters to the actual parameters of the numerical simulation. In order to minimize the computing resources required by the numerical investigation, I simulate MI measurements using multiple numerical runs. Each run investigates the plasma fluctuations generated by the emission of a different frequency. Hence, as discussed in section 4.1, I neglect the coupling between plasma perturbations generated by the emission of different frequencies. This is justified by the linear response of the plasma related to small emission amplitudes.

Figure 4.8 and Figure 4.9 show the MI spectrograms that I obtained in the presence of the plasma inhomogeneities listed in Table 4.1. The spectra are stacked in function of the distance d from the antennas, with increasing x_0 from top to bottom panel. Spectra from Figure 4.8 (resp. Figure 4.9) are derived in the case of localized inhomogeneities consistent with satellites charged to positive (resp. negative) electric potential. I show on top of the spectra the *local* plasma frequency profile (black dashed line) that I computed from the conversion of the density profile of the inhomogeneity (EQ. 4.6).

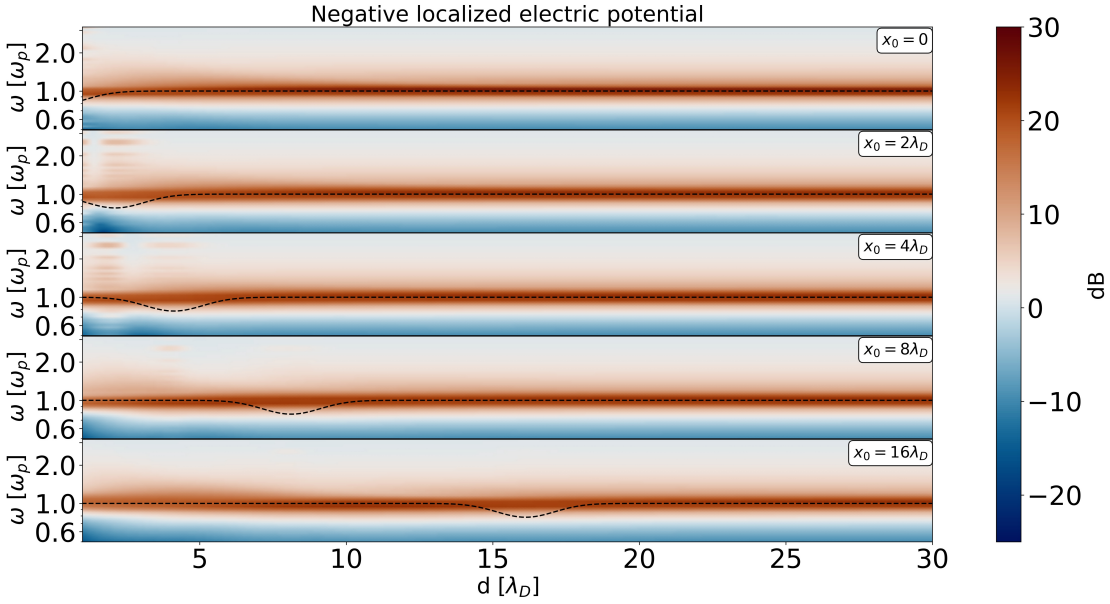

Figure 4.8: Mutual impedance spectra obtained near localized space charges, in function of the emitting-receiving antennas distance d and in function of the position x_0 of the inhomogeneity (Table 4.1). Spectra obtained for the inhomogeneity of satellites charged with negative electric potential. The black dashed line represents the local plasma frequency, obtained from the conversion of the electron density profile of the inhomogeneity.

MI experiments identify the plasma density from the frequency corresponding to the position of the resonant peak of MI spectra. Hence, I specifically investigate how the plasma inhomogeneity affects the resonant peak. I find that the resonant signature of MI spectra (i.e. the red colored region) does not follow the local plasma frequency profile of the inhomogeneity, both in the case of plasma inhomogeneities associated to satellites charged positively and negatively. This is a first, qualitative suggestion that the plasma density diagnostic performance is not affected by small-scale inhomogeneities. In the next section, I investigate quantitatively if the density diagnostic is affected by plasma inhomogeneities with size

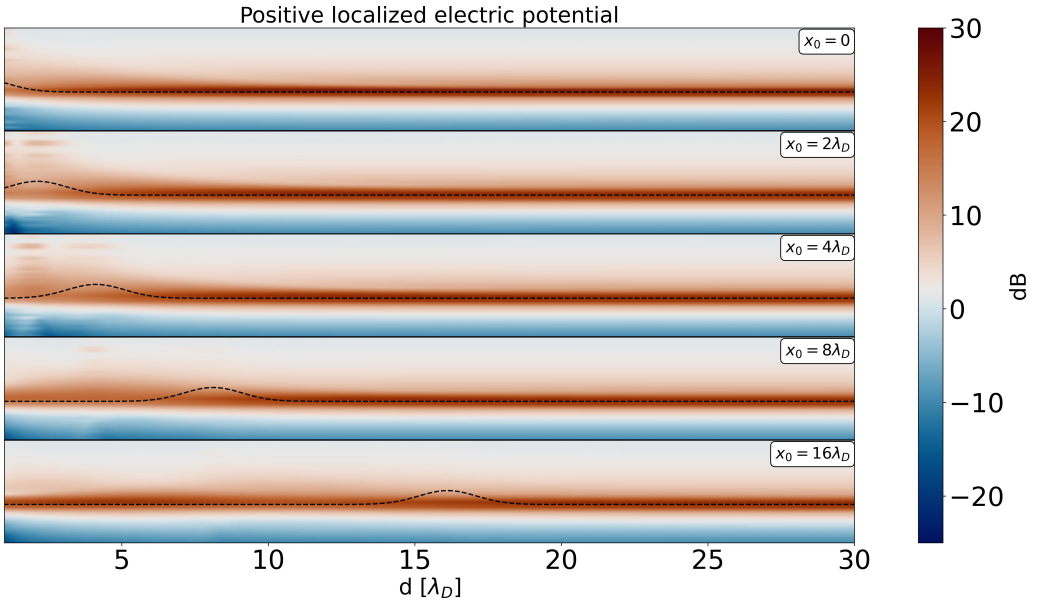

Figure 4.9: Same as Figure 4.8, for the case of plasma inhomogeneities associated to positive localized electric potentials.

comparable to that of the plasma sheath.

MI experiments identify the electron temperature from the shape of MI spectra. In particular, it is identified by comparing the MI spectra to reference (homogeneous) spectra. Hence, I also investigate how small-scale inhomogeneities impact the shape of the spectra. In Figure 4.10, I show the MI spectra obtained for distances $d = 5\ \lambda_D$ (top panel), $d = 10\ \lambda_D$ (middle panel) and $d = 20\ \lambda_D$ (bottom panel) from the emitting antennas. Practically, such spectra correspond to vertical cuts of the spectrograms from Figure 4.8 and Figure 4.9. The spectra are compared to the reference MI spectra computed for a homogeneous plasma (blue line).

My numerical simulations show that the most significant modifications of the shape of MI spectra caused by small-scale plasma inhomogeneities are found near the center of the inhomogeneity. For instance, in the top panels ($d_1 = 5\ \lambda_D$ and $d_2 = 10\ \lambda_D$), I find that the spectra obtained for $x_0 = 8\ \lambda_D$ (red line) present significant discrepancies with the reference spectra obtained for a homogeneous plasma (blue curve). In particular, the extent of the discrepancies depends on the sign of the satellite's electric potential that induces the inhomogeneity. In all, I find that small-scale inhomogeneities significantly impact the shape of MI spectra. I find differences from the reference spectra that amount to 5 dB (resp. 7 dB) for localized space charges corresponding to satellites charged to a negative (resp. positive) electric potential. Note that such differences exceed the typical 1 dB instrumental noise of MI spectra. This is a first, qualitative indication that the electron temperature diagnostic is expected to be significantly perturbed by the presence of small-scale plasma inhomogeneities, especially for inhomogeneities associated to positively charged satellites. In the following section, I investigate quantitatively the impact that such perturbations have on the diagnostic performance of MI experiments.

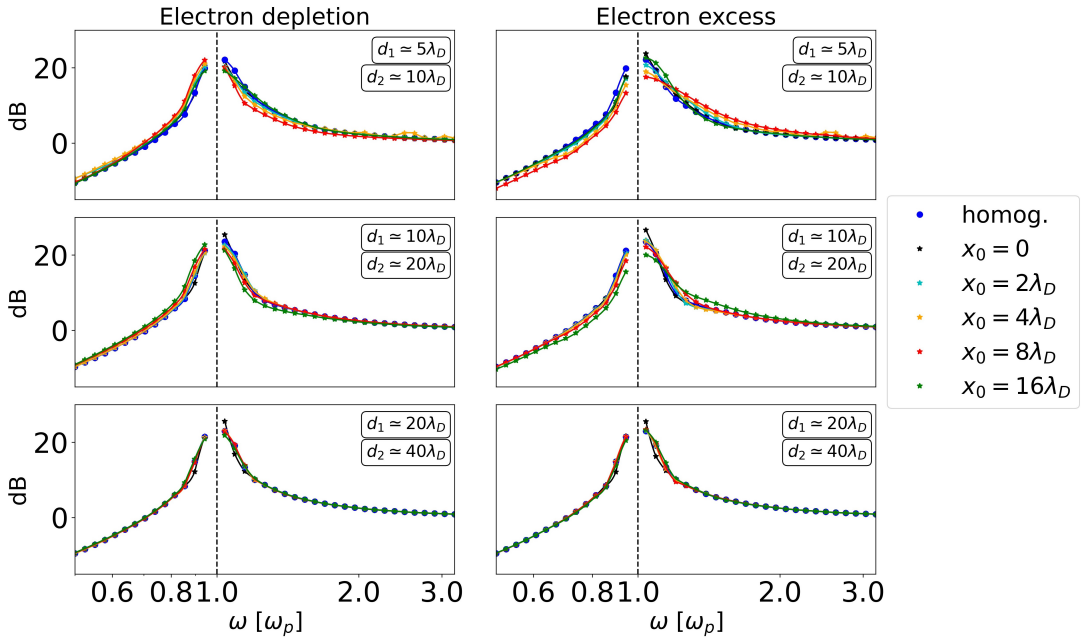

Figure 4.10: Mutual impedance spectra perturbed by the small-scale plasma inhomogeneities listed in Table 4.1. The spectra are obtained for $d = 5\ \lambda_D$ (top panel), $d = 10\ \lambda_D$ (middle panel) and $d = 20\ \lambda_D$ (bottom panel).

4.2.3 The Impact of Small-Scale Plasma Inhomogeneities such as the Plasma Sheath have on Plasma Density and Electron Temperature Diagnostic Performances

In this section, I use the spectra represented in Figure 4.8 and Figure 4.9 to quantify the impact that localized space charges have on the diagnostic performance of MI measurements. I derive such performance following the same procedure described in section 4.1, where I identify the plasma density and electron temperature performances in the case of strong emission amplitudes.

Plasma Density Diagnostic Performance

The plasma density diagnostic performance is assessed from the plasma density relative error derived from the spectra shown in Figure 4.8 and Figure 4.9. Such relative error is computed, as shown in EQ. 4.1, by comparing the *apparent* plasma density $n_{e,app}$ obtained from the measurements to the *actual* plasma density n_0 of the simulation. The apparent plasma densities are obtained from the apparent plasma frequencies, that correspond to the position of the resonant peaks of the spectra.
In Figure 4.11, top panels, I show the plasma density diagnostic performance that I derived in function of the distance d. The gray shaded area indicates the plasma density uncertainty associated to the frequency resolution of the measurement, that corresponds to the discretization of the investigated frequency range (i.e. Δ). The faded dotted lines represent the difference between the density profile of the localized space charges and the density of the homogeneous plasma. Solid and dotted lines that have the same color correspond to the same numerical simulation. My numerical simulations show quantitatively that the perturbations of the plasma density diagnostic in the presence of small-scale inhomogeneities (colored lines) are negligible. In particular, they are small with respect to the errors (dotted lines) expected in the case the MI experiment retrieved the local density of the plasma inhomogeneity instead of the density of the homogeneous plasma. My numerical simulations indicate that the investigated plasma inhomogeneities generate plasma density relative errors (colored lines) of the order of the resolution of

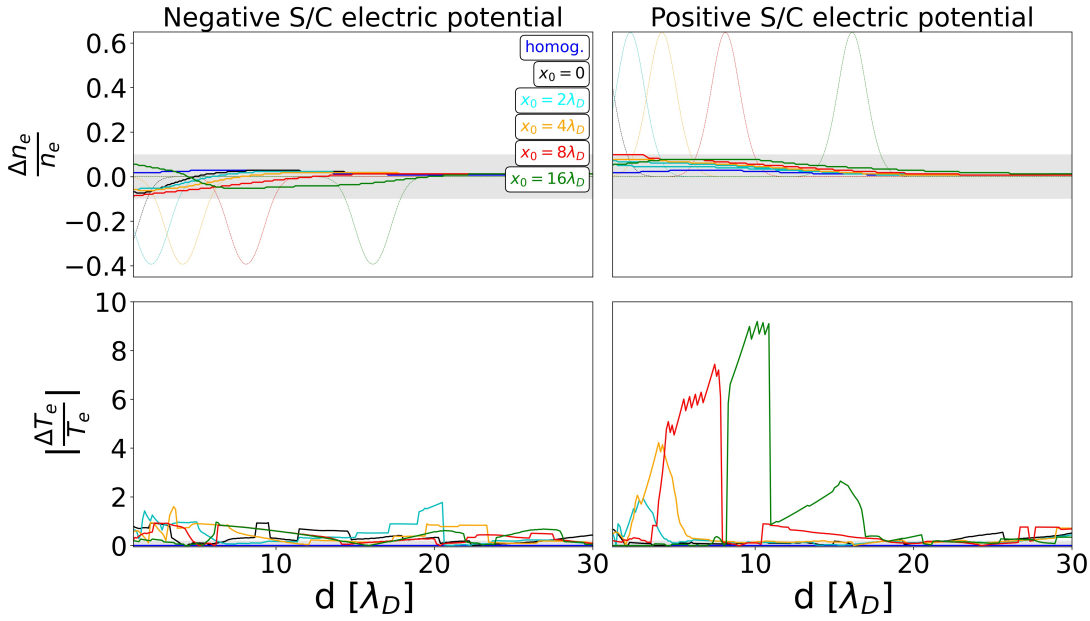

Figure 4.11: MI diagnostic performances in the presence of small-scale plasma inhomogeneities compatible with the size of the plasma sheath. Plasma density (top panels) and electron temperature (bottom panels) relative errors represented in function of the distance d from the emitting antennas. Left (resp. Right) panel: plasma sheath generated by satellites charged with negative (resp. positive) electric potential, where x_0 is the position of the inhomogeneity. The gray area (top panel) represents the reference uncertainty of 10% for the plasma density. The reference electron temperature uncertainty is 20% (bottom panel). The blue line represents the relative error obtained for a homogeneous plasma. Top panel: the faded dotted lines represent the density variations of the localized space charges used for initializing the numerical simulations.

the measurement (i.e. 10%).

Significant result. A first significant result of this investigation is that the plasma density diagnostic of MI instruments installed onboard nanosatellites is robust to small-scale inhomogeneities like the platform's plasma sheath. Thus, the density provided by the MI experiment is not affected by (small-scale) local variations of plasma density.

Electron Temperature Diagnostic Performance

The electron temperature diagnostic performance is computed as the electron temperature relative error (EQ. 4.2). Such relative error is obtained from the comparison between the *apparent* electron temperature $T_{e,app}$ derived from the spectra and the *actual* electron temperature T_e of the numerical simulations.

The comparison is performed by computing the root-mean-squared error between each spectrum from Figure 4.8 and Figure 4.9 and all the reference spectra obtained for a homogeneous plasma (reference spectra not shown here). Consequently, I associate to each perturbed spectrum a matching spectrum that is identified as the reference spectrum with the minimum root-mean-squared error. The distance at which the reference spectrum is computed is assumed to be the same distance d_{app} at which the observed spectrum is obtained. The ratio of the apparent distance d_{app} to the actual distance d gives the ratio of the actual to the apparent Debye length (EQ. 4.5) from which I derive the electron temperature relative error.

Figure 4.11 bottom panels show the electron temperature relative error in function of the distance d from the emitting antennas. The relative errors are compared to the reference error of 20% and the relative errors obtained for a homogeneous plasma (blue line).

Significant result. My numerical simulations indicate that small-scale inhomogeneities such as the plasma sheath significantly impact the electron temperature diagnostic of MI measurements, especially if the inhomogeneity is generated by positively localized electric potential. In particular, I find that the electron temperature relative error can be as large as a factor 2 (resp. 9) for plasma inhomogeneities due to negatively (resp. positively) charged satellites. Such large electron temperature relative errors exceed the typical accepted temperature uncertainty of 20%. This indicates one should not assume that the spectra measured in the presence of small-scale plasma inhomogeneities are similar to the spectra obtained for a homogeneous plasma. Note that this is what I initially assumed with my comparison between observed and reference spectra.

Significant result. In all, my numerical simulations indicate that the presence of the plasma sheath needs to be taken into account for the electron temperature diagnostic to ensure small electron temperature relative errors. In particular, the reference spectra that are used for deriving the temperature need to be obtained by modeling the plasma sheath embedding the instrument. This is especially required if the distance between the MI electric sensors is comparable to the size of the plasma inhomogeneity embedding them. Such kind of analysis has been performed in the recent empirical study of Wattieaux et al. [2020], that derived the electron temperature from RPC-MIP measurements (i.e. the MI instrument onboard Rosetta) by including a model of the plasma sheath based on a step-like function. Hence, I conclude that COMIX needs to model the plasma sheath when identifying the electron temperature from MI measurements.

Note that the electron temperature diagnostic errors decrease with d. This means that the presence of the plasma sheath can be neglected if the Debye length is small with respect to the distance between the plasma sheath and the MI electric sensors, i.e. for cold enough electrons.

4.2.4 Mutual Impedance Experiments for Medium to Large Scale Plasma Inhomogeneities

I have shown that the plasma density diagnostic of MI experiments is not perturbed by the presence of small-scale plasma inhomogeneities due to the satellite's plasma sheath. Does it mean that the MI experiment cannot detect the local density gradients that the instrument would encounter while crossing

medium to large scale inhomogeneous regions (e.g. as found in the Earth's ionosphere) ?

To address this question, I investigate in this section, for the first time, what impact medium to large scale plasma density variations have on MI measurements. For this reason, I initialize the numerical runs using the much broader plasma inhomogeneity L_50 from Table 4.1 with respect to the ones used in the previous sections to investigate the impact of the plasma sheath on MI measurements.

Figure 4.12 shows MI spectra obtained along the L_50 medium to large scale plasma inhomogeneity with excess (left panel) and depletion (right panel) of electrons, in function of the distance from the emitting antennas d. On top of the spectra, I show the *local* density profile of the inhomogeneity (black line), computed as the quadratic mean between the electron densities seen by the dipolar receiving antennas ($d_1 = d$ and $d_2 = 2\ d$).

Significant result. I find that the resonant signature of MI spectra (red region) follows the profile of the local plasma frequency. In particular, the discrepancy between the apparent plasma frequency and the local plasma frequency (found up to 7%) is of the order of the resolution of the measurement ($\Delta = 5\%$ corresponding to a density resolution of 10%). This means that, if the plasma inhomogeneity is of medium to large scale, then the *apparent* plasma density follows the *local* plasma density[2].

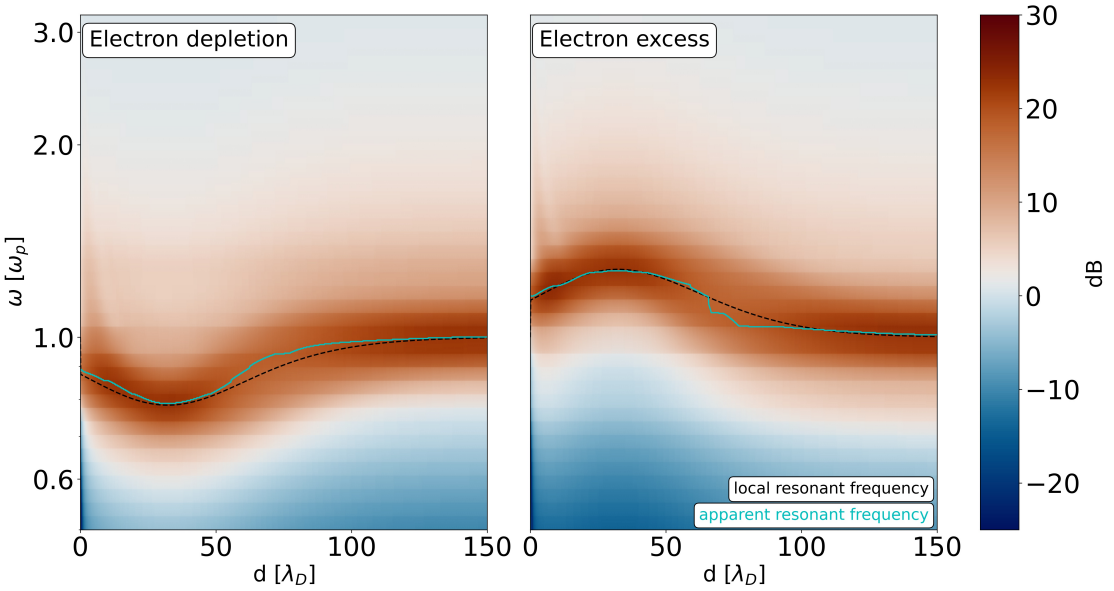

Figure 4.12: Mutual impedance spectra in the presence of medium to large scale plasma inhomogeneities, in function of the distance d. Left (resp. Right) panel obtained in the presence of inhomogeneous plasma with depletion (resp. excess) of electrons. The black dotted line corresponds to the local plasma frequency profile associated to the local plasma inhomogeneity. The light blue line indicates the apparent plasma frequency identified from the spectra.

This result agrees with the WKB solutions devised by Wentzel, Kramers and Brillouin [Wentzel, 1926, Kramers, 1926, Brillouin, 1926]. According to the theory, electric waves – such as the plasma waves triggered by MI emissions – that propagate through a stationary (i.e. over a time $\Delta t >> 2\pi/\omega$ with ω the frequency of the wave) medium to large scale (i.e. $\Delta z >> \lambda$ with λ the wavelength of the wave and

[2]Since the measurement is performed using a dipolar receiving configuration, the apparent plasma density follows the quadratic mean of the densities corresponding to the position of the two receiving MI electric sensors.

Δz the size of the inhomogeneity) plasma inhomogeneity are perturbed as:

$$E = Au^{-1/2} \exp\left(\pm ik_0 \int dz\ u\right) \tag{4.9}$$

with E the amplitude of the electric field of the wave, A a constant, $u = kc/\omega$ the refractive index, $k_0 = \omega/c$ the wavenumber of the wave when propagating in vacuum and z the direction over which the plasma is inhomogeneous. This means that, if the local density increases (resp. decreases) along the inhomogeneity (left and right panels of Figure 4.12, respectively), then the refraction index u decreases (resp. increases) and both the amplitude of the wave and its wavelength increase (resp. decrease). As the local density encountered by the wave increases (resp. decreases), then the ratio of the frequency of the wave to the local plasma frequency decreases (resp. increases). As a result, the Landau damping of the wave decreases (resp. increases). If the damping of the wave decreases, then the wave propagates through the inhomogeneity until the ratio of its frequency to the local plasma frequency becomes lower than 1. At that location, the wave is reflected. This process is similar to the reflection of radio waves observed in the Earth's ionosphere [Westcott, 1962].

MI experiments perturb the plasma over a wide frequency range, by emitting a succession of signals that oscillate at different frequencies. To such an emission, the inhomogeneous plasma responds with resonant oscillations at the local plasma frequency. As the plasma frequency varies with the position, according to the WKB solutions I expect the resonant signature of MI measurements to vary as well and to follow the profile of the local plasma frequency along the inhomogeneity. In all, my investigation confirms that medium to large scale plasma inhomogeneities are indeed detected by MI experiments.

Note that the WKB solutions are valid in the limit of slowly varying plasma inhomogeneities and, therefore, cannot be applied for waves propagating through the plasma sheath:

$$\left|\frac{3}{4}\left(\frac{1}{n^2}\frac{dn}{dz}\right)^2 - \frac{1}{2n^3}\frac{d^2n}{dz^2}\right| << \frac{\omega^2}{c^2} \tag{4.10}$$

Significant result. Regarding the fundamental question of locality of MI measurements, my numerical investigation shows that the MI plasma density diagnostic is not extremely local, as it neglects small-scale (few Debye lengths) plasma inhomogeneities. Instead, it detects medium to large scale inhomogeneities that extend over 10s of Debye lengths around the MI sensors. This result is consistent with the theory of MI measurements, based on the global excitation of the plasma surrounding MI electric sensors, at spatial scales much larger than the Debye length. This result explains a crucial advantage of MI experiments with respect to other types of plasma density diagnostic techniques: MI density diagnostic is immune to the local perturbations of the plasma density associated to spacecraft charging. Although this immunity to local inhomogeneities has been claimed several times in the past, especially in the case of instrumental proposals, there was so far no study to prove it. This PhD work is the first study towards such effort.

4.3 New Instrumental Modes for Fast Mutual Impedance Measurements

COMIX is designing new versions of MI instruments in preparation of future multi-point nanosatellite missions. The sensors of MI instruments are typically installed on long booms to minimize the spurious perturbations generated by the satellite platform. However, such types of perturbations affect not only MI experiments, but also other types of plasma diagnostic experiments such as those performed by Langmuir Probe (LP) [Johansson et al., 2020, 2021], Quasi-Thermal Noise (QTN) [Marchand et al., 2010] and particles instruments [Bergman et al., 2020]. Hence, multiple instruments strongly benefit from having their sensors deployed away from the main body of the satellite, for the sake of improving

their measurements. But, in the case of nanosatellites, the boom are short and can accommodate limited amounts of sensors. It follows that onboard nanosatellites different instruments are required to share their sensors both to minimize the mass and volume of the scientific payload and to simplify the nanosatellites architecture. Among others, MI instruments are expected to share their sensors. Consequently, their antenna occupation time and the time resolution of their measurements is reduced. Note that antenna sharing also occurs in the case of large satellite platforms. This is the case for recent MI instruments onboard large satellites: the PWI-AM2P instrument onboard the Mio spacecraft of the BepiColombo mission [Kasaba et al., 2020], the RPWI-MIME instrument included in the JUICE mission [Rauch et al., 2017] and DFP-COMPLIMENT onboard Comet Interceptor [Rothkaehl et al., 2021]. Such instruments are required to share their electric sensors with different plasma diagnostic experiments. Thus, MI antenna sharing causes reduced measurement time-resolutions both onboard large and small platforms. In this context, to support COMIX's adaptation of MI instruments to nanosatellite platforms and also MI experiments onboard large satellites, I have devised two new fast instrumental modes called the chirp mode and the multi-spectral mode (section 4.3.1). The goal of these new modes is to perform faster MI measurements compared to the reference frequency sweep mode (chapter 2), while providing equivalent plasma diagnostic performances. This topic is the subject of the submitted and positively reviewed publication showed in section 6.3.

To support COMIX, I test and validate these new fast instrumental modes. In particular, I use (i) numerical simulations to test the theoretical instrumental response of the modes (section 4.3.2) and (ii) experimental tests in plasma chamber to validate the modes in a plasma environment which is representative of space (section 4.3.3). Note that the new fast modes described in the following section have been the subject of the *COMIX Software requirements* document which I have co-redacted. Such document has been delivered to CNES in 2022 as one of COMIX R&D deliverables.

4.3.1 The Chirp and Multi-Spectral Modes

The frequency sweep mode (section 2.2) is the typical MI instrumental mode used for recent MI space applications. We recall that the frequency emissions perturb the plasma with a succession of j electric sinusoidal signals $V_{i,sw}$, with $i = 0, ..., j-1$. Each $i-th$ signal has a given amplitude A and a given frequency f_i. The $i-th$ emission duration T_i is chosen to correspond to $N = 20$ repetitions of the oscillation period of its frequency to mimic recent MI space applications such as the DFP-COMPLIMENT instrument of the Comet Interceptor mission. Hence, in this section, I use it as a reference for assessing the performances of the new fast modes. Similarly to the frequency sweep mode, also the chirp and multi-spectral modes consist of perturbing the plasma with a succession of electric sinusoidal signals. Hereafter, I describe these new fast instrumental modes.

The Chirp mode

The chirp mode differs from the frequency sweep mode by the fact that each $i-th$ signal is emitted for only one single repetition of the period of each successive frequency (i.e. $N = 1$). In particular, the $i-th$ emitted signals reads:

$$V_{ch} = A\ sin(2\pi f_i t) \quad (t_i < t < t_i + 1/f_i, 0 \leq i \leq j-1). \tag{4.11}$$

It follows that the duration of a chirp measurement is:

$$T_{ch} = \sum_{i=0}^{j-1} 1/f_i. \tag{4.12}$$

Hence, a chirp measurement is 20 times faster than a corresponding frequency sweep measurement investigating the same frequency range with the same frequency resolution. Note that the choice of the lower frequency and of the resolution of the frequency range determines the duration of the signal.

Short emission durations are expected to impact the analysis of the electric signals retrieved from the receiving antennas. The electric perturbations injected in the plasma by the emitting antennas require a certain transient time to propagate to the receiving antennas. While such transient time is negligible with respect to frequency sweep emission durations, it might not always be negligible with respect to the short chirp emissions associated to $N = 1$. This means that for a synchronous chirp analysis an $i-th$ reception performed at the same time as the associated $i-th$ emission might not contain the electric oscillations triggered in the plasma at frequency f_i. It follows that a synchronous DFT analysis (section2.2) cannot provide the same plasma response in the case of a chirp and a frequency sweep measurement. To ensure that the transient time of plasma waves does not affect chirp spectra, I use a Fast Fourier Transform (FFT) approach instead. In particular, instead of using different DFTs to analyze separately the electric perturbations due to the emission of different frequencies, I analyze all the received electric perturbations together using only one FFT. The impact that the use of an FFT instead of several DFTs has on the performances of MI measurements is discussed in section 4.3.4

The Multi-Spectral Mode

The multi-spectral mode differs from the frequency sweep mode by the fact that multiple frequencies are emitted simultaneously. Practically, each $i-th$ emission is not composed of a single sinusoidal signal, like for the frequency sweep mode, but the sum of different sinusoids. In my investigation, I consider the case where 9 different frequencies are emitted simultaneously. Note that, if a different number of frequencies is to be emitted simultaneously, the relations here below need to be modified accordingly.
The electric potential corresponding to the $i-th$ multi-spectral emission reads:

$$V_{ms,i} = \sum_{k=1}^{9} \frac{A}{9} \sin(2\pi f_{k,i} t) \quad (t_i < t < t_i + N/f_{0,i}, N = 20, 0 \leq i \leq j-1) \tag{4.13}$$

where $A/9$ is the amplitude of each sinusoid, $T_i = N/f_{0,i}$ is the $i-th$ emission duration and $f_{k,i}$ represents the frequencies emitted simultaneously, with $k = 0, ..., 8$ their index. By setting $N = 20$, I impose that the emission duration of the frequencies $f_{0,i}$ (i.e. the smallest frequency of each $i-th$ emission) is the same as that of the same frequencies for the corresponding frequency sweep measurements. The remaining frequencies, instead, have longer emission durations.

Note that the amplitude of each sinusoid is imposed 9 times smaller than what is used for a corresponding frequency sweep emission. Since the multi-spectral mode emits simultaneously 9 different sinusoidal signals, this limitation ensures that the maximum amplitude of the multi-spectral signals $V_{ms,i}$ does not exceed the maximum amplitude of the frequency sweep signals $V_{sw,i}$.

Similarly to frequency sweep received signals, multi-spectral receptions are analyzed using a synchronous DFT analysis. Hence, the DFTs of the k different frequencies emitted simultaneously during the $i-th$ emission are all computed using the same $i-th$ reception.

The risk of multi-spectral measurements is that interferences can be triggered. I find negligible interferences between frequencies emitted simultaneously [3] if in-between the frequencies there is a separation of at least $f_{k+1}/f_k \geq (1+\Delta)^y$, with $y = 5$. In such case, the interferences impact the measurements with modifications of the retrieved amplitudes up to 2% of their value, which in my investigation I assume negligible. In the following sections, I choose to emit simultaneously the frequencies $f_{k+1}/f_k = (1+\Delta)^y$, that correspond to the minimum measurement duration.

For repeatability purposes, I give an empirical rule to derive the different sets of frequencies emitted simultaneously: the $i-th$ emitted frequencies are $f_{k,i} = f_{min}(1+\Delta)^{y\ k+p_1+p_2}$ with $p_1 = i\ mod\ y$ and $p_2 = (9 \cdot y) \cdot (i\ div\ y)$ (where div represents the Euclidean division and mod the remainder of the Euclidean

[3] I remind the reader that the emitted frequencies are computed as $f_i = f_{min}(1+\Delta)^i$, with $\Delta = 0.05$ the frequency resolution. Such resolution corresponds to a density resolution of $|n_e|/n_e = 10\%$.

division). It follows that the amount of emissions required to perform one multi-spectral measurement is $p_3 = [(j-1)mod(9 \cdot y) + 1] \cdot y$. In the case of multi-spectral measurements investigating a frequency range composed of $j = 81$ frequencies, I find that the measurement is composed of $p_3 = 10$ emissions. The frequencies emitted during such emissions are:

$$\begin{array}{l} f_{0,0} = f_0, f_{1,0} = f_5, f_{2,0} = f_{10}, f_{3,0} = f_{15}, f_{4,0} = f_{20}, f_{5,0} = f_{25}, f_{6,0} = f_{30}, f_{7,0} = f_{35}, f_{8,0} = f_{40} \\ f_{0,1} = f_1, f_{1,1} = f_6, f_{2,1} = f_{11}, f_{3,1} = f_{16}, f_{4,1} = f_{21}, f_{5,1} = f_{26}, f_{6,1} = f_{31}, f_{7,1} = f_{36}, f_{8,1} = f_{41} \\ f_{0,2} = f_2, f_{1,2} = f_7, f_{2,2} = f_{12}, f_{3,2} = f_{17}, f_{4,2} = f_{22}, f_{5,2} = f_{27}, f_{6,2} = f_{32}, f_{7,2} = f_{37}, f_{8,2} = f_{42} \\ f_{0,3} = f_3, f_{1,3} = f_8, f_{2,3} = f_{13}, f_{3,3} = f_{18}, f_{4,3} = f_{23}, f_{5,3} = f_{28}, f_{6,3} = f_{33}, f_{7,3} = f_{38}, f_{8,3} = f_{43} \\ f_{0,4} = f_4, f_{1,4} = f_9, f_{2,4} = f_{14}, f_{3,4} = f_{19}, f_{4,4} = f_{24}, f_{5,4} = f_{29}, f_{6,4} = f_{34}, f_{7,4} = f_{39}, f_{8,4} = f_{44} \\ f_{0,5} = f_{45}, f_{1,5} = f_{50}, f_{2,5} = f_{55}, f_{3,5} = f_{60}, f_{4,5} = f_{65}, f_{5,5} = f_{70}, f_{6,5} = f_{75}, f_{7,5} = f_{80} \\ f_{0,6} = f_{46}, f_{1,6} = f_{51}, f_{2,6} = f_{56}, f_{3,6} = f_{61}, f_{4,6} = f_{66}, f_{5,6} = f_{71}, f_{6,6} = f_{76}, f_{7,6} = f_{81} \\ f_{0,7} = f_{47}, f_{1,7} = f_{52}, f_{2,7} = f_{57}, f_{3,7} = f_{62}, f_{4,7} = f_{67}, f_{5,7} = f_{72}, f_{6,7} = f_{77} \\ f_{0,8} = f_{48}, f_{1,8} = f_{53}, f_{2,8} = f_{58}, f_{3,8} = f_{63}, f_{4,8} = f_{68}, f_{5,8} = f_{73}, f_{6,8} = f_{78} \\ f_{0,9} = f_{49}, f_{1,9} = f_{54}, f_{2,9} = f_{59}, f_{3,9} = f_{64}, f_{4,9} = f_{69}, f_{5,9} = f_{74}, f_{6,9} = f_{79} \end{array} \tag{4.14}$$

The total duration of multi-spectra measurements is computed as:

$$T_{ms} = N \sum_{i=0}^{p_3-1} 1/f_{0,i}. \tag{4.15}$$

Differences Between the Three Investigated Modes: Frequency Sweep, Chirp and Multi-Spectral modes

In Table 4.2, I summarize the differences between the three investigated modes.

Table 4.2: Summary of the characteristics of the MI instrumental modes.

Mode	V [V]	N	T_i [s]	T_t [s]
Frequency Sweep	$V_{sw,i} = A\sin(2\pi f_i t)$	20	N/f_i	$\sum_{i=0}^{j-1} N/f_i$
Chirp	$V_{ch} = A\ sin(2\pi f_i t)$	1	$1/f_i$	$\sum_{i=0}^{j-1} 1/f_i$
Multi-Spectral	$\sum_{k=1}^{9} \frac{A}{9}\sin(2\pi f_{k,i} t)$	20	$N/f_{0,i}$	$N\sum_{i=0}^{p_3-1} 1/f_{0,i}$

In the following sections, I investigate both numerically and experimentally MI measurements performed following the instrumental procedures described in this section. In particular, I compare chirp and multi-spectral measurements against frequency sweep measurements. From the comparison, I assess if the new fast modes can be used in place of the reference frequency sweep mode for the purpose of improving the time resolution of MI measurements.

4.3.2 Full Kinetic Vlasov-Poisson Numerical Simulations of Mutual Impedance Experiments

I perform numerical simulations to test the theoretical response of the new fast MI instrumental modes angaist that of the reference frequence sweep mode. For this purpose, I use the 1D-1V Vlasov-Poisson numerical model described in section 3.1, initialized with a homogeneous plasma in equilibrium. I perturb the numerical box with small emission amplitudes, compatible with a linear plasma response. I model ions as a fixed background of positive charges, which is justified by the linear plasma response and by the short emission durations. I arrange in the box the MI emitting antennas according to the Model B configuration (section 3.1.2).

The emitting antennas perturb the plasma box with electric signals that correspond to the $i-th$ emission signals of the three modes ($V_{sw,i}$, $V_{ch,i}$ and $V_{ms,i}$). Such emissions trigger electric fluctuations in the plasma box. In this section, I retrieve the fluctuations and I use them for building MI spectra,

following the procedures described in chapter 2 and section 4.3.1. Then, I compare spectra obtained at specific distances from the emitting antennas, for the three different modes. In particular, I compare the chirp and multi-spectral measurements to the reference frequency sweep measurements.

In the case of the frequency sweep and multi-spectral measurements, I follow the same approach used in the previous investigations (section 4.1 and section 4.2) and I separate the measurements into different numerical runs. Each numerical run simulates a different $i-th$ emission. Hence, I neglect for those modes the coupling between plasma oscillations generated by different $i-th$ emissions. This is justified by the linear plasma response to the emissions. In the case of chirp measurements, I use instead one single numerical run because the analysis of the received signals is performed using one single FFT.

In Figure 4.13 I show numerical MI spectra obtained for the three different modes, at distances $d = 4\lambda_D$ and $d = 20\lambda_D$ (top and bottom panel, respectively) from the emitting antennas, for the frequency range $(0.5\ f_p, 3.2\ f_p)$. For both amplitude (left panels) and phase (right panels) spectra, I find that chirp (green) and multi-spectral (red) measurements agree with the reference frequency sweep (blue) measurements.

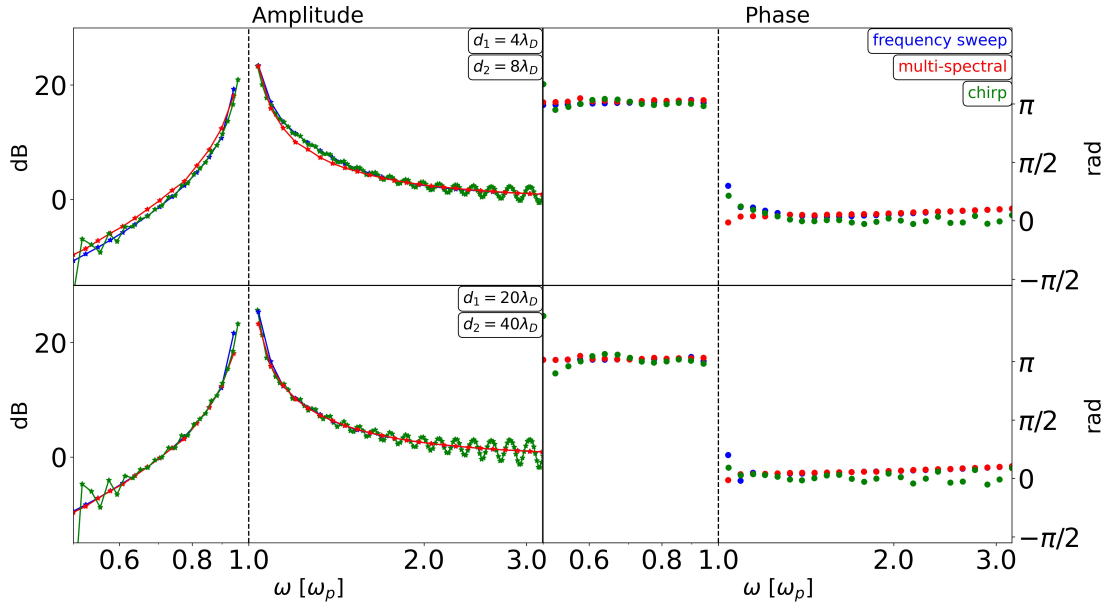

Figure 4.13: Mutual impedance amplitude and phase spectra (left and right panels, respectively) obtained numerically for the frequency sweep mode (blue line), chirp mode (green line) and multi-spectral mode (red line). Top and bottom panels are obtained for distances $d = 4\ \lambda_D$ and $d = 20\ \lambda_D$, respectively. The black dashed lines indicate the position of the plasma frequency.

As expected, I find that all amplitude spectra exhibit a resonant peak in correspondence to the plasma frequency [Grard, 1969, Storey et al., 1969, Béghin and Debrie, 1972, Rooy et al., 1972, Pottelette et al., 1975, Décréau et al., 1978, Pottelette and Storey, 1981, Bahnsen et al., 1988, Grard, 1997, Geiswiller et al., 2001, Gilet et al., 2017, Wattieaux et al., 2020]. Such signature is used to derive the plasma density, from the frequency corresponding to the position of the resonant peak, and the electron temperature, from the shape of the peak (chapter 2). Hereafter, I focus my discussion on the amplitude spectra.

I find that multi-spectral amplitude spectra differ from frequency sweep spectra at most by 2.5 dB in correspondence to the resonant signature. This difference is of the order of the typical MI instrumental noise of 1 dB and, therefore, I assume it negligible.
I find that chirp amplitude spectra differ from frequency sweep spectra at most by 2.5 dB for frequencies

near the resonant signature, in the range $[0.7\omega_p, 1.5\omega_p]$. Larger discrepancies, significant with respect to typical noise level, are found for frequencies far from the position of the resonant peak. Discrepancies at frequencies far from the plasma frequency are not expected to significantly impact the analysis of the spectra. Hence, they are assumed negligible.

Note that the plasma density and the electron temperature are derived from the resonances of the spectra. Hence, the small discrepancies I find between the resonant signatures of the different modes suggest that the chirp and multi-spectral modes should provide the same plasma diagnostic as frequency sweep measurements.

4.3.3 Plasma Chamber Experimental Tests of the New Fast Mutual Impedance Instrumental Modes

Numerical simulations show that the plasma diagnostic provided by chirp and multi-spectral mode is equivalent to that of the reference frequency sweep mode. In this section, I discuss the experimental tests that I performed to compare the actual instrumental responses of the three modes and, in particular, validate the new modes in plasma conditions that are representative of space. For this purpose, I used the plasma chamber facility of LPC2E. In particular, I use the antennas configuration described in section 3.2.4. The characteristics of the plasma generated in the chamber are described in section 3.2.3 and listed in Table 3.1.

Experimental frequency sweep measurements are obtained following the procedure described in chapter 2. Chirp and multi-spectral measurements are obtained following the procedures described in section 4.3.1.

The investigation is performed by setting the emission amplitude to $A = 1\ V$. Each measurement is repeated 11 times in order to retrieve statistical uncertainties for the spectra. Hereby, the illustrated spectra correspond to the median spectra resulting from the repetition of the measurements.

In Figure 4.14, I show experimental MI spectra in amplitude (left panels) and phase (right panels) obtained for the frequency sweep (blue), chirp (green) and multi-spectral (red) modes. The shaded colored areas represent the 3 σ uncertainty obtained from the repetition of the measurements. I find that chirp and multi-spectral measurements are very similar both in amplitude and phase to frequency sweep measurements for frequencies near the resonance, i.e. for the range 1 MHz,4 MHz. In particular, for such range I find discrepancies between multi-spectral (resp. chirp) and frequency sweep measurements up to 1.5 dB (resp. 2 dB) in amplitude and 0.42 rad (resp. 0.57 rad) in phase.

Significant result. In all, similarly to the numerical investigation, also my experimental tests show that the discrepancies between the measurements from different modes are negligible in correspondence to the resonance. *This means that the three instrumental modes provide the same plasma diagnostic.* As a consequence, both the chirp and multi-spectral modes can be used by COMIX to improve the time resolution of MI experiments.

Figure 4.14 also shows that faster MI experiments are obtained at the cost of a worse SNR: the uncertainties on chirp (green shaded area) and multi-spectral (red shaded area) measurements are generally much larger than frequency sweep (blue shaded area) uncertainties. Noise perturbs frequency sweep and multi-spectral measurements when spurious perturbations, which are not generated by MI emissions, trigger oscillations in the plasma at the frequencies investigated by the MI experiment. But, in the case of multi-spectral measurements, SNR is worse because the emission amplitude is 9 times smaller. Noise perturbs chirp measurements when spurious oscillations of the plasma at the emitted frequencies are generated during the measurement, not necessarily while the same frequencies are being emitted. On top of that, the durations of chirp emissions are very short, which makes the noise statistically more significant for chirp than frequency sweep measurements.

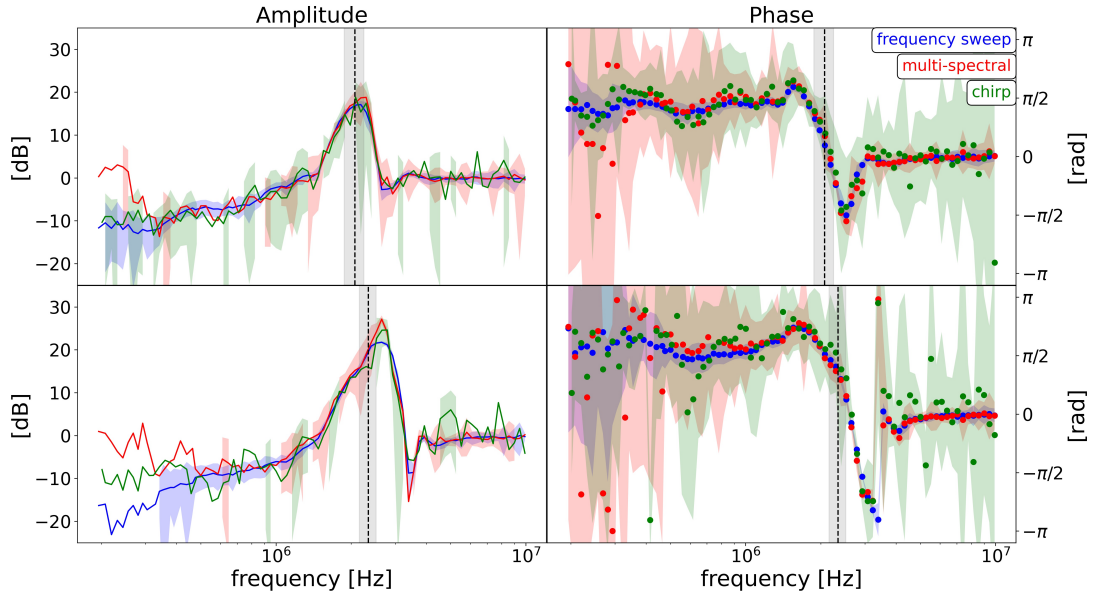

Figure 4.14: Experimental mutual impedance spectra in amplitude (left column) and phase (right column) obtained for the frequency sweep (blue line), chirp (green line) and multi-spectral (red line) modes. Top and bottom panels indicate tests performed for the plasmas listed in Table 3.1. The black dashed line indicates the reference plasma frequency obtained from an independent Langmuir probe measurement, with the gray shaded area the associated uncertainty.

To ensure the best SNR for MI experiments, COMIX should follow the results from section 4.1 and increase the antenna emission amplitude, especially for chirp and multi-spectral measurements.

4.3.4 Computing Resources and Duration of the New Mutual Impedance Instrumental Modes

In the previous sections, I have shown that chirp and multi-spectral measurements are equivalent to frequency sweep measurements both from a theoretical and an experimental point of view. In this section, I investigate from an instrumental point of view the performances of the three modes in terms of onboard computing resources required to perform one measurement. Practically, I quantify for each mode the minimum number of multiplications the onboard computer has to make to perform one measurement. The number of multiplications is directly related to the power consumption. Note that the values I provide hereby correspond to the minimum amount of computations required to perform MI measurements using classic DFT and FFT implementations. Therefore, they are only qualitative estimates. The exact amount of multiplications depends on the actual implementation of the modes, which might change depending on the space application of interest.

I identify the computing resources of the modes as the number of multiplications required to build the spectra, which is related to the amount of points of the received electric signals. I assume that the received signal is always sampled with the same frequency $f_s = 2\ f_{max}$, with investigated frequencies $f_i = f_{min}(1+\Delta)^i$ corresponding to the frequency range (f_{min}, f_{max}).

Cost of frequency sweep measurements

For the frequency sweep mode, the spectra are built using the synchronous DFT approach. The amount of multiplications required by the $i-th$ DFT is equivalent to the amount of points of the $i-th$ received signal. Hence, the total amount of multiplications for a frequency sweep measurement (R_{sw}) is given by summing up the number of points composing all the $i-th$ received electric signals. This corresponds to multiplying the duration of the measurement $T_{sw} = N\sum_{i=0}^{j-1} 1/f_i$ by the sampling frequency:

$$R_{sw} = N\sum_{i=0}^{j-1} f_s/f_i. \tag{4.16}$$

Cost of chirp measurements

For the chirp mode, the spectra are built using one FFT. The amount of multiplications of an FFT scales in $x\ \log_2(x)$, with $x = T_{ch}f_s = \sum_{i=0}^{j-1} f_s/f_i$ the amount of points of the total received electric signal. Therefore, the amount of multiplications for one chirp measurement is

$$R_{ch} = \left(\sum_{i=0}^{j-1} f_s/f_i\right)\log_2\left(\sum_{i=0}^{j-1} f_s/T_i\right). \tag{4.17}$$

Cost of multi-spectral measurements

For the multi-spectral mode, similarly to the frequency sweep mode, the spectra are built using DFTs. The difference is that multiple frequencies are emitted simultaneously. Therefore, the same $i-th$ received signal is used by different DFTs. Hence, the amount of multiplications corresponding to each $i-th$ reception is given by the amount of points of the signal multiplied by the number of simultaneously

emitted frequencies. In my case, I emit simultaneously 9 frequencies. It follows that the total amount of multiplications for one multi-spectral measurement is given by:

$$R_{ms} = 9 \sum_{i=0}^{p-1} f_s / f_i \tag{4.18}$$

with $p = j\ div\ 9$ if the amount of frequencies (j) within the investigated frequency range is a multiple of 9 and $p = j\ div\ 9 + j\ mod\ 9$ otherwise (where div represents the Euclidean division and mod the remainder of the Euclidean division).

Comparison of the costs of the three instrumental modes

I compare the three modes by identifying their instrumental performances when investigating the same frequency range. For this purpose, I fix $f_{min} = 10\ kHz$ and vary f_{max} from 15 kHz up to 20 MHz. Figure 4.15 shows the computing resources (top panels) and the duration (left panels) associated to frequency sweep (blue), chirp (green) and multi-spectral (red) measurements in function of the maximum emitted frequency. To highlight the difference between the new fast modes and the reference frequency sweep mode, I show in the left panels of Figure 4.15 the cost and the duration curves normalized with respect to the performances of the frequency sweep mode.

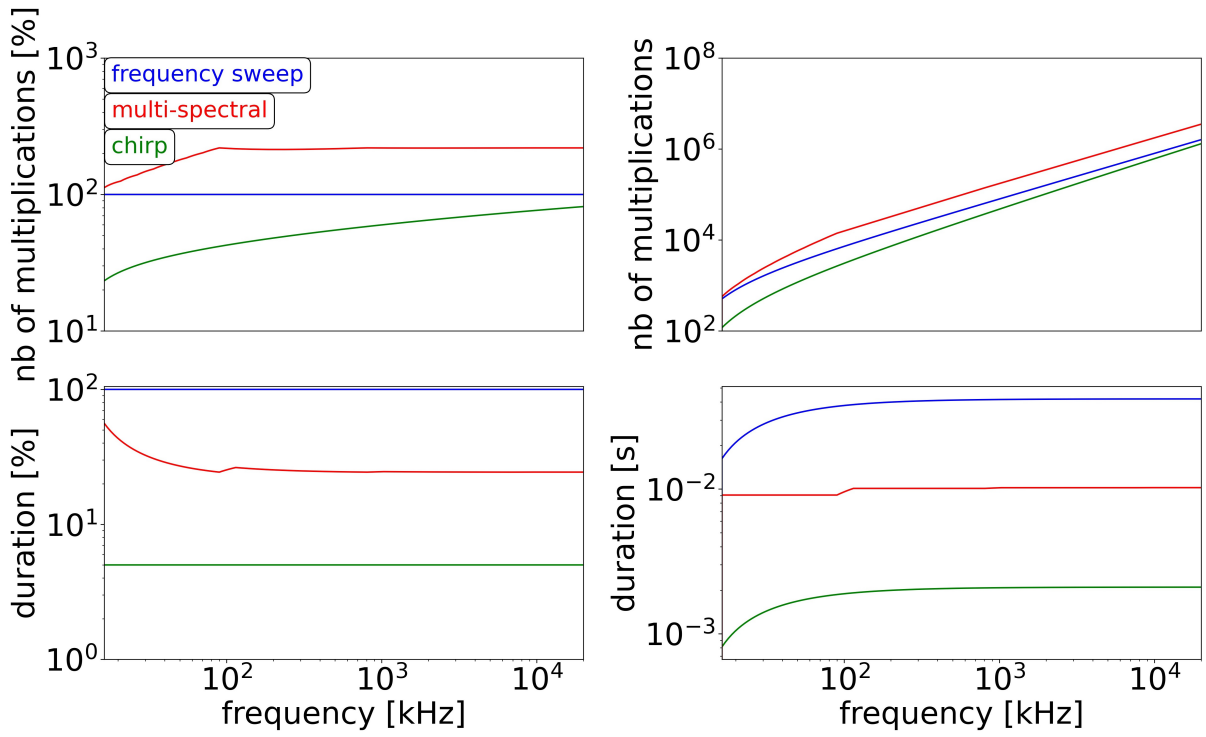

Figure 4.15: Comparison between onboard computing resources (costs shown in top panels) and sensors occupation time (measurement duration shown in bottom panels) of the chirp (green lines) and multi-spectral (red lines) modes with respect to the frequency sweep mode (dashed blue line). The frequency sweep performances are used as reference in the left panels. The cost and durations are represented in function of the maximum emitted frequency, considering a minimum investigated frequency of 10kHz and a frequency resolution $\Delta = 0.05$.

My numerical simulations show that the chirp mode is significantly faster than both frequency sweep and multi-spectral measurements. In terms of cost, I find multi-spectral measurements more demanding

than frequency sweep measurements. This was expected because high frequencies have longer durations for multi-spectral measurements than frequency sweep measurements. Chirp and frequency sweep measurements have instead similar costs, especially for wide investigated frequency ranges.

To conclude, I focus now on the largest investigated frequency range ($f_{min} = 10\ kHz$, $f_{max} = 20\ MHz$), which is the range of interest for MI experiments performed in the Earth's ionosphere.

Significant result. Multi-spectral measurements are up to 4 times faster than frequency sweep measurements, but they are twice as demanding in terms of onboard multiplications. Chirp measurements, instead, are up to 20 times faster and less demanding than both frequency sweep (20% less) and multi-spectral (50% less) measurements. Therefore, in order to improve the time resolution of MI experiments and answer the limited antenna occupation time due to sensors sharing onboard nanosatellites, from an instrumental point of view, COMIX or other future projects should implement chirp mode measurements in future versions of MI instruments. For instance, the chirp mode should be implemented for the MI instrument proposed for the M-MATISSE mission [Sanchez-Cano et al., 2022], for which the phase 0 study is currently ongoing.

Chapter 5

Discussion and Conclusions

In this chapter, I discuss both the results of my investigation (section 5.1) and the limitations inherent to my numerical (section 5.2) and experimental (section 5.3) tests. Then, I describe the difference between numerical and experimental measurements (section 5.4). I conclude by giving the future perspectives regarding COMIX and MI instrumental modeling (section 5.5). Note that a summary of my contribution to MI experiments is given in Appendix A.

5.1 Contribution to Mutual Impedance Modeling for Strong Emission Amplitudes, Inhomogeneous Plasmas and Rapid Measurements

Space exploration has improved for decades our knowledge of the physical mechanisms governing the solar system by relying on large satellite missions providing single-point measurements. Despite the broad understanding of space provided by such missions, one cannot distinguish from single-point measurements between spatial and temporal variations of the monitored properties. Such distinction is enabled by multi-point measurements [Paschmann and Daly, 1998]. However, multi-point missions using large satellites are very expensive due to the significant costs of large platforms. For this reason, they have often been avoided or not chosen during previous space mission selections (e.g. Cross Scale [Schwartz et al., 2009]). Recently, small satellites (e.g. nanosatellites) have lighted the interest of the scientific community. Nanosatellites are cheaper platforms. Hence, they are expected to facilitate future multi-point missions. However, the mass and volume of nanosatellites is significantly constrained. This means that scientific instruments previously designed for large satellites need to be re-designed to respect the strong limitations of small platforms. In this context, the R&D project COMIX is designing new versions of MI instruments for future multi-point nanosatellite applications. This PhD document describes the work I performed to improve the understanding and the modeling of MI experiments and to support the adaptation of MI instruments to fit the strong requirements of nanosatellite platforms.

Onboard large satellites, MI electric sensors are typically deployed on dedicated, long booms that locate them far from the satellite platform [Carr et al., 2007, Karlsson et al., 2020]. Onboard nanosatellites this is not possible because the booms are short [West et al., 2015]. As a consequence, MI sensors installed on nanosatellites are placed in the vicinity of the platform, where the sensors of other diagnostic instruments might be installed. On top of that, booms might carry sensors used by different instruments simultaneously, resulting in even closer sources of perturbation. The vicinity between MI and other instrument's electric sensors has different repercussions on MI measurements. I have investigated such perturbations using the 1D-1V Vlasov-Poisson model (section 3.1) and the testing facility of the French space laboratory LPC2E (section 3.2). Hereby, I summarize the impacts that short booms have on MI measurements and I recall the significant results of my investigation.

Note that I use a Vlasov-Poisson model to simulate MI experiments instead of the numerical models developed in the past by different authors [Geiswiller et al., 2001, Gilet et al., 2017]. The reason behind such choice is that past models considered a homogeneous plasma, affected by long duration emissions triggering linear perturbations of the plasma dielectric. In this PhD work, I focus instead on MI measurements that strongly perturb the plasma (section 4.1), MI experiments in the presence of plasma inhomogeneities (section 4.2) and fast MI measurements (section 4.3). Thus, I could not use the instrumental models developed in the past because they apply assumptions which are not compatible with the goals of my investigation.

Mutual Impedance Diagnostic Performance for Strong Emission Amplitudes

Electric instruments, electric devices and spacecraft sub-systems installed on the spacecraft platform perturb the environment by emitting spurious electric signals, potentially resulting in ElectroMagnetic Compatibility (EMC) [Youssef, 1996] issues between different devices. The amplitude of the spurious signals decreases with the distance from their source. If the source is far from the MI electric sensors, especially the receivers, as in the case of long deployable booms associated to large satellites, then such perturbations are negligible. If the source is near, as in the case of short booms associated to nanosatellites, then the spurious signals do not vanish at the position of the receiving sensors and, instead, they reduce the SNR of MI measurements. COMIX plans to mitigate such perturbations by increasing the emission amplitude. But strong emissions might significantly perturb the plasma dielectric and trigger non-linear plasma interactions. Such non-linear interactions are expected to modify the plasma response to MI emissions and, consequently, to perturb the MI diagnostic performance. In order to extend the modeling of MI experiments to the case of non-linear perturbations of the plasma dielectric and, at the same time, to support COMIX, I have performed full-kinetic Vlasov-Poisson numerical simulations to investigate the impact that strong emissions have on the diagnostic performance of MI experiments (section 4.1). In particular, I have identified the maximum amplitude for which the diagnostic of MI experiments is little perturbed, according to required MI instrumental performances.

I find that the maximum MI emission amplitude corresponds to the electric-to-thermal energy ratio $\alpha = 0.1$ (section 6.1). For such amplitude, the diagnostic performances agree with the typical performances of past and future MI space applications (e.g. DFP-COMPLIMENT onboard the Comet Interceptor mission). In particular, for such amplitude, I find plasma density diagnostic errors below 5% and electron temperature diagnostic errors below 20%, which are the performance requirements of the instrument.

My numerical investigation has also shown that the dynamics of ions provides a significant contribution to the non-linear perturbations of MI measurements. For this reason, in this part of the investigation, I have modeled the ion dynamics instead of simulating a fixed background of positive charges.

It is important to mention that these results strongly depend on the emission duration of the measurements. In particular, a specific emission amplitude that does not result in non-linear perturbations of the plasma over MI measurement time-scales might trigger strong non-linearities over longer durations. For instance, for the electric-to-thermal energy ratio $\alpha = 10^{-4}$ I find negligible perturbations of MI plasma diagnostic performance. But, in the case of the plasma observations of the solar wind performed by the STEREO spacecraft, past investigations have shown the presence of non-linear effects for the energy ratio $\alpha = 10^{-4}$ [Henri et al., 2011]. This apparent discrepancy is explained by the fact that the short emission duration of MI measurements does not enable to observe the development of non-linear plasma perturbations during the short time of operation (here about 20 periods of the emitted signal). In other words, the MI method can make use of the short measurement duration o be immune to nonlinear perturbations up to a significant amplitude of the oscillations. This means that, in the case of longer MI emissions (each frequency emitted for $N > 20$ periods), one might expect my results to overestimate the optimum emission amplitude. Therefore, the MI emission amplitude should be kept below $\alpha < 0.1$ to ensure acceptable diagnostic performances. As discussed in section 5.2, this result is a conservative lower limit due to the 1D cartesian geometry of the Vlasov-Poisson model.

Impact that Small-Scale Plasma Inhomogeneities Like the Plasma Sheath Surrounding the Spacecraft and the Sensors Have on Mutual Impedance Measurements

Spacecraft-plasma interaction processes charge electrically the satellite's platform to a given floating potential [Lai, 2012]. The electric potential perturbs the plasma, that reacts by forming inhomogeneous plasma regions enveloping the satellite. Such small-scale plasma inhomogeneities are called plasma sheath [Tonks and Langmuir, 1929]. The size of the plasma sheath scales with the Debye length, which is of the order of 0.001-0.01 m in the Earth's ionosphere, of about 10 m in the solar wind at 1AU. The plasma sheath is known to perturb different types of in situ plasma diagnostic instruments with the so-called spacecraft charging effects [Bergman et al., 2020, Marchand et al., 2010, Johansson et al., 2020, 2021]. The typical mitigation approach to such perturbations is to place the instrument far from the plasma sheath by using long deployable booms. But, in the case of nanosatellites it is not possible because the deployable booms are short [West et al., 2015]. This means that onboard nanosatellites the MI instrument is either placed close to or within the nanosatellite's plasma sheath. On top of that, also the instrument's surfaces undergo charging effects from their interaction with the plasma. As a result, similarly to the satellite platform, also the instrument is enveloped by its own plasma sheath (e.g. Bergman et al. [2020]). MI experiments perturb the plasma by triggering plasma waves that propagate from the emitting to the receiving MI sensors. In doing so, the emitted waves cross the small-scale density gradients associated to the plasma sheaths. This is believed to modify the properties of the waves and, therefore, to impact the MI plasma diagnostic performances. In order to support COMIX, I have quantified the impact of small-scale inhomogeneities like the plasma sheath on the MI diagnostic performance (section 4.2 and section 6.2).

I find that the perturbations of the MI plasma density diagnostic due to the localized inhomogeneities are negligible. In particular, for MI measurements in the presence of the considered plasma inhomogeneities I find plasma density relative errors below the plasma density resolution of the measurements (i.e. below 10%). Therefore, small-scale density gradients compatible with the size of the plasma sheath do not affect the density measurement of MI experiments. In particular, I find that MI experiments are able to retrieve the density of the homogeneous plasma unperturbed by the presence of the small-scale inhomogeneity. Instead, in the case of medium to large scale plasma inhomogeneities compatible with variations of the properties of the plasma crossed by the satellite, I find that MI experiments manage to retrieve the local density. Hence, the plasma density diagnostic of MI experiments is expected to be robust to the perturbations related to the spacecraft plasma sheath but also to be sensitive to the presence of plasma structures that the instrument is designed to observe. This is a significant result of my PhD work, as it answers a foundamental question regarding the locality of the plasma diagnostic provided by MI experiments.

For the electron temperature, instead, I find that the MI diagnostic performance is significantly perturbed by the presence of plasma inhomogeneities. Such perturbations are especially significant in the case of plasma sheaths due to positively charged satellites. In particular, I find electron temperature relative errors up to a factor 2 (resp. 9) in the case of the plasma sheath associated to a satellite with negative (resp. positive) electric potential. Both for negatively and positively charged satellites, the relative errors exceed the typical electron temperature uncertainty of 20%. If errors below 20% are required, then one needs to take into account the presence of the plasma inhomogeneity in the analysis of MI spectra. This is done by computing the reference spectra[1] using a model that includes the plasma sheath. This result is consistent with the work of Wattieaux et al. [2019, 2020], that included a step-like modeling of the plasma sheath of the RPC-MIP instrument onboard the Rosetta spacecraft in the analysis of RPC-MIP spectra for the identification of the electron temperature. What still remains to be investigated is the possible equivalence between the step-like model developed by Wattieaux et al. [2019] and the small-scale plasma inhomogeneities investigated in this PhD study.

[1]The electron temperature is obtained from best-fitting the MI spectra to reference spectra (chapter 2).

Note that this result is useful for the interpretation of the future measurements of PWI-AM2P instrument onboard the Mio spacecraft of the ESA-JAXA BepiColombo mission [Benkhoff et al., 2021]. Mio will monitor the plasma within Mercury's ionosphere, which is characterized by a Debye length λ_D ranging between (0.01 m, 10 m) in Mercury's magnetosphere. PWI-AM2P electric sensors are installed on 15 m wires attached to the spinning-stabilized Mio spacecraft [Karlsson et al., 2020]. But the size of the plasma sheath is of the order of λ_D. Therefore, in the case of large λ_D, the instrument antennas are placed near the satellite's plasma sheath. On top of that, Mio will be charged positively when in sunlight [2]. Thus, our results indicate that the identification of the electron temperature from PWI-AM2P spectra will require the inclusion of Mio's plasma sheath in the analysis of the measurements, as performed for RPC-MIP onboard Rosetta. Note that such procedure will not be required for the identification of the plasma density.

New Fast Mutual Impedance Instrumental Modes

Deployable booms are used for placing instruments and devices far from the satellite platform. In the case of plasma instruments, this is typically done to improve the Signal-to-Noise Ratio of the measurements. But the booms can only accommodate a limited amount of sensors due to the complexity that they introduce in the design of the deployable mechanism. In some cases, in order to optimize the sensors configuration, different instruments are required to share the same sensors (e.g. for the PWI plasma consortium onboard Mio for the BepiColombo mission [Kasaba et al., 2020]). This is the case for MI experiments, that have to share their electric sensors with other plasma diagnostic instruments, such as the Langmuir Probe (LP) and the Quasi-Thermal Nose (QTN) instruments. It follows that, onboard nanosatellites, MI experiments have a limited antenna occupation time. In particular, different experiments sharing the same sensors cannot always perform measurements simultaneously and, therefore, antenna sharing may result in a reduced time resolution.
In this context, COMIX plans to answer such constraints and limit the perturbations that MI emissions induce on nearby experiments by identifying new MI instrumental modes that perform faster measurements than the typical frequency sweep mode (section 2.2).

To support COMIX, I have used numerical simulations and experimental tests to investigate new fast MI instrumental modes called the chirp mode and the multi-spectral mode (section 4.3). I have validated the measurements of the new modes by comparison with the measurements of the classic MI instrumental mode called frequency sweep (section 4.3 and section 6.3).

From a plasma diagnostic point of view, I find both numerically and experimentally that chirp and multi-spectral measurements are equivalent to the reference frequency sweep measurements. In particular, the discrepancies between frequency sweep measurements and chirp (resp. multi-spectral) measurements amount to 2.15 dB (resp. 1.5 dB) in amplitude and 0.57 rad (resp. 0.42 rad) in phase for frequencies near the resonance of the measurements (i.e. for the range 1 MHz,4 MHz). Such discrepancies are of the order of the typical instrumental noise (about 1 dB) experienced for different MI space applications (e.g. RPC-MIP onboard Rosetta). The plasma density and the electron temperature are identified from the frequency corresponding to the resonant signature of the spectra and from the shape of the resonance, respectively. Hence, I conclude that the diagnostic performances of the new chirp and multi-spectral modes are equivalent to those of the reference frequency sweep mode.

From an instrumental point of view, I have investigated the computing resources required by each MI instrumental mode for obtaining a specific spectrum. In particular, I derive such computing resources as the amount of multiplications performed by the onboard computer unit for the production of MI spectra. For a given onboard computer unit, more multiplications correspond to larger power consumptions. This means that the instrumental mode corresponding to the lowest amounts of required multiplications is

[2] Preliminary unpublished SPIS simulations have shown that Mio will charge positively when in sunlight, due to the large amount of photoelectrons emitted from the satellite's surface.

associated to lower power consumptions. Practically, I focus on the frequency range ($f_{min} = 10\ kHz$, $f_{max} = 20\ MHz$) scanned using a specific frequency resolution and derive for the three modes both the duration and the computing resources required to perform one measurement. In terms of computing resources, I find that multi-spectral measurements require more onboard multiplications (up to 220%) than the frequency sweep measurements, while chirp measurements are less demanding (about 81%). In terms of duration, I find that multi-spectral (resp. chirp) measurements are 5 (resp. 20) times faster than frequency sweep measurements.

All in all, the chirp mode provides the fastest measurements. At the same time, it is also associated to less demanding measurements than both the frequency sweep mode and the multi-spectral mode. Therefore, COMIX and other future MI experiments should use the chirp mode to mitigate the reduced time resolution of MI measurements associated to antenna sharing or to increase the time resolution of future MI instruments.
Both in the case of chirp and multi-spectral modes, the cost of faster measurements is a worse SNR. Therefore, COMIX needs to consider increasing the MI emission amplitude, according to section 4.1, to ensure that the SNR is optimized also for the new fast instrumental modes. Note that strong emissions might perturb nearby experiments. This has to be taken into account when selecting the instrumental mode to be used for each specific mission. Note also that SNR could also be improved by averaging the measurements over time. However, such solution would result in longer measurement durations.

5.2 Limitations of the Numerical Simulations

The results described in this work have been obtained using a 1D-1V unmagnetized Vlasov-Poisson model in cartesian geometry to test numerically MI experiments for different plasmas and for different MI emissions. Such model presents different limitations.
First, the model is based on a 1D cartesian description of physical space. The 1D localized oscillating electric charges that I use to simulate MI emitting antennas in the 1D cartesian Vlasov-Poisson model correspond, in 3D, to infinite charged planes. Hence, the model investigates simplified geometric configuration of the investigated environment. This enables one to focus on specific properties of MI measurements while neglecting the contribution of superfluous details like, in the case of the investigation described in this document, the shape of the emitting sensors. The 1D cartesian model considers infinite plane grid antennas, while MI instruments typically use spherical sensors in actual space applications [Trotignon et al., 2007, Rauch et al., 2017, Kasaba et al., 2020, de Keyser et al., 2021]. Using infinite planes as emitting antennas means that the far-field component[3] of the electric field (the equivalent of the cold-plasma response [Chassériaux et al., 1972]) does not decrease with the distance from the emitting antennas. In particular, in 3D an emitting (spherical) point source would perturb the plasma with a far-field electric field component that decreases in $1/d_{ph}^2$ (i.e. α decreasing in $1/d_{ph}^4$) while in 1D the corresponding component is constant. This means that the numerical simulations discussed in this PhD work overestimate the SNR at large distances from the emitting antennas. In particular, in the case of the investigation of strong antenna emission amplitudes, the non-linear plasma interactions triggered in the numerical runs overestimate the actual interactions expected in 3D. Therefore, the maximum emission amplitude I derived is a conservative estimate. The actual estimate could be obtained by performing 1D *spherical* Vlasov-Poisson simulations. Such solution would not require additional computing power than that used for the analysis described in this PhD document. As discussed in section 5.5, a 1D spherical Vlasov-Poisson model might be a possibility for future improvements. Note that the impact of the actual geometry of MI electric sensors on the measurements might be investigated also using a 3D-3V numerical model. But at state-of-the-art, such 3D-3V simulations using large and refined spatial and velocity domains go beyond the computational power of modern supercomputers. Nevertheless, in the (not near) future it might be possible to perform such type of numerical runs. Thus, a 3D-3V Vlasov-Poisson investigation of MI measurements is left to future studies.
Second, this PhD work has investigated MI experiments in the case of plasmas described by Maxwellian

[3]The difference between far-field and close-field is described in section 3.1.2.

and drifting Maxwellian distribution functions. However, past studies have shown that different distribution functions might be required for the modeling of MI measurements depending on the specific plasmas probed by the experiment. Kappa-distrbutions [Gilet et al., 2019] and Bi-Maxwellian distributions [Gilet et al., 2017, 2019] are required for the modeling of plasmas composed of multiple electron components, such as the solar wind and the plasma composing the coma of comet 67P/CG, respectively. In fact, it has been shown that multiple electron components might modify significantly the shape of MI spectra and their analysis, for instance by introducing double-peaks in the MI resonant signature. This PhD work has neglected the contribution that non-Maxwellian distribution functions might give to MI measurements in the case of strong emission amplitudes, inhomogeneous plasmas and fast MI measurements. Such impact could be adressed by modifying accordingly the initialization of the Vlasov-Poisson model (section 3.1). These would represent minor modifications of the simulation setup I designed.

Note that, despite its limitations, the 1D-1V Vlasov-Poisson model has enabled the investigation of the impact that strong emissions associated to non-linear plasma perturbations, inhomogeneous plasmas and fast MI emissions have on MI measurements. Although past models [Geiswiller et al., 2001, Gilet et al., 2017, Wattieaux et al., 2019] enable a 3D geometric investigation of MI instrumental response, they are based on assumptions which are not compatible with the subject of this PhD work. In particular, both the model derived by Gilet et al. [2017] and the DSCD model from Geiswiller et al. [2001], Wattieaux et al. [2019] consider linear plasma perturbations triggered by long MI emission durations, in the case of homogeneous or homogeneous by step plasmas, respectively. The DSCD model even includes the impact that conductive surfaces (e.g. the satellite's surface) near MI electric sensors have on MI measurements. In all, despite being necessary for understanding MI measurements performed in space by different MI instruments, past MI models could not be used for performing the analysis discussed in this PhD work. Therefore, they had to be discarded in favor of the 1D-1V Vlasov-Poisson model that we adopted. Past models have been used in this PhD work only to validate the 1D-1V Vlasov-Poisson model.

The model used for this PhD investigation also presented some initial practical limitations. The initial numerical implementation of the model was not parallelized and, as a result, the numerical runs were very long and time-consuming. For this reason, I improved the implementation by parallelizing the model using an OpenMP architecture (Appendix C). If even faster runs will be required in the future, I suggest to implement an hybrid MPI/OpenMP architecture.

5.3 Limitations of the Experimental Tests

I have used the experimental facility of LPC2E for testing and validating the new MI instrumental modes in plasmas with specific characteristics. Such characteristics are dependent on the particular properties of the facility and of the equipment used for generating the plasma.
Reference Langmuir Probe (LP) measurements show that the plasma generated in the chamber is compatible with that found in the Earth's ionosphere between 100 km and 2000 km of altitude (section 3.2.3). LP measurements also show that the plasma is inhomogeneous along the chamber, with densities that can change by at most a factor 10 and electron temperatures that remain almost fixed. On the one hand, this means that different ambient plasmas can be tested depending on the position of the antennas inside the chamber. On the other hand, only a very specific range of plasmas can be generated in the chamber and, if different plasmas are of interest, then different types of plasma source are required.

The type of plasma generated in the chamber is specific to the particular characteristics of the plasma source. Other types of source might use different gas flow-rates, different electric settings, or even entirely different approaches for generating plasma. Future evolutions of the testing facility might include new types of source, which would expand the range of space plasmas that can be simulated in the chamber.
At state-of-the-art, the LPC2E plasma chamber is not equipped with particles instrument. Hence, the distribution function of the particles in the chamber is currently unknown. Future evolution of the equipment of the chamber might also include particles instruments to monitor the distribution function of the particles inside the chamber. Note that the measured distribution function could improve the validation

procedure of experimental MI measurements by being provided as input to MI models.

All in all, despite being delivered to LPC2E space laboratory very recently (June 2020), the plasma chamber is a real asset for the development and the validation of new instruments and new experimental procedures. A significant part of this PhD work would not have been possible without it.

5.4 Differences Between Numerical Simulations and Experimental Tests

In section 4.3, I discussed numerical and experimental MI measurements for the validation of new fast MI instrumental modes. In particular, I investigated numerically and experimentally the new chirp mode. I find that the electric signal measured from the plasma in the case of the numerical chirp measurement differs from that measured from the corresponding experimental test. This is shown in Figure 5.1, where chirp emitted (black) and received (green) signals are shown in function of time for both the numerical (panel a) and experimental (panel b) investigation. The comparison shows that the received signals

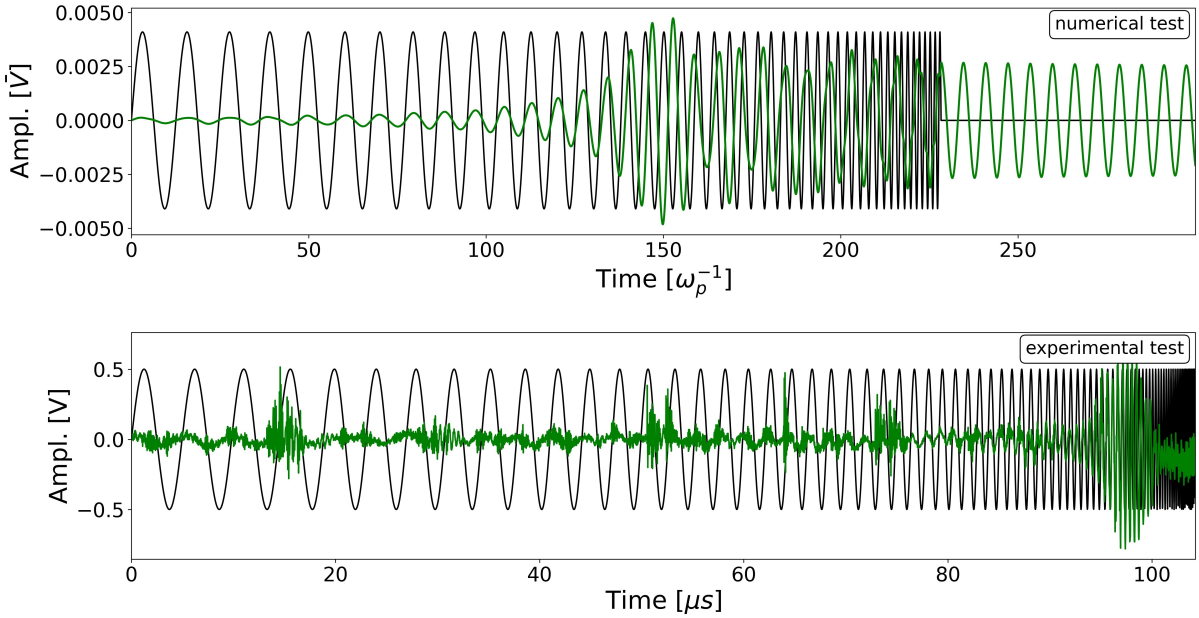

Figure 5.1: Comparison between numerical (panel a) and experimental (panel b) chirp measurements. The amplitude of emitted (black line) and received (green line) electric signals is represented in function of time.

resonates for a particular transmitted frequency. This is observed at time 150 ω_p^{-1} (top panel) and time 97 μs (bottom panel). But, after the resonance, the numerical tests (panel a) show that the resonant oscillations continue being measured by the receiving antennas for long after they have been triggered. This is consistent with the negligible Landau damping and group velocity associated to plasma waves that oscillate at frequencies close to the plasma frequency. The experimental test (panel b), instead, shows that the resonance is measured only for a short period of time. In particular, between 98 and 100 μs the received fluctuations do not oscillate with the same amplitude measured at the resonance.

I investigated two possible reasons for this discrepancy.

First, the numerical model simulates a collisionless plasma while the plasma in the chamber might be collisional near the antennas. In that case, electron-neutral collisions might damp the resonant oscillations triggered by the MI emission. Hence, I computed the electron-neutral mean-free-path l_{el} and compared it to the distance between emitting and receiving antennas inside the chamber. I find $l_{el} \simeq 500\ m$, which is significantly larger than the size of the chamber and of the Debye length ($0.008 - 0.023$ m).

Such mean-free-path has been computed using the electron-neutral (Argon) collisions ($l_{el} = 1/(\sigma_{el} n_{Ar})$, using the ambient pressure ($P_a \simeq 2.5\ x\ 10^{-3}\ Pa$) measured in the chamber, the ambient temperature ($T \simeq 300\ K$), the neutral Argon density $n_{Ar} = P_a/(k_B T)$, the elastic electron-neutral collision cross-section ($\sigma_{el} = 3\ x\ 10^{-21}\ m^2$ [Gargioni and Grosswendt, 2008]) and the thermal velocity of electrons ($v_{the} = 300\ km/s$). Thus, the plasma inside the chamber is found collisionless and it cannot explain the discrepancy between numerical and experimental chirp measurements.

Second, the numerical model simulates a plasma at rest while the plasma source generates a plasma that drifts along the chamber, with velocity v_D of about $(1 - 15)$ km/s (section 3.2.3). This means that, inside the chamber, the plasma excited by MI emissions drifts away from the MI antennas. If the time required by the plasma to cross half the chamber's length (MI antennas are placed in the middle of the chamber) is small compared to the measurement duration, the wave is advected away from the sensors, which could explain why the resonant plasma fluctuations disappear from the received signal. Thus, I consider the length of 0.9 m (i.e. half the length of the chamber) and I suppose that the plasma drifts along such length with velocity $v_D = 15$ km/s. By using the maximum drift velocity measured in the chamber, I obtain a conservative (minimum) travel time required by the resonant plasma to escape the MI antennas. I find that the resonant plasma escapes the MI antennas in $t_{tr} = 60\ \mu s$, which is significant with respect to the duration of MI chirp measurements performed during this PhD work (100 μs). It follows that also the drifting plasma cannot explain the discrepancy between numerical and experimental investigation.

Note that the plasma inside the chamber is unmagnetized during the tests thanks to the magnetic field compensation system. Hence, the particles' gyration in the chamber is negligible and it cannot explain the discrepancy neither.

However, discrepancies are expected because the model does not simulate the same experimental system found inside the chamber.
First, the numerical simulations use a periodic boundary in physical space. The experimental tests instead are confined within the walls of the chamber. Separate DSCD simulations (section 2.5), which are not illustrated here, have shown that the chamber's conductive walls modify significantly the shape of MI spectra and, in particular, they significantly reduce the amplitude increase associated to the resonance.
Second, the plasma inside the numerical box is homogeneous while the plasma in the chamber is drifting and inhomogeneous (section 3.2.3).
Third, the model simulates infinite charged grids that perturb the plasma (section 3.1.2) while the emitting antennas inside the chamber have a finite size (section 3.2.4).

All in all, the reason for this discrepancy remains an open question. From the investigation performed during this PhD work, the discrepancy seems to be related to the presence of the plasma chamber. The research of an answer with either additional tests in the plasma chamber or with experimental chirp measurements in space is left to future studies.

5.5 Future Perspectives

I conclude this PhD work by giving some perspectives on the future of both the COMIX R&D project in particular and MI instrumental modeling in general.

COMIX's future investigations concern the optimization of the telemetry of MI instruments and the integration of MI, Langmuir Probe and Quasi-Thermal Noise experiments:

- COMIX's objective is to have MI instruments take part to nanosatellite multi-point space exploration missions. In my investigation, I have focused on the analysis of MI spectra for the identification of the plasma density and electron temperature (i) in the case of strong amplitude emissions, (ii) in the presence of plasma inhomogeneities and (iii) for different MI instrumental modes. But the analysis of MI spectra is very expensive computationally (in particular the identification of the electron temperature). For this reason, in the past it has always been performed

on the ground. This means that, at the state-of-the-art, the telemetry available to MI instruments onboard satellites is not used for sending down to Earth the densities and temperatures identified from the measurements (i.e. two scalars). Instead, it is used for sending the full part of MI spectra (hundreds of scalars). This might represent an issue, especially in the case of space applications with limited telemetry, as it is expected onboard nanosatellites. This means that COMIX needs to find a way to analyze onboard most of the acquired spectra[4]. In the near future, COMIX will put effort into developing automatic algorithms for the onboard identification of the plasma density and electron temperature from MI measurements. Such algorithms will focus (i) on the identification of the frequencies corresponding to local minima and local maxima of MI spectra for the computation of the plasma frequency and plasma density and (ii) on the comparison of the shape of the spectra to a reference onboard dataset for the identification of the electron temperature. The algorithms will be tested and validated on the ground, using both synthetic spectra obtained from the DSCD code and experimental spectra obtained from the LPC2E plasma chamber. Note that heavy onboard computations, such as the computation of least-squared-errors between curves, have become possible only recently, thanks to the modern onboard computing units and their significantly improved performances.

- MI experiments onboard nanosatellites are likely to be required to share their sensors with other plasma experiments. The candidates for an optimal integration with MI experiments are the LP and the QTN. This is not the first time that such experiments share the same electric sensors. MI and LP instruments already share their sensors for the PWI-AM2P experiment onboard BepiColombo [Kasaba et al., 2020], for the RPWI-MIME experiment onboard JUICE [Rauch et al., 2017] and for the DFP-COMPLIMENT instrument onboard Comet Interceptor [de Keyser et al., 2021]. MI and QTN experiments will share sensors onboard the CIRCUS mission [Zaslavsky et al., 2013]. COMIX's challenge is to ensure that the miniaturization of the instrument and of the electronics from large satellites to small platforms does not impact the measurements. On top of that, for an optimal integration, COMIX will need to test in the future whether MI, LP and QTN experiments can be performed simultaneously. It is expected that MI and QTN experiments cannot perform measurements simultaneously, since QTN is a passive technique while MI is active. MI and LP experiments, instead, could be performed simultaneously since they operate with AC and DC signals, respectively.

Future improvements of the modeling of MI experiments consist of both theoretical and practical investigations. Future theoretical investigations concern the modeling of MI experiments in a magnetized plasma, the analysis of transient effects related to the MI emission, the creation of a spherical 1D-1V Vlasov-Poisson model that enables the simulation of MI measurements in spherical symmetry, the creation of a SPIS plug-in able to simulate MI experiments and follow-up studies.

- The modeling of MI experiments that this PhD work contributed to, similarly to other recent past studies [Gilet et al., 2017, 2019], has focused on unmagnetized plasmas. For an unmagnetized plasma, MI measurements have only one resonance for frequencies near the plasma frequency. For a magnetized plasma, instead, multiple resonances are expected [Bernstein, 1958, Pottelette et al., 1981]. But, in the near future, different MI instruments will explore magnetized plasma environments of our solar system. First, the PWI-AM2P experiment onboard BepiColombo will investigate the Hermean environment at Mercury. Second, the RPWI-MIME experiment will monitor the ionosphere at Ganymede [Carnielli et al., 2019]. In both cases, the contribution of the magnetic field to MI measurements is expected to be significant, because the electron cyclotron frequency ω_{ce} is of the order of the plasma frequency ω_{pe}. In such case, multiple eigenmodes of the system are found at frequencies of the order of the plasma frequency and, consequently, multiple resonant signature are observed in MI spectra.
  In this context, the modeling of MI experiments needs to be improved to include the magnetic

[4]Some spectra will nevertheless need to be sent to Earth for ensuring the automatic algorithm is working properly.

field contribution for better understanding the data collected in future missions.
To answer such needs, studies currently ongoing at LPC2E include the contribution of the magnetic field in the instrumental modeling of MI experiments. The improvement of the code will be validated by comparing the synthetic MI spectra from the simulation to the corresponding spectra obtained in the plasma chamber. Different experimental tests will be made using the magnetic field compensation system that enables one to modify the magnetic field at the MI sensors as required.

- The transient effects that electric emissions similar to MI emissions trigger in the plasma surrounding the instrument have been investigated in the past by Derfler and Simonen [1969]. Such transients correspond to the contribution of high-order poles to the plasma response generated by electric emissions. Future work might focus on the impact that such transients have on MI measurements and the possibility to use them to improve the performances of the experiment, both from a plasma diagnostic and a time resolution point of view. This is especially needed for the chirp mode, which is used for perturing the plasma with emission signals of very short duration.

- This PhD work benefits from numerical simulations performed using a Vlasov-Poisson model (section 3.1). Such model is implemented considering a Cartesian 1D geometry. But there is a gap between the 1D plasma perturbations investigated in this PhD work and the electric perturbations generated by MI emissions in 3D (section 5.2). Future work might focus on the development of a 1D spherically symmetric Vlasov-Poisson model to fill such gap.

- This PhD work investigated the impact of strong emission amplitudes by using a fixed duration of the measurements. This consists of fixing the amount of repetitions N, which is consistent with the characteristics of the DFP-COMPLIMENT experiment onboard Comet Interceptor. Future studies might investigate the dependency of the non-linear perturbations of the plasma on the duration of MI measurements (i.e. N). Indeed, one would expect that non-linearities are triggered more efficiently for long emission durations (i.e. $N >> 1$). Therefore, the actual emission amplitude threshold that ensures negligible non-linear perturbations of MI measurements is likely to increase for short emission durations, such as those associated to chirp measurements.

- This PhD work shows that MI experiments can be perturbed by the vicinity of MI sensors to the satellite platform. Thus, for each space mission, specific modeling is required for selecting the position of MI instruments onboard the satellite. At state-of-the-art, the reference tool used for modeling the interaction between the satellite platform and the plasma encountered during specific missions is the Spacecraft Plasma Interaction System (SPIS). Such tool evolves in time the (i) electric potential of the different surfaces composing the satellite by taking into account their materials and (ii) the position of the charged particles composing the plasma considering the feedback of the satellite's electric field. On top of that, SPIS is can also simulate in situ plasma measurements, such as Langmuir Probe and particles instruments measurements. Thus, it can provide significant insight on the impact that the position of the instruments has on in situ measurements. However, the latest SPIS version cannot currently simulate MI experiments. In this context, I have been in contact with SPIS developers to include in the software a plug-in able to simulate MI experiments. Test that have been performed by students that I followed show that the plug-in is still not able to properly simulate MI experiments and it needs further developing. In particular, the electric perturbations of the plasma triggered by the emission of specific signals in SPIS does not correspond, at state-of-the-art, to the perturbations expected analytically. Hence, the implementation of the plug-in needs to be updated. Note that, if future versions of the plug-in manage to perturb the simulated plasma as expected, then SPIS can be used for extending the results found by this PhD work. In particular, it can be used for investigating the impact that the 3D plasma sheath has on the diagnostic performance of MI experiments.

Future practical investigations of MI experiments concern the experimental validation of the numerical results discussed in this PhD work, in the context of (a) strong emission amplitudes (section 4.1) and (b) plasma inhomogeneities (section 4.2). (a) In the case of strong emissions, such tests should consist of comparing MI measurements obtained for different emission amplitudes. This has not been investigated during this PhD work due to lacking of time and equipment adapted for such an investigation. (b) In the case of inhomogeneous plasmas, such tests should consist of comparing MI measurements obtained for different emitting-receiving antennas distances (from the Debye length λ_D to about 20 λ_D) inside LPC2E plasma chamber, where the plasma is inhomogeneous. However, the Debye length inside the chamber is at most of the order of $\lambda_D \simeq 10^{-2}\ m$. Due to such a short Debye length, the tests would require a very fine control of the distance between the antennas, as well as that of the characteristics of the plasma in which the antennas are moved. The equipment available during my investigation did not allow such an investigation. Nevertheless, future extensions of the capabilities of LPC2E facility might enable such tests. Hence, this validation of my numerical results is left to future studies.

Chapter 6

Accepted and Submitted Papers

6.1 Paper 1 (Accepted by JGR): In Situ Space Plasma Diagnostics with Finite Amplitude Active Electric Experiments: Non-Linear Plasma Effects and Instrumental Performance of Mutual Impedance Experiments

JGR Space Physics

RESEARCH ARTICLE
10.1029/2022JA030813

Key Points:

- The plasma response to large antenna emission amplitudes triggering non-linear plasma perturbations is simulated
- Ion dynamics contributions to large amplitude propagating electric signals in the plasma are crucial and therefore should not be neglected
- Mutual impedance diagnostic performances are acceptable for emission amplitudes corresponding to electric-to-kinetic energy ratios up to 0.1

Correspondence to:
L. Bucciantini,
luca.bucciantini@cnrs.fr

Citation:
Bucciantini, L., Henri, P., Wattieaux, G., Califano, F., Vallières, X., & Randriamboarison, O. (2022). In situ space plasma diagnostics with finite amplitude active electric experiments: Non-linear plasma effects and instrumental performance of mutual impedance experiments. *Journal of Geophysical Research: Space Physics*, *127*, e2022JA030813. https://doi.org/10.1029/2022JA030813

Received 1 JUL 2022
Accepted 23 NOV 2022

The copyright line for this article was changed on 13 DEC 2022 after original online publication.

In Situ Space Plasma Diagnostics With Finite Amplitude Active Electric Experiments: Non-Linear Plasma Effects and Instrumental Performance of Mutual Impedance Experiments

L. Bucciantini[1], P. Henri[1,2], G. Wattieaux[3], F. Califano[4], X. Vallières[1], and O. Randriamboarison[1]

[1]Laboratoire de Physique et Chimie de l'Environnement et de l'Espace (LPC2E), CNRS, Université d'Orléans, Orléans, France, [2]Laboratoire Lagrange, OCA, UCA, CNRS, Nice, France, [3]Laboratoire Plasma et Conversion d'Energie (LAPLACE), CNRS, Université de Toulouse, Toulouse, France, [4]Dipartimento di Fisica, Università di Pisa, Pisa, Italy

Abstract Mutual impedance (MI) experiments are a kind of plasma diagnostic techniques for the identification of the in situ plasma density and electron temperature. These plasma parameters are retrieved from MI spectra, obtained by perturbing the plasma using a set of electric emitting antennas and, simultaneously, retrieving using a set of electric receiving antennas the electric fluctuations generated in the plasma. Typical MI experiments suppose a linear plasma response to the electric excitation of the instrument. In the case of practical space applications, this assumption is often broken: low temperature plasmas, which are usually encountered in ionized planetary environments (e.g., RPC-MIP instrument onboard the Rosetta mission, RPWI/MIME experiment onboard the JUICE mission), force toward significant perturbations of the plasma dielectric. In this context, we investigate MI experiments relaxing, for the first time, the assumption of linear plasma perturbations: we quantify the impact of large antenna emission amplitudes on the (a) plasma density and (b) electron temperature diagnostic performance of MI instruments. We use electrostatic 1D-1 V full kinetic Vlasov-Poisson numerical simulations. First, we simulate the electric oscillations generated in the plasma by MI experiments. Second, we use typical MI data analysis techniques to compute the MI diagnostic performance in function of the emission amplitude and of the emitting-receiving antennas distance. We find the plasma density and electron temperature identification processes robust (i.e., relative errors below 5% and 20%, respectively) to large amplitude emissions for antenna emission amplitudes corresponding to electric-to-thermal energy ratios up to $\left(\epsilon_0 E^2\right)/(n_0 k_B T_e) = 0.1$.

1. Introduction

Mutual impedance (hereafter MI) experiments are a kind of in situ plasma diagnostic instruments that enable measurements of the absolute plasma density and the electron temperature through the dynamical response of a probed plasma to an external electrical excitation. Such measurement techniques were proven successful for several ionospheric (Bahnsen et al., 1988; Béghin & Debrie, 1972; Décréau et al., 1978; Grard, 1997; Pottelette et al., 1975; Pottelette & Storey, 1981; Storey et al., 1969) (e.g., ISOPROBE experiment onboard the AUREOL-3 satellite, for the ARCAD-3 mission, Béghin et al., 1982) and planetary space missions (e.g., the RPC-MIP instrument, J. Trotignon et al., 2007, onboard the ESA Rosetta mission). Different versions of MI experiments will also contribute to new exploratory missions such as the joint ESA-JAXA BepiColombo mission with the PWI/AM2P experiment (Kasaba et al., 2020; J. Trotignon et al., 2006), the JUICE ESA mission with the RPWI/MIME experiment and the Comet Interceptor ESA mission with the DFP-COMPLIMENT instrument (Snodgrass & Jones, 2019). New versions of MI experiments are currently being developed to adapt to the constraints of nano/microsatellite platforms.

The basic principle of MI experiments is the following. Plasma parameters such as the electron density and temperature are obtained through the analysis of the so-called MI spectrum. It is defined as the electrical impedance between an emitting and a receiving electric antenna embedded in the plasma to diagnosed (Storey et al., 1969; Chasseriaux et al., 1972; Béghin, 1995; Gilet et al., 2017; Wattieaux et al., 2019). Practically, the electron density and temperature are derived as follows. The plasma environment is perturbed by the emission of a succession of elementary electric sinusoidal oscillations injected in the plasma through the emitting electric antennas. Simultaneously, the electric oscillations that propagate in the probed plasma are measured with the receiving antennas. Such oscillations correspond to the plasma response at the emitted frequency. This frequency is modified step by step to cover a given range of frequencies and build up the MI spectrum. We hereafter refer to this process as

frequency sweep. The MI spectrum is a function of the plasma dielectric and it exhibits resonant signatures at the plasma characteristic frequencies (plasma eigenmodes). For instance, in the case of an unmagnetized plasma, MI spectra present one resonant signature at the plasma frequency. The electron density and the temperature are retrieved from the position and the shape of the resonance, respectively (Chasseriaux, 1972; Chassériaux, 1974).

The state-of-the-art methods used to model the instrumental response of MI experiments consider a variety of situations or processes known to significantly impact the instrumental response: (a) in collisionless plasmas, various types of distribution functions that account for different plasma populations (Gilet et al., 2017; Wattieaux et al., 2019), (b) the peculiar boundary conditions imposed by a conductive spacecraft carrying the experiment (Geiswiller et al., 2001), and (c) the influence of spacecraft charging that generates a plasma sheath surrounding the spacecraft and the instrument (Wattieaux et al., 2019). These models are all based on the assumption of a linear response of the plasma to the electric excitation of the instrument. This means that such models assume that the emitting antennas introduce small enough electric perturbations within the plasma, so that its dynamics is defined by its linear dielectric (Grard, 1969). Therefore, they assume negligible non-linear effects triggered by the emission process. Hence, they assume that the electric energy injected by the emitting antenna is much smaller than the thermal energy of the plasma to be diagnosed.

To ensure small perturbations of the plasma dielectric, MI experiments are designed to emit low amplitude signals. Practically, this is done by limiting the voltage imposed on the emitting antenna. This also has the advantage of limiting the electric power consumption required for MI space experiments.

However, the voltage imposed on the emitting antenna cannot be too small to ensure a satisfactory signal-to-noise ratio.

First, the amplitude of the received signal is proportional to that of the emitted signal. A large enough emitted signal therefore corresponds to an increased amplitude for the received signal. Strong emissions are particularly needed if the distance between emitting and receiving antenna is large. This is the case for MI instruments designed to probe hot space plasmas, for example, with particles energy of the order of 10 eV. For instance, the so-called LDL mode of the RPC-MIP instrument on Rosetta designed to observe hot plasmas near comet 67P/CG, the PWI/AM2P experiment on BepiColombo that will monitor hot plasmas in Mercury's environment and the RPWI/MIME experiment on JUICE that will investigate hot plasmas in the ionosphere of Ganymede.

Second, the instrument design must ensure that the received signal is above the instrumental noise. Instrumental noise is essentially composed of two main sources. On the one hand, the background noise of the instrument itself. On the other hand, the overall electrical noise generated by the platform and the rest of the payload. This second source is often referred to as the electromagnetic compatibility (EMC) of the spacecraft (ECSS-E-ST-20-07C handbook of ECSS, Youssef, 1996). EMC is costly for standard platforms and particularly delicate for nanosatellite platforms. Sufficiently large amplitude emission signals therefore mitigate the lack of EMC by improving the signal-to-noise ratio. It is therefore expected that large amplitude emissions might be preferable for future MI experiments designs, especially those dedicated to nanosatellite platforms.

On the one hand, from a practical point of view, there is therefore a net benefit in increasing the amplitude of the signal emitted in the plasma to increase the signal-to-noise ratio. On the other hand, from a plasma diagnostic point of view, there are net benefits in decreasing the amplitude of the signal emitted in the plasma. First, it ensures that the plasma response is described by its linear dielectric. Second, it limits the perturbations on other instruments of the payload such as interferences due to the MI emitted signal. All in all, a trade-off is chosen to ensure a large enough signal to be measured, for a small enough signal to be emitted: between few 10s mV and 1 V in typical space plasmas.

However, even with such trade-off, the linear plasma response hypothesis is often broken in ionized planetary environments, especially in dense, low-energy plasma regions. A recent example is given by the cold cometary plasma probed by Rosetta in the inner coma of comet 67P/CG, with electron temperatures as low as 0.1 eV independently measured by both the MI RPC-MIP (Wattieaux et al., 2020) and the Langmuir Probe RPC-LAP (Eriksson et al., 2017; Odelstad et al., 2020). Similar situations are also expected to be encountered by the RPWI/MIME experiment onboard JUICE in the ionosphere of Ganymede. In such cases, the thermal energy of the electrons can hardly be considered much larger than the injected electric perturbation. Hence, non-linear plasma effects (e.g., wave-wave and wave-particle interactions) are expected to strongly modify the plasma response to MI emissions. The assumption of a linear plasma dielectric response to the instrument perturbation becomes

invalid. Consequently, it is necessary to assess the plasma diagnostic performance of MI experiments in such common situations.

In this context, the objective of this study is to assess how strong the electric emissions can be in active in situ plasma measurements such as MI experiments, while preventing significant losses in instrumental performance. To this purpose, this study aims at relaxing, for the first time, the assumption of linear perturbations of the local plasma environment in MI instrumental modeling in order to investigate the influence of the plasma non-linear effects on the MI instrumental response. Practically, we aim at quantifying the impact of non-linear effects on MI diagnostics by assessing the error both in electron density and temperature measurements for large emission amplitudes.

The investigation described in this paper is performed by means of 1D-1 V full kinetic numerical simulations that model the plasma response to an external electric antenna, by solving the Vlasov-Poisson coupled equations for both ions and electrons.

This document is organized as follows. The numerical models adopted in this investigation are described in Section 2. The initialization of the numerical model and its validation are described in Appendix A and Appendix B, respectively. For repeatability purposes, the parameters defining the numerical simulations described in this study are listed in Appendix C. The non-linear effects generated in the plasma by strong electrical antenna excitations are described in Section 3, and their consequence on plasma diagnostics performed by MI experiments is quantified in Section 4. We conclude by discussing the implication for both past and current space mission data analysis, as well as for future instrumental designs in Section 5.

2. Model Description: 1D-1V Vlasov-Poisson

We consider a non magnetized, homogeneous, collisionless plasma composed of electrons and ions initially described by a single Maxwellian velocity distribution function. An electrical antenna is used to inject an external electric field perturbation to which the plasma reacts self-consistently. We neglect in our model the perturbations arising from the presence of the plasma sheath surrounding the antennas used for MI measurements.

The simulation models used in this study are based on the numerical integration of the Vlasov-Poisson system of equations that describe the spatio-temporal evolution of electron and ion distribution functions ($f_e(t, x, v_e)$ and $f_p(t, x, v_i)$, respectively, where t is the time, x the position in the plasma and v the electrons and ions velocity). The numerical integration scheme is the one described by Mangeney et al. (2002). The Vlasov equation used to evolve in time the electron and ion distribution function, simplified considering a negligible magnetic field, reads:

$$\frac{\partial f_\gamma(x,t,v_\gamma)}{\partial t} + \vec{v_\gamma}\cdot\nabla f_\gamma(x,t,v_\gamma) + \frac{q_\gamma}{m_\gamma}\vec{E}\cdot\nabla_{\vec{v_\gamma}} f_\gamma(x,t,v_\gamma) = 0 \tag{1}$$

where $\gamma = e, i$ represents the species and E is the electric field.

We limit our study to the 1D-1V electrostatic case. We use the model previously used in Henri et al. (2010), modified adding multiple external emitting electric antennas modeled using oscillating charge densities in the Poisson equation:

$$\nabla\cdot\vec{E} = e\frac{n_i(x,t) - n_e(x,t)}{\epsilon_0} + \frac{\rho_{ext.}(x,t)}{\epsilon_0} \tag{2}$$

where n_e (resp. n_i) is the electron (resp. ion) density and $\rho_{ext.}$ the external charge density.

The equations are normalized using electron characteristic quantities: the elementary charge e, the electron mass m_e, the Debye length λ_D, the time ω_p^{-1}, with $\omega_p = \sqrt{(e^2 n_0)/(\epsilon_0 m_e)}$ the angular plasma frequency, and the mean density n_0. It follows that velocities are normalized by the electron thermal speed $v_{the} = \lambda_D\omega_p$, the electric field by $E = (m_e v_{the}\omega_p)/e$ and the charge density at the antenna by $\bar{\sigma} = e n_0 \lambda_D$.

The numerical simulations are performed using periodic boundary conditions in physical space and assuming electron and ion distribution functions equal to zero for velocities outside the given velocity range (i.e., $f_e(x, |v_e| > v_{e,\max}, t) = 0$ and $f_p(x, |v_i| > v_{i,\max}, t) = 0$). Tables C1 and C2 list the simulation parameters.

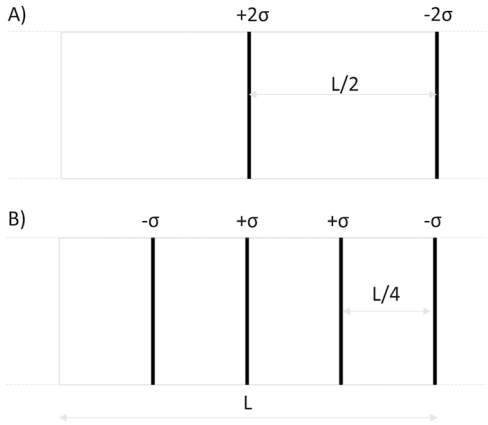

Figure 1. Representation of the emitting antennas configuration in the periodic simulation box. The top (resp. bottom) panel represents the model A (resp. B), characterized by two (resp. four) emitting antennas.

The simulations are initialized with uniform single Maxwellian distribution functions for ions and shifted Maxwellian distribution functions for the electrons to minimize transient effects. Such initialization is discussed in Appendix A. Transient signals will be investigated in a future dedicated work and are out of the scope of this study.

Each emitting antenna is modeled as the external source $\rho_{ext.}(x, t) = \sigma(t)\delta(x)$ characterized by the following oscillating charge term:

$$\sigma(t) = \sigma_0 \sin(\omega t) \tag{3}$$

where σ is the oscillating charge per unit surface, σ_0 is the amplitude of the oscillating charge, $\omega = 2\pi f$ is the angular frequency with f the emission frequency. Each of our 1D antennas is equivalent in 3D space to an oscillating, uniformly charged, infinite planar grid. Such a grid is supposed to be so thin that the collection of particles at its surface is negligible, resulting in particles moving freely across the antennas. This choice, also adopted in previous studies (Buckley, 1968), allows one to neglect the collection of electrons and ions from the emitting antenna. Each external antenna generates an oscillating electric signal composed of one uniform term (hereafter called far-field term) and a spatially damped term that propagates to the surrounding plasma from the position of the antenna (hereafter called close-field term) (Podesta, 2005). The far-field term corresponds to the electric field expected for the cold plasma limit (Chasseriaux et al., 1972) (i.e., $\omega \gg \omega_p$), while the close-field term represents the wave-component of the perturbation generated by the emitting antennas. Periodic boundary conditions on the simulation box require the use of, at least, two antennas of opposite oscillating charges. This configuration is equivalent to that of an oscillating capacitor, composed of two parallel infinite charged planes embedded in the plasma. Such capacitor perturbs the surrounding plasma with an electric field that is the sum of (a) a spatially constant far-field term and (b) close-field terms propagating in-between the two electrodes.

In our 1D model, the far-field term is equivalent, in 3D, to the electric field component that would decrease in $d_{ph.}^{-2}$ with the distance, $d_{ph.}$, from a point source emitting antenna. The close-field term is equivalent in 3D to the radial component of the wave that would propagate from the same emitting point source antenna to the surrounding plasma. We note that in 1D the amplitude of the electric field oscillations at large distances from the emitting antennas is overestimated w.r.t. that expected in 3D due to the far-field term. In order to account for this 1D artifact, we use in our study two different antennas configurations, hereafter called model A and model B (top and bottom panel of Figure 1).

Model A is optimized for the investigation of the non-linear effects triggered in the plasma by the MI emission signal. In particular, it benefits from the presence of the 1D artifact term: enhanced electric field fluctuation amplitudes correspond to enhanced growth-rate of the generated non-linear plasma perturbations. Thus, the simulation durations needed to study non-linear plasma perturbations are reduced. For this model, the positions of the emitting capacitors plates are chosen in order to maximize the distance between any two opposite charge electrodes. Practically, this is done by imposing the distance between the electrodes (represented as vertical lines in top panel of Figure 1) of each capacitor as half the length of the numerical spatial box and by superposing, for any two neighboring capacitors, the antennas that emit the same electric signal.

Model B is optimized for the quantitative investigation of MI diagnostic performance. It is devised to obtain MI spectra that either consider or neglect the effects of the 1D artifact depending on the position in the simulation box at which the electric fluctuations are retrieved. We consider (resp. neglect) the effects of the 1D electric-field artifact term by analyzing the electric oscillations generated in the plasma between two opposite (resp. same) charge antennas, where the far-field component is doubled (resp. canceled out). The positions of the antennas in the numerical box are chosen to maximize both the distance between neighboring capacitors and the distance between the plates of each capacitor. Practically, for this model, any two emitting antennas are separated by a distance equal to a quarter of the numerical spatial box length. This model allows one to investigate what non-linear effects are triggered by the close-field and far-field terms separately.

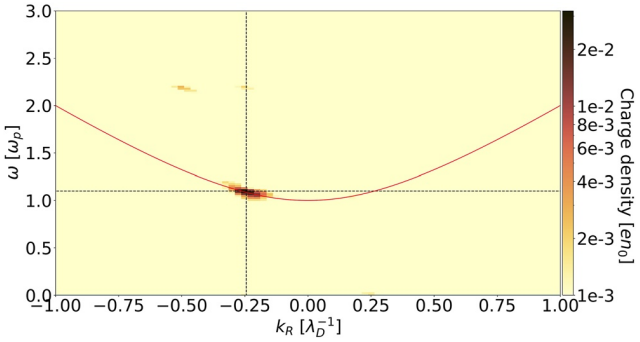

Figure 2. Charge density Fourier spectrum, in the real wavenumber-frequency space (k_R, ω), for simulation NF_01. The horizontal and vertical dotted black lines indicate the Langmuir wave at the antenna emission frequency ($-k_L$, ω_L). The Langmuir wave dispersion relation is shown as a red solid line.

Since the contribution of the far-field term is always present in 3D experimental MI spectra, for consistency with 3D MI experimental measurements, in this document we only discuss the plasma density and electron temperature obtained *including* such contribution. In the following, the plasma density and the electron temperature are obtained by applying the same data analysis techniques used for the investigation of experimental MI spectra (Gilet et al., 2017; Wattieaux et al., 2020).

3. Non-Linear Effects Generated in an Unmagnetized Space Plasma Excited by an External Large Amplitude Oscillating Antenna

In this section, we investigate the impact of moderate to strong electric antenna emission at a given frequency on the nearby perturbed plasma.

We define the electric-to-thermal energy ratio $\alpha = (E^2\epsilon_0)/(n_0 k_b T_e)$ as the parameter identifying the level of non-linearity associated to the electric field E, driven by the antenna emission. This ratio depends on the amplitude and on the frequency of the oscillating electric potential at the antenna. In particular, the electric field that propagates in the plasma scales with frequency ω as the inverse of the collisionless unmagnetized cold plasma dielectric permittivity, corresponding to $\left(1-\omega_p^2/\omega^2\right)^{-1}$ (Podesta, 2005) for $\omega \geq \omega_p$. In order to model different levels of α that can be achieved in MI experiments, we compare a number of simulations made using different frequencies but with same emission amplitudes.

The numerical simulations are set on the typical timescale of experimental MI emission durations, which turns out to be of the order of $N = 15$ oscillation periods of the emitted frequency. As a consequence, we neglect all effects that would develop over larger timescales. The total simulation time, the size of the physical box, the velocity range over which the ion and electron distribution functions are defined, as well as all other most relevant parameters are listed in Table C1.

In the following, we investigate with Model A (a) the non-linear perturbations triggered by single frequency emissions with a fixed ion background (Section 3.1) and (b) the impact of the ion dynamics on the perturbation evolution (Section 3.2).

3.1. Large Amplitude Perturbations of the Plasma Dielectric With Fixed Ions

In this section we consider the case of a fixed neutralizing background of ions and focus on the electron dynamics only. In particular, we investigate the plasma response to electric signals generated by an oscillating charge with amplitude $\sigma = 0.1\bar{\sigma}$ at three different frequencies: $0.5\omega_p$ (simulation NF_01), $1.1\omega_p$ (simulation NF_02) or $2.0\omega_p$ (simulation NF_03). The corresponding electric-to-thermal energy ratios are: 0.01, 0.33, 0.01.

On the one hand, for antenna emissions at $0.5\omega_p$ and $2.0\omega_p$, the electric perturbation that propagates in the plasma oscillates at the emission frequency. However, the perturbation is limited to regions close to the antennas, because it corresponds either to an evanescent wave (for $0.5\omega_p$) or to a propagating wave affected by strong Landau damping (for $2.0\omega_p$) (Brunetti et al., 2000) as consistent with a linear plasma response. In both cases, we do not observe any non-linear effect.

On the other hand, at frequency $\omega = 1.1\omega_p$ corresponding to wavenumber $k_L = -0.244\ \lambda_D^{-1}$, a non-linear plasma response occurs because of the conversion efficiency nearby the plasma frequency. The signature of this wave-wave interaction is shown in the charge density Fourier spectrum in Figure 2, where the black dashed lines indicate the emitted Langmuir wave at (k_L, ω_L) and the red line indicates the dispersion relation of Langmuir waves $\omega_L^2/\omega_p^2 = 1 + 3\lambda_D^2 k_L^2$.

First, on top of the emitted Langmuir wave, we also observe the so-called virtual wave at (2 k_L, 2 ω_L) (Dysthe & Franklin, 1970) which is represented as a localized increase in charge density at position ($k_R = -0.488\ \lambda_D^{-1}$, $\omega = 2.2\ \omega_p$) of Figure 2. Second, signatures of wave-particle interactions are observed. At the early stage of the

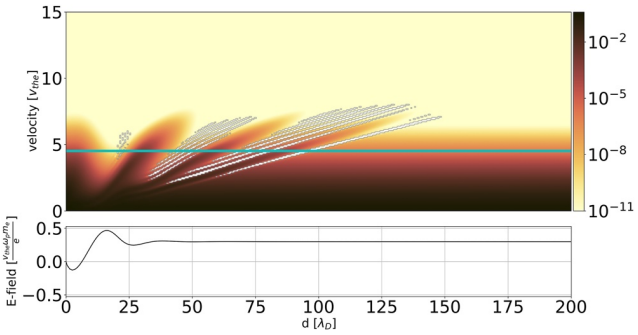

Figure 3. Efficient acceleration of electrons in regions close to the emitting antenna. Top panel: electron velocity distribution function in phase space; the blue line represents the phase velocity of the emitted Langmuir wave, for simulation NF_02 (emission frequency $\omega = 1.1\omega_p$) at time $t \simeq 20\omega_p^{-1}$. Bottom panel: corresponding electric field in the plasma, as a function of distance d from the emitting antenna, located at $d = 0$.

simulations $\left(t \simeq 20\omega_p^{-1}\right)$ we observe an efficient acceleration of the electrons pushed by the wave electric field and eventually propagating ballistically. In the (x, v_x) phase space domain, this process corresponds to the formation of finger-like filaments on the distribution function, as shown for the electron distribution function represented in top panel of Figure 3 between $v_e = 2v_{the}$ and $v_e = 7v_{the}$, at positions $[20\lambda_D{-}50\lambda_D]$, $[30\lambda_D{-}90\lambda_D]$, and $[50\lambda_D{-}130\lambda_D]$. We note that given the Langmuir wave packet propagating at group velocity $v_g = 0.67v_{the}$, the distance covered by the emitted wave packet in the plasma at $t \simeq 20\omega_p^{-1}$ is about $13\lambda_D$. At a later stage of the simulations $\left(t \simeq 120\omega_p^{-1}\right)$, the resonant electrons moving at nearly the phase velocity of the wave have been eventually trapped by the wave potential. This process leads to the formation of vortex-like structures in phase space. Such structures are visible in Figure 4 top panel at velocities near $v_\phi \simeq 4.5v_{the}$ which is the phase velocity of the emitted wave. We note that the Landau damping of the wave-packet does not affect the growth time rate of this trapping process, because the perturbing signal is *continuously* excited by the antenna emission. The oscillation period of these trapped electrons is $T_B = \sqrt{m_e/(eEk)}$ (O'Neil, 1965; Zakharov & Karpman, 1963). As expected, the trapping process starts nearby the emitting antenna, leading to nearly formed vortexes in phase space when the wave-packet propagating in the plasma reaches distance $L_v \simeq T_B v_\phi$. As the wave packet moves at group velocity v_g, no trapping is expected on timescales smaller than an *efficient* trapping time $t_{trap} \simeq L_v/v_g = T_B v_\phi/v_g = T_B\left(1 - \omega_p^2/\omega^2\right)^{-1} \gg T_B$. In the numerical experiment described in this section, we find $T_B \simeq 17\omega_p^{-1}$, for which vortexes in phase space form at a distance $L_v \simeq 75\lambda_D$ from the emitting antenna, starting from the *efficient* trapping time $t_{trap} \geq 113\omega_p^{-1}$. The above analysis is strongly limited by the fixed ions assumption to times shorter than the ion inertial time ($\sim m_i/m_e$ in dimensionless units) (Califano et al., 2007). This assumption is relaxed in the next section.

3.2. Large Amplitude Perturbations of the Plasma Dielectric for Moving Ions

In this section, we investigate the influence of the ion dynamics on the propagation of an antenna emitted oscillating electric potential by adding the ion Vlasov equation to the previous electron Vlasov-Poisson system (Equations 1 and 2). We use an ion-to-electron mass ratio $m_i/m_e = 100$ and an ion-to-electron temperature ratio $T_i/T_e = 0.1$. We consider a reduced mass ratio for computational reasons, while the temperature ratio is chosen to enable ion acoustic fluctuations to propagate.

We initialize the simulations with the same setup as in the fixed background limit discussed in Section 3.1. The investigated emission frequencies are $0.5\omega_p$ (simulation NI_01), $1.1\omega_p$ (simulation NI_02) and $2.0\omega_p$ (simulation NI_03), emission amplitude fixed to $\sigma = 0.1\ en_0\lambda_D$. The corresponding electric-to-thermal energy ratio in the plasma is 0.01, 0.33, and 0.01, respectively.

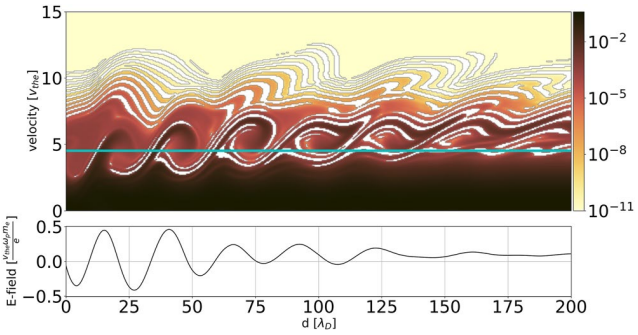

Figure 4. Signatures of particles trapping in phase space. Same as Figure 3 at time $t \simeq 120\omega_p^{-1}$.

At the emission frequencies of $0.5\omega_p$ and $2.0\omega_p$, the ion dynamics does not modify the propagation of the electric field in the plasma, as expected since no non-linear perturbations are observed (Section 3.1). The results (not shown here) are identical to those reported with fixed ions.

On the contrary, at emission frequency $\omega = 1.1\omega_p$, the ion dynamics strongly impacts the electric fluctuation propagating as a Langmuir wave at frequency $\omega_L = \omega$. Similarly to the model with fixed ions, we observe (a) ballistic electrons initially accelerated by the electric field escaping the wave packet, (b) wave-particle interaction signatures as phase space vortexes at the phase velocity of the emitted wave, (c) so-called virtual waves excited at $(-2k_L, 2\omega_L)$. On top of this, we also observe new signatures associated to the ion motion. Such signatures are shown in the ion (resp. charge) density Fourier spectrum in the bottom (resp. top) panel of Figure 5.

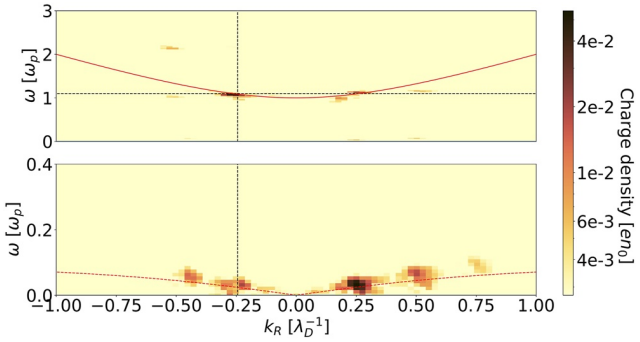

Figure 5. Charge and ion density Fourier spectra. Both top and bottom panel refer to simulation NI_02 (emission frequency $\omega = 1.1\omega_p$). Top panel: 2D Fourier transform of the net charge density, up to time $550\omega_p^{-1}$. The red solid line represents the Langmuir waves dispersion relation. The black dotted lines represent the ω_L and k_L of the emitted plasma wave. Bottom panel: 2D Fourier transform of the ion density, up to time $550\omega_p^{-1}$. The red dotted line represents the IAW waves dispersion relation. The black dotted line represents the k_L of the emitted plasma wave.

First, ion density oscillations show that ions are accelerated at the wavefront of the propagating Langmuir wave packet, resulting in the generation of ion acoustic oscillations propagating both forward and backward w.r.t. the Langmuir wave packet front (not shown here). The signature corresponding to these ion acoustic waves (IAW) is observed at $(\pm k_L, \omega_{IAW})$ in the Fourier space of the ion charge density (bottom panel of Figure 5), where $k_L = 0.244\lambda_D$ is the wavenumber of the excited Langmuir wave and $\omega_{IAW} = 0.025\omega_p$ is the corresponding IAW oscillation frequency. Such frequency is obtained from the IAW dispersion relation $\omega_{IAW}^2 = \left(k_{IAW}^2 C_s^2\right)/\left(1 + k_{IAW}^2 \lambda_D^2\right)$ with C_s the ion sound-speed. Note that these ion acoustic modes do not correspond to what one would expect in the case of parametric excitation processes. In that case, as three waves interaction processes are triggered, the energy of the emitted Langmuir wave ($k_L = -0.244\lambda_D^{-1}$, $\omega_L = 1.1\omega_p$) would excite wave pairs respecting the resonant relations (Dysthe & Franklin, 1970) $\omega_L = \omega_1 + \omega_2$ and $k_L = k_1 + k_2$, where (k_1, ω_1) and (k_2, ω_2) are modes of the system. The generation of these ion acoustic perturbations is attributed to the ponderomotive force (Califano & Lontano, 1999; Henri et al., 2011) triggered by the strong electric energy gradient at the front of the Langmuir wave packet that acts as an equivalent pressure gradient on the ions. By performing a series of secondary simulations with larger ion-to-electron temperature ratios (i.e., $T_i/T_e \simeq 1$), we observed that such IAWs vanish directly after being generated at the wavefront of the propagating Langmuir wave due to their significant damping rate.

Second, large ion acoustic density oscillations $\Delta n_i/n_i$ reflect the emitted forward Langmuir wave ($-k_L = -0.244\lambda_D^{-1}$, $\omega_L = 1.1\omega_p$) into a backward Langmuir wave ($k_L = 0.244\ \lambda_D^{-1}$, $\omega_L = 1.1\ \omega_p$) (Tkachenko et al., 2021). This effect is equivalent to the ionospheric reflection of radio waves. With an emission frequency $\omega = 1.1\omega_p$, the Langmuir wave reflection occurs only in regions where ion density oscillations exceed $\Delta n_i/n_i > 0.2$, as confirmed by our simulations. Third, non-linear beats of the IAW at $(\pm\, k_L = \pm 0.244\lambda_D^{-1}, \omega_{IAW} = 0.025\omega_p)$ trigger ion oscillations at the harmonic $(\pm\, 2k_L = \pm 0.488\lambda_D^{-1}, 2\omega_{IAW} = 0.05\omega_p)$, corresponding to the signature of localized charge density observed at that position in bottom panel of Figure 5. At later stages of the simulations, IAWs at the second harmonic $(3k_L, 3\omega_{IAW})$ resulting from the non-linear interaction between (k_L, ω_{IAW}) and $(2k_L, 2\omega_{IAW})$ are also observed in ion density oscillations (Figure 5, bottom panel). On top of that, virtual waves are observed at $(2k_L, \omega + \omega_{IAW})$ (Figure 5, top panel) as a result of the interaction between (k_L, ω) and (k_L, ω_{IAW}). The non-linear interactions described in this section have been identified in three steps. First, we investigated the time evolution of the energy location within the frequency-wavenumber domain. Second, we identified the resonant relations between wave triads. Third, we isolated the wave packets associated to each resonant mode by filtering them in Fourier space. Practically, this consists of isolating within the frequency-wavenumber domain each mode of interest and converting it back to time-space domain. By doing so, we have identified the location of the wave packets in physical space and confirmed at which time and location each identified three-wave interaction occurred. In this analysis, we have concentrated on three-wave interactions, associated to quadratic interactions, that is, the lower-order non-linear interactions in this model. We have also verified that higher order non-linear interactions are negligible in our simulations.

We conclude this section by emphasizing the necessity to self-consistently model the coupled electron and ion dynamics. This is particularly needed when targeting finite amplitude plasma oscillations at frequencies close to the plasma frequency, for which plasma non-linearities triggered by significant electric-to-thermal energy ratios come into play. Our simulations show that neglecting the ion motion results to a significant underestimation of the non-linear plasma interactions triggered by the instrument. When the ion motion is also modeled, IAWs can be triggered. This opens new channels for energy transfer from the emission frequency toward other frequencies, with an energy transfer that depends on both the emission frequency and the emission duration. This points out the need to self-consistently model both the electron and the ion dynamics when addressing the modeling and diagnostic performance of large MI emission amplitude likely to trigger non-linear plasma dynamics.

4. Significance for In Situ Density and Temperature Diagnostics Performed in Space Plasmas by Mutual Impedance Experiments

In this section, we quantify the consequences of the non-linear dynamics described in the previous Section 3 on the instrumental performance of MI experiments in space plasma diagnostics, focusing on in situ plasma density and electron temperature measurements. This objective is achieved by comparing and analyzing MI spectra modeled for both linear or non-linear responses of the diagnosed plasma. For this purpose, we simulate MI spectra obtained for electric antenna emissions ranging over electric-to-thermal energy ratio from 10^{-10} to 1. Note that we hereby define the electric-to-thermal energy ratio corresponding to each MI spectra as the energy ratio obtained for emission frequencies $\omega \gg \omega_p$. This choice is made to avoid any confusion associated to the frequency dependency of the electric potential oscillations in the plasma, during a MI frequency sweep, previously discussed in Section 3. In our analysis, we include the ions' dynamics, using an ion-to-electron mass ratio $m_i/m_e = 100$ (discussed in Section 4.5) and an ion-to-electron temperature ratio $T_i/T_e = 0.1$.

Note that the MI diagnostic technique used in experimental space applications is based on retrieving plasma parameters, such as the plasma density and electron temperature, from the shape of the MI spectra because it itself strongly depends on the *linear* plasma dielectric. This instrumental technique is therefore essentially based on the assumption of a *linear* response of the diagnosed plasma to the emitted electric perturbation. Practically, a linear plasma behavior is assumed when deriving plasma parameters using the MI diagnostic technique. From an instrumental point of view, whatever *non-linear* effect resulting from this emitted electric perturbation which would impact the shape of the MI spectra is therefore to be considered as spurious. Small perturbations of the plasma dielectric (i.e., a *quasi-linear* response of the diagnosed plasma) might be acceptable, from an instrumental point of view, as long as the resulting MI spectra does not differ much from the one expected in a linear case. For the above-mentioned reason, we also consider in this study a linear plasma response to the MI external electric excitation, in order to mimic typical experimental MI data analysis dedicated to the determination of both the plasma density and electron temperature. A linear plasma response is always assumed, even for plasma oscillations generated from significant antenna emission amplitudes for which *non-linear* perturbations of the plasma are occurring. The consequences of these *non-linear* plasma perturbations on the MI spectra might lead to a discrepancy between the *apparent* plasma density and electron temperature and the *actual* density and temperature. From the discrepancy between the *apparent* and the *actual* plasma parameters, we compute a diagnostic error, from which we derive the performance and robustness of the MI measurement technique. In particular, with this approach, we assess quantitatively the errors made in typical MI experiments when using data treatment techniques conceived for *linear* plasma perturbations to analyze MI spectra obtained for a *non-linear* plasma response.

4.1. Synthetic Mutual Impedance Spectra

MI spectra are built from the plasma response to MI emissions. A MI emitting electric antenna with oscillating electric signals of known amplitude A and frequency ω perturbs the plasma. *Simultaneously*, receiving electric antennas measure the electric potential fluctuations that have propagated in the diagnosed plasma, at the same frequency ω. The total duration of the emission signal is $t_\omega = NT_\omega$, where $T_\omega = 2\pi/\omega$ is the oscillation period and the amount of repetitions is chosen $N = 15$ in this work. This choice is consistent with the typical instrumental design of MI instruments. Practically, MI experiments successively scan one frequency after the other within a predefined frequency range of interest, to perform a MI frequency sweep. In our numerical experiments, we however choose to perform separate simulations for each emitted frequency. Therefore, we neglect any possible coupling between what would be successive emitted frequencies of a MI frequency sweep. In doing so, we assume that the waiting time between two successive emissions is sufficient for the plasma to relax back to its unperturbed state. This choice is discussed in Section 4.4.

Mimicking experimental MI applications, we investigate MI frequency sweeps characterized by a relative frequency resolution $\Delta\omega/\omega = 5\%$, that corresponds to a relative density resolution of $\Delta n_e/n_e = 10\%$. Such resolution is consistent with that used in recent MI experiments, such as the DFP-COMPLIMENT experiment of the ESA Comet Interceptor mission. This investigation is performed using model B, considering the contribution of the far-field term (described in Section 2). The list of settings parameter defining the simulations from which MI spectra are built is shown in Table C2.

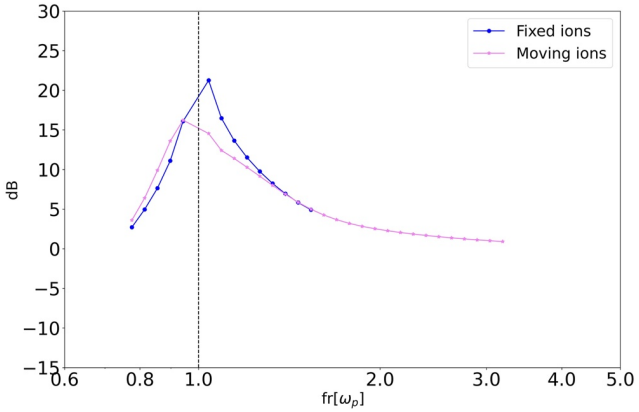

Figure 6. Mutual impedance spectra obtain with immobile (blue) and mobile (violet) ions. Both spectra are obtained for $\alpha = 0.6$ at distance $d = 5\lambda_D$ from the emitting antenna.

Using a dipolar reception antenna configuration, MI spectra are built from the electric potential oscillation difference measured between two electric antennas located at distance d and $2d$ from the emitting antenna, with d ranging from $5\lambda_D$ to $40\lambda_D$. These distances between the emission and reception antennas correspond to the typical MI experiment emitting-receiving antennas distances in previous and forthcoming space missions (Rosetta RPC-MIP, BepiColombo PWI/AM2P, JUICE RPWI/MIME, Comet Interceptor DFP-COMPLIMENT).

From the electric potential oscillations obtained in our numerical simulations, synthetic MI spectra are built using the following procedure.

1. First, we apply signal apodization to the electric potential oscillations. In this study, we adopted the Hann window, the same apodization technique currently adopted for the on-board analysis of MI measurements in previous space applications, such as RPC-MIP on Rosetta, AM2P on BepiColombo, and MIME on JUICE.
2. Second, we compute, at the emission frequency ω, the amplitude of the signal from a Discrete Fourier Transform of this windowed time series. We repeat this process for each emitted single frequency to obtain a spectrum.
3. Third, the obtained spectrum is normalized by the offset introduced by the Hann window, in order to correct for the apodization.
4. Finally, the resulting spectrum is normalized by the corresponding MI spectrum obtained in vacuum, a procedure usually performed with MI experiments (Henri et al., 2017). Indeed, under a linear plasma response assumption, this normalized MI spectrum is independent of the antenna emission amplitude. Therefore, this normalization procedure ensures an unbiased comparison between spectra obtained for different electric-to-thermal energy ratios. The resulting normalized MI spectrum is expressed in decibel scale, where the reference amplitude is that obtained for vacuum conditions.

For this investigation, we assume negligible perturbations of MI spectra related to noise. This assumption is not valid for experimental space applications, where the influence of *instrumental noise* on MI measurements is, at times, significant. The *instrumental noise*, related to the electronics of the MI instrument, affects the accuracy of the measurements. Typically, it affects experimental MI spectra with perturbations of the order of 1 dB and therefore, in order to mimic MI experimental space applications, we discard all perturbations of MI spectra up to 1 dB.

We have shown in Sections 3.1 and 3.2 that it is necessary to model both the electron and ion dynamics when investigating the propagation and evolution of finite amplitude waves associated to large amplitude emissions. We now illustrate (Figure 6) to what extent discarding the ion dynamics impacts MI measurements. We compare two MI spectra obtained either modeling (violet line) or neglecting (blue line) the motion of ions. Both spectra are computed at distance $d = 5\lambda_D$ from the emitting antennas and $\alpha = 0.6$ for which significant non-linear plasma interactions are expected. We note that the contribution of the ion dynamics significantly modifies the resonant shape of the spectra. In particular, we find differences up to 7 dB, which is well above the typical instrumental noise of MI measurements.

Therefore, in the rest of this work, we shall only consider numerical simulations that include both the electron and ion dynamics when investigating MI spectra. We now concentrate on the impact of finite amplitude emissions on MI spectra.

Examples of synthetic MI spectra are shown in Figure 7, for different electric-to-thermal energy ratios, for the emitting-receiving antennas distances $d \simeq 5\lambda_D$, $d \simeq 10\lambda_D$ and $d \simeq 20\lambda_D$, from top to bottom panels.

On the one hand, we observe that the MI synthetic spectra obtained for electric-to-thermal energy ratios $\alpha \leq 10^{-2}$ (corresponding to simulations SI1_01 to SI1_14) and represented as a light blue line are essentially identical (within the typical *instrumental noise* levels) to the linear spectra (corresponding to simulations SL_01 to SL_48) obtained for $\alpha = 10^{-10}$ and represented as a blue line.

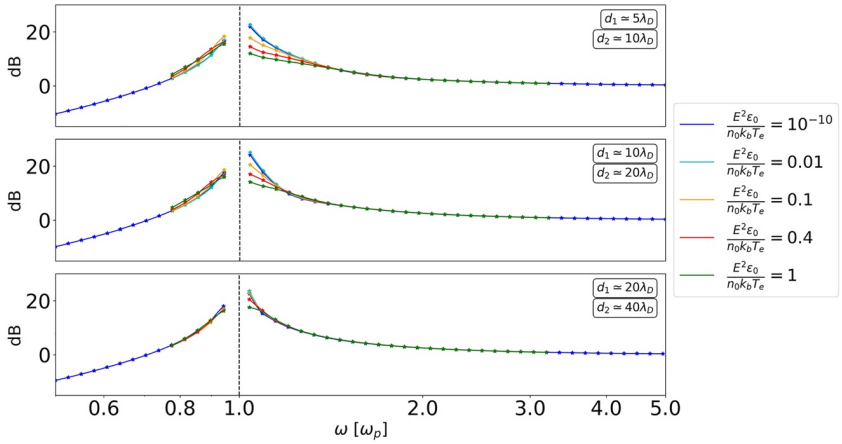

Figure 7. Mutual impedance spectra. The distances of the two receiving antennas from the emitting antenna are represented as d_1 and $d_2 = 2d_1$. From top to bottom panel, mutual impedance spectra are obtained for $d_1 \simeq 5\lambda_D$, $d_1 \simeq 10\lambda_D$, and $d_1 \simeq 20\lambda_D$, for different antenna emission amplitudes (solid lines).

On the other hand, when $\alpha > 10^{-2}$ (i.e., from simulations SI2_01 to SI2_14, SI3_01 to SI3_14, and SI4_01 to SI4_14), we observe instead significant differences between the associated spectra (i.e., orange, red, and green lines) and the reference spectra (blue line), especially at frequencies close to the plasma frequency for spectra obtained at $d \leq 20\lambda_D$. The discrepancies observed at frequencies close to the plasma frequency are consistent with the results of Section 3.2, where we have shown that the plasma is non-linearly perturbed by finite amplitude antenna emissions at frequency close to the plasma frequency ($\omega = 1.1\omega_p$). Note that, the discrepancies that we found exceeding typical *instrumental noise* levels are expected to be measurable in the case of experimental space applications for significant antenna emission amplitudes.

What is the expected trend of MI spectra disturbed by non-linear plasma perturbations induced by the finite amplitude antenna emission, compared to the undisturbed MI spectra associated to a linear plasma response?

The analysis performed in Section 3.2 suggests that the MI spectra, built from the electric oscillation measured in the plasma at the emission frequencies, should be affected by two counteracting phenomena, triggered by the finite amplitude antenna emission. On the one hand, non-linear wave-wave interactions open energy channels that redistribute the energy at frequencies different from the emission frequency. This results in a net *decrease* in the received (normalized) MI amplitude at the emission frequency, compared to the received (normalized) amplitude that would be measured in the linear case. On the other hand, wave-particle interactions also result in a non-linear feedback on the plasma distribution function (plateauing in velocity space) that decreases, or can even suppress, the spatial damping of the emitted wave packet. Note worthily, under a linear plasma response assumption, the MI spectra at frequencies above, and close to, the plasma frequency are strongly shaped by the spatial Landau damping of the Langmuir wave excited in the plasma by the emission antenna. Therefore, wave-particle interactions imply a net *increase* in the received (normalized) MI amplitude at the emission frequency, compared to the received (normalized) amplitude that would be measured in the linear case.

Because of these two counteracting phenomena, it is not straightforward to know the actual shape of the MI spectra close to the resonant frequency (in this study, the plasma frequency), hence the need for numerical simulations. For instance, in the specific conditions considered in this section (i.e., with antenna distances of $d \simeq 5\lambda_D$, $d \simeq 10\lambda_D$, and $d \simeq 20\lambda_D$), we find a maximum discrepancy between the MI synthetic spectra perturbed by non-linear plasma effects (e.g., green solid line in Figure 7) and the reference linear MI synthetic spectra (blue solid line in Figure 7) at the resonance peak of about 10 dB. This spectrally localized, but significant, discrepancy is well above the typical instrumental noise of MI instruments (e.g., 1 dB): we therefore expect such perturbations to actually be measurable, and possibly even dominant, for MI spectra obtained in low temperature space plasmas. It is therefore legitimate to assess quantitatively the impact of these "spurious" (from an instrumental diagnostic point of view) non-linear plasma perturbations of the MI spectra on plasma density and electron temperature measurements performance when using the MI diagnostic technique.

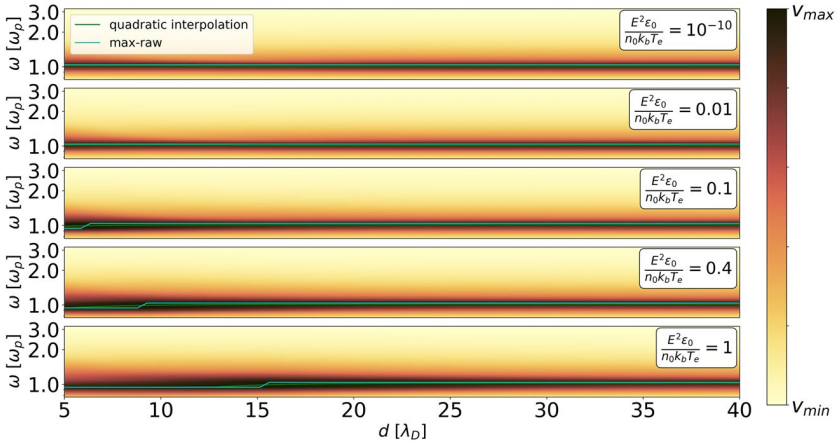

Figure 8. Mutual impedance dynamic spectra in function of the emitting-receiving antennas distance d. Each spectrum, normalized for the corresponding spectrum in vacuum, is represented between its minimum and maximum amplitudes. The plasma frequency is identified as the frequency of (a) the maximum of each spectrum (light blue line) and (b) the maximum of the quadratic interpolation of each spectrum (green line).

We describe in the following sections the procedure used to derive the plasma density (Section 4.2) and electron temperature (Section 4.3) from the normalized MI spectra, expressed in dB.

4.2. Plasma Density Diagnostic Performance for Strong Amplitude Emissions

We here focus on evaluating the plasma density diagnostic performance of MI experiments for finite amplitude antenna electric emissions likely to trigger non-linear effects in the diagnosed plasma. We do so in two steps. First, for each spectrum we estimate the plasma frequency (hereafter called *apparent* plasma frequency, $\omega_{p,app.}$). Second, we compute the plasma frequency relative error by comparing the apparent plasma frequency to the (known) *actual* plasma frequency (ω_p) of the spectrum as follows:

$$\frac{\Delta\omega_{p,app.}}{\omega_p} = \frac{\|\omega_{p,app.} - \omega_p\|}{\omega_p} \tag{4}$$

The MI plasma density diagnostic performance is then obtained by converting the plasma frequency relative error to plasma density relative error:

$$\frac{\Delta n_{e,app.}}{n_e} = \frac{\|n_{e,app.} - n_e\|}{n_e} = 2\frac{\Delta\omega_{p,app.}}{\omega_p}. \tag{5}$$

The considered frequency resolution of $\Delta\omega/\omega = 5\%$ corresponds to a plasma density resolution $\Delta n_e/n_e = 10\%$. We consider that MI experiment is robust against strong antenna amplitude emissions if the plasma density relative error is below this uncertainty.

We evaluate the plasma density diagnostic performance for antenna emission amplitudes corresponding to electric-to-thermal energy ratios $\alpha \in \left(10^{-10}, 1\right)$ (top to bottom panels of Figure 8), in function of the emitting-receiving antennas distance d ranging from $5\lambda_D$ to $40\lambda_D$.

The apparent plasma frequency is identified from MI spectra as the frequency corresponding to the position of the resonant peak signature in the spectra (Bahnsen et al., 1988; Béghin & Debrie, 1972; Décréau et al., 1978; Geiswiller et al., 2001; Gilet et al., 2017; Grard, 1997; Pottelette et al., 1975; Pottelette & Storey, 1981; Rooy et al., 1972; Storey et al., 1969). To account for the finite frequency resolution, we compute the apparent plasma frequency using three different methods. The first method consists of identifying the plasma frequency as the frequency corresponding to the maximum amplitude of the spectra (light blue line in Figure 8). This method is simple but with limited performances, since the difference between the *apparent* and *actual* plasma frequency is constrained by the discretization of the MI frequency sweep.

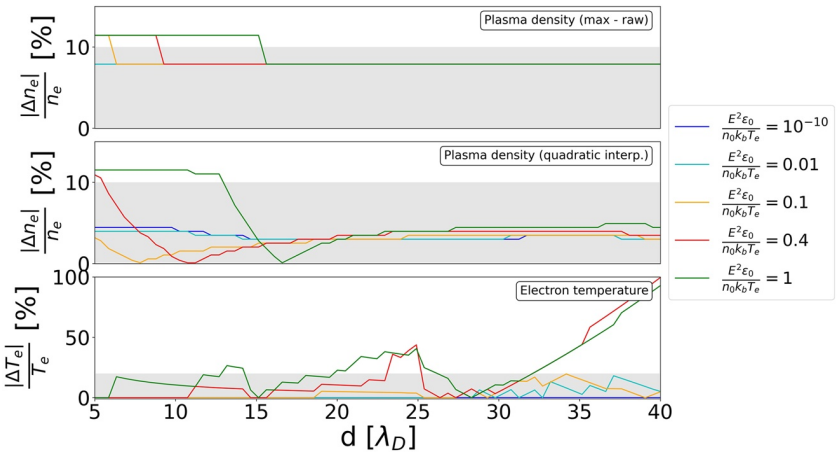

Figure 9. Mutual impedance plasma density and electron temperature diagnostic performance in function of the emitting-receiving antennas distance *d*. The diagnostic performance is obtained for electric-to-thermal energy ratios between 10^{-10} and 1 (solid lines). Plasma density resolution of 10% and electron temperature uncertainty of 20% represented as gray shaded areas. Plasma density relative errors obtained identifying the plasma frequency as the maximum of each spectrum (top panel) or the maximum of the quadratic interpolation of each spectrum (middle panel). Electron temperature relative error identified comparing the investigated spectra to reference spectra (bottom panel).

The second method consists of, first, interpolating the MI spectra using a polynomial interpolation of second order and, second, identifying the apparent plasma frequency as the frequency corresponding to the maximum amplitude of the interpolated spectra (green line in Figure 8). Using this method we mitigate the effect of the discretization in the MI frequency sweep.

The third method (not shown here) consists of, first, approximating the resonant peak signature of MI spectra using a Gaussian function and, second, identifying the apparent plasma frequency as the frequency corresponding to the maximum of such Gaussian function. Similarly to the second method, this method too is used to mitigate the effect of the discretization in the MI frequency sweep.

Apparent plasma frequencies derived using these methods are shown in Figure 8 in function of the distance from the emitting antennas, together with the MI spectra from which they are derived. The plasma density diagnostic performance of first and second method is shown in Figure 9 (top and middle panels, respectively).

Using this third method, the plasma density relative errors range between 6% and 50%. As they significantly exceed the uncertainty of 10%, our analysis indicates that the resonant peak of MI spectra is not well approximated by a Gaussian function and therefore this third method shall not be used for experimental applications.

For experimental space applications, we suggest the use of the second method (middle panel of Figure 9), for which the plasma density estimation errors, ranging between 0% and 12%, are minimized. The error on plasma density diagnostic due to plasma non-linearities remain below 5% (resp. 12%) for emission amplitudes corresponding to $\alpha < 0.1$ (resp. $\alpha = 1$). These errors are smaller than (resp. of the order of) the instrumental density resolution of 10% (gray shaded area in top and middle panels of Figure 9), associated to a frequency resolution of 5%. We conclude that the plasma density diagnostic performance of MI experiments is robust against the generation of non-linear plasma effects by strong antenna amplitude emissions.

4.3. Electron Temperature Diagnostic Performance for Strong Antenna Emission Amplitudes

We here focus on evaluating the electron temperature diagnostic performance and robustness of MI experiments when using finite amplitude antenna electric emissions, likely to trigger non-linear effects in the diagnosed plasma. We do so in three steps. First, we identify the apparent plasma density ($n_{e,app.}$) from MI spectra as described in the previous section. Second, we identify from the MI spectra the ratio between the (known)

emitting-receiving antennas distance and the (unknown) Debye length, hereafter called *apparent* Debye length $\lambda_{D,app.} = \sqrt{(\epsilon_0 k_B T_{e,app.})/(e^2 n_{e,app.})}$, from which the *apparent* temperature ($T_{e,app.}$) is obtained. Third, we evaluate the electron temperature diagnostic performance as the relative error between this *apparent* temperature and the *actual* (T_e) electron temperature we aim to measure.

$$\frac{\|\Delta T_{e,app.}\|}{T_e} = \frac{\|T_e - T_{e,app.}\|}{T_e} = \|1 - \frac{T_{e,app.}}{T_e}\| \tag{6}$$

This is done for the same emission amplitudes and emitting-receiving antennas distances as investigated in the previous section.

In previous space experiments, different techniques were used to derive the electron temperature from MI spectra in unmagnetized Maxwellian plasma. We hereafter recall three of those.

The first technique is based on identifying the frequencies at which anti-resonant signatures (i.e., local minima) are spotted on MI spectra (Geiswiller et al., 2001). Anti-resonances indicate that, for the corresponding frequencies, the wavelength of the wave emitted in the plasma is a multiple of the emitting-receiving antennas' distance d at which the MI spectrum is obtained. For anti-resonances to be spotted, the emitted electric fluctuations reaching the receiving antennas and used to build the spectra need to be composed of both the cold plasma electric field term (so-called far-field term) and the propagating wave term (so-called close-field term). Due to propagation effects, the close-field electric fluctuations, propagating in the plasma at group velocity, reach the positions of the receiving antennas after the delay time $t_{d.} = 2d/v_g$, where, for the anti-resonance to occur, d is expected to be a multiple of the wavelength of the emitted wave. For the emitted frequency ω, the delay time corresponds to $N_{d.} = t_{d.}/T$ repetitions of the oscillation period. Considering that the reception time period is synchronized to the emission, anti-resonances are expected to be spotted on the spectra if the delay time is negligible w.r.t. the total reception time period, corresponding to $N \gg N_{d.}$. For example, with a MI elementary sinusoidal signal emitted at $\omega = 1.1\omega_p$, the wavelength is $d \simeq 25.7\lambda_D$, the group velocity corresponds to $v_g = 0.67v_{the}$ and the delay amount of repetitions $N_{d.} \simeq 14$. Since in this study we focus on emission time periods corresponding to $N = 15$, anti-resonances are not expected to be spotted. As a consequence, this technique, designed for long emission durations, is discarded.

The second technique is based on the amplitude sharpness of the resonant peak of MI spectra (Chasseriaux et al., 1972; Décréau et al., 1978). This technique is also discarded here, since perturbations of MI spectra due to non-linear effects are enhanced at frequencies close to the plasma frequency (as found on Sections 3.2 and 4.1).

The third technique is based on a direct comparison between the experimental spectrum and different reference spectra (Wattieaux et al., 2020), which are theoretical spectra obtained assuming linear perturbations of the probed homogeneous plasma.

In our study, we use this third technique to identify the electron temperature associated to each *synthetic* MI spectrum.

We use as reference spectra those obtained for emission amplitudes corresponding to electric-to-thermal energy ratio $\alpha = 10^{-10}$, corresponding to a linear plasma response, that is, to negligible perturbations of the plasma dielectric. These reference spectra are obtained for emitting-receiving antennas distances $d_{f.}$.

To each *synthetic* spectrum, we associate a *reference* spectrum, hereafter called *matching* spectrum, defined as the one that minimizes the root mean squared error $\xi = \sqrt{\sum (x_i - y_i)^2 / L}$, where L is the amount of emitted frequencies for each spectrum, x_i and y_i are the Fourier components corresponding to the ith emitted frequency for the compared synthetic and reference spectra, respectively. To mimic typical experimental applications of this technique, the (known) actual plasma density of the reference spectra is imposed equal to the apparent plasma density of the synthetic spectrum (e.g., $n_{e,app.} = n_e$). As a consequence, this procedure is applied after the plasma frequency of the synthetic spectrum is identified following the procedure described in the previous section. From the emitting-receiving antennas distance corresponding to the matching spectrum, we estimate an apparent distance associated to the synthetic spectrum as $d_{app.} = d_{f.}$. Because of non-linear effects that might perturb the MI spectra, this apparent distance might differ from the actual distance d at which the synthetic spectrum

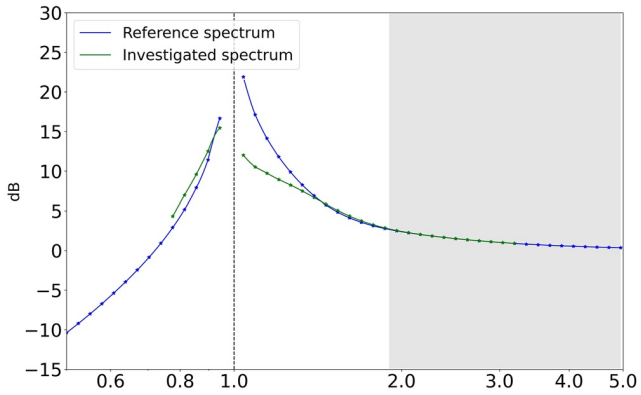

Figure 10. Illustration of the difference between the third technique and the improved third technique (gray region) for the identification of the electron temperature. Blue line represents the reference spectrum; green line represents the experimental (investigated) spectrum. The two spectra are computed for $\alpha = 10^{-10}$ and $\alpha = 1$ at distance $d = 5\lambda_D$. Using the third technique we compare the full spectra. Using the improved third technique we only compare the subpart of the spectra corresponding to the gray region.

is obtained. Both the apparent and actual distances correspond to the same *physical* distance:

$$d_{ph} = d_{app.}\lambda_{D,app.} = d\,\lambda_D \tag{7}$$

where d_{ph} is the (non-normalized) physical distance between emitting and receiving antennas, fixed by design of the MI instrument, $\lambda_{D,app.}$ the apparent Debye length and λ_D the actual Debye length. From the ratio between d and $d_{app.}$ we derive the electron temperature relative error as:

$$\frac{\|\Delta T_{e,app.}\|}{T_e} = \|1 - \frac{n_{e,app.}}{n_e}\left(\frac{d}{d_{app.}}\right)^2\| = \|1 - \left(\frac{d}{d_{app.}}\right)^2\| \tag{8}$$

In previous MI space applications, the uncertainty associated to this third technique was estimated of the order of 10%–30% (Décréau et al., 1978). In our study, in order to mimic experimental MI applications, we consider this technique robust against strong antenna emission amplitudes if the electron temperature relative error is below the threshold of 20%, hereby called *reference uncertainty*.

In our first attempt, we find significant electron temperature relative errors for the emission amplitude corresponding to the electric-to-thermal energy ratio of 1 (not shown here). These errors are above the reference uncertainty because in the comparison process is included also the resonant signature of MI spectra, for which enhanced perturbations are observed for strong emission amplitudes. Therefore, to improve the robustness of the process and reduce the electron temperature relative errors, we now modify the third technique by discarding the contribution of the resonant peak. We do so by filtering out, before the comparison, the Fourier components of MI spectra that correspond to frequencies below a given threshold frequency. In the range $1.0\omega_p$ to $2.0\omega_p$, the best electron temperature diagnostic performances are found for the threshold frequency of $1.9\omega_p$. The difference between the third technique and the improved third technique is illustrated in Figure 10. Using the third technique, the electron temperature is obtained by comparing one given experimental (investigated) spectrum (green line) to several different reference spectra (blue line). Using the improved third technique, the same comparison is performed but not using the full spectra: we use only a subpart of the spectra (i.e., the gray region) and discard the resonant peak, for which strong perturbations due to non-linear plasma interactions are expected.

Using this modified third technique, we find that for $\alpha = 1$ the electron temperature relative errors (green line in Figure 9 bottom panel) significantly exceed the expected temperature uncertainty (gray shaded area) for distances above $d \geq 34\lambda_D$. Since smaller α correspond to smaller electron temperature errors (as shown in Figure 9), a trade-off is required between (a) sufficiently strong emission amplitudes that ensure significant signal-to-noise ratios for MI measurements and (b) small temperature relative errors. Practically, we have identified the largest MI emission amplitude (colored lines in Figure 9) for which the electron temperature relative errors remain lower than the reference uncertainty (gray shaded area). In the investigated range of emitting-receiving antennas distances, we find that the maximum emission amplitude for which the electron temperature identification uncertainty is *always below* the reference uncertainty corresponds to $\alpha = 0.1$.

We conclude that, in 1D, the electron temperature identification process is affected by strong emission amplitudes. Small electron temperature diagnostic performance loss is ensured by perturbing the plasma with emission amplitudes corresponding to $\alpha \leq 0.1$. In Section 5, we discuss, on the basis of the results of our 1D investigation, what performances we expect for 3D MI experimental applications.

Our results suggest that only small modifications of the signatures of the normalized MI spectra are expected due to the excitation of non-linear effects. Therefore, in the case of experimental space applications, the use of an abacus of *reference* MI spectra might facilitate the identification process of the electron temperature. Note that this abacus should be derived for the particular MI experimental application of interest. In particular, it should consider both the specific geometric configuration of the spacecraft on which the instrument is mounted and the configuration of the MI instrument itself.

4.4. Diagnostic Impact of *Consecutive* Versus *Separate* Emission of Successive Frequencies

The MI emission signal is a composition of different elementary signals, each one corresponding to a different frequency. In the case of experimental MI space applications, MI spectra are built from the electric oscillations triggered in the plasma by the *consecutive* emission of all different elementary signals. In our investigation, instead, we simulate the perturbations of each elementary signal *separately*, performing different numerical simulations. In doing so, we *separate* the contributions of the different elementary signals and neglect any possible coupling between electric oscillations corresponding to different emitted frequencies. Practically, this corresponds to waiting for the plasma to regain its resting and unperturbed state between the emission of two successive elementary signals. While, for experimental space applications, this assumption is not always valid, in our investigation it is motivated by computational reasons. Indeed, the numerical investigation of the non-linear effects triggered by MI experiments requires a very large and detailed spatial domain. Such spatial domain coupled with a very fine velocity resolution mesh (mesh details given in Appendix C) results in unfeasible numerical simulations of the whole consecutive set of successive elementary signals.

Hereby, we quantify the error made when the coupling between plasma oscillations corresponding to the consecutive emission of different frequencies is neglected. To do so, we compare the MI spectra obtained from the (a) *separate* or (b) *consecutive* emission of given elementary signals. To this purpose, we build MI spectra, following the procedure described in Section 4.1, from the electric oscillations generated by the emission of elementary signals at frequencies $\omega_1 = 1.1\omega_p$, $\omega_2 = 1.32\omega_p$, and $\omega_3 = 1.584\omega_p$, for antenna emission amplitudes corresponding to electric-to-thermal energy ratios of $\alpha \simeq 10^{-10}$ and $\alpha \simeq 10^{-1}$. These frequencies are chosen because they discretize a large portion of the MI resonant peak signature, for which the perturbations due to finite antenna emission amplitudes are enhanced. For computational reasons, the perturbations are obtained for antenna emission amplitudes corresponding to an electric-to-thermal energy ratio up to $\alpha \simeq 10^{-1}$.

From the comparison between MI spectra obtained simulating (a) separately or (b) consecutively the emission of different elementary signals, we find a maximum discrepancy of about 2 dB. While this error exceeds the typical instrumental noise level of MI experimental space applications (which is also neglected), it still is of the same order. Due to such limited perturbations, we simplify the investigation and perform our numerical simulations by avoiding the consecutive emission of the different elementary signals.

4.5. Reduced Ion-To-Electron Mass Ratio and Limited MI Emission Time Period

In this section, we briefly discuss the choice of discarding representative ion-to-electron mass ratios like the proton-to-electron mass ratio $m_i/m_e \simeq 1{,}836$ in favor of the reduced mass ratio $m_i/m_e = 100$ for the investigation of MI diagnostic performance.

For experimental MI space applications, the amount of repetitions is typically chosen between $N = 10$ and $N = 100$ while in this analysis, for computational reasons, is set to $N = 15$. While the dependency of MI diagnostic performances on the amount of emitted repetitions, N, is outside the scope of this study, longer emission time periods indeed correspond to stronger non-linear perturbations of the plasma. In order to account for the selected limited amount of repetitions and investigate the perturbations of the MI diagnostic due to non-linear effects that would develop in the plasma for longer emission time periods, we choose to enhance the ion dynamics by increasing the ion acoustic frequency. In particular, for our investigation, we choose a reduced ion-to-electron mass ratio of $m_i/m_e = 100$ that enhances the ions' acoustic frequency by a factor ≥ 4.

5. Conclusions

MI instruments are in situ, active, electric experiments that provide plasma diagnostics, used to identify the plasma density and electron temperature in space plasmas. Such plasma parameters are derived from MI spectra which are obtained by actively perturbing the plasma to be diagnosed with a set of emitting antennas, while simultaneously retrieving the electric fluctuations generated in the same plasma. In practical instrumental design, the choice of the antenna emission amplitude is always the result of a trade-off. On the one hand, small antenna emission amplitudes ensure both small perturbations to other payload instruments and a linear plasma response. On the other hand, large emission amplitudes ensure signal-to-noise ratios suitable for both density and temperature identification. But, at the same time, they might trigger non-linear electric perturbations which could affect

the plasma diagnostic. In particular, diagnostic performance loss is expected when the electric energy of the emitted signal is large w.r.t. the electron thermal energy. In this study, for the first time, we relax in the modeling of MI experiments the hypothesis of a linear plasma response and investigate numerically the non-linear plasma perturbations on MI spectra generated by such experiments using the 1D-1V non-linear Vlasov-Poisson model.

We identify, for the first time, the maximum antenna emission amplitude that can be implemented to ensure robust and satisfactory diagnostic performances for both the plasma density and the electron temperature. In particular, we find that for antenna emission amplitudes corresponding to electric-to-thermal energy ratios up to 0.1 the relative errors on plasma density and electron temperature remain below 5% and 20%, respectively.

In situ space plasma observations performed in the solar wind by the STEREO spacecraft have shown that non-linear effects are present, in the range of frequency also used in MI experiments (i.e., close to the plasma frequency), for electric fluctuations of the plasma corresponding to electric-to-thermal energy ratios of $\alpha = 10^{-4}$ (Henri et al., 2011). For such energy ratios, our 1D numerical simulations show instead that negligible non-linear perturbations of MI spectra are expected. This means that, in the short MI emission duration, the growth time-rate associated to the non-linear effects triggered by such emission amplitude is not sufficient to develop perturbations that can significantly modify the spectra. Indeed, for larger antenna emission amplitudes the growth time-rate of the non-linear perturbations of the plasma is enhanced and modifications of the synthetic MI spectra are observed.

We note that our study suffers different limitations due to the numerical model we used. First, the use of our Vlasov-Poisson model prevented us from investigating emission amplitudes that corresponded to electric-to-thermal energy ratios significantly larger than 1, for which we found unstable numerical runs. Second, in our study the plasma nearby the antennas is assumed as homogeneous. In experimental space applications it is not the case, as plasma inhomogeneities (e.g., the antennas plasma sheath) envelope the antennas and affect the propagation of plasma waves. Dedicated studies will be performed in the near future to investigate how plasma inhomogeneities specifically affect MI measurements. Third, in our 1D description, the emitting antennas are modeled as infinite transparent plane grids. While the classic spherical or cylindrical shapes of MI antennas used for space application cannot be simulated, this choice enabled a significant simplification of the model. To investigate the impact of the antennas' shape on the MI measurements, models such as the DSCD model (Geiswiller et al., 2001; Wattieaux et al., 2019) could be used. However, these models are limited to the linear regime thus preventing the analysis in the presence of plasma non-linearities.

It is important to emphasize that our results overestimate the errors expected in the case of actual experimental measurements. Indeed, in our 1D numerical investigation, the electric field amplitudes remain mostly constant with the distance (far-field and close-field electric field components discussed in Section 2). Instead, in experimental 3D applications, the electric field oscillation amplitudes decrease with the distance from the emitting antennas in $1/d_{ph.}^2$, so that the electric-to-thermal energy ratio therefore decreases in $1/d_{ph.}^4$. Nevertheless our investigation represents the first step for the study of the non-linear plasma-antenna regime. For instance, let us consider a large amplitude MI emission ($\alpha = 1$) that triggers significant non-linear effects at a distance of 1 m from the emitting antennas. At a distance of 10 m, we expect significantly smaller non-linear perturbations as the electric field decreases by a factor 10^2 and α decreases by a factor 10^4. In other words, non-linear perturbation are likely to occur only in the vicinity of the emitting antenna. Thus, the maximum amplitude identified in this work (corresponding to $\alpha = 0.1$) is to be considered a conservative, lower value that ensures negligible plasma density and electron temperature identification errors. In order to go beyond this conservative maximum amplitude and account for both a fully realistic instrumental geometry and the associated spherical radial dependence of the potential, one would need to use a multidimensional (3D-3 V) Vlasov-Poisson model that would be extremely demanding computationally and out of reach of current supercomputers. This is out of the scope of this current paper but might be addressed in the future when computational resources allows it.

Part of the results found in our study are also applicable to another kind of active electric experiments dedicated to in situ space plasma diagnostics, namely, the so-called relaxation sounder experiments (hereafter called RS), such as the RS experiment(J. Trotignon et al., 1986) onboard the NASA ISEE spacecraft, the RS experiment(Harvey et al., 1979) onboard the ESA GEOS spacecraft, the wave experiment(Décréau et al., 1987) onboard the Swedish VIKING spacecraft, the RS experiment of the URAP instrument(Osherovich et al., 1993) onboard the NASA/ESA Ulysses spacecraft and the WHISPER experiment (Béghin et al., 2005; J. Trotignon et al., 2003; J. G. Trotignon et al., 2010) onboard the ESA CLUSTER spacecraft. RS are based on a measurement technique similar to that of MI experiments, with the main difference that emission and reception are not simultaneous.

For instance, in the case of the WHISPER instrument, emission occurs during 1 ms on a long-wire antenna while reception is performed on a double-sphere antenna a few ms later, measuring waves that are able to propagate near the characteristic frequencies of the plasma. This necessitates a relatively high amplitude excitation, corresponding to an excitation voltage greater than 50V. This emission amplitude is expected to trigger electric oscillations in the plasma with energy that strongly overcomes the thermal electron energy, therefore generating non-linear plasma perturbations. Combined with the large emitting-receiving antennas distance of such experiments (WHISPER antenna are 88 m in length), the high amplitude excitation allows the RS experiment probing a volume much larger w.r.t. the volume probed with MI experiments. On the one hand, non-linear effects are triggered by the large amplitude excitation. But, on the other hand, given the electric field amplitude decrease in distance as $1/d_{ph.}^2$, their influence is minimized in the overall response measured by the instrument. Moreover, considering the probed volume at play and also depending on the magnetospheric regions crossed by the CLUSTER satellite, plasma inhomogenities and non-Maxwellian electron distributions can be the main source of uncertainty. Several studies have been conducted to cross-validate simultaneous measurements from MI and RS instruments (Décréau et al. (1978) on GEOS, Béghin et al. (2005) on CLUSTER).

Our study provides guidelines for the choice of antenna emission amplitudes of experimental MI applications to ensure small non-linear perturbations of the plasma density and electron temperature diagnostic. Note that in our study we neglect all transient effects, which in the numerical simulations are damped by the chosen initialization of the model (Appendix A). The possible impact of transients on MI measurements diagnostic performance is left to future studies. Note also that these results should not concern double Maxwellian electron distribution functions, for which the MI resonance might appear at frequencies significantly below the plasma frequency.

Appendix A: Initialization of the Numerical Model

We hereby describe the initialization of the numerical simulations analyzed in this study. This initialization, based on the consistency between the Poisson and Ampère equations at the beginning of each numerical simulation, removes the initial transients of the simulation by imposing, at each position, the initial current expected from the cold plasma term of the electric field (so-called far-field term).

The net charge at any point in the simulation box is initialized to zero and the density of each species is initially uniform and equal everywhere in the simulation box.

$$n_e\,(x, t = 0) = n_i\,(x, t = 0) = n_0 \tag{A1}$$

$$n_{net}\,(x, t = 0) = n_i\,(x, t = 0) - n_e\,(x, t = 0) = 0 \tag{A2}$$

where x represents the position, t the time, n_e is the electron density, n_i is the ion density, n_0 is the unperturbed plasma density and n_{net} is the total charge density. The oscillating charges σ at the (infinite plane) emitting antennas are initialized to zero:

$$\sigma\,(t = 0) = 0. \tag{A3}$$

During the simulations, the oscillating charges at the antennas are imposed equal to $\bar{\sigma}\sin(\omega t)$, with $\bar{\sigma}$ its amplitude and ω the emission frequency. The electric field, computed from the initial net-charge, is zero everywhere in the simulation box:

$$E\,(x, t = 0) = 0 \tag{A4}$$

where E is the electric field. To ensure the consistency between the Poisson and Ampère equations at the beginning of each simulation, we initialize the current considering the current injected in the plasma at the emitting antenna and considering the time derivative of the initial electric field (Podesta, 2005) at each position in the simulated box.

The external current density injected from the emitting antenna in the plasma, at the beginning of the simulation, reads:

$$j_{ext}\,(t = 0) = \bar{\sigma}\omega \tag{A5}$$

where $\bar{\sigma}$ is the amplitude of the homogeneous charge per unit surface on the infinite charged plane. At each position, the expected current density, in the electrostatic 1D case, reads:

$$j_{tot}\,(t=0) = -\epsilon_0 \frac{\partial E}{\partial t} \tag{A6}$$

For emission frequencies close to the plasma frequency, the electric field reads (Podesta, 2005):

$$E = \frac{\bar{\sigma}\sin(t\omega)}{2\epsilon_0\left(1-\frac{\omega_p^2}{\omega^2}\right)}\mathrm{sgn}(x) \tag{A7}$$

where ω_p is the plasma frequency. The difference between the expected current density at each position and the current density sent in the plasma by the external antenna gives the initial current density we need to impose at each position in the simulation box. This current density is imposed via an offset on the velocity distribution functions with which we initialize the electrons, converting the initial Maxwellian distribution to a drifting Maxwellian. This velocity offset reads:

$$\frac{v_{offset}}{v_{the}} = \frac{\hat{\sigma}}{2}\frac{\hat{\omega}}{\frac{\omega^2}{\omega_p^2}-1} \tag{A8}$$

where v_{offset} is the velocity offset of the Maxwellian distributions of the electrons at initialization, v_{the} is the electron thermal velocity and $\hat{\sigma} = \sigma/\bar{\sigma}$ is the amplitude of the non-dimensional charge per unit surface imposed at the emitting antennas, with $\bar{\sigma}$ the planar charge distribution used to normalize the model.

This initialization minimizes the transients generated in the plasma when switching-on the emission at the electric antennas. This initialization is used in our study both for model A and model B.

Appendix B: Validation of the Model

In this appendix, we describe the validation of the two models (model A and model B) used in this study.

First, the numerical model is validated by comparing the simulated electric oscillations in the numerical box, at given distance from the emitting antenna and at given time after the beginning of the emission, against the electric oscillations expected analytically considering temporal and spatial Landau Damping of the emitted waves. These expected electric fluctuations are derived by solving the Vlasov-Poisson coupled equations as described, for example, in Krall and Thrivelpiece (1973), limiting the analysis to real frequencies and complex wavenumbers. A similar computation of the analytic expressions for this 1D-1 V case study is described in Podesta (2005). The validation of model A (resp. B) is illustrated in Panel a (resp. b) of Figure B1 as the comparison between the expected electric fluctuations (black line) and the simulated electric field oscillations (red line), computed for emission frequency $\omega = 1.1\omega_p$ at time $t = 100\omega_p^{-1}$ and in function of the emitting-receiving antennas distance. The emitted wave-packet propagates from the emitting antennas at group velocity and, along the distance it covers, the expected and simulated electric fluctuations agree. Note that limited differences are expected, since the analytic approximation is derived considering only the dominant pole and neglecting higher-order solutions (Podesta, 2005). The frequency-wavenumber couples used to obtain the analytic electric oscillations are computed using the linear Vlasov-Maxwell solver WHAMP (Roennmark, 1982), in the limit of an unmagnetized plasma. Second, we validate the MI spectra obtained numerically against spectra derived using the DSCD model (Béghin & Kolesnikova, 1998; Geiswiller et al., 2001; Wattieaux et al., 2019; Wattieaux et al., 2020) which is the reference numerical tool for the modeling of MI instrumental response in the case of electrostatic linear perturbations of the plasma. This model is typically used to validate MI experimental measurements because, at the state of the art, it is the only MI model capable of taking into account the presence of the satellite platform when deriving MI spectra. In contrast to our 1D model, the DSCD model supposes very long emission periods (e.g., MI emission starts at time $t = -\infty$) and neglects the transient (delay) time required by the wave-packet generated at the emitting antennas to cover the receiving-emitting antennas distance.

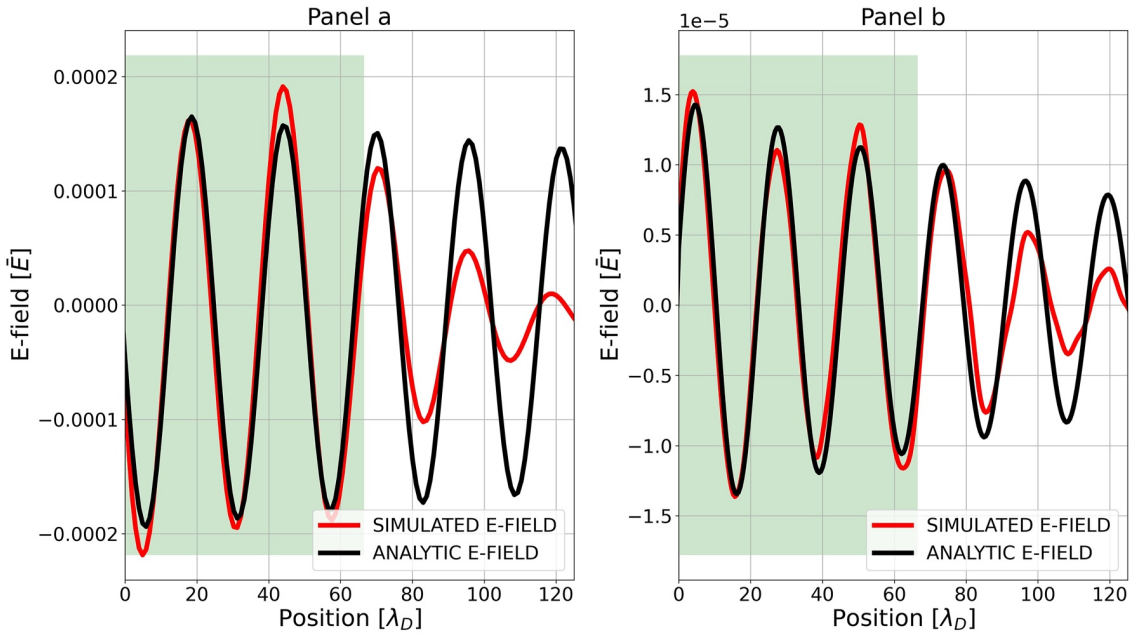

Figure B1. Validation of model A (panel A) and model B (panel b). Comparison between the electric fluctuations obtained numerically (red solid line) and those computed analytically (black solid line), in function of the emitting-receiving antennas distance, for the emission frequency $\omega = 1.1\omega_p$ and at time $t = 100\omega_p^{-1}$. At such time the emitted wave packet, propagating at group velocity $v_g = 0.67v_{the}$, has covered the distance $d = 67\lambda_D$ (green shaded area).

The comparison between spectra is performed for different emitting-receiving antennas distances and for antenna emission amplitudes corresponding to an electric-to-thermal energy ratio of 10^{-10}. The comparison is illustrated in Figure B2 for distances $d = 0.5\lambda_D$, $d = 5\lambda_D$, $d = 20\lambda_D$, and $d = 40\lambda_D$. On the one hand, for d smaller than $5\lambda_D$, the spectra disagree because of differences in the modeling of the emitting antennas between the two models. On the other hand, for d larger than $5\lambda_D$, the spectra agree. Therefore, to assess the diagnostic performance of MI experiments to finite emission amplitudes, we focus on emitting-receiving antennas distances larger than $5\lambda_D$ and neglect smaller distances.

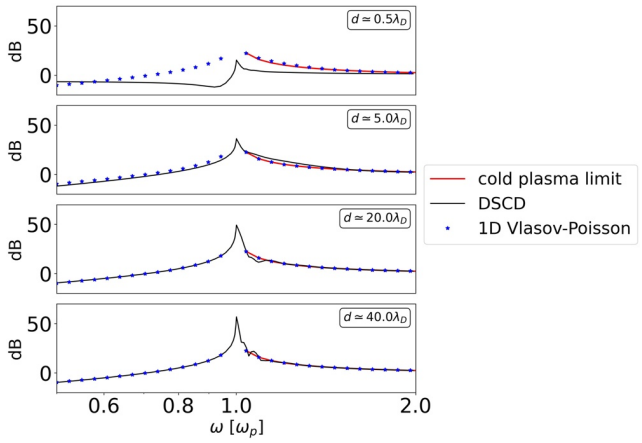

Figure B2. Comparison between spectra derived using our 1D Vlasov-Poisson model (blue points) and the DSCD model (black solid line). The red line represents the expected cold plasma response, valid for $\frac{\omega}{\omega_p} \gg 1$.

Appendix C: Model Parameters

In Table C1, for completeness and repeatability purposes, we show the parameters used for each numerical simulation.

Table C1

List of Numerical Simulation Settings Parameters for Investigating Non-Linear Perturbations of the Plasma: Total Length of the Simulation Box (X_{max}), Velocity Range for the Electron Distribution Function (V_e), Velocity Range for the Ion Distribution Function (V_i), Amount of Spatial Mesh Points (n_x), Amount of Velocity Mesh Points for Electrons (n_{ve}), Amount of Velocity Mesh Points for Ions (n_{vi}), Advancement Time Resolution of the Simulation (dt), Emission Frequency (ω), Oscillating Charges at the Antenna (σ), Ion-To-Electron Mass Ratio (m_i/m_e), Ion-To-Electron Temperature Ratio (T_i/T_e), and Electric-To-Thermal Energy Ratio ($E^2/(k_B T_e)$)

Name	M	$X_{\max}$ $[\lambda_D]$	$V_{\max\ e}$ $[v_{the}]$	v_i $[v_{thi}]$	n_x	n_{v_e}	n_{v_i}	dt $\left[\omega_p^{-1}\right]$	ω $[\omega_p]$	$\sigma[\bar{\sigma}]$	$\frac{m_i}{m_e}$	$\frac{T_i}{T_e}$	$\frac{E^2}{k_B T_e}$
LF_01	A	1,000	(−25,25)	(−25,25)	2,048	601	601	1e−3	0.5	1e−5	inf	0.1	1e−10
LF_02	A	1,000	(−25,25)	(−25,25)	2,048	601	601	1e−3	1.1	1e−5	inf	0.1	1e−8
LF_03	A	1,000	(−25,25)	(−25,25)	2,048	601	601	1e−3	2.0	1e−5	inf	0.1	1e−10
NF_01	A	1,000	(−25,25)	(−25,25)	2,048	601	601	1e−3	0.5	0.1	inf	0.1	0.01
NF_02	A	1,000	(−25,25)	(−25,25)	2,048	601	601	1e−3	1.1	0.1	inf	0.1	0.33
NF_03	A	1,000	(−25,25)	(−25,25)	2,048	601	601	1e−3	2.0	0.1	inf	0.1	0.01
NI_01	A	1,000	(−25,25)	(−25,25)	2,048	601	601	1e−3	0.5	0.1	100	0.1	0.01
NI_02	A	1,000	(−25,25)	(−25,25)	2,048	601	601	1e−3	1.1	0.1	100	0.1	0.33
NI_03	A	1,000	(−25,25)	(−25,25)	2,048	601	601	1e−3	2.0	0.1	100	0.1	0.01

Note. M represents the antennas configuration (model) used for these simulations.

In Tables C1 and C2 for completeness and repeatability purposes we show the parameters used for each numerical simulation. Table C1 (resp. Table C2) refers to the simulations supporting the discussion of Section 3 (resp. Section 4). LF (resp. SL) means Low Fixed (resp. Sweep Low) and indicates simulations used to investigate the plasma perturbations due to *single* fixed frequency (resp. sweep) emission(s) in the case of low amplitudes, associated to a linear plasma response. NI (resp. SI) means Non-linear Ions (resp. Sweep Ions) and simulate instead fixed frequency (resp. sweep) emissions in the case of moving ions with large emission amplitudes, associated to significant perturbations of the plasma. NF means Non-linear Fixed and indicates simulations supporting the discussion of Section 3.1, where we investigate plasma perturbations due to strong amplitude signals in the case of a fixed background of positive charges. MI sweep measurements are built using a number of different numerical runs with same numerical boxes but different emitted frequency. If one line is used to indicate in Table C2 each emitted frequency, the result would be a very long table with very diluted information. For simplicity purposes and to help the reader focus on the significant information of the table, we give instead the frequency resolution of the sweep measurement (last column of Table C2) which one can use to extrapolate the information regarding all emitted frequencies. Therefore, for each simulated MI sweep we only give two lines. One line corresponding to the first emitted frequency of the sweep and one corresponding to the last frequency of the sweep. For instance, SL_01 is the numerical simulation used to investigate the first frequency, $\omega_{SL,01} = 0.5\omega_p$, of one sweep measurement. SL_48 is the simulation investigating the last frequency, $\omega_{SL48} = 4.95\omega_p$, of the same measurement. The rest of the simulated frequencies of the sweep are obtained as $\omega_{n+1} = 1.05\omega_n$. We note that the LF simulations of Table C1 have not been used in the discussion of Section 3, but rather served us as reference during the analysis.

Table C2

List of Numerical Simulation Settings Parameters for Building MI Spectra: Total Length of the Simulation Box (X_{max}), Velocity Range for the Electron Distribution Function (V_e), Velocity Range for the Ion Distribution Function (V_i), Amount of Spatial Mesh Points (n_x), Amount of Velocity Mesh Points for Electrons (n_{ve}), Amount of Velocity Mesh Points for Ions (n_{vi}), Advancement Time Resolution of the Simulation (dt), Emission Frequency (ω), Oscillating Charges at the Antenna (σ), Ion-To-Electron Mass Ratio (m_i/m_e), Ion-To-Electron Temperature Ratio (T_i/T_e), and Frequency Sweep Resolution (ω_{n+1}/ω_n)

Name	M	$X_{\max}$ $[\lambda_D]$	$V_{\max\ e}$ $[v_{the}]$	v_i $[v_{thi}]$	n_x	n_{v_e}	n_{v_i}	dt $\left[\omega_p^{-1}\right]$	ω $[\omega_p]$	σ $[\bar{\sigma}]$	$\frac{m_i}{m_e}$	$\frac{T_i}{T_e}$	$\frac{\omega_{n+1}}{\omega_n}$
SL_01	B	4,000	(−25,25)	(−25,25)	8,192	601	601	1e−3	0.5	1e−5	100	0.1	1.05
SL_48	B	4,000	(−25,25)	(−25,25)	8,192	601	601	1e−3	4.95	1e−5	100	0.1	1.05
SI1_01	B	4,000	(−25,25)	(−25,25)	8,192	601	601	1e−3	0.77	0.1	100	0.1	1.05
SI1_14	B	4,000	(−25,25)	(−25,25)	8,192	601	601	1e−3	1.53	0.1	100	0.1	1.05
SI2_01	B	4,000	(−25,25)	(−25,25)	8,192	601	601	1e−3	0.77	0.31	100	0.1	1.05
SI2_14	B	4,000	(−25,25)	(−25,25)	8,192	601	601	1e−3	1.53	0.31	100	0.1	1.05
SI3_01	B	4,000	(−25,25)	(−25,25)	8,192	601	601	1e−3	0.77	0.6	100	0.1	1.05
SI3_14	B	4,000	(−25,25)	(−25,25)	8,192	601	601	1e−3	1.53	0.6	100	0.1	1.05
SI4_01	B	4,000	(−40,40)	(−25,25)	8,192	1,001	601	5e−4	0.77	1.0	100	0.1	1.05
SI4_14	B	4,000	(−40,40)	(−25,25)	8,192	1,001	601	5e−4	1.53	1.0	100	0.1	1.05

Note. *M* represents the antennas configuration (model) used for these simulations.

Data Availability Statement

Data sets for this research are available at Bucciantini (2022), together with a detailed explanation on how to use them. The model used to produce such data set is described in Section 2. It is based on the model implemented by Mangeney et al. (2002). The 1D-1 V Vlasov-Poisson version of the model, which corresponds to the one we use in our investigation, is described in Henri et al. (2010).

Acknowledgments

The work performed at LPC2E is supported by CNES APR. The Scientific colour map "lajolla" (Crameri, 2021) is used in this study to prevent visual distortion of the data and exclusion of readers with colour-vision deficiencies(Crameri et al., 2020). We acknowledge the use of the WHAMP software Roennmark (1982) for the validation of the model. We benefited from the computing resources provided by CaSciModOT. This work was granted access to the HPC/AI resources of TGCC under the allocation 2021-A0100412428 made by GENCI. L. B. was supported by funds from Région Centre Val de Loire (France).

References

Bahnsen, A., Jespersen, M., Ungstrup, E., Pottelette, R., Malingre, M., Decreau, P., et al. (1988). First VIKING results: High frequency waves. *Physica Scripta*, *37*(3), 469–474. https://doi.org/10.1088/0031-8949/37/3/032

Béghin, C. (1995). Series expansion of electrostatic potential radiated by a point source in isotropic Maxwellian plasma. *Radio Science*, *30*(2), 307–322. https://doi.org/10.1029/94RS03167

Béghin, C., & Debrie, R. (1972). Characteristics of the electric field far from and close to a radiating antenna around the lower hybrid resonance in the ionospheric plasma. *Journal of Plasma Physics*, *8*(3), 287–310. https://doi.org/10.1017/S0022377800007157

Béghin, C., Décréau, P. M. E., Pickett, J., Sundkvist, D., & Lefebvre, B. (2005). Modeling of cluster's electric antennas in space: Application to plasma diagnostics. *Radio Science*, *40*(6). https://doi.org/10.1029/2005RS003264

Béghin, C., Karczewski, J. F., Poirier, B., Debrie, R., & Masevich, N. (1982). The ARCAD-3 ISOPROBE experiment for high time resolution thermal plasma measurements. *Annales de Geophysique*, *38*(5), 615–629.

Béghin, C., & Kolesnikova, E. (1998). Surface-charge distribution approach for modeling of quasi-static electric antennas in isotropic thermal plasma. *Radio Science*, *33*(3), 503–516. https://doi.org/10.1029/97RS03588

Brunetti, M., Califano, F., & Pegoraro, F. (2000). Asymptotic evolution of nonlinear Landau damping. *Physical Review E - Statistical Physics, Plasmas, Fluids, and Related Interdisciplinary Topics*, *62*(3), 4109–4114. https://doi.org/10.1103/PhysRevE.62.4109

Bucciantini, L. (2022). *1D-1V Vlasov-Poisson simulations of mutual impedance experiments for strong antenna emission amplitudes*. Zenodo. https://doi.org/10.5281/zenodo.7149358

Buckley, R. (1968). Radio frequency properties of a plane grid capacitor immersed in a hot collision-free plasma. *Journal of Plasma Physics*, *2*(3), 339–351. https://doi.org/10.1017/S0022377800003871

Califano, F., Galeotti, L., & Briand, C. (2007). Electrostatic coherent structures: The role of the ions dynamics. *Physics of Plasmas*, *14*(5), 052306. https://doi.org/10.1063/1.2724807

Califano, F., & Lontano, M. (1999). Vlasov-Poisson simulations of strong wave-plasma interaction in conditions of relevance for radio frequency plasma heating. *Physical Review Letters*, *83*(1), 96–99. https://doi.org/10.1103/PhysRevLett.83.96

Chasseriaux, J., Debrie, R., & Renard, C. (1972). Electron density and temperature measurements in the lower ionosphere as deduced from the warm plasma theory of the h.f. quadrupole probe. *Journal of Plasma Physics*, *8*(2), 231–253. https://doi.org/10.1017/S0022377800007108

Chasseriaux, J. M. (1972). Potential set up by a point charge oscillating in magnitude in an inhomogeneous plasma. *Plasma Physics*, *14*(8), 763–781. https://doi.org/10.1088/0032-1028/14/8/002

Chassériaux, J. M. (1974). Excitation of the plasma and upper hybrid resonances in a warm magnetoplasma by an alternating electric dipole. *Journal of Plasma Physics*, *11*(2), 225–252. https://doi.org/10.1017/S0022377800024624

Crameri, F. (2021). *Scientific colour maps*. Zenodo. https://doi.org/10.5281/zenodo.5501399

Crameri, F., Shephard, G. E., & Heron, P. J. (2020). The misuse of colour in science communication. *Nature Communications*, *11*(1), 5444. https://doi.org/10.1038/s41467-020-19160-7

Décréau, P. M. E., Beghin, C., & Parrot, M. (1978). Electron density and temperature, as measured by the mutual impedance experiment on board GEOS-1 (Article published in the special issues: Advances in Magnetospheric Physics with GEOS- 1 and ISEE - 1 and 2.). *Space Science Reviews*, *22*(5), 581–595. https://doi.org/10.1007/BF00223942

Décréau, P. M. E., Hamelin, M., Massif, R., de Feraudy, H., & Pawela, E. (1987). Plasma probing by active wave experiments on the Viking satellite. *Annales Geophysicae*, *5*, 181–185.

Dysthe, K. B., & Franklin, R. (1970). Non-linear interactions of coherent electrostatic plasma waves. *Plasma Physics*, *12*(9), 705–721. https://doi.org/10.1088/0032-1028/12/9/005

Eriksson, A. I., Engelhardt, I. A. D., André, M., Boström, R., Edberg, N. J. T., Johansson, F. L., et al. (2017). Cold and warm electrons at comet 67p/churyumov-gerasimenko. *A&A*, *605*, A15. https://doi.org/10.1051/0004-6361/201630159

Geiswiller, J., Béghin, C., Kolesnikova, E., Lagoutte, D., Michau, J. L., & Trotignon, J. G. (2001). Rosetta spacecraft influence on the mutual impedance probe frequency response in the long Debye length mode. *Planetary and Space Science*, *49*(6), 633–644. https://doi.org/10.1016/S0032-0633(00)00173-2

Gilet, N., Henri, P., Wattieaux, G., Cilibrasi, M., & Béghin, C. (2017). Electrostatic potential radiated by a pulsating charge in a two-electron temperature plasma. *Radio Science*, *52*(11), 1432–1448. https://doi.org/10.1002/2017RS006294

Grard, R. (1969). Coupling between two electric aerials in a warm plasma. *Alta Frequency*, *38*, 97–101.

Grard, R. (1997). Influence of suprathermal electrons upon the transfer impedance of a quadrupolar probe in a plasma. *Radio Science*, *32*(3), 1091–1100. https://doi.org/10.1029/97RS00254

Harvey, C. C., Etcheto, J., & Mangeney, A. (1979). Early results from the isee electron density experiment. In K. Knott, A. Durney, & K. Ogilvie (Eds.), *Advances in magnetospheric physics with GEOS-1 and ISEE* (pp. 533–552). Springer Netherlands. https://doi.org/10.1007/978-94-009-9527-7_34

Henri, P., Califano, F., Briand, C., & Mangeney, A. (2010). Vlasov-Poisson simulations of electrostatic parametric instability for localized Langmuir wave packets in the solar wind. *Journal of Geophysical Research*, *115*(A6), A06106. https://doi.org/10.1029/2009JA014969

Henri, P., Califano, F., Briand, C., & Mangeney, A. (2011). Low-energy Langmuir cavitons: Asymptotic limit of weak turbulence. *EPL (Europhysics Letters)*, *96*(5), 55004. https://doi.org/10.1209/0295-5075/96/55004

Henri, P., Vallières, X., Hajra, R., Goetz, C., Richter, I., Glassmeier, K.-H., et al. (2017). Diamagnetic region(s): Structure of the unmagnetized plasma around comet 67p/cg. *Monthly Notices of the Royal Astronomical Society*, *469*(Suppl_2), S372–S379. https://doi.org/10.1093/mnras/stx1540

Kasaba, Y., Kojima, H., Moncuquet, M., Wahlund, J., Yagitani, S., Sahraoui, F., et al. (2020). Plasma wave investigation (PWI) aboard Bepi-Colombo Mio on the trip to the first measurement of electric fields, electromagnetic waves, and radio waves around mercury. *Space Science Reviews*, *216*(65), 65. https://doi.org/10.1007/s11214-020-00692-9

Krall, N., & Thrivelpiece, A. (1973). *Principles of plasma physics*. McGraw-Hill.

Mangeney, A., Califano, F., Cavazzoni, C., & Travnicek, P. (2002). A numerical scheme for the integration of the Vlasov-Maxwell system of equations. *Journal of Computational Physics*, *179*(2), 495–538. https://doi.org/10.1006/jcph.2002.7071

Odelstad, E., Eriksson, A. I., André, M., Graham, D. B., Karlsson, T., Vaivads, A., et al. (2020). Plasma density and magnetic field fluctuations in the ion gyro-frequency range near the diamagnetic cavity of comet 67P. *Journal of Geophysical Research: Space Physics*, *125*(12). https://doi.org/10.1029/2020JA028192

O'Neil, T. (1965). Collisionless damping of nonlinear plasma oscillations. *The Physics of Fluids*, *8*(12), 2255–2262. https://doi.org/10.1063/1.1761193

Osherovich, V. A., Benson, R. F., Fainberg, J., Stone, R. G., & MacDowall, R. J. (1993). Sounder stimulated d_n resonances in Jupiter's io plasma torus. *Journal of Geophysical Research*, *98*(E10), 18751–18756. https://doi.org/10.1029/93JE01481

Podesta, J. J. (2005). Spatial Landau damping in plasmas with three-dimensional k distributions. *Physics of Plasmas*, *12*(5), 052101. https://doi.org/10.1063/1.188547

Pottelette, R., Rooy, B., & Fiala, V. (1975). Theory of the mutual impedance of two small dipoles in a warm isotropic plasma. *Journal of Plasma Physics*, *14*(2), 209–243. https://doi.org/10.1017/S0022377800009533

Pottelette, R., & Storey, L. R. O. (1981). Active and passive methods for the study of non-equilibrium plasmas using electrostatic waves. *Journal of Plasma Physics*, *25*(2), 323–350. https://doi.org/10.1017/S0022377800023151

Roennmark, K. (1982). *Waves in Homogeneous, Anisotropic Multicomponent Plasmas*. WHAMP.

Rooy, B., Feix, M. R., & Storey, L. R. O. (1972). Theory of a quadripolar probe for a hot isotropic plasma. *Plasma Physics*, *14*(3), 275–300. https://doi.org/10.1088/0032-1028/14/3/005

Snodgrass, C., & Jones, G. H. (2019). The European space agency's comet interceptor lies in wait. *Nature Communications*, *10*(5418), 5418. https://doi.org/10.1038/s41467-019-13470-1

Storey, L., Aubry, L., & Meyer, P. (1969). Mutual impedance techniques for space plasma measurements. *Measurement techniques in space plasmas - Fields Geophysical Monograph Series*, *103*, 155–160. https://doi.org/10.1029/GM103p0155

Tkachenko, A., Krasnoselskikh, V., & Voshchepynets, A. (2021). Harmonic radio emission in randomly inhomogeneous plasma. *The Astrophysical Journal*, *908*(2), 126. https://doi.org/10.3847/1538-4357/abd2bd

Trotignon, J., Béghin, C., Lagoutte, D., Michau, J., Matsumoto, H., Kojima, H., et al. (2006). Active measurement of the thermal electron density and temperature on the mercury magnetospheric orbiter of the bepicolombo mission. *Advances in Space Research*, *38*(4), 686–692. https://doi.org/10.1016/j.asr.2006.03.031

Trotignon, J., Etcheto, J., & Thouvenin, J. (1986). Automatic determination of the electron density measured by the relaxation sounder on board ISEE 1. *Journal of Geophysical Research*, *91*(A4), 4302. https://doi.org/10.1029/JA091iA04p04302

Trotignon, J., Michau, J. L., Lagoutte, D., Chabassiere, M., Chalumeau, G., Colin, F., et al. (2007). RPC-MIP: The mutual impedance probe of the Rosetta plasma Consortium. *Space Science Reviews*, *128*(1–4), 713–728. https://doi.org/10.1007/s11214-006-9005-1

Trotignon, J., Rauch, J., Décréu, P., Canu, P., & Lemaire, J. (2003). Active and passive plasma wave investigations in the earth's environment: The cluster/whisper experiment. *Advances in Space Research*, *31*(5), 1449–1454. https://doi.org/10.1016/S0273-1177(02)00959-6

Trotignon, J. G., Décréau, P. M. E., Rauch, J. L., Vallières, X., Rochel, A., Kougblénou, S., et al. (2010). The whisper relaxation sounder and the cluster active archive.

Wattieaux, G., Gilet, N., Henri, P., Vallières, X., & Bucciantini, L. (2019). Rpc-mip observations at comet 67p/churyumov-gerasimenko explained by a model including a sheath and two populations of electrons. *A&A*, *630*, A41. https://doi.org/10.1051/0004-6361/201834872

Wattieaux, G., Henri, P., Gilet, N., Vallières, X., & Deca, J. (2020). Plasma characterization at comet 67p between 2 and 4 au from the sun with the rpc-mip instrument. *A&A*, *638*, A124. https://doi.org/10.1051/0004-6361/202037571

Youssef, E. (1996). ECSS - European Cooperation for Space Standardization. In *Space programs and technologies conference*. https://doi.org/10.2514/6.1996-4305

Zakharov, V. E., & Karpman, V. I. (1963). On the nonlinear theory of the damping of plasma waves. *Soviet Journal of Experimental and Theoretical Physics*, *16*, 351.

6.2 Paper 2 (Submitted to JGR): Space Plasma Diagnostics in Strongly Inhomogeneous Plasmas: the Impact of Plasma Inhomogeneities on Mutual Impedance Experiments.

Space Plasma Diagnostics and Spacecraft Charging. The Impact of Plasma Inhomogeneities on Mutual Impedance Experiments.

L. Bucciantini[1], P. Henri[1,2], G. Wattieaux[3], F. Lavorenti[2,4], P. Dazzi[1,5], X. Vallières[1]

[1]Laboratoire de Physique et Chimie de l'Environnement et de l'Espace (LPC2E), CNRS, Université d'Orléans, Orléans, France
[2]Laboratoire Lagrange, OCA, UCA, CNRS, Nice, France
[3]Laboratoire Plasma et Conversion d'Energie (LAPLACE), CNRS, Université de Toulouse, Toulouse, France
[4]Dipartimento di Fisica, Università di Pisa, Pisa, Italy
[5]Laboratoire d'Études Spatiales et d'Instrumentation en Astrophysique (LESIA), Paris Observatory, Paris, France

Key Points:

- The impact of plasma inhomogeneities on the diagnostic performance of mutual impedance experiments is investigated for the first time.
- Local inhomogeneities do not affect mutual impedance plasma density measurements but can impact the electron temperature diagnostic.
- The locality of mutual impedance plasma diagnostic is investigated using 1D-1V cartesian Vlasov-Poisson numerical simulations.

Corresponding author: Luca Bucciantini, luca.bucciantini@cnrs.fr

Abstract

Plasma diagnostic instruments are carried into space by satellites to measure in situ the properties of space plasmas. However, due to spacecraft charging, satellites perturb the surrounding plasma, that reacts by enveloping the platform and its instruments with a short scale, strongly inhomogeneous plasma region called plasma sheath. Such plasma sheath perturbs particles and electric field measurements performed onboard the satellite. Mutual impedance experiments are a type of in situ diagnostic technique used in several space missions for the identification of the plasma density and the electron temperature. The technique is based on the electric coupling between emitting and receiving electric sensors embedded in the plasma to diagnose. Such sensors are surrounded by the plasma sheath, which is expected to affect the plasma response to mutual impedance emissions. In this context, we quantify for the first time the impact of the plasma sheath on the diagnostic performance of mutual impedance experiments. For this purpose, we use a full kinetic Vlasov-Poisson model to simulate numerically mutual impedance experiments in an inhomogeneous medium. For the first time, we explain the locality of mutual impedance measurements. We find that mutual impedance plasma density diagnostic are not affected by the plasma sheath. The experiment retrieves the density of the plasma unperturbed by the satellite's presence. The electron temperature diagnostic, instead, presents significant perturbations if the plasma sheath is ignored. To mitigate such electron temperature errors, the plasma sheath needs to be included in the analysis of mutual impedance measurements.

1 Introduction

In the context of space exploration, satellites carry scientific instruments to observe both in situ and remotely the properties of various parts of our solar system. Such observations rely on the assumption that the monitored properties are not perturbed by the presence of the satellites on which the monitoring instruments are installed. However, as a consequence of spacecraft-plasma interaction processes, satellites in space acquire an electric DC potential which is of the order of the plasma (DC) potential (Grard et al., 1983; Lai, 2012). The satellite's potential perturbs in multiple ways the characteristics of the local environment and, therefore, it can affect different types of in situ observations (Johansson et al., 2021). First, the electric potential gradient surrounding the satellite generates an electric field that affects both wave and particles measurements. In particular, electric field lines (Marchand et al., 2010) and particles trajectories (Bergman et al., 2020) are modified by the DC electric field of the satellite, resulting in perturbations of both electric field, particle and velocity distribution measurements performed onboard (Miyake & Usui, 2016). Second, the DC electric charge of the satellite is Debye shielded (i.e. neutralized) by the plasma, which forms strong small-scale (of the order of the Debye length) inhomogeneous plasma regions around the satellite platform. Such inhomogeneous regions are called plasma sheath (Tonks & Langmuir, 1929; Laframboise, 1966; Riemann, 2008; Allen, 2008). The plasma sheath is expected to modify the properties of plasma waves propagating from the satellite platform and, consequently, it is expected to impact plasma wave instruments. In this study, we focus on a particular type of electric experiment, called Mutual Impedance (MI) experiment. The objective of this study is to quantify the impact that plasma inhomogeneities have on MI diagnostic performance.

MI experiments are plasma diagnostic techniques used for the identification of the in situ plasma density and electron temperature. In the past, different versions of MI instruments were included in the scientific payload of space exploration missions targeting both near (e.g. the Earth and its ionosphere) (Storey et al., 1969; Béghin & Debrie, 1972; Pottelette et al., 1975; Décréau et al., 1978; Pottelette & Storey, 1981; Bahnsen et al., 1988; Grard, 1997) and far (e.g. comet 67P/CG investigated by the ESA Rosetta mission (Taylor et al., 2017) carrying the RPC-MIP instrument) (Trotignon et al., 2007) objects of our solar system. Recently, new versions of MI instruments have been included in ongoing and future exploration missions, such as the ESA/JAXA mission BepiColombo (Benkhoff et al., 2021) (PWI-AM2P experiment) (Kasaba et al., 2020; Trotignon et al., 2006) that will investigate Mercury, the ESA mission

JUICE (RPWI-MIME experiment) that will explore Jovian moons and the ESA mission Comet Interceptor (DFP-COMPLIMENT instrument) that will perform a multi-point fly-by observation of a pristine comet entering the solar system for the first time (Snodgrass & Jones, 2019).

MI instruments consist of a set of emitting and receiving electric antennas. The emitting antennas excite the plasma with electric sinusoidal signals. Simultaneously to the emission, the receiving antennas measure the plasma fluctuations generated by the emitting sensors at the emission frequency. Such fluctuations are used for building MI spectra, which show resonant signatures in correspondence to characteristic frequencies of the probed plasma. The plasma density and electron temperature are identified from the position and shape of such resonant signatures, respectively (Storey et al., 1969; Décréau et al., 1978; Gilet et al., 2017; Wattieaux et al., 2020).

In the case of typical space applications, different spurious electric signals generated in the surroundings of MI antennas are expected to affect MI measurements. The most significant sources of perturbation are: (i) electronic components (e.g. active electric instruments) installed onboard the satellite, (ii) the spacecraft platform and (iii) the MI instrument itself.

(i) Electronic components onboard the satellite emit electric signals which might affect MI measurements both directly, by being detected by MI receiving antennas, and indirectly, by modifying the plasma probed by the MI experiment. The effects of such perturbations on the measurements depend on how close the perturbation source is to the MI electric sensors. Thus, their impact is typically minimized by placing the sensors of the instrument far from the satellite platform by means of long deployable booms. Note that this type of perturbation is typically handled when ensuring the ElectroMagnetic Compatibility (EMC) between the different sub-systems composing the satellite (Youssef, 1996).

(ii) The spacecraft platform interacts with the plasma and triggers the formation of a plasma sheath that embeds the satellite. MI electric sensors installed near the satellite platform can be surrounded by such plasma sheath. If that is the case, the inhomogeneous plasma region embedding the sensors might modify the characteristics of MI emitted signals and, as a consequence, might affect the MI diagnostic performance. To mitigate such perturbations, MI sensors are typically installed on long booms. However, long booms cannot always be used. For instance, in the case of missions probing plasmas with large Debye lengths with respect to the size of the satellite (e.g. $\lambda_D \simeq 10\ m$ in the solar wind at $1\ AU$), sufficiently long booms might not be emabarked on the spacecraft. This is also the case for nanosatellites, for which volume and mass are very constrained and long booms cannot be carried by the platform (West et al., 2015). Hence, the impact of the plasma sheath on MI measurements is not always negligible and, in some cases, cannot be ignored.

(iii) Similarly to satellite platforms, also MI instruments interact with the surrounding plasma and get charged to a given electric potential. In response to such potential, a plasma sheath forms around MI antennas. As this plasma sheath surrounds the instrument, its impact on the measurements cannot be reduced by changing the instrument's location. Hence, to better understand MI measurements, the instrument's self impact on the measurements needs to be accounted for.

In the case of the RPC-MIP instrument onboard the Rosetta mission, the minimization of spurious electric perturbations was accomplished by installing the MI instrument on a boom of approximately 1.5 m (Carr et al., 2007) attached to the spacecraft body ($\lambda_D \simeq 0.1m$ inside the coma of 67P/CG) (Gilet et al., 2017). This mitigation strategy reduced the perturbations generated by (i) electronic components onboard the satellite and by (ii) the satellite plasma sheath. But, due to their nature, perturbations caused by (iii) the instrument's plasma sheath could not be prevented and had to be taken into account. Past models of the MI instrumental response assumed a linear plasma response to MI excitation signal, a homogeneous plasma and negligible transient effects (Geiswiller et al., 2001; Gilet et al., 2017). Hence, they could not be used for investigating the impact of the plasma sheath on RPC-MIP measurements. This issue was investigated by Wattieaux, G. et al. (2019); Wattieaux et al. (2020), that obtained the instrumental response of RPC-MIP by modeling the plasma sheath embedding the instrument as a step-like vacuum sheath surrounding the sensors.

Similar investigations will be required for future MI space applications, where significant perturbations of MI measurements related to the presence of the plasma sheath are expected. This is the case for the PWI-AM2P instrument onboard the Mio spacecraft of the Bepi-Colombo mission. PWI-AM2P uses two emitting and two receiving electric antennas installed on four 15 m wires (Karlsson et al., 2020) and the local Debye length is expected to range between 1 m and 10 m in Mercury's magnetosphere (Kasaba et al., 2010). Hence, Debye length encountered by PWI-AM2P is not always expected to be negligible with respect to the distance between MI electric sensors. It results that the PWI-AM2P deployable wires cannot always ensure negligible (ii) perturbations of PWI-AM2P measurements caused to the satellite plasma sheath. Therefore, the impact of the plasma sheath on the measurements will need to be accounted for. We note that the effect of the plasma sheath is not expected to be negligible also for the RPWI-MIME mutual impedance experiment onboard the JUICE ESA mission, which launch is scheduled for April 2023. RPWI-MIME will investigate the ionospheric environment of Jupiter's moons, among which Ganymede, where the Debye length is expected to range from about 1 m to about 10 m between 200 km and 500 km of altitude. Such Debye lengths are not negligible with respect to the distance between the sensor and the satellite platform (i.e. 3 m) or to the emitting-receiving electric sensors distance of the instrument (i.e. about $5-10$ m). As a consequence, the impact of the plasma sheath on the measurements of RPWI-MIME onboard JUICE needs to be taken into account.

In all, the procedure used by Wattieaux et al. (2020) in the case of RPC-MIP provides an accurate instrumental response for specific plasma inhomogeneities surrounding the antennas. Indeed, such an approach is extremely efficient and can be used to improve our understanding of MI measurements for any specific space application (e.g. PWI-AM2P onboard Bepi-Colombo). However, due to its dependence on the measurements, it provides an understanding of the plasma sheath's effects that is specific to certain MI space applications. To support future MI instruments, in this study we focus on the general impact that local space charge inhomogeneities compatible with the (ii) satellite's and (iii) instrument's plasma sheath have on MI experiments, independently of the particular geometric configuration of the MI antennas or of the satellite platform.

While the effect of small-scale (i.e. of the order of the Debye length) plasma inhomogeneities on MI measurements is unknown, wave propagation over large-scale inhomogeneities (i.e. wavelength small with respect to the inhomogeneity's size) is a topic extensively investigated by different authors (e.g. (Krasnoselskikh et al., 2019; Tkachenko et al., 2021)). The equations describing the evolution of electric waves along large-scale inhomogeneities are referred to as WKB solutions (Wentzel, 1926; Kramers, 1926; Brillouin, 1926), in honor of those that devised the method. WKB solutions show that propagating electromagnetic waves crossing large-scale plasma inhomogeneities characterized by a slowly varying refraction index (i.e. $d\alpha/\alpha << dz/z$ with α the refraction index and z the direction along which the plasma is inhomogeneous) react with a variation of their wavelength along the inhomogeneity as $\lambda = \lambda_0/\alpha$ with λ_0 the wavelength of the wave when propagating in the vacuum. Do the satellite's and instrument's plasma sheath have the same impact on the propagation of plasma waves such as MI emission signals?

In this context, with this investigation we aim to answer a fundamental question regarding MI experiments, which is to understand the locality of in situ MI plasma diagnostic. In particular, we want to quantify the impact that small-scale plasma inhomogeneities with a typical size of the spacecraft plasma sheath have on MI plasma density and electron temperature diagnostic performances. For this purpose, we use a full kinetic 1D-1V cartesian Vlasov-Poisson numerical model to simulate the plasma response to MI emissions under different plasma density gradients. Note that we only consider MI experiments perturbing unmagnetized plasmas (i.e. $\omega_{ce} << \omega_p$).

This document is organized as follows. In section 2, we describe the numerical model and the plasma density profiles used to numerically simulate plasma inhomogeneities at different positions with respect to MI emitting antennas. In section 3, we show the results of our numerical simulations. In section 4, we compare the impact on MI measurements of small-

scale plasma inhomogeneities to that of large-scale inhomogeneities. In section 5, we finalize our investigation by discussing our conclusions.

2 Full Kinetic Electrostatic 1D-1V Cartesian Vlasov-Poisson Model with Plasma Inhomogeneities

We perform numerical simulations to investigate the impact of local space charge inhomogeneities on MI measurements. We use a 1D-1V cartesian full kinetic Vlasov-Poisson model to evolve in time a box of unmagnetized, collisionless plasma perturbed by MI emission signals. The model solves the Vlasov-Poisson system of equations following the eulerian algorithm of Mangeney et al. (2002). Such numerical model has been adapted and validated in Bucciantini et al. (2022) for the investigation of the impact of large emission amplitudes on MI plasma diagnostic performance.

MI measurements are performed over time scales much shorter than ion scales. Hence, small electric field amplitudes ensure a negligible contribution of the ion dynamics to MI measurements. This allows one to simplify the model by assuming the ions as a fixed background of positive charges (i.e. $\partial f_p/\partial t = 0$) with a given density profile. Note that such assumption enables one to significantly reduce the computing resources required for performing this analysis. Thus, we only evolve in time the Vlasov equation for electrons and we neglect the ion motion by discarding the Vlasov equation for ions:

$$\frac{\partial f_e\left(x,t,v_e\right)}{\partial t} + v_e \frac{\partial}{\partial x} f_e\left(x,t,v_e\right) - \frac{e}{m_e} E \frac{\partial}{\partial v_e} f_e\left(x,t,v_e\right) = 0 \tag{1}$$

where f_e is the electron distribution function, x is the position, v_e is the electron velocity, t is the time, e is the electron charge, m_e is the electron mass and E is the electric field. The electric field influencing the motion of electrons is computed self-consistently, using the Poisson equation:

$$\frac{\partial E}{\partial x} = e \frac{n_i(x) - n_e\left(x,t\right)}{\epsilon_0} + \frac{\rho_{ext}\left(x,t\right)}{\epsilon_0} \tag{2}$$

where $n_i(x)$ is the ion density profile is considered fixed in time, $n_e(x,t)$ is the electron density and $\rho_{ext}(x,t))$ is a source term used for the simulation of MI emitting antennas. The oscillating electric charge ρ_{ext} reads:

$$\rho_{ext}\left(x,t\right) = \sigma_0 \delta(x) \ \sin\left(2\pi f t\right) \tag{3}$$

where σ_0 is the emission amplitude and f the emission frequency. The emission amplitude is chosen to ensure the excitation of small amplitude signals in the plasma, which are associated to a linear plasma response (i.e. $(E^2\epsilon_0)/(n_0 k_b T_e) < 0.1$) (Bucciantini et al., 2022).

The boundary conditions of the model are periodic in physical space while, in velocity space, the distribution functions are imposed equal to zero for velocities outside a given range (i.e. $f_e\left(x, |v_e| > v_{max\ e}, t\right) = 0$, where $v_{max\ e} = 10\ v_{the}$).

A periodic physical space requires the antennas to be arranged in such a way that the electric field and electric potentials are also periodic in the box. Practically, this means that for each antenna polarized with a specific electric charge we put in the box a second antenna polarized with opposite charge. This second antenna generates an electric field which is opposite to that of the first antenna. As a result, the far-field electric field (Podesta, 2005) of the two antennas is neutralized and the fields in the plasma box are periodic.

We chose to use the same geometric configuration used for a past study by Bucciantini et al. (2022) (Model B configuration). Hence, we perturb the plasma box using a succession of four emitting antennas charged with opposite electric charge by pairs. Practically, the configuration of the antennas corresponds to that of the electrodes of two capacitors in series. The distance between two neighbor electrodes is always the same and it corresponds to one fourth of the spatial size of the numerical box.

Plasma inhomogeneities are simulated by initializing the numerical model with given electron and ion density profiles. Such profiles are obtained as follows.

Table 1. Parameters defining the simulated inhomogeneities in our numerical runs.

Simulation	x_0/λ_D	L^2	A/V_0
S_00	0	1.95	±0.5
S_01	1	1.95	±0.5
S_02	2	1.95	±0.5
S_04	4	1.95	±0.5
S_08	8	1.95	±0.5
S_16	16	1.95	±0.5
L_50	50	4000	±0.5

First, electrons are modeled as Maxwellian:

$$\frac{n_e(x,t=0)}{n_0} = \exp\left(\frac{V(x,t=0)}{V_0}\right) \tag{4}$$

where $n_e(x,t)$ is the electron density, n_0 the normalization density of the numerical model corresponding to the density far from the plasma inhomogeneity, $V(x,t)$ the electric potential in the plasma, $V_0 = k_B T_e/e$ the normalization electric potential of the model, with e the electron charge, k_B the Boltzmann constant and T_e the normalization electron temperature.

Second, we impose in the numerical plasma box an initial gaussian profile for the electric potential:

$$V(x,t=0) = A\ \exp\left[-\left(\frac{x-x_0}{L\lambda_D}\right)^2\right] \tag{5}$$

where A is the amplitude of the electric potential at the center of the inhomogeneity, x_0 is the position of the plasma inhomogeneity with respect to the MI emitting antenna, L the scale of the inhomogeneity and λ_D the Debye length. We note that a positive (resp. negative) value of A corresponds to a plasma inhomogeneity with excess (resp. depletion) of electrons.

Third, we compute self-consistently the ion density profile (n_p) using the Poisson equation.

$$\nabla^2 V(x,t=0) = -e\frac{n_p\,(x,t=0) - n_e\,(x,t=0)}{\epsilon_0}. \tag{6}$$

We note that the numerical box is perturbed by MI signals emitted from multiple electric antennas, according to the Model B configuration discussed above. For the sake of symmetric perturbations of the plasma box, we choose to simulate plasma inhomogeneities localized at distance x_0 from each emitting antenna. It follows that a small-scale inhomogeneity at $x_0 = 0$ corresponds to a plasma inhomogeneity centered at the mutual impedance emitting antennas.

In Table 1 we list the parameters defining the plasma sheath used for initializing our numerical runs. For the numerical runs S_00 to S_16 the size of the plasma inhomogeneity is assumed small, of the order of the Debye length. For the numerical run L_50 the inhomogeneity is a localized space charge of size significantly larger than the Debye length. The density profiles used for our analysis differ from the actual solution of the 1D plasma sheath (Riemann, 1991). Such solution was discarded because it presented non-smooth density profiles at the position of the antennas, that resulted in unstable numerical runs due to the spatial periodicity of the numerical box. Hence, to ensure stable numerical runs, we use simplified inhomogeneity profiles over the same spatial scales as the plasma sheath, both in the case of positive and negative electric potential profiles (EQ. 5).

All numerical runs simulate a plasma box of length $X_{max} = 4000\ \lambda_D$, with $n_x = 8192$ spatial grid points. The electron distribution function is assumed non-zero for the electron velocity v_e in the range ($-10\ v_{the}$, $10\ v_{the}$), discretized with $n_v = 101$ velocity grid points. The time-step of the numerical runs is set to $dt = 10^{-3}\omega_p^{-1}$. The amplitude of the emitted signals

is $\sigma = 10^{-5}\hat{\sigma}$ with $\hat{\sigma} = en_0\lambda_D$ the normalized amplitude of the charges at the emitting antennas. MI spectra are obtained for the frequency range (0.5 ω_p, 3.2 ω_p) with a relative discretization of the MI spectra of $\Delta\omega/\omega_n = 0.05$. Such frequency resolution corresponds to a plasma density resolution of 10%, which is used as reference in the following section.

3 Diagnostic Performance of Mutual Impedance Experiments in the Presence of Inhomogeneous Plasma Regions

In this section, we use the 1D-1V Vlasov-Poisson model (section 2) to investigate the diagnostic performance of MI experiments in the presence of small-scale plasma inhomogeneities (density profiles from section 2). First, we describe MI experiments and show how MI spectra are obtained from our numerical simulations (section 3.1). Second, we assess the impact of localized plasma inhomogeneities on both MI plasma density (section 3.2) and electron temperature (section 3.3) diagnostic performance.

3.1 Description and modeling of Mutual Impedance Measurements

MI instruments consist of a set of emitting and a set of receiving electric antennas. The measurement is performed as follows. (i) The emitting antennas excite the plasma with given electric signals. Simultaneously, (ii) the receiving antennas measure the plasma electric potential fluctuations triggered by the emission. (iii) MI spectra are built from the retrieved fluctuations. Then, (iv - v) the plasma density and electron temperature are derived from the position and the shape of the resonant signatures of MI spectra, respectively. These different steps of MI measurements are modelled as follows.

(i) MI emission signals are composed of a succession of j elementary sinusoidal signals, each oscillating at a given frequency. The $i{-}th$ elementary signal (with $i = 0, ..., j{-}1$) is injected in the plasma by polarizing the emitting antennas with the electric charge σ_i, that reads:

$$\sigma_i(\omega_i, t) = \sigma \sin \omega_i t \tag{7}$$

where $\omega_i = \omega_{min}(1+\Delta)^i$ is the $i-th$ emitted frequency, σ the amplitude, ω_{min} the lowest investigated frequency and Δ the frequency resolution. The signal σ_i is emitted for the duration $T_i = 2\pi N/\omega_i$, with N the amount of repetitions of the period of frequency ω_i.

In order to mimic typical MI experimental space applications such as the DFP-COMPLIMENT instrument onboard the Comet Interceptor mission, we choose both N and Δ to be the same for all emitted frequencies. In our case, we fix $N = 20$ and $\Delta = 0.05$. To such resolution corresponds a relative plasma density uncertainty of $|\Delta n_e|/n_e = 10\%$ that we use as a reference for the plasma density detection errors in the following sections.

The range of investigated frequencies is $(\omega_{min}, \omega_{max}) = \left(0.5\ \omega_p, 3.2\ \omega_p\right)$ that embeds the plasma frequency ω_p.

(ii) While the emitting antennas perturb the plasma, the receiving antennas measure its electric potential fluctuations. Such fluctuations are measured using a dipolar receiving antennas configuration. It consists of measuring the electric potential difference between two receiving antennas placed at distance d and $2d$ from the emitting antennas. Mimicking typical experimental space applications, we focus on emitting-receiving antennas distances going from $d = 5\lambda_D$ to $d = 100\lambda_D$.

(iii) MI spectra are built by computing, from the received signal, the spectral energy components corresponding to the emitted frequencies. In particular, for each emitted frequency, we compute a Discrete Fourier Transform (DFT) on the electric fluctuations measured while that frequency was being emitted. This is called a synchronous DFT analysis. Then, to highlight the response of the plasma to the emission, we mimic typical MI space applications (e.g. RPC-MIP onboard Rosetta (Trotignon et al., 2007)) and normalize each spectrum to the corresponding vacuum response (i.e. MI spectrum obtained in vacuum). Such MI spectra have resonant signatures in correspondence to the characteristic frequencies of the probed plasma

(Storey et al., 1969; Béghin & Debrie, 1972; Grard, 1997; Gilet et al., 2017). In the case of a negligible magnetic field, as in our investigation, the spectra have only one resonance at the plasma frequency $\omega_p = \sqrt{(e^2 n_e)/(\epsilon_0 m_e)}$, where n_e is the plasma density.

In Figure 1, we show the MI spectra in decibel (dB) scale where the reference are the corresponding measurements obtained in vacuum. Such spectra are obtained for the small-scale inhomogeneous plasmas located at different positions, as listed in Table 1 in function of the distance d between emitting and receiving antennas. Left (resp. Right) panels show the spectra obtained for the inhomogeneities associated to negative (resp. positive) electric potential profiles. The black dashed lines show the local plasma frequencies, computed using the plasma density profiles that describe the inhomogeneities (see section 2). We observe that the reso-

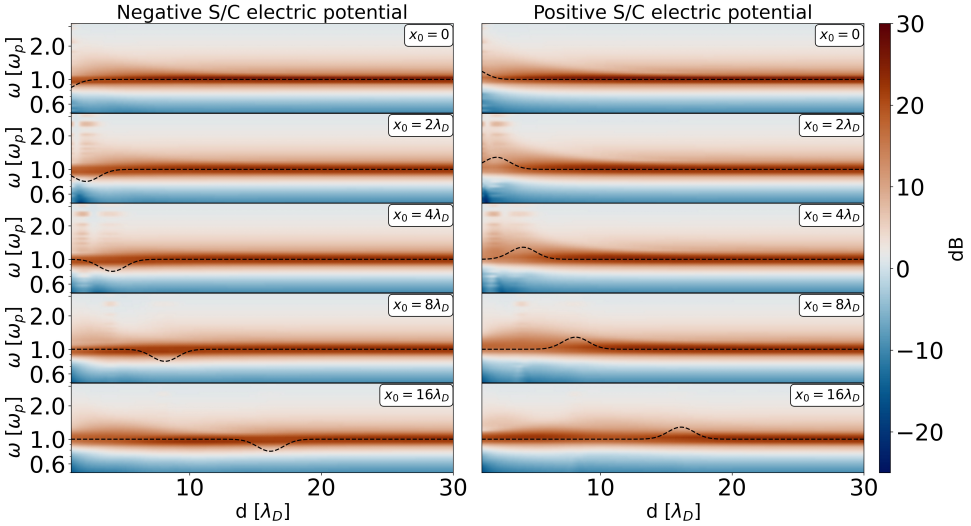

Figure 1. Mutual impedance spectra in the presence of a local space charge with negative (left panels) or positive (right panels) electric potential, in function of the emitting-receiving antennas distance d. The plasma sheath is centered at distance x_0 (Table 1) with respect to the emitting antennas. The black dashed line represents the local plasma frequency, obtained from the conversion of the electron density profile of the inhomogeneity.

nant signature of the spectra (red colored region) does not follow the local plasma frequency variations related to the local space charge, both in the case of negative and positive electric potential profiles. Instead, it remains near ω_p which is the resonant frequency of the homogeneous plasma unperturbed by the inhomogeneity. For instance, in the left bottom panel ($x_0 = 16\lambda_D$), the resonant signature of the MI spectra does not follow the local resonant frequency variations imposed at position $d = x_0$. As discussed in section 4, this trend is fundamentally different from what is found for MI spectra obtained for large-scale plasma inhomogeneities.

To better understand the effects that the plasma sheath has on MI measurements, we compare in Figure 2 the MI spectra obtained at specific distances from the emitting antennas (d from $5\lambda_D$ to $20\lambda_D$) and for different local space charges ($x_0 = 0, 2\lambda_D, 4\lambda_D, 8\lambda_D, 16\lambda_D$ represented with colored lines). Practically, the spectra shown in Figure 2 correspond to vertical cuts of the dynamic spectra represented in Figure 1. The reference spectra obtained for a homogeneous plasma are represented as blue lines.

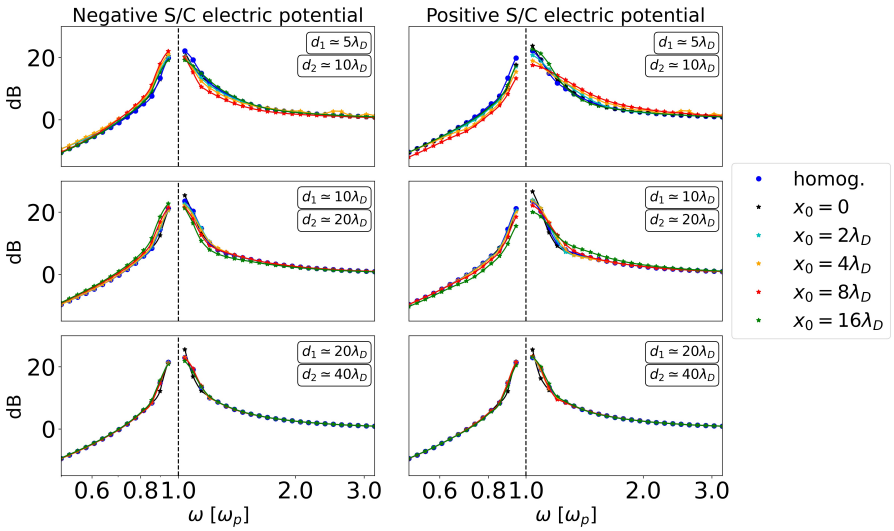

Figure 2. Examples of mutual impedance spectra obtained in the presence of the sensor/satellite plasma sheath. Left (resp. right) panels correspond to the plasma sheath of a satellite with negative (resp. positive) electric potential, placed at distance x_0 from the emitting antenna (Table 1).

Perturbations of MI measurements due to plasma inhomogeneities are essentially observed at frequencies close to the plasma frequency. However, such perturbations are significant only for spectra obtained near the position of the inhomogeneity (i.e. $d \simeq x_0$). In particular, we find negligible (resp. significant) differences between the perturbed spectra and the reference spectra when the receiving antennas are far from (resp. near) the inhomogeneity itself, as shown at frequency of about 1.04 ω_p (resp. 0.94 ω_p) in the top left (resp. right) panel of Figure 2. We also find that the extent of the perturbation depends on the sign of the electric potential profile inducing the inhomogeneity. In the case of a negative (resp. positive) electric potential profile, we find that the inhomogeneity generates perturbations of the MI spectra up to 5 dB (resp. 7 dB) with respect to the reference spectra derived in the case of an homogeneous plasma. Such discrepancies are considered significant since they exceed 1 dB, which is the typical MI instrumental noise for space experimental applications.

In the following section 3.2 and section 3.3, we investigate the impact that the perturbations of the spectra have on the (iv) plasma density and (v) electron temperature diagnostic performance, respectively. Although they are used in a different context, we note that the procedures used in the following sections to quantify the electron density and temperature diagnostics are identical to those developed and validated in (Bucciantini et al., 2022).

3.2 Plasma Density Diagnostic Performance

In this section, we quantify the MI plasma density diagnostic performance in the presence of local space charges near MI electrodes. This is performed in three successive steps.

First, we perform a quadratic interpolation of MI spectra. Past studies showed that it improves the plasma density diagnostic performance (Bucciantini et al., 2022). Second, we estimate the apparent plasma frequency ($\omega_{p,app}$) for each spectrum shown in Figure 1. We identify it as the frequency corresponding to the position of the (interpolated) resonant peak of the spectra, according to typical MI data analysis techniques (Storey et al., 1969; Rooy et al., 1972; Pottelette et al., 1975; Décréau et al., 1978; Pottelette & Storey, 1981; Bahnsen et al., 1988;

Gilet et al., 2017). In particular, we compute $\omega_{p,app}$ as the position of the maximum of the resonance. We note that the apparent plasma frequency $\omega_{p,app}$ derived from the spectra might differ from the known actual plasma frequency ω_p of our numerical simulations. Third, we compare the apparent and actual plasma frequencies and compute the plasma frequency relative error:

$$\frac{\Delta\omega_p}{\omega_p} = \frac{\omega_{p,app} - \omega_p}{\omega_p} \tag{8}$$

where ω_p is the plasma frequency of the homogeneous plasma, which is equivalent to the plasma frequency far from the plasma inhomogeneity.

The plasma density diagnostic performance of MI experiments is, then, obtained by converting the plasma frequency relative error to plasma density relative error:

$$\frac{\Delta n_e}{n_e} = 2\frac{\Delta\omega_{p,app}}{\omega_p} \tag{9}$$

where n_e is the density of the homogeneous plasma.

In the top panels of Figure 3, we show the plasma density relative errors obtained for local space charges induced by a negative (left panel) or positive (right panel) electric potential profiles, in function of the emitting-receiving antennas distance d. The gray shaded area represents the reference density uncertainty $|\Delta n_e| \,/\, n_e = 10\%$. The dashed colored lines represent the discrepancy between the density profiles of the inhomogeneous and homogeneous plasmas. We find that plasma density relative errors (solid colored lines) are negligible, as they

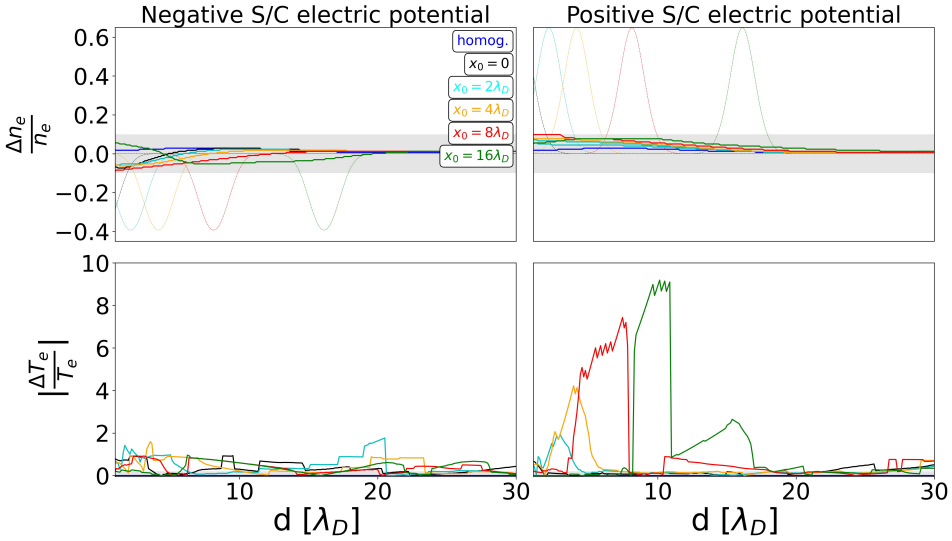

Figure 3. Plasma density (top panels) and electron temperature (bottom panels) relative errors derived from mutual impedance spectra in function of the distance d from the emitting antennas. Both top and bottom panels indicate the errors that one would make if the presence of local space charges near MI electrodes is neglected in the analysis. Left (resp. Right) panel: local space charge associated to negative (resp. positive) electric potential profiles. x_0 is the central position of the plasma sheath. Top panel: the gray shaded area represents the reference density uncertainty of 10%. The solid blue lines represent the relative error obtained for a homogeneous plasma. In matching colors, the solid and dashed lines represent the obtained plasma density relative error and the corresponding discrepancy between inhomogeneous density profile and reference homogeneous profile. Bottom panel: the colored lines represent the electron temperature uncertainties.

are always of the same order of magnitude as the reference 10% density uncertainty (gray shaded area) of the measurements. On top of that, we find that the density relative errors are negligible with respect to the difference between the inhomogeneous and homogeneous plasma density profiles (dashed lines). For instance, in the case of a local space charge due to a negative electric potential profile at $x_0 = 16\lambda_D$ (top left panel), the obtained uncertainty (green line) remains within the reference density uncertainty (gray area). The discrepancy between the reference homogeneous plasma and the inhomogeneous density profile (green dashed line), instead, significantly exceeds the error of 10%.

All in all, our results indicate that small-scale density inhomogeneities (i.e. of the order of the Debye length) compatible with plasma sheath plasma inhomogeneities have negligible impact on performance of the plasma density diagnostic provided by MI experiments.

3.3 Electron Temperature Diagnostic Performance

In this section, we quantify the impact of local space charges on the electron temperature diagnostic performance. This technique is composed of two successive steps.

First, we use the apparent plasma density $n_{e,app}$ identified from the analysis of the spectra (section 3.2) to derive, for each MI spectrum, the ratio of the apparent Debye length $\lambda_{D,app} = \sqrt{\left(\epsilon_0 k_B T_{e,app}\right) / \left(e^2 n_{e,app}\right)}$ to the actual Debye length $\lambda_D = \sqrt{(\epsilon_0 k_B T_e) / (e^2 n_e)}$. Following the same technique used by Wattieaux et al. (2020) for the analysis of RPC-MIP measurements in the case of the Rosetta mission, we compute the ratio between apparent and actual Debye lengths from the comparison between the modeled MI spectra and reference spectra obtained for a homogeneous plasma. Each reference spectrum is associated to the emitting-receiving antennas distance d_{ph} at which it is obtained. The comparison consists of computing the root-mean-squared error $\chi = \sqrt{\sum (x_i - y_i)^2 / S}$, where S is the amount of Fourier components of each MI spectrum (i.e. number of emitted frequencies), x_i and y_i are the $i{-}th$ Fourier components of the observed and reference MI spectra, respectively. To mimic similar space applications of this method, the error χ is computed only after imposing the equivalence between the plasma density of the reference spectra and the apparent plasma density.

The reference spectrum associated to the minimum root-mean-squared error is called the *matching* spectrum. The matching spectrum is assumed to be the (homogeneous) equivalent of the observed (inhomogeneous) spectrum. Hence, we assume that the observed and matching spectrum are obtained for the same distance d_{app}, which is the distance for which the matching spectrum is computed. We note that such distance might differ from the actual distance d at which the observed spectrum is obtained. The relation between the apparent distance d_{app} and the actual distance d of the observed spectrum reads:

$$d_{ph} = d_{app}\lambda_{D,app} = d\lambda_D \tag{10}$$

where d_{ph} is the (non-normalized) physical distance between emitting and receiving MI antennas, which is fixed by design of the instrument. The ratio between apparent and actual distances corresponds to the ratio between the actual and apparent Debye lengths. Second, we compare the apparent and actual electron temperatures and compute the electron temperature relative error:

$$\frac{\left|\Delta T_{e,app}\right|}{T_e} = \frac{\left|T_e - T_{e,app}\right|}{T_e} = \left|1 - \frac{T_{e,app}}{T_e}.\right| \tag{11}$$

Such error represents the perturbation of the MI electron temperature diagnostic due to the presence of the satellite's plasma sheath near MI electric sensors. Taking into account the ratio between apparent and actual Debye lengths, the electron temperature relative error is computed as:

$$\frac{\Delta T_{e,app}}{T_e} = 1 - \left(\frac{d}{d_{app}}\right)^2. \tag{12}$$

Past studies found that the typical electron temperature uncertainty required for standard science objectives is of the order of 10% – 30% (Décréau et al., 1978).

In the bottom panels of Figure 3, we show the electron temperature relative errors obtained for small-scale inhomogeneities with negative (left panel) and positive (right panel) electric potential profiles, in function of the distance from the antennas. In the case of the plasma sheath of a satellite with negative electric potential, we find electron temperature relative errors up to a factor 2. In the case of the plasma inhomogeneities associated to positive electric potential profiles, the error can be as large as a factor 9 depending on the position of the inhomogeneity and on the position at which the spectra are obtained. In both cases, the errors significantly exceed the reference errors of 10%−30%. This means that the spectra obtained in the presence of local space charges of the same scale as the plasma sheath of a satellite are not sufficiently similar to the spectra expected in the case of a homogeneous plasma. In those extreme cases, the shape of the MI spectra obtained in the presence of a local plasma inhomogeneity are so different from the MI spectra expected in the absence of such inhomogeneity, that the confidence level of the fit drops significantly. Let us put ourselves in the position of an observer, confronted with such data, but who ignores the presence (and the effect) of the local plasma inhomogeneity on the MI measurements. A careful observer, confronted with such discrepancies, would have certainly not concluded by providing an electron temperature that would be unacceptably false. Instead, he would have concluded that the instrument model is not compatible with the measurement : he would therefore have not provided any temperature estimations from the MI spectra. All in all, we conclude that it is not satisfactory to ignore the presence of the plasma sheath surrounding a charged spacecraft when performing electron temperature measurements using MI experiments. Instead, it is necessary to account for such local plasma inhomogeneity.

4 Mutual Impedance Spectra Obtained in the Presence of Large-Scale Plasma Inhomogeneities

We have shown that MI measurements provide the density of the plasma unperturbed by the presence of localized space charges. In particular, MI plasma density measurements are not affected by small-scale plasma density variations (e.g. satellite's plasma sheath). But, if the instruments carried by the satellite cross regions with large-scale plasma density variations, are in situ MI experiments able to retrieve the slowly varying plasma density? Large-scale plasma inhomogeneities are known to modify the properties of propagating plasma waves. In this section, we investigate for the first time what is their repercussion on MI measurements.

For this purpose, we derive MI spectra for the plasma inhomogeneity identified as *L_50* in Table 1. In particular, MI measurements are obtained both for inhomogeneities with depletion (left panel) and excess (right panel) of electrons. Figure 4 shows the MI spectra we obtained in function of the distance d. The spectra are compared to the profile of the local plasma frequency (black dashed line), which is derived from the density profile of the inhomogeneity. We remind the reader that the MI spectra investigated in this study are built using a dipolar antenna configuration. In particular, spectra at position d are obtained using the electric potential difference measured between a first antenna at $d_1 = d$ and a second antenna at $d_2 = 2d$. According to the density profile of the inhomogeneity, the local plasma density at the positions of the two antennas might differ (i.e. $n_e(x = d_1) \neq n_e(x = d_2)$). Hence, for sake of simplicity, we choose to use as reference local density the quadratic mean of the densities seen by the two antennas. The corresponding local plasma frequency is obtained from the conversion of the local plasma density (black dotted line). The apparent plasma frequency, identified as the frequency associated to the maximum of the resonant peak of the spectra, is represented as a light-blue line.

We find that both the resonant signature (red colored region) of the spectra and the apparent plasma frequency (light blue line) follow the local plasma frequency profile of the inhomogeneity (black dotted line). The discrepancy between the apparent and local plasma frequency is found up to 7%, which is of the order of the frequency resolution of the measurement ($\Delta = 5\%$ corresponding to a density resolution of 10%). Since such apparent and local frequencies are associated to the apparent and local plasma density, our investigation in-

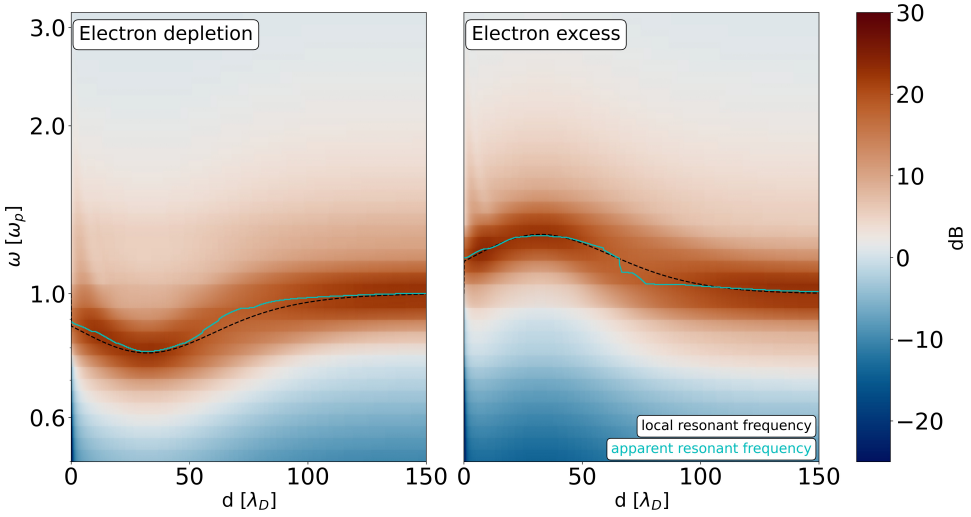

Figure 4. Mutual impedance spectra in the presence of large-scale plasma inhomogeneities, in function of the distance d. Left (resp. Right) panel obtained in the presence of inhomogeneous plasma with depletion (resp. excess) of electrons. The black dotted line represents the local plasma frequency profile associated to the local plasma inhomogeneity. The light blue line represents the apparent plasma frequency identified from the measurements.

dicates that MI experiments are indeed able to measure the large-scale density variations of the plasma surrounding MI electric sensors.

This result agrees with the (WKB) theory of plasma waves propagating through large-scale plasma inhomogeneities. Such theory was first devised by Wentzel, Kramers and Brillouin (Wentzel, 1926; Kramers, 1926; Brillouin, 1926). They showed that electromagnetic waves (e.g. MI emitted signals in the limit of an electrostatic plasma) propagating through stationary (i.e. over a time $\Delta t >> 2\pi/\omega$ with ω the frequency of the wave) plasma inhomogeneities of large-scale (i.e. $\Delta z >> \lambda$ with λ the wavelength of the wave) are perturbed as predicted by the WKB solutions:

$$E = A\alpha^{-1/2} \exp\left(\pm ik_0 \int dz\ \alpha\right) \tag{13}$$

where E is the amplitude of the electric field of the wave, A is a constant, $\alpha = kc/\omega$ the refractive index, $k_0 = \omega/c$ the wavenumber of the wave when propagating in vacuum and z the direction over which the plasma is inhomogeneous.

Electrostatic waves propagating through large-scale inhomogeneities with increasing (resp. decreasing) plasma density, corresponding to an increasing (resp. a decreasing) local plasma frequency, encounter a decreasing (resp. an increasing) refraction index. Thus, as the ratio between the wave's frequency and the local plasma frequency decreases (resp. increases), Landau damping on the wave decreases (resp. increases) and the wave resonates (resp. vanishes). For strong increase in plasma density, the ratio between the frequency of the wave and the local plasma frequency becomes lower than 1 and the wave is reflected. As an example, this process is similar to the reflection of radio waves in the Earth ionosphere (Westcott, 1962).

In the case of MI experiments, a succession of signals oscillating at different frequencies is injected in the plasma. Such emission perturbs the plasma and triggers oscillations at the emitted frequencies. Depending on the position of the emitted waves along the inhomogeneity, different oscillations resonate depending on the local plasma frequency. MI instruments

retrieve the frequency of the resonant oscillations of the plasma. Therefore, by construction, they retrieve the local plasma frequency variations of the large-scale inhomogeneity.

Before concluding this section, it is noteworthy to remember that the WKB solutions are valid in the limit of slowly varying plasma inhomogeneities:

$$\left|\frac{3}{4}\left(\frac{1}{\alpha^2}\frac{d\alpha}{dz}\right)^2 - \frac{1}{2\alpha^3}\frac{d^2\alpha}{dz^2}\right| << \frac{\omega^2}{c^2}. \tag{14}$$

Therefore, the WKB solutions cannot be applied in the case of small-scale inhomogeneities (discussed in section 3)

5 Summary and Conclusions

Spacecraft charging effects are known to impact the performances of different in situ plasma diagnostic techniques. In particular, small-scale plasma inhomogeneities (plasma sheath) triggered by the electric potential of the satellite affect both particle and wave instruments. In this context, we have investigated what is the impact of localized space charges on the performances of MI experiments, a plasma diagnostic technique used for the identification of the in situ plasma density and electron temperature. For this purpose, we have performed 1D-1V Vlasov-Poisson simulations to model MI instrumental response in the presence of plasma inhomogeneities. This study represents a first step towards understanding how local the plasma diagnostic of MI experiments is.

We find that the MI plasma density diagnostic performance is not perturbed by small-scale plasma inhomogeneities (of the order of few Debye Lengths) such as those generated in the plasma sheath of a charged spacecraft. Quantitatively, we find that the plasma density relative error does not exceed the plasma density uncertainty of 10%, which corresponds to the resolution of our measurements. This relative error decreases with the size of the emitter-receiver distance with respect to the size of the inhomogeneity. This means that MI experiments actually retrieve the density of the unperturbed plasma away from the spacecraft sheath in which the MI sensor might be embedded. On top of that, while being unaffected by small-scale (up to few Debye lengths) inhomogeneities like the plasma sheath, we find that the plasma density diagnostic of MI experiments is able to retrieve large-scale density variations (from few tens of Debye lengths) encountered by the MI sensors (section 4). This means that the experiment is able to measure the density gradients naturally generated in space plasmas by, e.g., plasma instabilities or turbulence, down to scales of few tens of Debye lengths.

Instead, for the electron temperature diagnostic performance, we find significant discrepancies between the instrumental response obtained in the presence of the plasma sheath with respect to that expected in its absence, resulting in errors that could be up to a factor 2 (resp. 9) for measurements performed in the vicinity of a spacecraft sheath associated to a negative (resp. positive) electric charge. In both cases, the error exceeds a desired electron temperature uncertainty of $10\% - 30\%$. To mitigate the impact of the spacecraft sheath on the temperature diagnostic, one has to model the small-scale plasma inhomogeneity surrounding the instrument and/or the spacecraft when computing the reference spectra used for the derivation of the temperatures. Our results are in agreement with the work of Wattieaux et al. (2020), that has shown the necessity to account for the plasma sheath surrounding the Rosetta spacecraft and/or instrument to satisfactorily derived the electron temperatures from RPC-MIP measurements. In that study, a step-like function was used to model the plasma sheath of the negatively charged Rosetta satellite platform in the model used for computing the reference MI spectra.

From a science of measurement point of view, our study indicates that the plasma diagnostic provided by MI experiments is not strictly local. Instead, it is the result of the excitation of the plasma over a range of tens of Debye lengths surrounding the electric sensors. Consequently, MI plasma density measurements are found to be immune to the local perturbations of the plasma generated by the floating electric potential of the satellite on which MI sensors are accommodated. With this result, this work provides for the first time an unambigu-

ous answer to the fundamental question about the locality of MI plasma diagnostic. Moreover, our study also illustrates that MI experiments plasma density measurements, unaffected by local perturbations associated to spacecraft charging, present a crucial advantage compared to other complementary, in situ, plasma diagnostic techniques.

This result can be understood and interpreted as follows. The MI technique is essentially based on the measurement of the plasma dielectric, from which plasma diagnostics such as the electron density and temperature are retrieved. The plasma dielectric itself is based on the notion of collective behavior of charged particle in a plasma. Such collective plasma behavior only exists on scales larger than the Debye length. Practically, in an unmagnetized plasma, the features observed MI spectra at frequencies close to the plasma frequency are associated with the generation and the propagation of Langmuir waves. Those waves carry information on scales much larger than the Debye length: therefore the MI emitter is actually exciting the plasma over a spatial range much larger than the Debye length. Those collective oscillations are actually blind to small-scale fluctuations of the order of the Debye length itself, such as the spacecraft sheath, over which they propagate undisturbed, and oscillate at the eigenfrequency of the unperturbed plasma (the plasma frequency) away from such small-scale inhomogeneity. This is why the retrieved plasma frequency is that of the unpertubed plasma away from the spacecraft sheath, and so is the plasma density diagnostic. However, for a hot plasma (i.e. for a plasma such that the Debye length is not short compared to the emitter-receiver distance of the MI experiment), the temperature diagnostic is based on the Landau damping of the generated waves. Such damping depend on the amount of charged particles, along the wave path, that can exchange energy with the generated electric signal (essentially absorb it). It can therefore directly be impacted by a local plasma inhomogeneity, especially for strongly damped Langmuir waves. This is why the temperature diagnostic depends on the nature of the spacecraft sheath in the case that the MI sensors or located within.

From a practical point of view, our results will be directly useful for the PWI-AM2P experiment onboard the Mio spacecraft of the ESA-JAXA BepiColombo mission that will investigate the surroundings of Mercury. At Mercury, photoelectric effects are expected to charge positively the Mio spacecraft when in sunlight. This means that we expect, at least for a significant part of the mission, a plasma sheath characterized by a local excess of electrons. The size of such plasma sheath shall be of the order of the Debye length λ_D that is expected to be in the range 1 m-10 m in the plasma environment of Mercury, while the electric sensors (the MEFISTO antennas (Karlsson et al., 2020)) are 15 m long. Our investigation indicates that one has to include the plasma sheath of the Mio spacecraft in the modeling and the analysis of PWI-AM2P spectra to retrieve satisfactorily the electron temperature.

We note also that this study will be useful for all future space applications of MI experiments, among which we recall the RPWI-MIME onboard the JUICE mission (resp. the CDFP-OMPLIMENT instrument onboard Comet Interceptor), where the local Debye length of the plasma encountered by the satellite is expected to be of the same order as the distance between RPWI-MIME (resp. DFP-COMPLIMENT) electric sensors.

6 Open Research

Datasets for this research are available at *linktodatasetonzenodo*, together with a detailed explanation on how to use them.

The model used to produce such dataset is described in section 2. It is based on the model implemented by Mangeney et al. (2002). The 1D-1V Vlasov-Poisson version of the model, which corresponds to the one we use in our investigation, is described in Henri et al. (2010).

Acknowledgments

The work performed at LPC2E is supported by CNES APR. The Scientific colour map "lajolla" (Crameri, 2021) is used in this study to prevent visual distortion of the data and exclusion of readers with colour-vision deficiencies(Crameri et al., 2020). We benefited from the computing resources provided by CaSciModOT. This work was granted access to the HPC/AI

resources of TGCC under the allocation 2021-A0100412428 made by GENCI. L.B. was supported by funds from Région Centre Val de Loire (France).

References

Allen, J. E. (2008). The plasma–sheath boundary: its history and Langmuir's definition of the sheath edge. *Plasma Sources Science and Technology*, *18*(1), 014004. doi: https://doi.org/10.1088/0963-0252/18/1/014004

Bahnsen, A., Jespersen, M., Ungstrup, E., Pottelette, R., Malingre, M., Decreau, P. M. E., ... Pedersen, B. M. (1988). First VIKING results: high frequency waves. *Physica Scripta*, *37*(3), 469-474. doi: https://doi.org/10.1088/0031-8949/37/3/032

Benkhoff, J., Murakami, G., Baumjohann, W., Besse, S., Bunce, E., Casale, M., ... Zender, J. (2021). Bepicolombo - mission overview and science goals. *Space Science Reviews*, *217*, 90. doi: https://doi.org/10.1007/s11214-021-00861-4

Bergman, S., Stenberg Wieser, G., Wieser, M., Johansson, F. L., & Eriksson, A. (2020). The influence of spacecraft charging on low-energy ion measurements made by RPC-ICA on Rosetta. *Journal of Geophysical Research: Space Physics*, *125*(1), e2019JA027478. doi: https://doi.org/10.1029/2019JA027478

Brillouin, L. (1926). La nouvelle mécanique atomique. *J. Phys. Radium*, *7*(5), 135-160. doi: https://doi.org/10.1051/jphysrad:0192600705013500

Bucciantini, L., Henri, P., Wattieaux, G., Califano, F., Vallières, X., & Randriamboarison, O. (2022). In situ space plasma diagnostics with finite amplitude active electric experiments: non-linear plasma effects and instrumental performance of mutual impedance experiments. *Journal of Geophysical Research: Space Physics*, *127*(12), e2022JA030813. doi: https://doi.org/10.1029/2022JA030813

Béghin, C., & Debrie, R. (1972). Characteristics of the electric field far from and close to a radiating antenna around the lower hybrid resonance in the ionospheric plasma. *Journal of Plasma Physics*, *8*(3), 287–310. doi: https://doi.org/10.1017/S0022377800007157

Carr, C., Cupido, E., Lee, C. G. Y., Balogh, A., Beek, T., Burch, J. L., ... Trotignon, J. G. (2007). Rpc: The Rosetta Plasma Consortium. *Space Science Reviews*, *128*, 629-647. doi: https://doi.org/10.1007/s11214-006-9136-4

Crameri, F. (2021, September). *Scientific colour maps.* Zenodo. doi: https://doi.org/10.5281/zenodo.5501399

Crameri, F., Shephard, G. E., & Heron, P. J. (2020). The misuse of colour in science communication. *Nature Communications*, *11*. doi: https://doi.org/10.1038/s41467-020-19160-7

Décréau, P. M. E., Beghin, C., & Parrot, M. (1978). Electron density and temperature, as measured by the mutual impedance experiment on board geos-1. *Space Science Reviews*, *22*(5), 581-595. doi: https://doi.org/10.1007/BF00223942

Geiswiller, J., Béghin, C., Kolesnikova, E., Lagoutte, D., Michau, J., & Trotignon, J. (2001). Rosetta spacecraft influence on the mutual impedance probe frequency response in the long Debye length mode. *Planetary and Space Science*, *49*(6), 633-644. doi: https://doi.org/10.1016/S0032-0633(00)00173-2

Gilet, N., Henri, P., Wattieaux, G., Cilibrasi, M., & Béghin, C. (2017). Electrostatic potential radiated by a pulsating charge in a two-electron temperature plasma. *Radio Science*, *52*, 1432-1448. doi: https://doi.org/10.1002/2017RS006294

Grard, R. (1997). Influence of suprathermal electrons upon the transfer impedance of a quadrupolar probe in a plasma. *Radio Science*, *32*(3), 1091-1100. doi: https://doi.org/10.1029/97RS00254

Grard, R., Knott, K., & Pedersen. (1983). Spacecraft charging effects. *Space Science Reviews*, *34*, 289-304. doi: https://doi.org/10.1007/BF00175284

Henri, P., Califano, F., Briand, C., & Mangeney, A. (2010). Vlasov-Poisson simulations of electrostatic parametric instability for localized Langmuir wave pack-

ets in the solar wind. *Journal of Geophysical Research*, *115*, A06106. doi: https://doi.org/10.1029/2009JA014969

Johansson, F. L., Eriksson, A. I., Vigren, E., Bucciantini, L., Henri, P., Nilsson, H., ... Odelstad, E. (2021). Plasma densities, flow, and solar EUV flux at comet 67P. *Astronomy and Astrophysics - A&A*, *653*(4), A128. doi: https://doi.org/10.1051/0004-6361/202039959

Karlsson, T., Kasaba, Y., Wahlund, J.-E., Henri, P., Bylander, L., Puccio, W., ... Morooka, M. (2020). The mefisto and wpt electric field sensors of the plasma wave investigation on the bepicolombo mio spacecraft. *Space Science Reviews*, 132-216. doi: https://doi.org/10.1007/s11214-020-00760-0

Kasaba, Y., J.-L., B., Blomberg, L., Kojima, H., Yagitani, S., Moncuquet, M., ... Matsumoto, H. (2010). The plasma wave investigation (pwi) onboard the bepicolombo/mmo: First measurement of electric fields, electromagnetic waves, and radio waves around mercury. *Planetary and Space Science*, *58*(1), 238-278. doi: https://doi.org/10.1016/j.pss.2008.07.017

Kasaba, Y., Kojima, H., Moncuquet, M., Wahlund, J., Yagitani, S., Sahraoui, F., ... Usui, H. (2020). Plasma Wave Investigation (PWI) aboard BepiColombo Mio on the trip to the first measurement of electric fields, electromagnetic waves, and radio waves around Mercury. *Space Science Reviews*, *216*(65). doi: https://doi.org/10.1007/s11214-020-00692-9

Kramers, H. A. (1926). Wellenmechanik und halbzahlige quantisierung. *Zeitschrift für Physik*, *39*, 828-840. doi: https://doi.org/10.1007/BF01451751

Krasnoselskikh, V., Voshchepynets, A., & Maksimovic, M. (2019). On the efficiency of the linear-mode conversion for generation of solar type iii radio bursts. *The Astrophysical Journal*, *879*(1), 51. doi: https://doi.org/10.3847/1538-4357/ab22bf

Laframboise, J. G. (1966). Theory of spherical and cylindrical langmuir probes in a collisionless, maxwellian plasma at rest.

Lai, S. T. (2012). *Fundamentals of spacecraft charging*. Princeton: Princeton University Press. doi: https://doi.org/10.1515/9781400839094

Mangeney, A., Califano, F., Cavazzoni, C., & Travnicek, P. (2002). A Numerical Scheme for the Integration of the Vlasov-Maxwell System of Equations. *Journal of Computational Physics*, *179*. doi: https://doi.org/10.1006/jcph.2002.7071

Marchand, R., Burchill, J. K., & Knudsen, D. J. (2010). Modelling electrostatic sheath effects on swarm electric field instrument measurements. *Space Science Reviews*, *156*(1-4), 73-87. doi: https://doi.org/10.1007/s11214-010-9735-y

Miyake, Y., & Usui, H. (2016). Particle-in-cell modeling of spacecraft-plasma interaction effects on double-probe electric field measurements. *Radio Science*, *51*(12), 1905-1922. doi: https://doi.org/10.1002/2016RS006095

Podesta, J. J. (2005). Spatial Landau damping in plasmas with three-dimensional k distributions. *Physics of plasmas*, *12*. doi: https://doi.org/10.1063/1.188547

Pottelette, R., Rooy, B., & Fiala, V. (1975). Theory of the mutual impedance of two small dipoles in a warm isotropic plasma. *Journal of Plasma Physics*, *14*(2), 209–243. doi: https://doi.org/10.1017/S0022377800009533

Pottelette, R., & Storey, L. R. O. (1981). Active and passive methods for the study of non-equilibrium plasmas using electrostatic waves. *Journal of Plasma Physics*, *25*(2), 323-350. doi: https://doi.org/10.1017/S0022377800023151

Riemann, K. U. (1991). The Bohm criterion and sheath formation. *Journal of Physics D: Applied Physics*, *24*(4), 493-518. doi: https://doi.org/10.1088/0022-3727/24/4/001

Riemann, K.-U. (2008). Plasma and sheath. *Plasma Sources Science and Technology*, *18*(1), 014006. doi: https://doi.org/10.1088/0963-0252/18/1/014006

Rooy, B., Feix, M. R., & Storey, L. R. O. (1972). Theory of a quadripolar probe for a hot isotropic plasma. *Plasma Physics*, *14*(3), 275-300. doi: https://doi.org/10.1088/0032-1028/14/3/005

Snodgrass, C., & Jones, G. H. (2019). The European Space Agency's Comet Interceptor lies in wait. *Nature Communications*, *10*(5418). doi: https://doi.org/10.1038/s41467-019

-13470-1

Storey, L., Aubry, L., & Meyer, P. (1969). Mutual impedance techniques for space plasma measurements. *In Measurement techniques in space plasmas - Fields, Geophysical Monograph Series*, *103*, 155. doi: https://doi.org/10.1029/GM103p0155

Taylor, M. G. G. T., Altobelli, N., Buratti, B. J., & Choukroun, M. (2017). The Rosetta mission orbiter science overview: the comet phase. *Philosophical Transactions of the Royal Society A: Mathematical, Physical and Engineering Sciences*, *375*(2097), 20160262. doi: https://doi.org/10.1098/rsta.2016.0262

Tkachenko, A., Krasnoselskikh, V., & Voshchepynets, A. (2021). Harmonic radio emission in randomly inhomogeneous plasma. *The Astrophysical Journal*, *908*(2), 126. doi: https://doi.org/10.3847/1538-4357/abd2bd

Tonks, L., & Langmuir, I. (1929). A general theory of the plasma of an arc. *Phys. Rev.*, *34*, 876-922. doi: https://doi.org/10.1103/PhysRev.34.876

Trotignon, J., Béghin, C., Lagoutte, D., Michau, J., Matsumoto, H., Kojima, H., ... Pottelette, R. (2006). Active measurement of the thermal electron density and temperature on the Mercury Magnetospheric Orbiter of the BepiColombo mission. *Advances in Space Research*, *38*(4), 686-692. doi: https://doi.org/10.1016/j.asr.2006.03.031

Trotignon, J., et al. (2007). RPC-MIP: The Mutual Impedance Probe of the Rosetta Plasma Consortium. *Space Science Reviews*, *128*, 713–728.

Wattieaux, G., Henri, P., Gilet, N., Vallières, X., & Deca, J. (2020). Plasma characterization at comet 67P between 2 and 4 AU from the Sun with the RPC-MIP instrument. *A&A*, *638*, A124. doi: https://doi.org/10.1051/0004-6361/202037571

Wattieaux, G., Gilet, N., Henri, P., Vallières, X., & Bucciantini, L. (2019). RPC-MIP observations at comet 67P/Churyumov-Gerasimenko explained by a model including a sheath and two populations of electrons. *A&A*, *630*, A41. doi: https://doi.org/10.1051/0004-6361/201834872

Wentzel, G. (1926). Eine verallgemeinerung der quantenbedingungen für die zwecke der wellenmechanik. *Zeitschrift für Physik*, *38*, 518-529. doi: https://doi.org/10.1007/BF01397171

West, S. T., White, C., Celestino, C., Philpott, S., & Pankow, M. (2015). Design and testing of deployable carbon fiber booms for cubesat non-gossamer applications. In *56th aiaa/asce/ahs/asc structures, structural dynamics, and materials conference.* doi: https://doi.org/10.2514/6.2015-0206

Westcott, B. (1962). Ionospheric reflection processes for long radio-waves—I. *Journal of Atmospheric and Terrestrial Physics*, *24*(5), 385-399. doi: https://doi.org/10.1016/0021-9169(62)90233-7

Youssef, E. (1996). Ecss - european cooperation for space standardization. In *Space programs and technologies conference.* doi: https://doi.org/10.2514/6.1996-4305

6.3 Paper 3 (Accepted by JGR): Instrumentation for Ionized Space Environments: New High Time Resolution Instrumental Modes of Mutual Impedance Experiments.

JGR Space Physics

METHOD
10.1029/2022JA031055

Instrumentation for Ionized Space Environments: New High Time Resolution Instrumental Modes of Mutual Impedance Experiments

L. Bucciantini[1], P. Henri[1,2], P. Dazzi[1,3], G. Wattieaux[4], F. Lavorenti[2,5], X. Vallières[1], J. Y. Brochot[1], F. Colin[1], M. C. Katrougkalou[6,7], G. Vengeons[1], T. Lecas[1], and O. Le Duff[1]

[1]Laboratoire de Physique et Chimie de l'Environnement et de l'Espace (LPC2E), CNRS, Université d'Orléans, Orléans, France, [2]Laboratoire Lagrange, OCA, UCA, CNRS, Nice, France, [3]Laboratoire d'Études Spatiales et d'Instrumentation en Astrophysique (LESIA), Paris Observatory, Paris, France, [4]Laboratoire Plasma et Conversion d'Energie (LAPLACE), CNRS, Université de Toulouse, Toulouse, France, [5]Dipartimento di Fisica, Università di Pisa, Pisa, Italy, [6]Institute de Recherche en Astrophysique et Planétologie (IRAP), Toulouse, France, [7]Royal Institute of Technology (KTH), Stockholm, Sweden

Key Points:

- New mutual impedance instrumental modes (chirp and multi-spectral) for higher time resolution measurements are defined, tested and validated
- The time resolution of mutual impedance measurements is improved by 20 times and the required onboard computing resources are reduced by 20%
- New fast mutual impedance instrumental procedures are tested and validated using 1D-1V Vlasov-Poisson simulations and plasma chamber tests

Correspondence to:
L. Bucciantini,
luca.bucciantini@cnrs.fr

Citation:
Bucciantini, L., Henri, P., Dazzi, P., Wattieaux, G., Lavorenti, F., Vallières, X., et al. (2023). Instrumentation for ionized space environments: New high time resolution instrumental modes of mutual impedance experiments. *Journal of Geophysical Research: Space Physics*, *128*, e2022JA031055. https://doi.org/10.1029/2022JA031055

Received 28 SEP 2022
Accepted 19 JAN 2023

Abstract Mutual impedance experiments are in situ plasma diagnostic techniques for the identification of the plasma density and the electron temperature. Different versions of mutual impedance instruments were included in past and present space missions (e.g., Rosetta, BepiColombo, JUICE and Comet Interceptor). New versions are currently being devised to fit the strong mass, volume and power constraints on nanosatellite platforms for future multi-point space missions. In this study, our goal is to define and validate two new instrumental modes (i.e., chirp and multi-spectral modes) to improve the time resolution of the experiment with respect to typical mutual impedance instrumental modes (i.e., frequency sweep). Higher time resolution measurements are expected to simplify the integration of mutual impedance experiments onboard nanosatellite platforms by facilitating antenna sharing between different experiments. The investigation is performed both (a) numerically, using a 1D-1V electrostatic full kinetic Vlasov-Poisson model and, (b) experimentally, with laboratory tests using a vacuum chamber and a plasma source. From a plasma diagnostic point of view, we find that both the chirp and multi-spectral modes provide measurements identical to the (reference) frequency sweep mode. From an instrumental point of view, multi-spectral measurements are faster than frequency sweep measurements but they require larger amounts of onboard computing resources (i.e., larger power consumption). Chirp measurements, instead, outperform frequency sweep measurements both in terms of measurement duration (20 times faster) and onboard processor usage (20% less).

1. Introduction

Mutual impedance (MI) experiments are in situ plasma diagnostic instrumental techniques used to determine the local plasma density and electron temperature. Different versions of MI experiments have been selected for past (Bahnsen et al., 1988; Béghin & Debrie, 1972; Béghin et al., 1982; Décréau et al., 1978; Grard, 1997; Pottelette et al., 1975; Pottelette & Storey, 1981; Storey et al., 1969) and present space exploration missions. We here recall the RPC-MIP instrument (Trotignon et al., 2007) onboard the ESA mission Rosetta, the PWI/AM2P experiment (Kasaba et al., 2020; Trotignon et al., 2006) onboard the ESA-JAXA BepiColombo mission, the RPWI/MIME experiment onboard the ESA mission JUICE and the DFP/COMPLIMENT instrument onboard the ESA mission Comet Interceptor (Snodgrass & Jones, 2019). New preliminary versions of MI instruments for future nanosatellite space missions are being developed.

Despite the expertise built over the past decades on the use of large satellite platforms for in situ space exploration, small platforms (e.g., nanosatellites) recently sparked the interest of the scientific community. As an example, the Comet Interceptor mission will investigate a pristine comet entering for the first time the solar system using three satellite platforms: one main (large) satellite supported by two (smaller) nanosatellites.

Why should we choose small satellites over larger ones?

On the one hand, large satellites can accommodate several payload instruments thanks to their significant volumes. Because of their complex architecture and varied set of sub-systems, these platforms are typically very expensive. Therefore, they are used for single-satellite missions (e.g., single-point measurements) which allow for local investigations of the plasma environment while ignoring the status of the global system at different locations.

On the other hand, small satellites typically accommodate a very limited amount of payload instruments due to mass, volume, and power consumption constraints. Because of their few components, such single platforms typically correspond to low costs. For a given capitalized cost, it enables one to use several small platforms, thus facilitating multi-satellite missions to provide multi-point simultaneous observations of physical phenomena acting on different (e.g., electron, ion, fluid) spatial scales (Retinò et al., 2021).

Using several small satellite platforms for future multi-point missions, we expect to complement the understanding of the space environment provided by large platforms, for both space weather monitoring and planetary exploration missions.

However, not all the sub-systems previously designed for large satellites are suitable for small platform applications. This is the case for MI instruments, for which past and present instrumental versions do not match the strong constraints of small satellites. Therefore, new versions of MI instrument are currently being developed to comply with these constraints. For this purpose, effort is put into (a) miniaturizing the instrument's electronics and (b) simplifying the system architecture. This is not sufficient to install the instrument on small platforms because a significant part of the mass and volume of MI instrument is associated with its electric antennas and their support structure. Miniaturization of these components is not possible because it would result in significant modifications of MI measurements. Therefore, we propose to follow a different strategy: since other experiments for in situ plasma diagnostic use similar antennas, we propose to reduce the overall mass and volume of the satellite payload by having the antennas shared between different experiments. Thus, instead of putting effort on the miniaturization of the MI antennas, we are focusing on (c) integrating the MI instrument with other plasma diagnostic instruments. The drawback to sharing the same antennas among different experiments is that the simultaneous use of the same integrated components by different experiments is not always possible. As a consequence, each experiment has limited available time to perform its measurements and shared scheduling between integrated experiments is required. Since this would limit the range of dynamic processes the instrument can observe, we need to improve its time resolution to both ensure the observation of the fast processes perturbing the environment and facilitate the integration with other instruments.

Although small satellites facilitate multi-point missions, they are associated to critical technical challenges, especially for scientific electric instruments.

The deployable booms of small satellites are typically very short, at most of the order of 1 m. This means that electric instruments are deployed near the platform, which is the source of different spurious electric perturbations to the measurements. First, electric devices installed on the satellite generate spurious electric signals that perturb the environment and, therefore, electric measurements performed nearby. Second, inhomogeneous plasma regions (i.e., plasma sheath) envelope the satellite platform as a consequence of spacecraft plasma interaction processes. Instruments deployed near the platform are placed near the satellite's plasma sheath, that is known to perturb in situ plasma diagnostic measurements.

On top of that, small satellites are associated with small charging times. This means that their ground electric potential is very sensitive to the currents collected from the plasma and, therefore, a fixed ground potential cannot always be ensured by the platform during the measurements. This is an issue for electric instruments because a varying ground potential can have significant effects on the measurements (Ranvier et al., 2019).

In the following, we neglect the impact of spurious electric signals on MI measurements, and we focus on the reduced time resolution of MI experiments related to antenna sharing. The study of the repercussion that short deployable booms have on MI measurements is left to future investigations.

In this context, we define and validate two new experimental procedures to improve MI experiment time resolution. These procedures correspond to two new instrumental modes (the so-called chirp mode and multi-spectral mode). The measurements of these two modes are validated against those of a reference mode (the so-called frequency sweep mode) typically used in past (e.g., the Rosetta mission) and current (e.g., BepiColombo) space missions. We note that all future MI instruments, both for small or large satellites applications, will benefit from a higher time resolution that will allow for the observation of faster processes.

The two new MI instrumental modes are investigated both numerically (Section 3.1) by means of 1D-1V Vlasov-Poisson numerical simulations (Henri et al., 2010; Mangeney et al., 2002), and experimentally (Section 3.2) by means of plasma chamber validation tests. Numerical simulations and experimental tests have different goals.

Numerical simulations model a simplified interaction between MI experiments and the surrounding plasma. They are used to obtain the (theoretical) instrumental response of the two new MI modes and to ensure it corresponds to that of typical MI experiments. After the theoretical equivalence between the modes is ensured, plasma chamber tests are used to validate the new modes in a representative ionospheric-like environment.

This document is organized as follows. In Section 2 we describe in detail the MI instrumental modes we developed. In Section 3.1 and Section 3.2 we describe the numerical model and experimental facility used to test the different MI instrumental modes, respectively. In Section 4 we discuss the results of the numerical and experimental investigation. In Section 4.4 we present the cost of the different instrumental modes in terms of the computational load on the onboard computer. In Section 6 we present our conclusions. In Appendix A we describe the characteristics of our experimental facility. In Appendix B we list for repeatability purposes the parameters defining our numerical simulations.

2. Description of MI Instrumental Modes

MI experiments are used to identify in situ the plasma density and electron temperature by, first, perturbing the plasma using a set of emitting antennas in a frequency range encompassing the electron plasma frequency and, second, retrieving the electric fluctuations in the plasma by means of a set of receiving antennas. The emission signal and the data treatment technique to be applied to the retrieved fluctuations depend on the chosen instrumental mode.

To improve the time resolution of MI measurements, we propose (for the first time) two new MI instrumental modes: the chirp mode and the multi-spectral mode. Such new modes are validated by testing their measurements against those of the nominal instrumental mode (Trotignon et al., 2007) which we call here frequency sweep mode and use as a reference.

In the following sections, we recall the experimental procedure of the frequency sweep mode and describe the new chirp and multi-spectral modes.

2.1. Description of the Frequency Sweep Mode

The frequency sweep mode is the state-of-the-art of MI experimental procedures and it is typically used in space applications as the MI nominal instrumental mode. Using this mode, MI spectra are built in four steps.

First, the plasma is excited by a sequence of elementary sinusoidal signals from the emitting electric antennas. The electric potential imposed at the antennas for the emission of the $i-th$ elementary signal reads:

$$V_{sw,i} = A\ \sin(2\pi f_i t) \quad (t_i < t < t_i + N/f_i, N = 20, 0 \le i \le j-1) \tag{1}$$

where $V_{sw,i}$ is the electric potential, A is the (fixed) emission amplitude, $f_i = f_{\min}(1+\Delta)^i, i = 0, \ldots, j-1$ is the frequency, $T_i = N/f_i$ is the emission duration, t_i is the beginning time of the emission of the $i-th$ frequency, $f_{\min}$ is the lower scanned frequency, $j = 1 + \log(f_{\max}/f_{\min})/\log(1+\Delta)$ is the number of emitted frequencies, Δ is the relative frequency resolution of the measurement and N is the amount of emitted oscillations per frequency (repetitions). To mimic typical MI space applications (e.g., the COMPLIMENT instrument onboard Comet Interceptor) we choose $\Delta = 0.05$.

Second, simultaneously to the emission process, the electric fluctuations generated in the plasma are measured by the receiving antennas.

Third, Discrete Fourier Transforms (DFTs) of the received electric signals are computed around the emitted frequencies. In particular, for the received electric fluctuations corresponding to the $i-th$ elementary signal, we compute the DFT at frequency f_i. This is done for all emitted frequencies.

Fourth, from the DFT components, we build spectra in phase and amplitude. MI spectra are then obtained by normalizing such spectra to the corresponding reference spectral response for the instrument. This reference response is identified by spectra obtained either in vacuum or in low density plasmas, such as weakly active solar wind conditions, following the procedure described above.

The frequency range ($f_{\min}$, $f_{\max}$) investigated with MI measurements is chosen in function of the probed plasma environment and therefore changes between different missions with different targets.

In past and current MI experimental space applications (e.g., Rosetta/RPC-MIP, BepiColombo/RPWI/AM2P, JUICE/PWI/MIME), the emission duration is fixed whatever the emitted frequency. As a consequence, the amounts of repetitions N is dependent on the emitted frequency. Overall, for such applications we find repetitions ranging between $N = 8$ and $N = 1{,}000$. In the case of DFP-COMPLIMENT onboard the future Comet Interceptor mission, instead, $N = 20$ has been chosen for all frequencies. As a consequence, different frequencies will correspond to different emission durations. In our investigation, we choose to mimic DFP-COMPLIMENT and fix the amount of repetitions to $N = 20$. Therefore, the total duration of the frequency sweep measurements investigated in our study corresponds to $T_{t,sw} = N \sum_{i=0}^{j-1} 1/f_i$.

2.2. Description of the Chirp Mode

The chirp mode is a new MI instrumental mode designed to minimize the time required by MI experiments to perform one single measurement. This is achieved by following the same procedure used for the frequency sweep mode, but by emitting each elementary signal for only one repetition (i.e., $N = 1$). For this mode, MI spectra are built from the components of the Fast Fourier Transform (FFT) of the whole received signal. Contrary to the frequency sweep mode that treats each frequency sequentially, the chirp mode treats all frequencies at once. When required, we use a Hann window to reduce the spectral leakage related to the non-periodicity of the electric potential retrieved by the receiving antennas. The need for the windowing of this signal is discussed in Section 4.3.

The oscillating electric potential used to polarize MI electrodes for the chirp emission reads:

$$V_{ch} = A \ \sin(2\pi f_i t) \quad (t_i < t < t_i + 1/f_i, 0 \le i \le j-1) \tag{2}$$

Hence, using this chirp mode, the MI measurement duration is reduced by about N times with respect to a corresponding frequency sweep mode measurement. The total duration of one chirp measurement is $T_{t,ch} = \sum_{i=0}^{j-1} 1/f_i$.

2.3. Description of the Multi-Spectral Mode

Similarly to the chirp mode, the multi-spectral mode is also a new instrumental mode devised to minimize the duration of MI measurements. The difference from the frequency sweep mode is that multiple elementary signals are emitted simultaneously. This choice reduces the measurement duration, but at the same time affects the amplitude of the emitted signals. Indeed, the instrument electronics can deliver to the electric antennas a signal with given maximum amplitude and, therefore, the superposition of different elementary signals has to respect this constraint. All in all, the choice of how many signals should be emitted simultaneously is the result of a trade-off between short measurement duration and strong enough received electric signals to ensure a satisfactory Signal-to-Noise Ratio. In our investigation we choose to emit simultaneously nine different elementary signals each with amplitude $A/9$. For the $i-th$ emission, the electric potential imposed at the antennas reads:

$$V_{ms,i} = \sum_{k=1}^{9} \frac{A}{9} \sin(2\pi f_{k,i} t) \quad (t_i < t < t_i + N/f_{0,i}, N = 20, 0 \le i \le j-1) \tag{3}$$

where $V_{ms,i}$ is the electric potential, $f_{0,i}$, ..., $f_{8,i}$ are the frequencies emitted simultaneously, and $T_i = N/f_{0,i}$ is the $i-th$ emission duration with $N = 20$ oscillations. Similarly to the frequency sweep mode procedure, the electric fluctuations generated in the plasma are retrieved simultaneously to each $i-th$ emission of the signal $V_{ms,i}$. Then, MI spectra are built by computing DFTs of those fluctuations for the corresponding emitted frequencies $f_{k,i}$ with $k = 0, .., 8$.

Depending on which frequencies we emit simultaneously, we obtain different MI emission durations. The minimum duration is obtained by grouping the lower frequencies in the same $i-th$ emission. But, if the simultaneously emitted signals have frequencies too close to each other, they can interfere and generate beats. In such case, the energy injected in the plasma at the emitted frequencies would shift to other frequencies and the measurements would be affected. In order to minimize this effect, we need to impose that the minimum difference between the frequencies we emit simultaneously is larger than some multiples of the frequency resolution of our spectral analysis. For each $i-th$ emission, such resolution corresponds to the inverse of the emission duration (i.e., $\Delta_{A,i} = f_{1,i}/N$). Considering (a) a measurement resolution of $\Delta = 0.05$ and (b) $N = 20$ for the lower frequencies

of the same $i-th$ emission, we find negligible interferences if the frequencies emitted simultaneously are spaced by at least $y=5$ other frequencies along the frequency range of interest. This means that the frequencies that are part of the same $i-th$ emission are different by at least a factor $(1+\Delta)^5$. The value of y is found empirically, by imposing that the DFT of $V_{ms,i}$ gives for the frequencies $f_{k,i}$ the amplitude $A/9$ with a precision of 2%.

For completeness, we give an empirical rule to compute the different sets of frequencies emitted simultaneously. For the $i-th$ emission, we emit the frequencies $f_{k,i}=f_{\min}(1+\Delta)^{y\ \ k+p_1+p_2}$ with $k=0,\ldots,8$ their index, $p_1=i \bmod y$ and $p_2=(9\cdot y)\cdot(i \operatorname{div} y)$ (where div represents the Euclidean division and mod the remainder of the Euclidean division). Note that one multi-spectral measurement is composed of $p_3=[(j-1)\bmod(9\cdot y)+1]\cdot y$ simultaneous emissions and receptions. Let us consider the case where the multi-spectral measurement scans $j=81$ frequencies with resolution $\Delta=0.05$, $N=20$ (i.e., $y=5$) and a maximum of 9 frequencies emitted simultaneously. Then, the measurement is composed of $p_3=10$ emissions and the frequencies emitted simultaneously are:

$$
\begin{aligned}
&f_{0,0}=f_0, f_{1,0}=f_5, f_{2,0}=f_{10}, f_{3,0}=f_{15}, f_{4,0}=f_{20}, f_{5,0}=f_{25}, f_{6,0}=f_{30}, f_{7,0}=f_{35}, f_{8,0}=f_{40}\\
&f_{0,1}=f_1, f_{1,1}=f_6, f_{2,1}=f_{11}, f_{3,1}=f_{16}, f_{4,1}=f_{21}, f_{5,1}=f_{26}, f_{6,1}=f_{31}, f_{7,1}=f_{36}, f_{8,1}=f_{41}\\
&f_{0,2}=f_2, f_{1,2}=f_7, f_{2,2}=f_{12}, f_{3,2}=f_{17}, f_{4,2}=f_{22}, f_{5,2}=f_{27}, f_{6,2}=f_{32}, f_{7,2}=f_{37}, f_{8,2}=f_{42}\\
&f_{0,3}=f_3, f_{1,3}=f_8, f_{2,3}=f_{13}, f_{3,3}=f_{18}, f_{4,3}=f_{23}, f_{5,3}=f_{28}, f_{6,3}=f_{33}, f_{7,3}=f_{38}, f_{8,3}=f_{43}\\
&f_{0,4}=f_4, f_{1,4}=f_9, f_{2,4}=f_{14}, f_{3,4}=f_{19}, f_{4,4}=f_{24}, f_{5,4}=f_{29}, f_{6,4}=f_{34}, f_{7,4}=f_{39}, f_{8,4}=f_{44}\\
&f_{0,5}=f_{45}, f_{1,5}=f_{50}, f_{2,5}=f_{55}, f_{3,5}=f_{60}, f_{4,5}=f_{65}, f_{5,5}=f_{70}, f_{6,5}=f_{75}, f_{7,5}=f_{80}\\
&f_{0,6}=f_{46}, f_{1,6}=f_{51}, f_{2,6}=f_{56}, f_{3,6}=f_{61}, f_{4,6}=f_{66}, f_{5,6}=f_{71}, f_{6,6}=f_{76}, f_{7,6}=f_{81}\\
&f_{0,7}=f_{47}, f_{1,7}=f_{52}, f_{2,7}=f_{57}, f_{3,7}=f_{62}, f_{4,7}=f_{67}, f_{5,7}=f_{72}, f_{6,7}=f_{77}\\
&f_{0,8}=f_{48}, f_{1,8}=f_{53}, f_{2,8}=f_{58}, f_{3,8}=f_{63}, f_{4,8}=f_{68}, f_{5,8}=f_{73}, f_{6,8}=f_{78}\\
&f_{0,9}=f_{49}, f_{1,9}=f_{54}, f_{2,9}=f_{59}, f_{3,9}=f_{64}, f_{4,9}=f_{69}, f_{5,9}=f_{74}, f_{6,9}=f_{79}
\end{aligned}
\tag{4}
$$

The total duration of one multi-spectral measurement is $T_{t,ms}=N\sum_{i=0}^{p_3-1}1/f_{0,i}$.

3. Methods

In this section, we describe the numerical model and the experimental facility we used to test and characterize the chirp and multi-spectral modes against the reference frequency sweep mode.

3.1. Full-Kinetic Electrostatic 1D-1V Vlasov-Poisson Simulation Model

We investigate numerically the new MI instrumental modes by performing numerical simulations of an unmagnetized, collisionless, homogeneous plasma perturbed by MI emitting electric antennas. For this purpose, we use a 1D-1V full kinetic electrostatic model (Bucciantini et al., 2022; Henri et al., 2010) based on the solution of the Vlasov-Poisson system (following the integration scheme of Mangeney et al. (2002)) to simulate the evolution in time and space of the electron distribution function ($f_e(t,x,v_e)$, where t is the time, x the position and v is the velocity) of a numerical plasma box. In particular, the electron distribution functions at different positions in the numerical box are evolved in time by using the Vlasov equation:

$$
\frac{\partial f_e(x,t,v_e)}{\partial t}+v_e\frac{\partial}{\partial x}f_e(x,t,v_e)-\frac{e}{m_e}E\frac{\partial}{\partial v_e}f_e(x,t,v_e)=0 \tag{5}
$$

where e is the electron charge, m_e is the electron mass, and E is the electric field of the plasma box. Such electric field is computed self-consistently using the Poisson equation:

$$
\frac{\partial E}{\partial x}=e\frac{n_i-n_e(x,t)}{\varepsilon_0}+\frac{\rho_{ext}(x,t)}{\varepsilon_0} \tag{6}
$$

where n_i is the fixed homogeneous ion density in the numerical box and ρ_{ext} is an external source term that we use to model MI emitting antennas. For each emitting antenna, the external source term reads:

$$
\rho_{ext}(x,t)=\sigma_0\delta(x)\ \ \sin(2\pi f t) \tag{7}
$$

where σ_0 is the emission amplitude and f is the emitted frequency. Each MI emitting antenna modeled in 1D as a localized oscillating external electric charge corresponds, in 3D, to a uniformly charged infinite planar grid. Such a grid is assumed transparent, so that the currents collected at its surfaces are negligible.

We use periodic boundary conditions in physical space, and we assume that the distribution functions are equal to zero for velocities outside the chosen velocity space range (e.g., $f_e(x, |v_e| > v_{\max\ e}, t) = 0$). The periodic boundary conditions require a spatially periodic electric field and electric potential in the box. But the plasma located on the two sides of each emitting (infinite planar grid) antenna is perturbed with electric fields of opposite signs. It follows that the spatial periodicity of the system cannot be ensured by the use of only one emitting antenna. Therefore, we use multiple antennas and arrange them so that their resulting electric field and electric potential are periodic in the box. Practically, we use four emitting antennas: two antennas with positive charge and two antennas with negative charge, equally spaced along the 1D numerical box and ordered as a sequence of negatively-positively-positively-negatively charged antennas. Such configuration mimics a succession of two infinite plate capacitors, where each capacitor is composed of two contiguous antennas with opposite charge. The two capacitors induce in-between their electrodes opposite electric fields, resulting in opposite electric potential variations of the plasma. As a result, our configuration ensures the periodicity of both the electric field and electric potential in the box.

Ions are modeled as a homogeneous neutralizing fixed background of positive charges. This is justified because both the MI antenna emission amplitudes and the MI measurement durations ensure a negligible contribution of the ion dynamics to MI measurements. First, the chosen emission amplitudes (Appendix B) correspond to electric-to-thermal energy ratios well below 0.1. Therefore, the energy injected by the MI antennas in the plasma is small with respect to the kinetic energy of electrons and no non-linear interactions (e.g., wave-wave or wave-particle interactions) are triggered. Second, our numerical simulations are focused on MI measurement durations that are much shorter than ion time scales.

To minimize possible transient effects, the model is initialized by imposing the respect of both the Poisson and Ampère-Maxwell equation at $t = 0$.

For repeatability purposes, we list in Appendix B the parameters defining the numerical simulations discussed in our investigation.

3.2. PEPSO: Plasma Chamber Experimental Facility

In this section, we describe the plasma chamber testing facility used to validate the diagnostic performance of MI instrumental modes. This testing facility was developed in the framework of the PEPSO project (Plasma Environment Platform for Satellite tests in Orléans) at the LPC2E (CNRS, Orléans, France) space laboratory. It is composed of a vacuum chamber, a pumping system, a plasma source, a magnetic field control system, and various diagnostics devices.

The vacuum chamber is a cylindrical chamber in AlSI304 L alloy, measuring 1 m in diameter and 1.8 m in length.

The pumping system, composed of a primary pump (Pfeiffer/ACP40) and a secondary turbo-molecular pump (Pfeiffer/ATH3204M), is used to bring the ambient pressure in the chamber down to 10^{-6} mbar (i.e., about 10^{-4} Pa).

The plasma source is a Kaufman type (Kaufman et al., 1982) electric source, composed of an ionization chamber, a cathode (tungsten) filament, a filtering electric grid, a neutralizing (tungsten) filament and an external solenoid. Inert neutral gas (Argon >99.999%) is injected in the ionization chamber. The cathode filament is heated and electrons are thermionically emitted. The neutral gas flow entering the source is ionized through collisions with these electrons. Positive ions produced by the collisions are accelerated outside the source by the filtering grid while released electrons are kept inside it in order to maintain the ionization process of the gas. Similarly to the cathode, the neutralizing filament outside the source is heated and electrons are thermionically emitted. Such electrons do not remain near the filament but, instead, are attracted by the positive potential of the ion flow. As a result, the electrons join the ion flow and form a globally neutral plasma which drifts along the chamber. The external solenoid is used to modify the magnetic field inside the source in order to constrain the movement of electrons and increase the ionization of the gas. At the middle of the chamber (where we typically place our instrumentation), the injected plasma has a density ranging between 5×10^4 and 4×10^5 cm^{-3} and an electron

Table 1
List of Plasma Density and Electron Temperature Parameters Characterizing the Two Experimental Tests Discussed in Section 4

Test	n_e[cm^{-3}]	T_e[eV]
T_01	53,156 ± 3195	0.47 ± 0.20
T_02	67,970 ± 3485	0.49 ± 0.03

temperature of the order of 0.5 eV. The corresponding Debye length is of the order of 0.008–0.023 m, which is small compared to the size of the vacuum chamber.

Modifications of the neutral gas flow rate and/or settings of the plasma source enable one to control the characteristics of the generated plasma. In the following sections, we illustrate two examples of experimental tests, performed using the two different sets of plasma parameters listed in Table 1. We discuss the stability and the homogeneity of the plasma flow injected in the vacuum chamber, together with its drift velocity, in a dedicated Appendix A.

After the plasma is generated in the chamber, we perform MI measurements using a monopolar electric emitting antenna, a dipolar set of receiving antennas and one electronic card. The two antennas are aluminum spherical antennas (radius of 0.01 m) placed close to the axis of the cylindrical plasma chamber, perpendicular to the plasma flow and at a distance of 0.15 m between each other. The geometric configuration of the antennas in the plasma chamber is represented in Figure 1.

The receiving antenna is connected to an amplifier which increases the received signal amplitude by a factor 8.7 (i.e., 18.79 dB). The electronic card is used to perform MI measurements following the emission/reception procedures described in Section 2 for the different investigated instrumental modes. For this purpose, we choose the Eclypse evaluation board which integrates a Zynq7000 processor (Xilinx), equipped with Digital-to-Analog and Analog-to-Digital converters.

At the position of the electric antennas, the Earth's magnetic field amplitude amounts to 3.8×10^4 nT (i.e., 0.38 G). To this magnetic field corresponds the plasma cyclotron frequency $f_{ce} = 1.1$ MHz, which we note is of the same order as the plasma frequency in the plasma chamber. In this case, Larmor radius is estimated to be 4 cm. If the electron cyclotron frequency is of the same order as the plasma frequency, the Larmor radius is also of the same order as Debye length. Hence, the contribution of Earth's magnetic field to MI spectra is non-negligible.

Figure 1. Plasma chamber. Experimental configuration of the electric antennas used to validate the new MI instrumental modes.

To mimic typical planetary and cometary ionized environments characterized by a low magnetic field, we need to significantly reduce Earth's background magnetic field at the position of MI antennas. For this purpose, we use a magnetic field control system. Such system is composed of three perpendicular pairs of wire coils, each coil is located on one face of a cube, and its diameter is equal to the cube side length, in a configuration similar to three Helmholtz coils (as in Figure 1). By sending currents in the coils, we modify the amplitude of the magnetic field at the antenna location down to about 6% of its ambient value. As a result of such reduction in magnetic field strength, the approximation of an unmagnetized plasma (i.e., $\omega_p/\omega_{ce} \gg 1$) is valid. We note that our numerical model (Section 3.1) is consistent with this unmagnetized plasma experimental setup.

4. Results

In this section, we compare frequency sweep mode measurements to chirp and multi-spectral mode measurements. We obtain MI spectra following the experimental procedures described in Section 2.

This investigation is performed both numerically, using the model described in Section 3.1, and experimentally, using the plasma chamber described in Section 3.2.

4.1. Numerical Investigation

We simulate MI measurements for the frequency range $(0.5f_p, 3.2f_p)$ with frequency resolution $\Delta = 0.05$ ($j = 39$), consistent with the resolution used

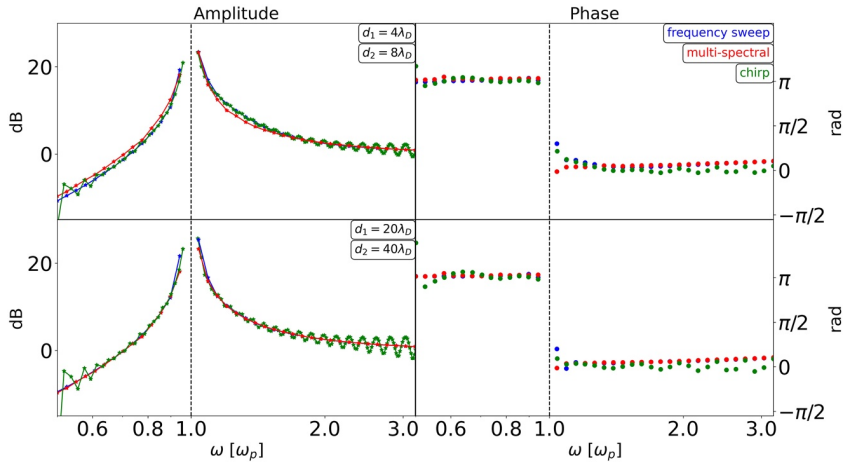

Figure 2. Mutual impedance amplitude and phase spectra (left and right panels, respectively) obtained numerically for the frequency sweep mode (blue line), chirp mode (green line) and multi-spectral mode (red line). Top and bottom panels are obtained for distances $d = 4\ \lambda_D$ and $d = 20\ \lambda_D$, respectively. The black dashed lines indicate the position of the plasma frequency.

by the DFP-COMPLIMENT instrument onboard the Comet Interceptor mission. This resolution corresponds to a relative plasma density uncertainty of $\Delta n_e/n_e = 10\%$, with n_e the plasma density, consistent with space exploration missions needs and requirements.

MI spectra are built from the electric potential difference measured between two receiving antennas, one at distance d and one at 2 d from the emitting antennas. We limit our investigation to distances d ranging from 4 λ_D to 100 λ_D, which corresponds to the typical distance between emitting and receiving antennas for experimental space applications.

Depending on the investigated instrumental mode, we employ either a single or multiple numerical run(s) to simulate one given MI measurement.

First, for the frequency sweep mode (simulations FS_01 to FS_48 in Table B1), instead of using one single run to simulate the emission of a succession of elementary signals, we use several runs to simulate separately the emission of each single signal $V_{sw,i}$. In our case, given the investigated frequency range and frequency resolution, we perform 39 different runs. Since our numerical box is periodic and wave reflections are to be avoided, by doing so we reduce the size of the numerical spatial box and the computational cost of our simulations. This is achieved at the expense of neglecting the coupling between electric fluctuations of the plasma corresponding to the emission of different elementary signals. This approach is justified by the use of small emission amplitudes that ensures the absence of non-linear interactions between plasma perturbations at different frequencies. Second, for the chirp mode (simulation CH_01), the emission process is simulated using one single numerical run. Third, for the multi-spectral mode (simulations MS_01 to MS_06), similarly to the frequency sweep mode case, we simulate separately the emission of each signal $V_{ms,i}$. In our case, given the investigated frequency range and its resolution, we perform six different runs.

Different examples of numerical MI spectra obtained for the frequency sweep (solid blue line), chirp (solid green line) and multi-spectral (solid red line) modes are shown in Figure 2, for distances $d = 4\ \lambda_D$ and $d = 20\ \lambda_D$ (top and bottom panel, respectively). The reference plasma frequency is shown using black vertical dashed lines. These spectra are represented in decibel scale, where the 0 dB corresponds to the electric potential difference obtained in vacuum, using the same normalization as usually performed in the post-treatment of space missions MI spectra.

All spectra exhibit a resonant peak in correspondence to the plasma frequency. This is the signature of MI measurements which enables one to identify, from the frequency location of the resonance at the plasma frequency, the plasma density and, from the shape of the resonance itself, the electron temperature (Bahnsen et al., 1988; Béghin & Debrie, 1972; Décréau et al., 1978; Geiswiller et al., 2001; Gilet et al., 2017; Grard, 1969, 1997; Pottelette et al., 1975; Pottelette & Storey, 1981; Rooy et al., 1972; Storey et al., 1969; Wattieaux et al., 2020).

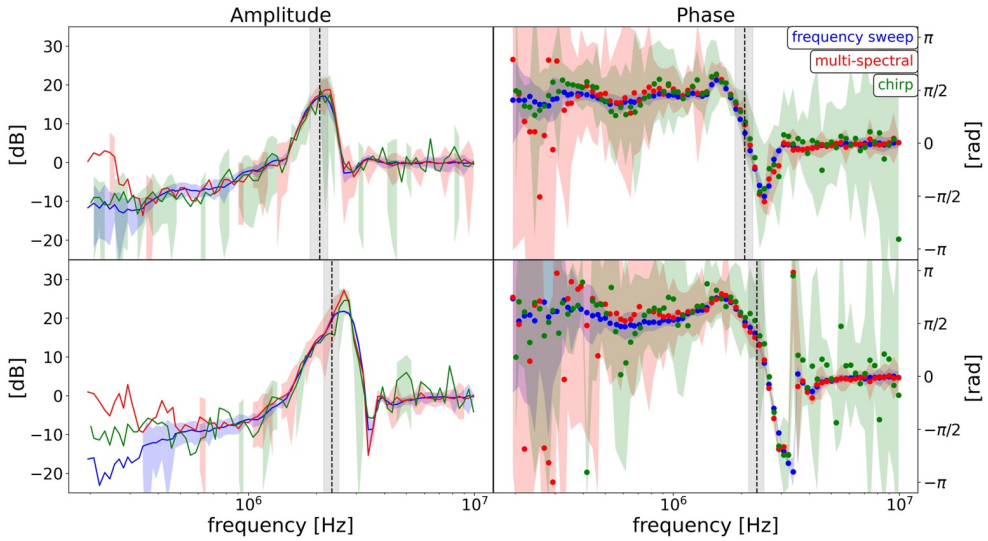

Figure 3. Mutual impedance spectra in amplitude (left column) and phase (right column) obtained experimentally for the frequency sweep mode (blue line), chirp mode (green line) and multi-spectral mode (red line). Each row represents tests performed for a different plasma (plasma densities listed in Table 1, increasing from top to bottom row). The black dashed line indicates the reference plasma frequency obtained from an independent measurement and the gray shaded area the associated uncertainty.

We find that multi-spectral measurements and reference frequency sweep measurements differ at most of 2.5 dB in correspondence to the plasma resonance. We consider such difference negligible because of the order of the typical 1 dB MI instrumental noise found in space applications.

Chirp and frequency sweep measurements have differences of 2.5 dB only for frequencies close to the plasma frequency (i.e., in the range [0.7 ω_p, 1.5 ω_p]). For frequencies far from the plasma frequency (i.e., below 0.7ω_p or above 1.5 ω_p), instead, the discrepancies significantly exceed (i.e., larger than 5 dB) the typical instrumental noise levels.

Since small discrepancies are observed for the resonant signature of the two MI measurements, which is used to derive the plasma density and electron temperature, we conclude that the three instrumental modes should provide identical densities and temperatures.

In the following section, we validate experimentally the new MI instrumental modes by comparing multiple spectra obtained in the plasma chamber.

4.2. Experimental Investigation

We obtain experimental MI spectra within the frequency range (200 kHz, 10 MHz), using the frequency resolution Δ (i.e., $\Delta n_e/n_e = 10\%$) resulting in $j = 81$. For this purpose, we use the MI antennas configuration described in Section 3.2.

Typical examples of experimental MI spectra in amplitude and phase are shown in Figure 3 (left and right panels, respectively). Such spectra are obtained using the frequency sweep (blue line), chirp (green line) and multi-spectral (red line) modes to probe plasmas in the chamber characterized by different plasma densities (increasing from top to bottom panel), with densities listed in Table 1). The spectrum obtained for each mode is the median spectrum computed from a repetition of 11 independent successive measurements. The colored shaded areas represent the uncertainty of the measurements, identified to the standard deviation of each Fourier component derived from the 11 measurements. For the sake of comparison with the other instrumental modes, we only show the Fourier components computed for the emitted frequencies, even for the chirp mode spectrum that is obtained using an FFT.

For frequency ranges encompassing the resonant signature of the spectra, we find both small uncertainties (i.e., a small standard deviation) and identical spectra (both in amplitude and in phase) for the three investigated

instrumental modes. In particular, for such frequency ranges (e.g., for the range 1 MHz to 4 MHz), we find discrepancies up to 2.15 dB (resp. 1.5 dB) in amplitude and 0.57 rad (resp. 0.42 rad) in phase for chirp (resp. multi-spectral) measurements. Larger discrepancies are found, instead, for frequencies outside the resonant regions.

We note that the measurements' uncertainty is larger for the chirp and multi-spectral modes than for the frequency sweep mode. Indeed, the experimental system noise affects the measurements differently, depending on the instrumental mode. Noise affects frequency sweep and multi-spectral measurements when spurious electric oscillations at a given frequency and with sufficiently large amplitude are present in the plasma, while that same frequency is emitted by the instrument. For the multi-spectral mode, the same perturbations experienced by frequency sweep measurements generates a signal-to-noise ratio nine times smaller because the emission amplitude itself is nine times smaller (see Section 2.3). Chirp measurements, instead, are affected by noise when spurious oscillations perturb the probed plasma during the measurement, whenever during the entire measurement and not only when the corresponding frequency is being emitted. As a consequence, noise perturbations are more likely to affect chirp than frequency sweep measurements.

We note that the MI spectra uncertainties found experimentally significantly exceed the typical 1 dB uncertainty expected for MI measurements performed in space. Such uncertainties are due to the vicinity to the MI antennas of the vacuum chamber and plasma source, that affect the measurements with their presence. Smaller uncertainties, of the order of 1 dB for the frequency sweep measurements, are expected in space.

For both our numerical and experiment investigations, we have shown that the MI spectra obtained for the new MI instrumental modes are almost identical to the reference frequency sweep measurements. We have therefore decided to compare directly the different measured spectra, instead of the physical parameters derived from each spectrum. The identification of physical plasma parameters (i.e., the plasma density and electron temperature) from the MI spectra in the case of frequency sweep measurements is out of the scope of this paper, as it has been already described in previous papers (Bahnsen et al., 1988; Béghin, 1995; Béghin & Debrie, 1972; J. Chasseriaux et al., 1972; J. M. Chasseriaux, 1972; J. M. Chasseriaux, 1974; Décréau et al., 1978; Geiswiller et al., 2001; Gilet et al., 2017; Grard, 1997; Pottelette et al., 1975; Pottelette & Storey, 1981; Rooy et al., 1972; Storey et al., 1969; Wattieaux, G. et al., 2019). Our current study shows that this instrumental theory can directly be used to also provide plasma parameters from MI spectra obtained from both the multi-spectral and the chirp instrumental modes.

4.3. Difference Between Numerical and Experimental Chirp Measurements

In the previous section, we have compared the new MI chirp and multi-spectral measurements to the nominal frequency sweep measurements in order to assess the impact of short emission durations on the MI plasma diagnostic. We have found that chirp and multi-spectral measurements are very similar (see Section 4) to frequency sweep measurements. To achieve such results, we had to introduce for the numerical tests of the chirp mode a window function (i.e., Hann) in the procedure. In this section, we explain why such windowing is needed for the numerical investigation of the chirp mode while it is not for its experimental counterpart.

Examples of emitted (black line) and received (green line) electric potential signals corresponding to both numerical (top panel) or experimental (bottom panel) chirp measurements are shown in Figure 4.

Both in simulations (top panel) and in the plasma chamber (bottom panel), the emission process triggers oscillations of the plasma at the emitted frequencies. For emitted signals at frequencies far from the resonant frequency of the system (i.e., the plasma frequency) the plasma reacts with small oscillation amplitudes at those frequencies, as expected. In particular, the high frequencies emitted at time 220 ω_p^{-1} (top panel) and time 105 μs (bottom panel) correspond to received electric potential oscillations associated to negligible amplitudes. This is consistent with the strong Landau damping expected at these frequencies, so that the signal cannot propagate for long. For emitted signals at frequencies close to the plasma frequency, the amplitude of the oscillations increases as the plasma resonates, as expected. This is observed at time 150 ω_p^{-1} (top panel) and time 97 μs (bottom panel). However, after the resonance is triggered, two different features are observed for the numerical and experimental investigation. Numerical tests suggest that oscillations at the plasma frequency do not disappear from the received electric signal even after the emission process stops (i.e., after time $t = 225\ \omega_p^{-1}$, top panel). This is consistent with the fact that (a) the Landau damping of Langmuir waves is negligible at the plasma frequency and (b) the group velocity of Langmuir waves vanishes at the plasma frequency. Therefore, the oscillation at the plasma

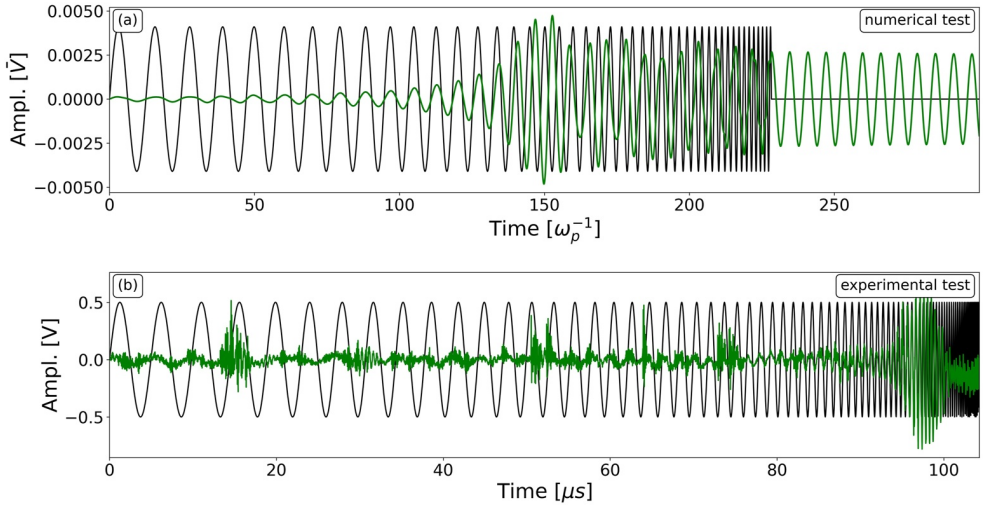

Figure 4. Example of numerical and experimental chirp measurements. The amplitude of emitted (black line) and received (green line) electric signals is represented in function of time. Panel (a) (resp. Panel (b)) represents the signals obtained numerically (resp. experimentally).

frequency is indeed expected to remain observable at the instrument location. Experimental tests, instead, show that oscillations at the plasma frequency are not measured for long after they are triggered. In particular, between 98 and 100 μs in Figure 4 (bottom panel) the plasma does not oscillate at the resonant frequency registered at 97 μs. Instead, it is synchronized with the emission. Note that, in this analysis, we neglect the plasma fluctuations at high frequencies (e.g., 105 μs) and we only focus on plasma fluctuations that oscillate at the resonant frequency (i.e., at about 97 μs). The reason behind such choice is that both the plasma density and the electron temperature are derived from the resonance of MI spectra. Hence, the resonance is the only signature of MI measurements that is of interest in this investigation. Since the chirp analysis is performed on the electric potential oscillations measured synchronously to the emission, the total analyzed signal is quasi-periodic only in the experimental case and not in the numerical case. Some apodization procedure is therefore required in the numerical case. For consistency with the frequency sweep and multi-spectral mode, before building the chirp spectra from Figure 2 we used a Hann window to filter the electric oscillations retrieved by the chirp reception.Let us now investigate the possible reasons for such different behavior observed with numerical and experimental chirp measurements.

First, the numerical model assumes a collisionless plasma. Is the plasma in the chamber collisional in the regions close to the antennas? If that is the case, the resonant plasma oscillations would be damped by electron-neutral collisions with a damping rate corresponding to the electron-neutral collision frequency. This could explain why they are not observed for as long as our numerical investigation suggests.

We have computed the electron-neutral mean-free-path in the chamber to assess if the generated plasma is collisional. We obtain $l_{el} \simeq 500$ m, which is much larger than both the distance between the MI electric sensors (i.e., 0.3 m) and the Debye length (i.e., 0.008–0.023 m). Such mean free path of electron-neutral (Argon) collisions ($l_{el} = 1/(\sigma_{el} n_{Ar})$ was computed using the ambient pressure ($P_a \simeq 2.5 \times 10^{-3}$ Pa) measured in the chamber during the experimental tests, the ambient temperature ($T \simeq 300$ K), the neutral Argon density $n_{Ar} = P_a/(k_B T)$, the elastic electron-neutral collision cross-section ($\sigma_{el} = 3 \times 10^{-21}$ m^2 (Gargioni & Grosswendt, 2008)) and the thermal velocity of electrons ($v_{the} = 300$ km/s). Therefore, the plasma in the chamber is confirmed to be collisionless, and collisions cannot explain the disappearance of the resonant oscillations from the received signal in the experimental tests.

Second, the numerical model assumes a non-drifting plasma while the plasma in the chamber is actually drifting from the plasma source, at velocity v_D of about (1–15) km/s (Appendix A). Is this drift velocity large enough to enable the oscillating plasma to drift away from MI antennas over a characteristic time that is negligible compared to chirp measurement durations? For convenience, let us assume that the plasma drifts along the chamber with constant velocity $v_D = 15$ km/s. Since the chamber measures 1.8 m, over a characteristic travel time $t_{tr.} = 1.8$ m/$v_D = 120$ μs the plasma travels along its whole length, from the plasma source to the back wall of the chamber.

Considering that MI antennas are placed in the middle of the chamber, the plasma drifts away from them in about $t_{tr.}/2 = 60$ µs. This characteristic time is not negligible with respect to chirp measurement durations, which in our investigation amounts to about 100 µs. Therefore, the drift velocity in the chamber is not fast enough to explain the disappearance of resonant oscillations from the experimental chirp measurements.

We note that the magnetic field compensation system reduces the magnetic field amplitude at the position of the plasma probed by the antennas (Section 3.2). Therefore, the gyration of particles can be neglected in this study and the magnetic field cannot explain the difference between numerical and experimental measurements.

Since, for the experimental tests, our two hypotheses can not explain the disappearance of plasma frequency oscillations from the retrieved electric potential measurements, this discussion remains open. To date, we have no robust explanation for this observed discrepancy between numerical and experimental chirp measurements. Since it seems to be related to the presence of the testing facility and its effects on MI measurements, we leave the resolution of this discrepancy to future space measurements using the newly designed chirp mode.

4.4. Computing Resources Evaluation for Frequency Sweep, Chirp and Multi-Spectral Measurements

In the previous sections, we have compared, using numerical and experimental approaches, MI measurements performed following the frequency sweep, chirp and multi-spectral procedures. In this section, we take a practical (instrumental) point of view and compare the amount of onboard computations that would be required for these three modes. The onboard calculator is identified to be the critical function, to discriminate the three modes in terms of electric power consumption. For this reason, we quantify and compare the amount of arithmetical operations needed by each mode to produce a single MI measurement. This is directly proportional to the power required by the onboard computer to perform the measurement. We note that the purpose of this section is only to provide a reference value of the computing resources (thus the power consumption) of the three MI instrumental modes. More precise estimates require the exact definition of the algorithms used to build the MI spectra, which depend on the particular space application of interest and are out of the scope of this paper.

We assume that the received signal is sampled using the same sampling frequency f_s for the three modes. Such frequency is chosen equal to the Nyquist frequency of the investigated frequency range (i.e., $f_s = 2 f_{\max}$).

For the frequency sweep mode, each frequency f_i with $i = 0, \ldots j-1$ is emitted for the emission duration $T_i = N/f_i$ with $N = 20$. The electric fluctuations generated in the plasma by the emission of frequency f_i are retrieved by means of the receiving antennas and converted by the Analog-to-Digital Converter (ADC) to a digital signal composed of $T_i f_s$ points. The Fourier component of f_i is computed from this digital signal using a DFT technique, resulting in $T_i f_s$ multiplications. The total amount of multiplications performed by the onboard computer to produce one frequency sweep measurement is obtained as the sum of the contributions of all the emitted frequencies, corresponding to $\sum_{i=0}^{j-1} T_i f_s = N f_s \sum_{i=0}^{j-1} 1/f_i$.

For the chirp mode, each frequency f_i is emitted for the duration $T_i = 1/f_i$. The corresponding electric fluctuations triggered in the plasma are retrieved by the receiving antennas and converted to a signal composed of $f_s \sum_{i=0}^{j-1} T_i$ points. Since for this mode we use the FFT technique to build the spectra, the required amount of multiplications scales as $x \log_2(x)$, with x the amount of points in the received signal. Therefore, the amount of onboard computations expected for the chirp mode is $\left(f_s \sum_{i=0}^{j-1} T_i\right)\log_2\left(f_s \sum_{i=0}^{j-1} T_i\right) = \left(f_s \sum_{i=0}^{j-1} 1/f_i\right)\log_2\left(f_s \sum_{i=0}^{j-1} 1/f_i\right)$.

For the multi-spectral mode, frequencies emitted simultaneously have the same emission duration. Considering the total amount of emissions p needed to perform one measurement, for the i-th emission the frequencies $f_{k,i} = f_{\min}(1+\Delta)^{y\ \ k+p_1+p_2}$ (with $k = 0, \ldots, 8$) are emitted for the duration $T_i = N/f_{0,i}$ with $N = 20$. For those frequencies, the received electric fluctuations are converted to a signal of $T_i f_s$ points and the Fourier components are computed using DFTs. As a result, for each of those frequencies the onboard computer executes $T_i f_s$ multiplications. We note that only the frequencies $f_{0,i}$ are emitted for the same duration in the case of both multi-spectral and frequency sweep measurements. All other frequencies have longer durations in the multi-spectral case. Therefore, multi-spectral measurements require more onboard computations than frequency sweep measurements. The total amount of multiplications required to perform one measurement using this technique is $\sum_{i=0}^{p-1} 9 T_i f_s = 9 f_s \sum_{i=0}^{p-1} 1/f_i$, with $p = j$ div 9 if the amount of emitted frequencies (j) is a multiple of 9 (i.e., the amount of simultaneously emitted frequencies), $p = j$ div $9 + j$ mod 9 if not.

To compare the three instrumental modes in terms of duration and computing resources, we consider a practical case where the frequency range of interest is (10 kHz, $f_{\max}$), and we compute both the measurement duration and

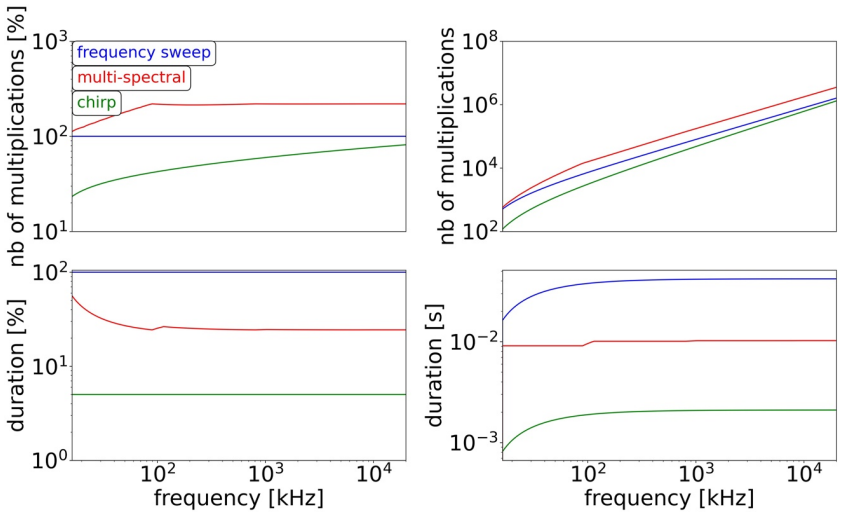

Figure 5. Comparison between software occupation (costs) and sensors occupation time (measurement duration) of the chirp (green lines) and multi-spectral (red lines) modes with respect to the frequency sweep mode (dashed blue line) which is used as reference. Top panels: cost of one mutual impedance measurement in terms of number of multiplications performed by the onboard computer to build one spectrum. The cost is represented in function of the maximum emitted frequency, considering a minimum investigated frequency of 10 kHz and a frequency resolution $\Delta = 0.05$. Bottom panels: MI measurement duration corresponding to the costs of top panel. Left panels illustrate the cost and duration of the three modes normalized to the corresponding frequency sweep curves.

the associated amount of computations as a function of the upper frequency range f_{max}. This is performed with same fixed resolution $\Delta = 0.05$. We show in Figure 5 the cost profile (top panels) and measurement duration (bottom panels) of the new MI instrumental modes in function of the maximum emitted frequency, computed as described above. Costs and duration are illustrated for the chirp (green line) and multi-spectral (red line) modes with respect to the reference cost and duration of the frequency sweep mode (blue dashed line). Both left and right panels represent the same cost and duration curves for the three MI instrumental modes. But, to better highlight the difference of chirp and multi-spectral performances with respect to the frequency sweep mode, the left panels are normalized to the frequency sweep performances.

In Table 2, we list the costs and measurement durations for the frequency sweep, chirp and multi-spectral measurements considering a fixed frequency range (10 kHz, 20 MHz) that is a typical range for ionospheric MI space applications.

Figure 5 and Table 2 show that multi-spectral measurements are up to 4 times faster than frequency sweep measurements, but they require at least twice the amount of operations (i.e., more multiplications) to be performed by the onboard computer. Chirp measurements, instead, are found to be both up to 20 times faster and less demanding (20% less) than frequency sweep and multi-spectral measurements.

Table 2
Comparison of Cost and Duration of the Three Investigated MI Instrumental Modes Considering the Frequency Range (10 kHz, 20 MHz) and the Frequency Resolution $\Delta = 0.05$

Mode	Cost [# of multiplications]	Duration [s]
Frequency sweep	1 6,15 ,868	0.042
Multi-spectral	3 5,41 ,191	0.010
Chirp	1 3,17 ,090	0.002

5. Distinction Between Numerical and Experimental Investigations

In the previous sections, we investigated new MI instrumental modes both numerically and experimentally. For this purpose, we obtained numerical (Figure 2) and experimental (Figure 3) spectra for the frequency sweep, multi-spectral and chirp modes. By comparing such spectra, we note significant differences between theoretical and experimental measurements. Such differences are expected, since the conditions simulated by our numerical model differ considerably from the conditions characterizing our experimental tests.

First, our numerical simulations use periodic boundary conditions in space, while our experimental tests are confined by the plasma chamber. Separate numerical tests performed using the DSCD numerical code (Geiswiller et al., 2001; Wattieaux, G. et al., 2019) show that the presence of the conductive plasma chamber near the MI antennas significantly impacts the measurements.

Second, numerical tests simulate MI measurements in the presence of a steady homogeneous plasma while the plasma within the chamber is an inhomogeneous (Appendix A) drifting (Section 4.3) plasma.

Third, numerical tests assume point emitting antennas as source of the MI emission, while for the experimental tests we use finite size antennas, not negligible with respect to the characteristic length (i.e., Debye length) of the plasma (Section 3.2).

We remind that the goal of our numerical investigation is to enable a comparison of the three MI instrumental modes in a simplified 1D symmetric homogeneous configuration, that aims at providing a physical understanding of the plasma response to MI measurements. Our experimental results, instead, are obtained from a realistic laboratory plasma and, therefore, are directly representative of MI measurements performed in space.

6. Discussion and Conclusions

In order to improve the time resolution of MI experiments, we have defined two new MI instrumental modes called the chirp (Section 2.2) and the multi-spectral modes (Section 2.3). These modes will have a direct application to all the missions where antenna sharing between MI experiments and different experiments occurs, for example, to answer the need for mass and volume minimization onboard nanosatellites. Such new modes are compared numerically and experimentally to the nominal MI instrumental mode, called frequency sweep mode (Section 2.1).

On the one hand, from a plasma diagnostic point of view, we find in our numerical model that chirp and multi-spectral measurements reproduce frequency sweep measurements with negligible amplitude and phase differences. We confirm the results of our model experimentally, as we find that the differences between chirp or multi-spectral measurements and frequency sweep measurements are negligible (i.e., of the order of noise level) for frequencies close to the plasma frequency. Plasma density and electron temperature are directly identified from the analysis of the resonant signature of the spectra, we therefore conclude that these new chirp and multi-spectral modes will have diagnostic performances identical to those of the (reference) frequency sweep mode.

On the other hand, from an instrumental point of view, we focused on both the onboard computation needs, associated to the instrument power consumption, and the time duration of the measurements, associated to the electric sensor occupation.

First, we have shown that multi-spectral measurements require a significantly larger amount of onboard computations (up to 220%) while chirp measurements are significantly less demanding (about 81%) than frequency sweep measurements. The instrument energy consumption strongly depends on the onboard computer energy consumption itself, which is directly related to the amount of onboard computation operations to be performed.

Second, we have shown that both multi-spectral and chirp modes enable to significantly reduce the sensor occupation with respect to the reference frequency sweep mode. Under realistic instrumental assumptions, when performing one single measurement, the multi-spectral mode decreases the antenna occupation by a factor of 5, while the chirp mode decreases it by a factor 20. This means that the time resolution of MI measurements of plasma density and electron temperature will significantly improve (respectively by a factor of 5 or 20) with these new modes.

The associated smaller measurement durations come at the cost of lower signal-to-noise ratios, especially far from the resonance. The newly designed modes should therefore be preferred to the standard frequency sweep mode in cold, dense plasma (i.e., plasmas characterized by a Debye length much smaller than the emitter-receiver distance), where the signal-to-noise ratios of MI measurements is high. However, we warn that the additional noise introduced by these new modes might affect both the electron density and temper-

ature diagnostic performance when the signal-to-noise ratios of MI measurements is low, for example, in low density and/or high temperature plasmas where the Debye length is of the order of the emitter-receiver distance. The MI electron density and temperature diagnostic performance using these new modes might also be affected in the case of multiple electron populations. Past studies (Gilet et al., 2017; Wattieaux et al., 2020) showed that multiple peaks can be found in the resonant signature of MI spectra for plasmas with multiple electron populations. If the spectral noise is significant, single MI measurements with spurious noisy maxima might then be mistaken as a signature of multiple electron populations. If such situations appear, a mitigation solution is to make use of the higher time resolution obtained with these new modes to acquire more measurements, and therefore more statistics to disentangle noise from signal. The modeling of MI spectra in the presence of non-Maxwellian electron distribution functions has been performed successfully in the past (Gilet et al., 2017; Gilet et al., 2019; Wattieaux et al., 2019) for the frequency sweep mode, and our study suggests that the MI spectra will remain unchanged with the newly designed chirp and multi-spectral modes. However, the diagnostic performance of the newly designed chirp and multi-spectral modes in non-Maxwellian plasmas remains out of the scope of this present study and is left for future investigations.

The chirp mode enables to both decrease instrument power consumption, while increasing time resolution and/or reducing at the same time the occupation of a shared sensor, with diagnostic performance almost identical to those obtained with the MI modes used in past space missions. Therefore, all things considered, we conclude that the chirp mode would be the MI instrumental mode to be favored in future space missions.

Appendix A: Properties of the Plasma Generated in the Testing Facility of LPC2E

In this section, we describe the properties of the plasma generated in the testing facility of LPC2E.

Prior to performing our experimental tests, the properties of the plasma injected in the LPC2E vacuum chamber have been investigated with characterization tests. Hereafter, we discuss (a) the stability and (b) the dependency of the plasma parameters on the axial and radial position of the instruments in the chamber. Then, we (c) give the range of drifting velocities found for the plasma inside the chamber.

For these purposes, we use two Langmuir Probes to measure the plasma density and electron temperature inside the chamber. The probes have spherical tips and the sensor's diameter is 0.05 m. The first probe has a fixed boom supporting the sensor and is placed on the axis of the chamber, at about 1.3 m from the source. The second probe has the sensor attached to a flexible support and is installed on a moving device at about 1 m from the plasma source. The moving device is used to shift and rotate the sensor, therefore enabling measurements at different positions in the chamber for the same plasma flow.

The stability of the plasma is investigated by monitoring its properties while modifying them. This is achieved by performing Langmuir Probe measurements right after the electric settings of the plasma source have been modified. The measurements show that, initially, the plasma parameters undergo significant variations. Then, after a given delay, the plasma flow reaches steady state conditions and the parameters become almost fixed. From that instant on, the plasma is stable and MI experiments can be performed. Our tests show that the plasma is stable after a delay of about 30 s. Afterward, the plasma parameters fluctuate around a given value with variations of the order of 2%. As such variations are lower than the typical resolution of MI measurements, it is acceptable to ignore these fluctuations.

The homogeneity of the plasma is investigated by performing Langmuir Probe measurements at different spatial positions in the chamber. This is done by translating and rotating the second Langmuir probe, while keeping the plasma stable. These measurements show the presence of plasma density and electron temperature inhomogeneities in the chamber. In particular, the density (resp. temperature) decreases by a factor 10 (resp. 5) along 46 cm. For a fixed distance from the plasma source, the plasma density is found to be quasi-homogeneous. Therefore, by placing the MI antennas at a fixed distance from the plasma source, the effects of plasma inhomogeneities on MI measurement are neglected in our analysis.

The plasma is generated and injected in the chamber by a Kaufman (Kaufman et al., 1982) electric source which, first, ionizes the inlet neutral Argon gas, second, accelerates with a given electric field its positive ion particles

and, third, neutralizes the flow of ions. It results that the plasma injected in the chamber drifts with a certain drift velocity. Hereafter, we describe the two approaches we used to estimate such velocity.

First, we identify the drift velocity from the electrostatic acceleration of the positive Argon ions at the plasma source. As a first (simplified) estimate, we find that the ions (thus the plasma) drifts in the chamber with drift velocity $v_{D,1} \simeq 15$ km/s, considering the accelerating potential $V_A = 20$ V and the positive Argon ion (Ar^+) mass $m_{Ar} = 3.01 \times 10^{-26}$ kg.

Second, we derive the drift velocity of the plasma flow from Langmuir Probe measurements. To do so, we focus on the ion saturation part of the I-V curve and assume that (i) the ion thermal velocity is negligible with respect to the drift velocity and (ii) the plasma in the chamber is quasi-neutral (i.e., $n_i = n_e$, with n_e the electron density measured by the Langmuir Probe). Then, following the procedure described in Odelstad et al. (2018) (Equation 7), we identify the ion drift velocity from the slope of the ion current. Such relation reads:

$$\frac{\partial I}{\partial V} = \frac{Aq^2 n_i}{2m_i} \frac{\sqrt{(8k_B T_i)/(\pi m_i) + v_D^2}}{(2k_B T_i)/(m_i) + v_D^2} \tag{A1}$$

where I is the ion saturation current, V is the electric potential, $A = 4\pi r^2$ is the surface of the Langmuir Probe, $q = e$ and $m_i = m_{Ar}$ are the charge and mass of the Ar^+ and T_i is the ion temperature. By fitting the equation above to different Langmuir probe data, we find drift velocities in the range $v_{D,2} = 1$–12.5 km/s.

All in all, the two independent estimates agree. Therefore, we consider that the plasma in the chamber drifts with velocity in the range 1–15 km/s, where 15 km/s is to be considered its upper theoretical limit (given V_A).

Appendix B: Setting Parameters for Our Numerical Simulations

In Table B1 we list the setting parameters defining our numerical simulations.

FS, MS, and CH refer to Frequency Sweep, Multi-Spectral and CHirp instrumental modes, respectively. As discussed in Section 4.3, to obtain one measurement for the frequency sweep and multi-spectral modes multiple runs (i.e., 39 and 6 runs, respectively) were needed. For the chirp mode only one run was performed. Since to the different runs of the same instrumental measurement corresponds the same perturbed plasma, we simplified Table B1 by only giving for each measurement the details of the simulations related to the first and last emitted frequencies. The details regarding the remaining simulations can be extrapolated from Table B1 by using the frequency resolution of the measurements (last column).

Table B1
List of Parameters Used to Set Our Numerical Simulations: Total Length of the Simulation Box (X_{max}), Absolute Value of Maximum and Minimum Frequency of the Velocity Range for the Electron Distribution Function ($V_{max,e}$), Amount of Spatial Mesh Points (n_x), Amount of Velocity Mesh Points for Electrons (n_{ve}), Advancement Time Resolution of the Simulation (dt), Emission Frequency (ω), Oscillating Charges at the Antenna (σ), Ion-To-Electron Mass Ratio (m_i/m_e), Ion-To-Electron Temperature Ratio (T_i/T_e), Frequency Sweep Resolution (f_{n+1}/f_n)

Name	$X_{\max}[\lambda_D]$	$v_{\max,e}[v_{the}]$	n_x	n_{v_e}	Dt $[\omega_p^{-1}]$	$\omega[\omega_p]$	$\sigma[\bar{\sigma}]$	$\frac{f_{n+1}}{f_n}$
FS_01	4,000	10	8,192	101	1e−3	0.5	1e−5	1.05
FS_39	4,000	10	8,192	101	1e−3	0.5	1e−5	1.05
MS_01	4,000	10	8,192	101	1e−3	0.5	1e−5	1.05
MS_06	4,000	10	8,192	101	1e−3	0.5	1e−5	1.05
CH_01	4,000	10	8,192	101	1e−3	0.5–5	1e−5	1.05

Data Availability Statement

Datasets for this research are available at Bucciantini (2022), together with a detailed explanation on how to use them.

The model used for the production of such dataset is described in Section 3.1. It is based on the model implemented by Mangeney et al. (2002). The 1D-1V Vlasov-Poisson version of the model, which corresponds to the one we use in our investigation, is described in Henri et al. (2010).

Acknowledgments

The work performed at LPC2E is supported by CNES APR. We benefited from the computing resources provided by CaSciModOT. This work was granted access to the HPC/AI resources of TGCC under the allocation 2021-A0100412428 made by GENCI. L.B. was supported by funds from Région Centre Val de Loire (France).

We thank E. Odelstad for the support he provided for the identification of the plasma drift velocity in the chamber.

References

Bahnsen, A., Jespersen, M., Ungstrup, E., Pottelette, R., Malingre, M., Decreau, P., et al. (1988). First VIKING results: High frequency waves. *Physica Scripta*, *37*(3), 469–474. https://doi.org/10.1088/0031-8949/37/3/032

Béghin, C. (1995). Series expansion of electrostatic potential radiated by a point source in isotropic Maxwellian plasma. *Radio Science*, *30*(2), 307–322. https://doi.org/10.1029/94RS03167

Béghin, C., & Debrie, R. (1972). Characteristics of the electric field far from and close to a radiating antenna around the lower hybrid resonance in the ionospheric plasma. *Journal of Plasma Physics*, *8*(3), 287–310. https://doi.org/10.1017/S0022377800007157

Béghin, C., Karczewski, J. F., Poirier, B., Debrie, R., & Masevich, N. (1982). The ARCAD-3 ISOPROBE experiment for high time resolution thermal plasma measurements. *Annales de Geophysique*, *38*(5), 615–629.

Bucciantini, L. (2022). nov) New high time resolution mutual impedance measurements. *Zenodo*. https://doi.org/10.5281/zenodo.7278491

Bucciantini, L., Henri, P., Wattieaux, G., Califano, F., Vallières, X., & Randriamboarison, O. (2022). In situ space plasma diagnostics with finite amplitude active electric experiments: Non-linear plasma effects and instrumental performance of mutual impedance experiments. *JGR: Space Physics*, *127*(12). https://doi.org/10.1029/2022ja030813

Chasseriaux, J., Debrie, R., & Renard, C. (1972). Electron density and temperature measurements in the lower ionosphere as deduced from the warm plasma theory of the h.f. quadrupole probe. *Journal of Plasma Physics*, *8*(2), 231–253. https://doi.org/10.1017/S0022377800007108

Chasseriaux, J. M. (1972). Potential set up by a point charge oscillating in magnitude in an inhomogeneous plasma. *Plasma Physics*, *14*(8), 763–781. https://doi.org/10.1088/0032-1028/14/8/002

Chasseriaux, J. M. (1974). Excitation of the plasma and upper hybrid resonances in a warm magnetoplasma by an alternating electric dipole. *Journal of Plasma Physics*, *11*(2), 225–252. https://doi.org/10.1017/S0022377800024624

Décréau, P. M. E., Beghin, C., & Parrot, M. (1978). Electron density and temperature, as measured by the mutual impedance experiment on board GEOS-1 (Article published in the special issues: Advances in Magnetospheric Physics with GEOS- 1 and ISEE - 1 and 2. *Space Science Reviews*, *22*(5), 581–595. https://doi.org/10.1007/BF00223942

Gargioni, E., & Grosswendt, B. (2008). Electron scattering from argon: Data evaluation and consistency. *Reviews of Modern Physics*, *80*(2), 451–480. https://doi.org/10.1103/RevModPhys.80.451

Geiswiller, J., Béghin, C., Kolesnikova, E., Lagoutte, D., Michau, J. L., & Trotignon, J. G. (2001). Rosetta spacecraft influence on the mutual impedance probe frequency response in the long Debye length mode. *Planetary and Space Science*, *49*(6), 633–644. https://doi.org/10.1016/S0032-0633(00)00173-2

Gilet, N., Henri, P., Wattieaux, G., Cilibrasi, M., & Béghin, C. (2017). Electrostatic potential radiated by a pulsating charge in a two-electron temperature plasma. *Radio Science*, *52*(11), 1432–1448. https://doi.org/10.1002/2017RS006294

Gilet, N., Henri, P., Wattieaux, G., Myllys, M., Randriamboarison, O., Béghin, C., & Rauch, J.-L. (2019). Mutual impedance probe in collisionless unmagnetized plasmas with suprathermal electrons—Application to BepiColombo. *Frontiers in Astronomy and Space Sciences*, *6*. https://doi.org/10.3389/fspas.2019.00016

Grard, R. (1969). Coupling between two electric aerials in a warm plasma. *Alta Frequency*, *38*, 97–101.

Grard, R. (1997). Influence of suprathermal electrons upon the transfer impedance of a quadrupolar probe in a plasma. *Radio Science*, *32*(3), 1091–1100. https://doi.org/10.1029/97RS00254

Henri, P., Califano, F., Briand, C., & Mangeney, A. (2010). Vlasov-Poisson simulations of electrostatic parametric instability for localized Langmuir wave packets in the solar wind. *Journal of Geophysical Research*, *115*(A6), A06106. https://doi.org/10.1029/2009JA014969

Kasaba, Y., Kojima, H., Moncuquet, M., Wahlund, J., Yagitani, S., Sahraoui, F., et al. (2020). Plasma wave investigation (PWI) aboard Bepi-Colombo mio on the trip to the first measurement of electric fields, electromagnetic waves, and radio waves around mercury. *Space Science Reviews*, *216*(65), 65. https://doi.org/10.1007/s11214-020-00692-9

Kaufman, H. R., Cuomo, J. J., & Harper, J. M. E. (1982). Technology and applications of broad-beam ion sources used in sputtering. part i. ion source technology. *Journal of Vacuum Science and Technology*, *21*(3), 725–736. https://doi.org/10.1116/1.571819

Mangeney, A., Califano, F., Cavazzoni, C., & Travnicek, P. (2002). A numerical scheme for the integration of the Vlasov-Maxwell system of equations. *Journal of Computational Physics*, *179*(2), 495–538. https://doi.org/10.1006/jcph.2002.7071

Odelstad, E., Eriksson, A. I., Johansson, F. L., Vigren, E., Henri, P., Gilet, N., et al. (2018). Ion velocity and electron temperature inside and around the diamagnetic cavity of comet 67P. *Journal of Geophysical Research: Space Physics*, *123*(7), 5870–5893. https://doi.org/10.1029/2018JA025542

Pottelette, R., Rooy, B., & Fiala, V. (1975). Theory of the mutual impedance of two small dipoles in a warm isotropic plasma. *Journal of Plasma Physics*, *14*(2), 209–243. https://doi.org/10.1017/S0022377800009533

Pottelette, R., & Storey, L. R. O. (1981). Active and passive methods for the study of non-equilibrium plasmas using electrostatic waves. *Journal of Plasma Physics*, *25*(2), 323–350. https://doi.org/10.1017/S0022377800023151

Ranvier, S., Anciaux, M., De Keyser, J., Pieroux, D., Baker, N., & Lebreton, J.-P. (2019). Slp: The sweeping Langmuir probe instrument to monitor the upper ionosphere on board the PICASSO nano-satellite.

Retinò, A., Khotyaintsev, Y., Le Contel, O., Marcucci, M. F., Plaschke, F., Vaivads, A., et al. (2021). Particle energization in space plasmas: Towards a multi-point, multi-scale plasma observatory. *Experimental Astronomy*. https://doi.org/10.1007/s10686-021-09797-7

Rooy, B., Feix, M. R., & Storey, L. R. O. (1972). Theory of a quadripolar probe for a hot isotropic plasma. *Plasma Physics*, *14*(3), 275–300. https://doi.org/10.1088/0032-1028/14/3/005

Snodgrass, C., & Jones, G. H. (2019). The European Space Agency's Comet interceptor lies in wait. *Nature Communications*, *10*(5418), 5418. https://doi.org/10.1038/s41467-019-13470-1

Storey, L., Aubry, L., & Meyer, P. (1969). Mutual impedance techniques for space plasma measurements. *Measurement techniques in space plasmas - Fields Geophysical Monograph Series*, *103*, 155–160. https://doi.org/10.1029/GM103p0155

Trotignon, J., Béghin, C., Lagoutte, D., Michau, J., Matsumoto, H., Kojima, H., et al. (2006). Active measurement of the thermal electron density and temperature on the mercury magnetospheric orbiter of the BepiColombo mission. *Advances in Space Research*, *38*(4), 686–692. https://doi.org/10.1016/j.asr.2006.03.031

Trotignon, J., Michau, J. L., Lagoutte, D., Chabassière, M., Chalumeau, G., Colin, F., et al. (2007). RPC-MIP: The mutual impedance probe of the rosetta plasma consortium. *Space Science Reviews*, *128*(1–4), 713–728. https://doi.org/10.1007/s11214-006-9005-1

Wattieaux, G., Gilet, N., Henri, P., Vallières, X., & Bucciantini, L. (2019). Rpc-mip observations at comet 67P/Churyumov-Gerasimenko explained by a model including a sheath and two populations of electrons. *Astronomy & Astrophysics*, *630*, A41. https://doi.org/10.1051/0004-6361/201834872

Wattieaux, G., Henri, P., Gilet, N., Vallières, X., & Deca, J. (2020). Plasma characterization at comet 67P between 2 and 4 au from the Sun with the RPC-MIP instrument. *Astronomy & Astrophysics*, *638*, A124. https://doi.org/10.1051/0004-6361/202037571

Appendices

Appendix A

My Contribution to Mutual Impedance Experiment

In all, this PhD document focuses on the work that I have performed to understand the impact that short booms and small platforms like nanosatellites have on MI experiments. To reach such goal, I have given my contribution to MI modeling both with numerical and experimental efforts.

Numerical contribution. I have modified an existing numerical tool to enable the numerical simulation of MI experiments (section 3.1) in the case of (i) non-linear perturbations of the plasma dielectric (section 4.1), (ii) inhomogeneous plasmas (section 4.2) and (iii) fast MI measurements (section 4.3). Such investigations, coupled with the results provided performing experimental tests (see below my contribution), are the subject of three publications (the accepted publication shown in section 6.1, the submitted publication shown in section 6.2 and the positively revised publication shown in section 6.3, respectively). Note that the modifications to the existing numerical model include (a) the addition of MI emitting antennas for different geometric configurations (section 3.1.2), (b) the validation of such emitting antennas for the different identified geometries (section 3.1.3), (c) the definition and implementation of specific initial conditions for minimizing transient effects (section 3.1), (d) the OpenMP parallelization of the numerical implementation of the model.

Experimental contribution. I have purchased, assembled, characterized, used and maintained the new plasma chamber of LPC2E space laboratory (section 3.2) to enable the experimental testing of MI experiments. In particular, I have followed the purchase of the vacuum chamber and its associated pumping system. I have installed the chamber, the pumping system and the plasma source at LPC2E French laboratory with the support of the LPC2E technical team. I have defined the safety procedures to be followed during the use of the plasma chamber[1]. I have purchased a commercial Langmuir Probe to have reference measurements of the parameters characterizing the plasma flow generated in the chamber by the source. I have performed a partial characterization of the plasma in the chamber. I have supervised student internships that aimed at extending such characterization. I have defined and documented[2] the procedures defining the new fast MI instrumental modes. I have tested such new procedures and, by doing so, I have validated on the ground the new fast MI modes.

Other contributions. In parallel to the work described in this PhD document, I have given my contribution to a variety of topics regarding MI experiments:

- I have started and animated a working group regarding the use of machine learning and deep learning algorithms for the automatic analysis of MI measurements. Such work has been of interest also to the analysis of measurements coming from other types of plasma diagnostic instruments, namely the WHISPER instrument onboard the ESA CLUSTER mission [Trotignon et al., 2003, Béghin et al., 2005, Trotignon et al., 2010]. The application of machine learning algorithms to the analysis of WHISPER measurements has led to the publication from Gilet et al. [2021] to which I

[1] The safety procedures have been documented by an intern student that I supervised.

[2] Such documents have been delivered to CNES by COMIX as one of the deliverable documents of the COMIX R&D project.

contributed as co-author.

- I have both (i) performed myself and (ii) supervised students performing SPIS numerical simulations to identify what plasma environment is expected to embed DFP-COMPLIMENT sensors for different antennas configurations onboard the mother satellite of the Comet Interceptor ESA mission. The outputs of such numerical simulations have been, among others, a motivating factor for the selection of the current DFP-COMPLIMENT antennas configuration. This work has been documented in a technical note delivered to ESA in the cotext of the Comet Interceptor mission.

- I have taken part in the experimental testing of the DFP-COMPLIMENT merged sensor [de Keyser et al., 2021] that will embark onboard Comet Interceptor. Such merged sensor consists of an outer spherical electric sensor that encapsulates a small magnetic sensor. The spherical sensor is used for performing both MI and Langmuir Probe measurements, while the encapsulated sensor is used for monitoring the magnetic field. This is the first time that electric and magnetic sensors are integrated in such a way onboard satellites. Hence, despite the high TRL of both the electric and magnetic sensors, experimental tests have been performed in the plasma chamber of LPC2E to ensure minimum electromagnetic perturbations (EMC) between the magnetic sensors generates on the MI measurements of DFP-COMPLIMENT. These experimental tests have been described in a deliverable document to ESA.

- I have performed preliminary SPIS simulations of the Mio spacecraft of BepiColombo to investigate to what floating electric potential the Mio spacecraft will charge during specific parts of its orbit around Mercury. Such preliminary simulations have been shown to the annual meeting of the SPIS community (SPINE) which was held at ESTEC (Noordwijk, Netherlands).

- During the early phases of my PhD, I have taken part to COMIX's technical definition of the characteristics of electric antennas adapted for both MI and Quasi-Thermal Noise experiments onboard nanosatellites. Such specifications have been used as input by an R&D project internal to CNES. Recently, CNES has sent COMIX an antennas prototype based on the specifications we provided and I have contributed to the preliminary tests of such prototypes.

- I have tested the demo of a UV emitting device with the intent of extending the equipment of LPC2E testing facility. Such devices can be used for generating photoelectron currents at the surface of electric antennas, similarly to the current emission processes observed in space. Tests in the plasma chamber have shown that the tested UV device produces a UV light that is not strong enough to trigger significant modifications of the floating potentials of the probes in the chamber. For this reason, the tested UV device was not purchased.

- I have performed SPIS simulations to investigate the optimum configuration for the Electrostatic Dust Analyzer (EDA) instrument [Wang et al., 2021]. Such instrument was proposed for the NASA DALI program to be included in the payload of a lunar rover. My numerical simulations helped to identify the impact that different configurations might have on EDA measurements.

- Before the beginning of my PhD study, I have performed SPIS numerical simulations of the RPC-MIP instrument onboard the Rosetta spacecraft to quantify the thickness of the plasma sheath expected around the electric sensors of the instrument for different phases of the Rosetta mission. The results of such analysis have been used by Wattieaux et al. [2019] for the identification of the electron temperature from the spectra of RPC-MIP.

- Prior to my PhD study, I have aslo worked for the production of a cross-calibrated cometary plasma density dataset, for the Rosetta archive, that aimed at increasing the time resolution of the mutual impedance RPC-MIP density measurements using the high time-resolution spacecraft potential measurements provided by the Langmuir Probe RPC-LAP [Eriksson et al., 2007]. I implemented a numerical code that automatically produced the RPC-MIP/LAP cross-calibrated dataset[3] for the whole Rosetta mission. In this context, I have given my contribution as co-author to a study investigating the properties of the singing comet waves observed in the coma of comet 67P/CG using this high time-resolution density dataset [Breuillard et al., 2019]. During my PhD, I have used this expertise to contribute and co-author to a study investigating the properties of the ion flow near the comet [Johansson et al., 2021] using, among other parameters, the cross-calibrated Rosetta densities that I produced before my PhD.

- The expertise I acquired on space plasma data calibration and cross-calibration have also allowed me to contribute to the Phase 0 study of the ESA mission DAEDALUS, for which I have defined the cross-calibrated data that DAEDALUS was able to produce, according to its scientific payload. My contribution has been the subject of a technical document delivered to ESA.

- As part of the RPC-MIP team, I have also contributed to the assessment of the cometary ionospheric Total Electron Content (TEC) observed in the surroundings of comet 67P/CG during the Rosetta mission. This has been the topic of the study from Hajra et al. [2020] to which I contributed as co-author.

[3]The RPC-MIP/LAP cross-calibrated dataset is available on the Planetary Science Archive.

Appendix B

Open Research

B.1 Dataset, Model and Colorbars

Datasets for this research are available at:

- Bucciantini [2022a] for the investigation of the impact of non-linear plasma interactions on MI diagnostic performances (section 4.1);
- *(This link will be generated after the first revision of the associated paper)* for the study of how the plasma sheath impacts MI measurements;
- Bucciantini [2022b] for the theoretical test and experimental validation of the new fast MI instrumental modes.

The model used for the production of such datasets is described in section 3.1.

The figures in this PhD work use a scientific colorbar developed by Crameri [2021], Crameri et al. [2020] to ensure that colors do not introduce a bias on the shown images.

B.2 Settings Defining the Numerical Runs

In this section, I list for repeatability purposes the settings that define the numerical runs performed to reach the objectives of this PhD work.

Settings: mutual impedance experiments for strong emission amplitudes

In Table B.1 and Table B.2 are listed for completeness and repeatability purposes the settings parameters that define the numerical runs discussed in section 4.1. Parameters from Table B.1 define the numerical simulations investigating what types of non-linear interactions are triggered by MI emissions (section 4.1.2). Parameters from Table B.2 define the numerical runs that are used for building MI spectra for strong emission amplitudes (section 4.1.2). LF (resp. SL) stands for Low Fixed (resp. Sweep Low) and it indicates simulations that investigate the plasma perturbations triggered by fixed frequencies (resp. frequency sweep) emission(s). NI (resp. SI) stands for Non-linear Ions (resp. Sweep Ions) and it indicates fixed (resp. sweep) emissions performed including the ion dynamics. NF stands for Non-linear Fixed and indicates the simulations that neglect the contribution of the motion of ions to the non-linear plasma interactions triggered by MI emissions.

MI measurements are simulated by separating the emission of different frequencies into different numerical runs. The numerical box of the different runs is defined by the same parameters settings. Hence, in Table B.2 I indicate for each measurement the settings associated to the runs corresponding to the first and last emitted frequencies. The settings regarding the remaining runs can be extrapolated using the resolution of the measurement (last column of Table B.2). For instance, SL_01 is the numerical

simulation that investigates the emission of the frequency $\omega_{SL,01} = 0.5\omega_p$. SL_48 investigates for the same MI measurement the emission of frequency $\omega_{SL48} = 4.95\omega_p$. The frequencies emitted in the numerical simulations going from SL_02 to SL_47 are to be derived using the relation $\omega_{n+1} = 1.05\omega_n$.

Settings: mutual impedance experiments in the presence of plasma inhomogeneities

The numerical runs investigating the impact of plasma inhomogeneities on MI measurements (section 4.2) simulate a plasma box of length $X_{max} = 4000\ \lambda_D$ and $n_x = 8192$ spatial grid points. The electron distribution function is assumed non-zero for the electron velocity v_e in the range ($-10\ v_{th,e}$, $10\ v_{th,e}$), refined with $n_v = 101$ velocity grid points. The time-step of the numerical runs is set to $dt = 10^{-3}\omega_p^{-1}$. The amplitude of the emitted signals is $\sigma = 10^{-5}\hat{\sigma}$ with $\hat{\sigma} = en_0\lambda_D$ the normalized amplitude of the charges at the emitting antennas. MI spectra are obtained for the frequency range ($0.5\ \omega_p$, $3.2\ \omega_p$) with frequency resolution of the measurements $\omega_{n+1}/\omega_n = 1.05$.

Settings: fast mutual impedance experiments

In Table B.3 are listed the setting parameters defining the numerical simulations that investigate the new fast MI instrumental modes (section 4.3). FS, MS and CH stand for Frequency Sweep, Multi-Spectral and CHirp instrumental modes, respectively. Each MI measurement is built using multiple numerical runs. As for the previous sections, I indicate for each MI measurement only the settings associated to the first and last emitted frequencies. The remaining settings can be extrapolated by considering the resolution of the measurement. Note that the chirp measurement (CH) is simulated using only one numerical run.

Table B.1: List of parameters associated to the numerical simulations investigating the non-linear plasma interactions triggered by strong emission amplitudes: total length of the simulation box (X_{max}), velocity range for the electron distribution function (V_e), velocity range for the ion distribution function (V_i), amount of spatial mesh points (n_x), amount of velocity mesh points for electrons ($n_{v,e}$), amount of velocity mesh points for ions ($n_{v,i}$), advancement time resolution of the simulation (dt), emission frequency (ω), oscillating charges at the antenna (σ), ion-to-electron mass ratio (m_i/m_e), ion-to-electron temperature ratio (T_{ion}/T_e), electric-to-thermal energy ratio ($E^2/(k_B T_e)$). M represents the antennas configuration (model) used for these simulations.

Name	M	X_{max} $[\lambda_D]$	V_{maxe} $[v_{th,e}]$	v_i $[v_{th,i}]$	n_x	$n_{v,e}$	$n_{v,i}$	dt $[\omega_p^{-1}]$	ω $[\omega_p]$	σ $[\bar{\sigma}]$	$\frac{m_i}{m_e}$	$\frac{T_{ion}}{T_e}$	$\frac{E^2}{k_B T_e}$
LF_01	A	1000	(-25,25)	(-25,25)	2048	601	601	1e-3	0.5	1e-5	inf	0.1	1e-10
LF_02	A	1000	(-25,25)	(-25,25)	2048	601	601	1e-3	1.1	1e-5	inf	0.1	1e-8
LF_03	A	1000	(-25,25)	(-25,25)	2048	601	601	1e-3	2.0	1e-5	inf	0.1	1e-10
NF_01	A	1000	(-25,25)	(-25,25)	2048	601	601	1e-3	0.5	0.1	inf	0.1	0.01
NF_02	A	1000	(-25,25)	(-25,25)	2048	601	601	1e-3	1.1	0.1	inf	0.1	0.33
NF_03	A	1000	(-25,25)	(-25,25)	2048	601	601	1e-3	2.0	0.1	inf	0.1	0.01
NI_01	A	1000	(-25,25)	(-25,25)	2048	601	601	1e-3	0.5	0.1	100	0.1	0.01
NI_02	A	1000	(-25,25)	(-25,25)	2048	601	601	1e-3	1.1	0.1	100	0.1	0.33
NI_03	A	1000	(-25,25)	(-25,25)	2048	601	601	1e-3	2.0	0.1	100	0.1	0.01

Table B.2: List of parameters associated to the numerical simulations investigating the impact of strong emission amplitudes on MI measurements: total length of the simulation box (X_{max}), velocity range for the electron distribution function (V_e), velocity range for the ion distribution function (V_i), amount of spatial mesh points (n_x), amount of velocity mesh points for electrons ($n_{v,e}$), amount of velocity mesh points for ions ($n_{v,i}$), advancement time resolution of the simulation (dt), emission frequency (ω), oscillating charges at the antenna (σ), ion-to-electron mass ratio (m_i/m_e), ion-to-electron temperature ratio (T_{ion}/T_e), frequency sweep resolution (ω_{n+1}/ω_n). M represents the antennas configuration (model) used for these simulations.

Name	M	X_{max}	V_{maxe}	v_i	n_x	$n_{v,e}$	$n_{v,i}$	dt	ω	σ	$\frac{m_i}{m_e}$	$\frac{T_{ion}}{T_e}$	$\frac{\omega_{n+1}}{\omega_n}$
		$[\lambda_D]$	$[v_{th,e}]$	$[v_{th,i}]$				$[\omega_p^{-1}]$	$[\omega_p]$	$[\bar{\sigma}]$			
SL_01	B	4000	(-25,25)	(-25,25)	8192	601	601	1e-3	0.5	1e-5	100	0.1	1.05
SL_48	B	4000	(-25,25)	(-25,25)	8192	601	601	1e-3	4.95	1e-5	100	0.1	1.05
SI1_01	B	4000	(-25,25)	(-25,25)	8192	601	601	1e-3	0.77	0.1	100	0.1	1.05
SI1_14	B	4000	(-25,25)	(-25,25)	8192	601	601	1e-3	1.53	0.1	100	0.1	1.05
SI2_01	B	4000	(-25,25)	(-25,25)	8192	601	601	1e-3	0.77	0.31	100	0.1	1.05
SI2_14	B	4000	(-25,25)	(-25,25)	8192	601	601	1e-3	1.53	0.31	100	0.1	1.05
SI3_01	B	4000	(-25,25)	(-25,25)	8192	601	601	1e-3	0.77	0.6	100	0.1	1.05
SI3_14	B	4000	(-25,25)	(-25,25)	8192	601	601	1e-3	1.53	0.6	100	0.1	1.05
SI4_01	B	4000	(-40,40)	(-25,25)	8192	1001	601	5e-4	0.77	1.0	100	0.1	1.05
SI4_14	B	4000	(-40,40)	(-25,25)	8192	1001	601	5e-4	1.53	1.0	100	0.1	1.05

Table B.3: List of parameters defining the numerical runs investigating the new fast MI instrumental modes: total length of the simulation box (X_{max}), absolute value of maximum and minimum frequency of the velocity range for the electron distribution function ($V_{max,e}$), amount of spatial mesh points (n_x), amount of velocity mesh points for electrons ($n_{v,e}$), advancement time resolution of the simulation (dt), emission frequency (ω), frequency sweep resolution (f_{n+1}/f_n).

Name	X_{max} $[\lambda_D]$	$v_{max,e}$ $[v_{th,e}]$	n_x	$n_{v,e}$	dt $[\omega_p^{-1}]$	ω $[\omega_p]$	σ $[\bar{\sigma}]$	$\frac{f_{n+1}}{f_n}$
FS_01	4000	10	8192	101	1e-3	0.5	1e-5	1.05
FS_39	4000	10	8192	101	1e-3	0.5	1e-5	1.05
MS_01	4000	10	8192	101	1e-3	0.5	1e-5	1.05
MS_06	4000	10	8192	101	1e-3	0.5	1e-5	1.05
CH_01	4000	10	8192	101	1e-3	0.5-5	1e-5	1.05

Appendix C

OpenMP parallelization of the numerical implementation of the Vlasov-Poisson 1D-1V model

As shown in section 4.1, section 4.2 and section 4.3, the principal tool that I have used for the investigation of MI experiments is the Vlasov-Poisson numerical model described in section 3.1. Such model is a new updated version of the past model used by Henri et al. [2010] to study the Langmuir Electrostatic Decay processes observed by the STEREO spacecraft.
The past version of the model was not parallelized. Instead, it was coded using a serial approach where all computations are performed sequentially. Thus, the model could not fully exploit the modern High Power Computing (HPC) facilities and their multi-thread characteristics.
But a serial implementation was not sufficient for my investigation. Despite the 1D-1V description of the model, my numerical runs were supposed to be very time-consuming due to the refined spatial and velocity domains required by my analysis, especially for the investigation of the impact of non-linear plasma interactions on the diagnostic performance of MI experiments. As already discussed in the previous chapter, to speed up the numerical runs I (i) separate each MI measurement into different numerical runs that investigate separately the emission of different frequencies and, (ii) whenever possible, I model the ions as a fixed background of positive charges so that only the Vlasov equation for the electrons has to be evolved in time. On top of that, I have updated the implementation of the model and parallelized the numerical code using an OpenMP architecture.

I validated the parallelized implementation of the model by performing a chosen numerical run using different numbers of parallel threads. Figure C.1 shows the strong scaling of the parallelized model. The serial (gray) curve represents the clock time needed to run the part of the model that has not been parallelized, while the parallel (blue) curve represents the clock time of the parallelized part. The total clock time (yellow curve) of the numerical simulation is equal to the sum of the serial and parallel clock time. The ideal (orange) curve represents the expected clock time and it is computed as:

$$t_{id} = t_s + t_p \tag{C.1}$$

where t_{id} is the ideal clock time, t_s is the serial clock time, $t_p = t_p[threads = 1]/n_{threads}$ is the parallel clock time, with $t_p[threads = 1]$ the parallel clock time when only one thread is used and $n_{threads}$ the number of parallel threads.
In all, Figure C.1 shows that the total clock time of the numerical run decreases almost ideally with the increasing number of parallel threads if the serial clock time is negligible. But, for large numbers of parallel threads, the parallel clock time reduces to the same order as the serial clock time and the variations of total clock time for increasing $n_{threads}$ become negligible.

Note that the OpenMP architecture, such as the one I chose for paralleling the model, is a *shared memory* architecture. Consequently, it limits the amount of parallel threads used for the numerical run

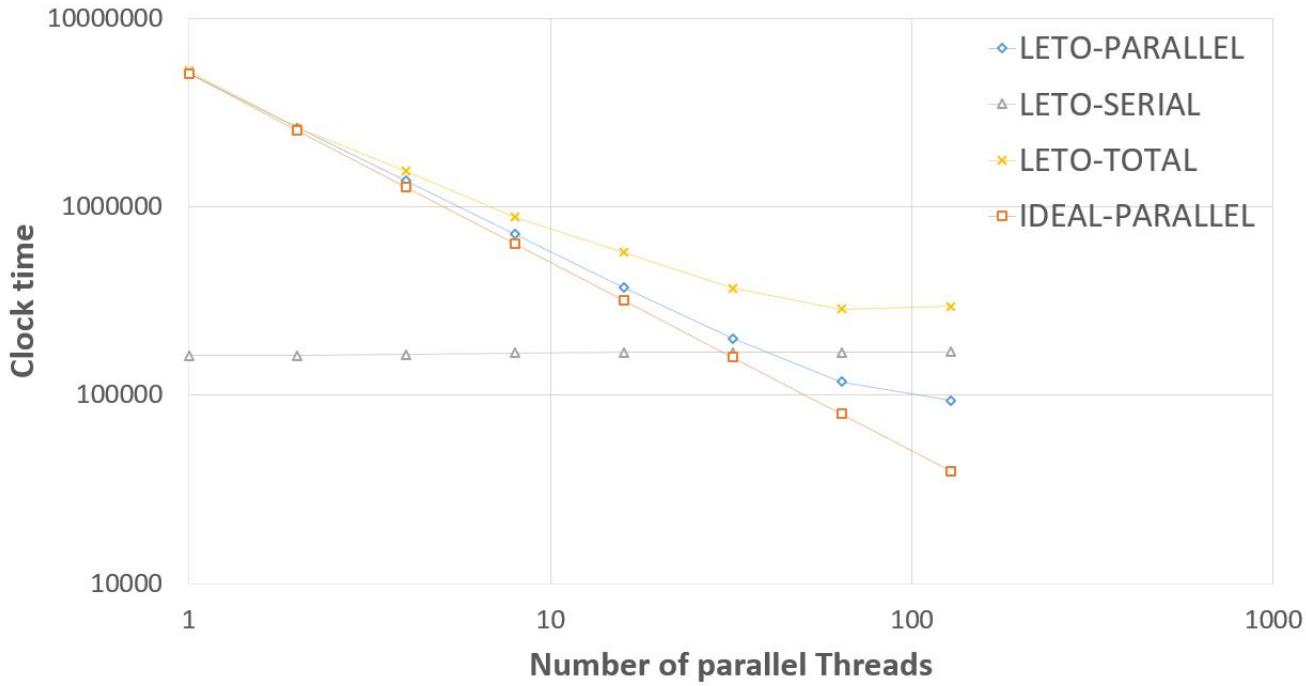

Figure C.1: Scaling of the parallelized code: computation time vs number of parallel threads

to the number of cores of the node. If more parallel threads are needed for the running the simulations, then an MPI architecture is required.

Appendix D

Publications

Hereafter, I list the scientific publications to which I contributed as first-author or co-author.

- L. Bucciantini, P. Henri, P. Dazzi, G. Wattieaux, F. Lavorenti (2023). *The Impact of Plasma Inhomogeneities on Mutual Impedance Experiments.* Sumbitted at JGR: Space Physics.
- Bucciantini, L., Henri, P., Dazzi, P., Wattieaux, G., Lavorenti, F., Vallières, X., et al., *Instrumentation for ionized space environments: New high time resolution instrumental modes of mutual impedance experiments.* Journal of Geophysical Research: Space Physics, 2023, 128, e2022JA031055. DOI: 10.1029/2022JA031055
- L. Bucciantini, P. Henri, G. Wattieaux, F. Califano, X. Vallières and O. Randriamboarison, *In situ space plasma diagnostics with finite amplitude active electric experiments: Non-linear plasma effects and instrumental performance of mutual impedance experiments.* Journal of Geophysical Research: Space Physics, 2022, DOI : 10.1029/2022JA030813
- Gilet, N., De Leon, E., Gallé, R., Vallières, X., Rauch, J.-L., Jegou, K., Bucciantini, L. et al. (2021). *Automatic detection of the thermal electron density from the WHISPER experiment onboard CLUSTER-II mission with neural networks.* Journal of Geophysical Research: Space Physics, 126, e2020JA028901. https://doi.org/10.1029/2020JA028901
- F. L. Johansson, A. I. Eriksson, E. Vigren, L. Bucciantini, P. Henri, H. Nilsson, S. Bergman, N. J. T. Edberg, G. Stenberg Wieser and E. Odelstad, *Plasma densities, flow, and solar EUV flux at comet 67P - A cross-calibration approach*, A&A, 2021, DOI : 10.1029/2020JA028901
- G. Wattieaux, N. Gilet, P. Henri and L. Bucciantini, *RPC-MIP observations at comet 67P/Churyumov-Gerasimenko explained by a model including a sheath and two populations of electrons*, A&A, 2019, DOI : 10.1051/0004-6361/201834872
- H. Breuillard, P. Henri, L. Bucciantini, M. Volwerk, T. Karlsson, A. Eriksson, F. Johansson, E. Odelstad, I. Richter, C. Goetz, X. Vallières and R. Hajra, *Properties of the singing comet waves in the 67P/Churyumov-Gerasimenko plasma environment as observed by the Rosetta mission*, A&A, 2019, DOI : 10.1051/0004-6361/201834876

Appendix E

Résumé en Français

E.1 Introduction

Récemment, les satellites de petite taille (e.g. les nanosatellites) ont suscité l'intérêt de la communauté scientifique [Camps, 2019]. Grâce à leurs coûts limités, les nanosatellites sont considérés comme le moyen de réduire le prix des missions multipoint et d'accélérer l'évolution des missions monopoint. [1] Mais leurs contraintes très fortes en termes de masse, de volume et de consommation d'énergie, limitent à la fois la quantité et le type d'instruments scientifiques qu'ils peuvent embarquer. Par conséquent, les missions de petits satellites sont susceptibles de se concentrer sur l'observation de propriétés spécifiques, alors que les grands satellites devraient permettre une surveillance beaucoup plus large de l'environnement exploré. Cela signifie que la distinction entre les variations temporelles et spatiales de propriétés données pourrait être faite en comparant les mesures obtenues simultanément par différents petits satellites situés à des positions différentes [Paschmann and Daly, 1998]. Cela dépasse la compréhension que les mesures ponctuelles passées et récentes peuvent apporter. C'est pourquoi de plus en plus de projets multipoints (par exemple, la mission Helioswarm [Spence, 2019]) sont récemment conçus car ils sont considérés comme la prochaine étape de l'exploration spatiale.
Les petits satellites améliorent considérablement l'étude des phénomènes physiques affectant l'espace à différentes échelles spatiales. [2] Par conséquent, comme ils fournissent des observations de certaines caractéristiques spécifiques de l'environnement sondé, ils compléteront la compréhension fournie par les missions mono-point des grands satellites.

Pour la préparation des futures missions nanosatellites multipoints, les instruments construits par le passé pour être embarqués sur grands satellites doivent être conformes aux exigences de volume, de masse et de puissance des nanosatellites. Entre autres, les instruments de charge utile tels que les instruments de diagnostic du plasma doivent s'assurer qu'ils respectent les exigences des petites plateformes. Les instruments de diagnostic du plasma sont le sujet principal de ce travail de thèse.

Les instruments de diagnostic in situ du plasma mesurent les propriétés des environnements plasma rencontrés par le satellite, tels que le vent solaire, les ionosphères et les magnétosphères des planètes. Selon le type d'instrument, ils mesurent des paramètres tels que la densité, la température, les fonctions de distribution ou la vitesse de dérive des particules chargées composant le plasma, ainsi que le champ électromagnétique local. Ce manuscrit se focalise sur la sonde à impédance mutuelle [Storey et al., 1969] (e.g. RPC-MIP [Trotignon et al., 2007] embarqué sur la mission Rosetta), une technique de diagnostic plasma pour la mesure de densité du plasma et température des électrons.

Le récent intérêt pour les petites plateformes pousse à la miniaturisation des instruments de diagnostic

[1] Grâce à leur coût limité et à la rapidité de leur profil de mission, les nanosatellites ont été sélectionnés à plusieurs reprises pour des missions d'étudiants au cours de la dernière décennie.

[2] Notons que les missions de nanosatellites comportant un nombre important de plates-formes pourraient même surveiller simultanément des paramètres à différentes échelles spatiales.

du plasma (e.g. Berthomier et al. [2022]) pour assurer le respect des fortes contraintes des nanosatellites. Dans le cas des sondes à impédance mutuelle, le projet COmpact Mutual Impedance eXperiment (COMIX), projet de R&T en cours au laboratoire LPC2E (Orléans, France) et financé par le Centre National d'Études Spatiales (CNES), vise à définir de nouvelles versions plus petites d'instruments d'impédance mutuelle qui respectent les fortes limitations des nanosatellites en préparation de futures missions multipoint. Pour soutenir le développement instrumental de la R&T COMIX, cette étude de thèse se concentre sur la mitigation des effets de la miniaturisation des sondes à impédance mutuelle (MI) sur le diagnostic plasma.

Les instruments MI sont composés d'antennes électriques émettrices et réceptrices immergées dans le plasma à diagnostiquer. Les antennes émettrices perturbent le plasma en émettant une succession de signaux sinusoïdaux d'amplitude et de fréquence données. Les antennes réceptrices mesurent les oscillations du plasma déclenchées par l'émission. Ces signaux reçus sont utilisés pour construire les spectres MI. Ces spectres présentent des résonances correspondant aux fréquences caractéristiques du plasma. Dans le cas d'un plasma non magnétisé avec une seule population d'électrons, les spectres MI ne présentent qu'une seule résonance. La densité du plasma est dérivée à partir de la position en fréquence de la résonance, alors que la température des électrons est dérivée de sa forme.

À bord des grands satellites, les capteurs électriques des instruments MI sont généralement installés sur de longs mécanismes déployables (boom) qui les positionnent loin de la plateforme du satellite. Cette configuration minimise les perturbations électromagnétiques de la plateforme captées par l'instrument, car les signaux électriques parasites générés à bord du satellite doivent parcourir de longues distances pour atteindre les capteurs de l'instrument. La longueur des bras est généralement de quelques mètres, en fonction de la stratégie de stabilisation de l'attitude du satellite et de la taille de la plateforme.
À bord des petits satellites, par contre, les mécanismes à déploiement long sont difficiles à mettre en œuvre. Les nanosatellites ont des longueurs de côté d'environ $0,1$ à $0,3$ m, ce qui donne des longueurs déployables typiques d'environ 1 m pour les nanosatellites stabilisés sur 3 axes [West et al., 2015]. Une telle distance n'est pas considérée comme suffisante pour négliger les perturbations électriques parasites générées par le nanosatellite. Des perturbations des mesures encore plus importantes sont attendues si les booms sont courts par rapport à la longueur de Debye du plasma exploré par le nanosatellite. De plus, les nanosatellites ne peuvent intégrer qu'un nombre limité de bras déployables. Par conséquent, si les capteurs de différents instruments doivent être déployés, il peut être nécessaire qu'ils partagent le même bras [de Keyser et al., 2021]. Dans certains cas, pour minimiser la masse, différents instruments doivent même partager les mêmes capteurs électriques. Cela a des conséquences sur le temps d'occupation de l'antenne et, par conséquent, sur la résolution temporelle de l'instrument. Il en résulte que différents problèmes se posent lors de l'adaptation des instruments MI aux plateformes de type nanosatellites.

E.1.1 Les Signaux Électriques Parasites Perturbent les Mesures d'Impédance Mutuelle

Les dispositifs électroniques à bord du satellite émettent des signaux électriques qui se propagent dans le plasma environnant. Après avoir parcouru la courte distance entre la plateforme du nanosatellite et l'instrument, ces signaux atteignent les antennes du MI et perturbent les mesures en réduisant leur rapport signal/bruit. Des rapports signal/bruit plus faibles impactent l'analyse des spectres et les performances de diagnostic du plasma de l'instrument. À noter que ce type de perturbation des mesures est généralement appelé compatibilité électromagnétique (EMC) [Youssef, 1996]. Afin de limiter la perte de performance de diagnostic des sondes MI, COMIX prévoit d'atténuer les problèmes de EMC en augmentant l'amplitude de l'émission MI. Cela augmentera l'amplitude des oscillations dans le plasma et, par conséquent, l'amplitude des signaux reçus. En conséquence, le rapport signal/bruit devrait être amélioré. Il faut toutefois noter que des émissions plus fortes de MI pourraient perturber les mesures effectuées par les instruments plasma à proximité des capteurs.
D'une part, si la réponse du plasma aux émissions de MI est linéaire, des émissions plus fortes correspondent à des signaux reçus plus forts. Si le bruit des mesures n'est pas corrélé, alors le rapport signal/bruit

des mesures du MI s'améliore en augmentant l'amplitude d'émission. En revanche, si l'émission MI est trop forte, alors l'énergie injectée dans le plasma peut être importante par rapport à l'énergie thermique des électrons (c'est-à-dire des rapports énergie électrique/énergie thermique importants). Dans ce cas, la grande amplitude des ondes injectées dans le plasma déclenche différents types d'interactions non linéaires dans le plasma susceptibles de dégrader la qualité de la mesure, comme les interactions onde-particule et onde-onde.

Dans le cas de fortes émissions, les ondes plasma émises par l'instrument MI sont perturbées par des interactions onde-particule, qui modifient la fonction de distribution des électrons, et par des interactions onde-onde, qui drainent l'énergie des fortes ondes de plasma vers d'autres oscillations. Mais les procédures typiquement utilisées pour l'analyse des mesures MI supposent que le plasma est caractérisé par des fonctions de distribution spécifiques et que l'énergie injectée par les antennes émettrices excite le plasma uniquement aux fréquences émises. On s'attend donc à ce que les interactions non linéaires du plasma perturbent les performances de diagnostic des sondes MI. Dans ce contexte, mon premier objectif est d'étudier les perturbations du plasma générées par les fortes amplitudes d'émission des antennes MI et de quantifier la plus grande amplitude pour laquelle les performances de diagnostic MI sont acceptables (c'est-à-dire similaires aux performances typiques, selon les récentes applications spatiales MI).

E.1.2 Les Inhomogénéités du Plasma à Petite Échelle Perturbent les Mesures d'Impédance Mutuelle

Les satellites et leurs appendices (par exemple, les bras portant des instruments) interagissent avec le plasma en collectant des courants de charge à leur surface. Les courants chargent les satellites, qui acquièrent donc un potentiel électrique donné [Grard et al., 1983, Lai, 2012]. Ce potentiel électrique perturbe le plasma qui, à son tour, forme une région inhomogène à petite échelle (c'est-à-dire de l'ordre de la longueur de Debye λ_D) autour de la surface du satellite et de ses instruments. Telle région est appelée gaine plasma [Tonks and Langmuir, 1929, Riemann, 2008, Allen, 2008]. La gaine plasma est connue pour perturber différents types de mesures du plasma.
Premièrement, les trajectoires des particules du plasma sont modifiées lorsque les particules sont accélérées/décélérées en raison du gradient de potentiel électrique à l'intérieur de la gaine. Deuxièmement, le champ électrique du plasma est modifié par le gradient de potentiel électrique de la gaine plasma. Troisièmement, la gaine plasma est inhomogène et, par conséquent, elle perturbe le diagnostic de la densité du plasma de certaines techniques de surveillance qui correspondent à des mesures très locales (par exemple, les mesures de sonde de Langmuir) [Johansson et al., 2020, 2021].
Pour minimiser les perturbations que la gaine du plasma introduit sur les mesures, les instruments de diagnostic du plasma sont généralement placés loin de la plate-forme du satellite. Dans le cas des nanosatellites, cela n'est pas possible. Malgré leur installation sur des bras, les instruments restent proches de la plate-forme.

Bien que l'on connaisse l'impact des inhomogénéités à moyenne et grande échelle sur la propagation des ondes plasma, il n'existe à ce jour aucun modèle analytique pour la propagation des signaux d'émission MI à travers la gaine. Par conséquent, en préparation de futures missions nanosatellite, COMIX doit quantifier l'impact des inhomogénéités du plasma sur la performance de diagnostic plasma des mesures de MI. Pour soutenir COMIX, le deuxième objectif de cette thèse est de quantifier pour la première fois l'impact des inhomogénéités du plasma à petite échelle, comme la gaine plasma, sur la performance du diagnostic MI du plasma. De plus, avec ce travail je vérifie si les inhomogénéités du plasma à petite échelle (comme celles générées par la charge des satellites) et à moyenne ou grande échelle (comme celles générées par les fluctuations compressibles du plasma) ont les mêmes effets sur les mesures MI.

E.1.3 Le Partage d'Antenne Réduit la Résolution Temporelle des Mesures

Les contraintes de masse et de volume des nanosatellites limitent non seulement la taille des booms, mais aussi le nombre de booms transportés par les nanosatellites. Cela signifie que, si plusieurs instruments de mesure du plasma sont transportés, chaque bras peut devoir déployer plusieurs instruments. Récemment,

afin de minimiser la masse de la charge utile, les différents instruments de diagnostic plasma doivent même partager leurs capteurs. Même si la masse de la plateforme est optimisée, les expériences qui partagent leurs capteurs doivent planifier le temps d'occupation des antennes. Par conséquent, la résolution temporelle des mesures MI à bord des nanosatellites serait affectée. COMIX prévoit de répondre à cette perturbation en définissant de nouvelles procédures expérimentales (plus rapides) (modes instrumentaux) qui permettront des mesures à plus haute résolution temporelle. Pour soutenir COMIX, mon troisième objectif est de définir, de tester et de valider les nouveaux modes instrumentaux de mesure MI (notamment les modes chirp et multi-spectral).

E.2 Les Simulations 1D-1V Vlasov-Poisson et la Chambre Plasma

Cette étude est rendue possible par deux outils principaux. Premièrement, un modèle full-cinétique Vlasov-Poisson 1D-1V que j'utilise pour simuler numériquement les mesures de MI. Deuxièmement, l'installation d'essai du laboratoire spatial LPC2E, que j'utilise pour réaliser des expériences MI dans un milieu de plasma représentatif de l'espace. J'utilise ces outils pour (i) quantifier l'impact sur les performances du diagnostic MI générés par les interactions non linéaires du plasma déclenchées par de fortes amplitudes d'émission, (ii) évaluer les effets de la gaine plasma du nanosatellite sur les mesures MI et (iii) tester et valider les performances des nouveaux modes instrumentaux MI qui sont rapides par rapport à celles du mode nominal de balayage de fréquence utilisé comme référence.

E.3 Résultats

E.3.1 Performance du Diagnostic des Sondes à Impédance Mutuelle pour les Fortes Amplitudes d'Émission

Mon travail montre que l'amplitude maximale acceptable d'émission MI correspond au rapport énergie électrique/énergie thermique $\alpha = 0,1$. Pour une telle amplitude, les performances de diagnostic sont en accord avec les performances typiques des applications spatiales MI passées et futures (par exemple, DFP-COMPLIMENT à bord de la mission Comet Interceptor). En particulier, pour une telle amplitude, je trouve des erreurs de diagnostic de la densité du plasma inférieures à 5% et des erreurs de diagnostic de la température des électrons inférieures à 20%, qui sont les exigences de performance de l'instrument.

Il est important de mentionner que ces résultats dépendent fortement de la durée d'émission des mesures. En particulier, une amplitude d'émission donnée qui ne produit pas de perturbations non linéaires du plasma sur des échelles de temps de mesure MI peut déclencher de fortes non-linéarités sur des durées plus longues. Cela signifie que, dans le cas d'émissions MI plus longues (chaque fréquence émise pendant $N > 20$ périodes), on peut s'attendre à ce que mes résultats surestiment l'amplitude d'émission optimale. Par conséquent, l'amplitude de l'émission MI doit être maintenue en dessous de $\alpha < 0,1$ pour garantir des performances de diagnostic acceptables.

E.3.2 Impact des Inhomogénéités Plasma de Petite Échelle

Mon travail montre que les perturbations du diagnostic de la densité du plasma de MI dues aux inhomogénéités localisées sont négligeables. En particulier, pour les mesures de MI en présence des inhomogénéités de plasma considérées, je trouve des erreurs relatives de densité de plasma inférieures à la résolution de densité de plasma des mesures (c.-à-d. inférieures à 10%). Par conséquent, les gradients de densité à petite échelle compatibles avec la taille de la gaine du plasma n'affectent pas la mesure de la densité des expériences MI. En particulier, mon travail montre que les sondes MI sont capables de retrouver la densité du plasma homogène non perturbée par la présence de l'inhomogénéité à petite échelle. Par contre, dans le cas d'inhomogénéités du plasma à moyenne ou grande échelle compatibles avec les variations des propriétés du plasma traversé par le satellite, mon travail montre que les expériences MI parviennent à retrouver la densité locale. Par conséquent, le diagnostic de la densité du plasma

des expériences MI devrait être robuste aux perturbations liées à la gaine plasma du nanosatellite, mais aussi sensible à la présence des structures du plasma que l'instrument est conçu pour observer.

Pour la température des électrons, au contraire, je trouve que la performance du diagnostic MI est significativement perturbée par la présence d'inhomogénéités plasma. Ces perturbations sont particulièrement importantes dans le cas des gaines plasma dues à des satellites chargés positivement. En particulier, je trouve des erreurs relatives de température des électrons jusqu'à un facteur 2 (resp. 9) dans le cas de la gaine de plasma associée à un satellite à potentiel électrique négatif (resp. positif). Tant pour les satellites à charge négative que pour ceux à charge positive, les erreurs relatives dépassent l'incertitude typique de la température des électrons de 20%. Si des erreurs inférieures à 20% sont requises, il faut tenir compte de la présence de l'inhomogénéité plasma dans l'analyse des spectres MI. Pour cela, les spectres de référence doivent être calculés à l'aide d'un modèle qui inclut la gaine plasma. Ce résultat est cohérent avec les travaux de Wattieaux et al. [2019, 2020], qui ont inclus une modélisation par paliers de la gaine plasma de l'instrument RPC-MIP à bord du satellite Rosetta dans l'analyse des spectres RPC-MIP pour l'identification de la température des électrons.

E.3.3 Nouveaux Modes Instrumentaux Rapides de Sonde à Impédance Mutuelle

Du point de vue du diagnostic MI du plasma, je trouve, tant numériquement qu'expérimentalement, que les mesures chirp et multi-spectral sont équivalentes aux mesures de balayage de fréquence de référence. En particulier, les écarts entre les mesures de balayage de fréquence et les mesures chirp (resp. multi-spectral) s'élèvent à $2,15$ dB (resp. $1,5$ dB) en amplitude et $0,57$ rad (resp. $0,42$ rad) en phase pour les fréquences proches de la résonance des spectres (c'est-à-dire pour la gamme 1 MHz,4 MHz). Ces écarts sont de l'ordre du bruit instrumental typique (environ 1 dB) rencontré pour différentes applications spatiales du MI (par exemple, RPC-MIP à bord de Rosetta). La densité du plasma et la température des électrons sont identifiées à partir de la fréquence correspondant à la signature de résonance des spectres et de la forme de la résonance, respectivement. Je conclus donc que les performances de diagnostic des nouveaux modes chirp et multi-spectral sont équivalentes à celles du mode de balayage de fréquence de référence.

D'un point de vue instrumental, j'ai étudié les ressources de calcul requises par chaque mode instrumental de MI pour obtenir un spectre donné. En particulier, je trouve les ressources de calcul comme la quantité de multiplications effectuées par l'unité informatique embarquée pour la production de spectres MI. Pour une unité informatique embarquée donnée, un plus grand nombre de multiplications correspond à une plus grande consommation d'énergie. Cela signifie que le mode instrumental correspondant aux plus faibles quantités de multiplications requises est associé à des consommations d'énergie plus faibles. En pratique, je me concentre sur la gamme de fréquences ($f_{min} = 10\ kHz$, $f_{max} = 20\ MHz$) balayée à l'aide d'une résolution de fréquence donnée et je calcule, pour les trois modes, la durée et les ressources informatiques nécessaires pour effectuer une même mesure. En termes de ressources informatiques, mon travail montre que les mesures multi-spectral nécessitent plus de multiplications à bord (jusqu'à 220%) que les mesures de balayage de fréquence, tandis que les mesures de chirp sont moins exigeantes (environ 81%). En termes de durée, je trouve que les mesures multi-spectral (resp. chirp) sont 5 (resp. 20) fois plus rapides que les mesures nominales par balayage de fréquence.

Globalement, le mode chirp fournit les mesures les plus rapides. En même temps, il est également associé à des mesures moins exigeantes que le mode balayage de fréquence et le mode multi-spectral. Par conséquent, COMIX et d'autres expériences MI futures devraient utiliser le mode chirp pour mitiger l'impact d'une résolution temporelle réduite des mesures MI associée au partage d'antenne ou pour augmenter la résolution temporelle des futurs instruments MI.

Bibliography

F. Allegrini, R. F. Wimmer-Schweingruber, P. Wurz, and P. Bochsler. Determination of low-energy ion-induced electron yields from thin carbon foils. *Nuclear instruments and methods in physics research section B: beam interactions with materials and atoms*, 211(4):487–494, 2003. URL https://doi.org/10.1016/S0168-583X(03)01705-1. (Cited on page 2.)

J. E. Allen. The plasma–sheath boundary: its history and Langmuir's definition of the sheath edge. *Plasma Sources Science and Technology*, 18(1):014004, 2008. URL https://doi.org/10.1088/0963-0252/18/1/014004. (Cited on pages 7 and 163.)

V. Angelopoulos. The THEMIS mission. *Space Science Reviews*, 141, 2008. URL https://doi.org/10.1007/s11214-008-9336-1. (Cited on page 1.)

D. Auslander, J. Cermenska, G. Dalton, M. de la Pena, C. K. H. Dharan, W. Donokowski, R. Duck, J. Kim, D. Pankow, A. Plauche, M. Rahmani, S. Sulack, T. F. Tan, P. Turin, and T. Williams. Instrument boom mechanisms on the THEMIS satellites; magnetometer, radial wire, and axial booms. *Space Science Reviews*, 141:185–211, 2008. URL https://doi.org/10.1007/s11214-008-9386-4. (Cited on page 7.)

A. Bahnsen, M. Jespersen, E. Ungstrup, R. Pottelette, M. Malingre, P. Decreau, M. Hamelin, H. de Feraudy, S. Perraut, and B. Pedersen. First VIKING results: high frequency waves. *Physica Scripta*, 37(3):469–474, 1988. URL https://doi.org/10.1088/0031-8949/37/3/032. (Cited on pages 5, 15 and 63.)

J. Benkhoff, G. Murakami, W. Baumjohann, S. Besse, E. Bunce, M. Casale, G. Cremosese, K.-H. Glassmeier, H. Hayakawa, D. Heyner, H. Hiesinger, J. Huovelin, H. Hussmann, V. Iafolla, L. Iess, Y. Kasaba, M. Kobayashi, A. Milillo, I. G. Mitrofanov, E. Montagnon, M. Novara, S. Orsini, E. Quemerais, U. Reininghaus, Y. Saito, F. Santoli, D. Stramaccioni, O. Sutherland, N. Thomas, I. Yoshikawa, and J. Zender. BepiColombo - mission overview and science goals. *Space Science Reviews*, 217:90, 2021. URL https://doi.org/10.1007/s11214-021-00861-4. (Cited on pages 2 and 72.)

J. E. S. Bergman, J. E. Wahlund, O. Witasse, and V. Cripps. The Radio & Plasma Wave Investigation (RPWI) for JUICE - from Jupiter's magnetosphere, through the ice shell, and into the ocean of Ganymede. In *European Planetary Science Congress*, pages EPSC2017–373, 2017. URL https://ui.adsabs.harvard.edu/abs/2017EPSC...11..373B. (Cited on page 5.)

S. Bergman, G. Stenberg Wieser, M. Wieser, F. L. Johansson, and A. Eriksson. The influence of spacecraft charging on low-energy ion measurements made by RPC-ICA on Rosetta. *Journal of Geophysical Research: Space Physics*, 125(1):e2019JA027478, 2020. URL https://doi.org/10.1029/2019JA027478. (Cited on pages 8, 50, 59 and 71.)

H. L. Berk and K. V. Roberts. Nonlinear study of Vlasov's equation for a special class of distribution functions. *The Physics of Fluids*, 10(7):1595–1597, 1967. URL https://doi.org/10.1063/1.1762331. (Cited on pages vii and 9.)

I. B. Bernstein. Waves in a plasma in a magnetic field. *Phys. Rev.*, 109:10–21, 1958. URL https://doi.org/10.1103/PhysRev.109.10. (Cited on page 77.)

M. Berthomier, G. Hénaff, F. Leblanc, J.-D. Techer, S. Pledel, and C. Berthod. A plasma camera for high-time resolution 3D imaging of space plasmas. In *44th COSPAR Scientific Assembly. Held 16-24 July*, volume 44, page 1632, 2022. URL https://ui.adsabs.harvard.edu/abs/2022cosp...44.1632B. (Cited on pages 4 and 162.)

N. Besse. Contributions to mathematical analysis and to numerical approximation in plasma physics. *FRNC-TH–9748*, 2009. URL http://inis.iaea.org/search/search.aspx?orig_q=RN:48064493. (Cited on page 20.)

C. Birdsall and A. Langdon. *Plasma Physics via Computer Simulation*. Series in Plasma Physics and Fluid Dynamics. Taylor & Francis, 2004. ISBN 9780750310253. URL https://books.google.fr/books?id=S2lqgDTm6a4C. (Cited on page 41.)

H. Breuillard, P. Henri, L. Bucciantini, M. Volwerk, T. Karlsson, A. Eriksson, F. Johansson, E. Odelstad, I. Richter, C. Goetz, X. Vallières, and R. Hajra. Properties of the singing comet waves in the 67P/Churyumov-Gerasimenko plasma environment as observed by the rosetta mission. *A&A*, 630:A39, 2019. URL https://doi.org/10.1051/0004-6361/201834876. (Cited on page 149.)

L. Brillouin. La nouvelle mécanique atomique. *J. Phys. Radium*, 7(5):135–160, 1926. URL https://doi.org/10.1051/jphysrad:0192600705013500. (Cited on pages 10 and 58.)

M. Brunetti, F. Califano, and F. Pegoraro. Asymptotic evolution of nonlinear Landau damping. *Phys. Rev. E*, 62:4109–4114, 2000. URL https://doi.org/10.1103/PhysRevE.62.4109. (Cited on page 43.)

L. Bucciantini. Dataset. 1D-1V Vlasov-Poisson simulations of mutual impedance experiments for strong antenna emission amplitudes. *Zenodo*, 2022a. URL https://doi.org/10.5281/zenodo.7149358. (Cited on page 151.)

L. Bucciantini. Dataset. New high time resolution mutual impedance measurements. *Zenodo*, 2022b. URL https://doi.org/10.5281/zenodo.7278491. (Cited on page 151.)

R. Buckley. Radio frequency properties of a plane grid capacitor immersed in a hot collision-free plasma. *J. Plasma Physics*, 2:339–351, 1968. URL https://doi.org/10.1017/S0022377800003871. (Cited on page 21.)

J. L. Burch, T. E. Moore, R. B. Torbert, and B. L. Giles. Magnetospheric multiscale overview and science objectives. *Space Science Reviews*, 199:5–21, 2016. URL https://doi.org/10.1007/s11214-015-0164-9. (Cited on page 1.)

C. Béghin. Series expansion of electrostatic potential radiated by a point source in isotropic Maxwellian plasma. *Radio Science*, 30:307–322, 1995. URL https://doi.org/10.1029/94RS03167. (Cited on pages 16 and 21.)

C. Béghin and R. Debrie. Characteristics of the electric field far from and close to a radiating antenna around the lower hybrid resonance in the ionospheric plasma. *Journal of Plasma Physics*, 8(3):287–310, 1972. URL https://doi.org/10.1017/S0022377800007157. (Cited on pages 5, 14 and 63.)

C. Béghin and E. Kolesnikova. Surface-charge distribution approach for modeling of quasi-static electric antennas in isotropic thermal plasma. *Radio Science*, 33(3):503–516, 1998. URL https://doi.org/10.1029/97RS03588. (Cited on page 24.)

C. Béghin, J. F. Karczewski, B. Poirier, R. Debrie, and N. Masevich. The ARCAD-3 ISOPROBE experiment for high time resolution thermal plasma measurements. *Annales de Geophysique*, 38(5):615–629, 1982. URL https://ui.adsabs.harvard.edu/abs/1982AnG....38..615B. (Cited on pages vii, 14 and 15.)

C. Béghin, P. M. E. Décréau, J. Pickett, D. Sundkvist, and B. Lefebvre. Modeling of Cluster's electric antennas in space: application to plasma diagnostics. *Radio Science*, 40(6), 2005. URL https://doi.org/10.1029/2005RS003264. (Cited on pages 3 and 147.)

F. Califano and M. Lontano. Vlasov-Poisson simulations of strong wave-plasma interaction in conditions of relevance for radio frequency plasma heating. *Phys. Rev. Lett.*, 83:96–99, 1999. URL https://doi.org/10.1103/PhysRevLett.83.96. (Cited on page 45.)

A. Camps. Nanosatellites and applications to commercial and scientific missions. In *Satellites Missions and Technologies for Geosciences*, chapter 9. IntechOpen, 2019. URL https://doi.org/10.5772/intechopen.90039. (Cited on pages 1 and 161.)

G. Carnielli, M. Galand, F. Leblanc, L. Leclercq, R. Modolo, A. Beth, H. Huybrighs, and X. Jia. First 3D test particle model of Ganymede's ionosphere. *Icarus*, 330:42–59, 2019. URL https://doi.org/10.1016/j.icarus.2019.04.016. (Cited on page 77.)

C. Carr, E. Cupido, C. G. Y. Lee, A. Balogh, T. Beek, J. L. Burch, C. N. Dunford, A. I. Eriksson, R. Gill, K. H. Glassmeier, R. Goldstein, D. Lagoutte, R. Lundin, K. Lundin, B. Lybekk, J. L. Michau, G. Musmann, H. Nilsson, C. Pollock, I. Richter, and J. G. Trotignon. RPC: the Rosetta Plasma Consortium. *Space Science Reviews*, 128:629–647, 2007. URL https://doi.org/10.1007/s11214-006-9136-4. (Cited on pages 5, 50 and 69.)

J. Chassériaux, R. Debrie, and C. Renard. Electron density and temperature measurements in the lower ionosphere as deduced from the warm plasma theory of the h.f. quadrupole probe. *J. Plasma Physics*, 8:231–253, 1972. URL https://doi.org/10.1017/S0022377800007108. (Cited on pages vii, 14, 16, 22 and 73.)

G. A. Collinson and D. O. Kataria. On variable geometric factor systems for top-hat electrostatic space plasma analyzers. *Measurement Science and Technology*, 21(10):105903, 2010. URL https://doi.org/10.1088/0957-0233/21/10/105903. (Cited on page 3.)

F. Crameri. Software. Scientific colour maps. Version 7.0.1. *Zenodo*, 2021. URL https://doi.org/10.5281/zenodo.5501399. (Cited on page 151.)

F. Crameri, G. E. Shephard, and P. J. Heron. The misuse of colour in science communication. *Nature Communications*, 11, 2020. URL https://doi.org/10.1038/s41467-020-19160-7. (Cited on page 151.)

G. Curzi, D. Modenini, and P. Tortora. Large constellations of small satellites: a survey of near future challenges and missions. *Aerospace*, 7(9), 2020. URL https://doi.org/10.3390/aerospace7090133. (Cited on page 2.)

J. de Keyser, S. Ranvier, J. Maes, J. Pawlak, E. Neefs, F. Dhooghe, U. Auster, B. Chares, N. Edberg, J. Fredriksson, A. Eriksson, P. Henri, O. Le Duff, and J. Peterson. A combined Langmuir Probe - fluxgate magnetometer sensor design for Comet Interceptor. In *vEGU21*, 2021. URL https://doi.org/10.5194/egusphere-egu21-7197. (Cited on pages 7, 27, 73, 77, 148 and 162.)

D. Delcourt, Y. Saito, J.-M. Illiano, N. Krupp, J.-J. Berthelier, D. Fontaine, M. Fraenz, F. Leblanc, H. Fischer, S. Yokota, H. Michalik, M. Godefroy, E. Saint-Jacques, J.-D. Techer, B. Fiethe, J. Covinhes, J. Gastou, and D. Attia. The mass spectrum analyzer (MSA) onboard BepiColombo MMO: Scientific objectives and prototype results. *Advances in Space Research*, 43(5):869–874, 2009. URL https://doi.org/10.1016/j.asr.2008.12.002. (Cited on page 2.)

D. Delcourt, Y. Saito, F. Leblanc, C. Verdeil, S. Yokota, M. Fraenz, H. Fischer, B. Fiethe, B. Katra, D. Fontaine, J.-M. Illiano, J.-J. Berthelier, N. Krupp, U. Buhrke, F. Bubenhagen, and H. Michalik. The Mass Spectrum Analyzer (MSA) on board the BepiColombo MMO. *Journal of Geophysical Research: Space Physics*, 121(7):6749–6761, 2016. URL https://doi.org/10.1002/2016JA022380. (Cited on page 2.)

H. Derfler and T. C. Simonen. Higher-order Landau modes. *The Physics of Fluids*, 12(2):269–278, 1969. URL https://doi.org/10.1063/1.1692477. (Cited on pages 21, 24 and 78.)

K. B. Dysthe and R. Franklin. Non-linear interactions of coherent electrostatic plasma waves. *Plasma Physics*, 12(9):705–721, 1970. URL https://doi.org/10.1088/0032-1028/12/9/005. (Cited on pages vii and 39.)

P. M. E. Décréau, C. Béghin, and M. Parrot. Electron density and temperature, as measured by the mutual impedance experiment on board GEOS-1. *Space Science Reviews*, 22(5):581–595, 1978. URL https://doi.org/10.1007/BF00223942. (Cited on pages 5, 14, 16, 38 and 63.)

P. M. E. Décréau, M. Hamelin, R. Massif, H. de Feraudy, and E. Pawela. Plasma probing by active wave experiments on the VIKING satellite. *Annales Geophysicae*, 5:181–185, 1987. URL https://ui.adsabs.harvard.edu/abs/1987AnGeo...5..181D. (Cited on page 3.)

A. I. Eriksson, R. Boström, R. Gill, L. Åhlén, S.-E. Jansson, J.-E. Wahlund, M. André, A. Mälkki, J. A. Holtet, B. Lybekk, A. Pedersen, L. G. Blomberg, and T. L. Team. RPC-LAP: The Rosetta Langmuir probe instrument. *Space Science Reviews*, 128:729–744, 2007. URL https://doi.org/10.1007/s11214-006-9003-3. (Cited on pages 3 and 149.)

C. P. Escoubet, M. Fehringer, and M. Goldstein. The Cluster mission. *Annales Geophysicae*, 19(10/12): 1197–1200, 2001. URL https://doi.org/10.5194/angeo-19-1197-2001. (Cited on page 1.)

J. M. Fernandez. *Sheath-based rollable lenticular-shaped and low-stiction composite boom*. United States Patent: US 2017/0058524A1, 2017. (Cited on page 7.)

G. Fraser. The ion detection efficiency of microchannel plates (MCPs). *International Journal of Mass Spectrometry*, 215(1):13–30, 2002. URL https://doi.org/10.1016/S1387-3806(01)00553-X. (Cited on page 3.)

E. Gargioni and B. Grosswendt. Electron scattering from argon: Data evaluation and consistency. *Rev. Mod. Phys.*, 80:451–480, 2008. URL https://doi.org/10.1103/RevModPhys.80.451. (Cited on page 76.)

J. Geiswiller, C. Béghin, E. Kolesnikova, D. Lagoutte, J. L. Michau, and J. G. Trotignon. Rosetta spacecraft influence on the mutual impedance probe frequency response in the long Debye length mode. *Planetary and Space Science*, 49(6):633–644, 2001. URL https://doi.org/10.1016/S0032-0633(00)00173-2. (Cited on pages 15, 16, 24, 63, 70 and 74.)

N. Gilet, P. Henri, G. Wattieaux, M. Cilibrasi, and C. Béghin. Electrostatic potential radiated by a pulsating charge in a two-electron temperature plasma. *Radio Science*, 52:1432–1448, 2017. URL https://doi.org/10.1002/2017RS006294. (Cited on pages 15, 17, 21, 63, 70, 74 and 77.)

N. Gilet, P. Henri, G. Wattieaux, M. Myllys, O. Randriamboarison, C. Béghin, and J.-L. Rauch. Mutual Impedance Probe in collisionless unmagnetized plasmas with suprathermal electrons—Application to BepiColombo. *Frontiers in Astronomy and Space Sciences*, 6, 2019. URL https://doi.org/10.3389/fspas.2019.00016. (Cited on pages 74 and 77.)

N. Gilet, E. De Leon, R. Gallé, X. Vallières, J.-L. Rauch, K. Jegou, L. Bucciantini, V. Savreux, P. Décréau, and P. Henri. Automatic detection of the thermal electron density from the WHISPER experiment onboard CLUSTER-II mission with neural networks. *Journal of Geophysical Research: Space Physics*, 126(3):e2020JA028901, 2021. URL https://doi.org/10.1029/2020JA028901. (Cited on page 147.)

R. Grard. Coupling between two electric aerials in a warm plasma. *Alta Frequency*, 38:97–101, 1969. (Cited on page 63.)

R. Grard. Influence of suprathermal electrons upon the transfer impedance of a quadrupolar probe in a plasma. *Radio Science*, 32(3):1091–1100, 1997. URL https://doi.org/10.1029/97RS00254. (Cited on pages 5, 15 and 63.)

R. Grard, K. Knott, and Pedersen. Spacecraft charging effects. *Space Science Reviews*, 34:289–304, 1983. URL https://doi.org/10.1007/BF00175284. (Cited on pages 7 and 163.)

R. Hajra, P. Henri, X. Vallières, M. Galand, M. Rubin, B. T. Tsurutani, N. Gilet, L. Bucciantini, and Z. Nemeth. Ionospheric total electron content of comet 67P/Churyumov-Gerasimenko. *A&A*, 635:A51, 2020. URL https://doi.org/10.1051/0004-6361/201937022. (Cited on page 149.)

C. C. Harvey, J. Etcheto, and A. Mangeney. *Early Results from the ISEE Electron Density Experiment*, pages 533–552. Springer Netherlands, 1979. ISBN 978-94-009-9527-7. URL https://doi.org/10.1007/978-94-009-9527-7_34. (Cited on page 3.)

P. Henri, F. Califano, C. Briand, and A. Mangeney. Vlasov-Poisson simulations of electrostatic parametric instability for localized langmuir wave packets in the solar wind. *Journal of Geophysical Research*, 115: A06106, 2010. URL https://doi.org/10.1029/2009JA014969. (Cited on pages 19, 24 and 157.)

P. Henri, F. Califano, C. Briand, and A. Mangeney. Low-energy Langmuir cavitons: asymptotic limit of weak turbulence. *EPL (Europhysics Letters)*, 96(5):55004, 2011. URL https://doi.org/10.1209/0295-5075/96/55004. (Cited on pages 45 and 70.)

P. Henri, X. Vallières, R. Hajra, C. Goetz, I. Richter, K.-H. Glassmeier, M. Galand, M. Rubin, A. I. Eriksson, Z. Nemeth, E. Vigren, A. Beth, J. Burch, C. Carr, H. Nilsson, B. Tsurutani, and G. Wattieaux. Diamagnetic region(s): structure of the unmagnetized plasma around comet 67P/CG. *Monthly Notices of the Royal Astronomical Society*, 469:S372–S379, 2017. URL https://doi.org/10.1093/mnras/stx1540. (Cited on page 33.)

K. Issautier, N. Meyer, M. Moncuquet, S. Hoang, and D. J. Mccomas. Quasi-thermal noise in a drifting plasma: Theory and application to solar wind diagnostic on Ulysses. *Journal of Geophysical Research*, 104:6691–6704, 1999. URL https://doi.org/10.1029/1998JA900165. (Cited on page 3.)

F. L. Johansson, A. I. Eriksson, N. Gilet, P. Henri, G. Wattieaux, M. G. G. T. Taylor, C. Imhof, and F. Cipriani. A charging model for the Rosetta spacecraft. *A&A*, 642:A43, 2020. URL https://doi.org/10.1051/0004-6361/202038592. (Cited on pages 8, 50, 59, 71 and 163.)

F. L. Johansson, A. I. Eriksson, E. Vigren, L. Bucciantini, P. Henri, H. Nilsson, S. Bergman, N. J. Edberg, G. Stenberg Wieser, and E. Odelstad. Plasma densities, flow, and solar EUV flux at comet 67P. *Astronomy and Astrophysics - A&A*, 653(4):A128, 2021. URL https://doi.org/10.1051/0004-6361/202039959. (Cited on pages 3, 8, 50, 59, 71, 149 and 163.)

T. Karlsson, Y. Kasaba, J.-E. Wahlund, P. Henri, L. Bylander, W. Puccio, S.-E. Jansson, L. Åhlen, E. Kallio, H. Kojima, A. Kumamoto, K. Lappalainen, B. Lybekk, K. Ishisaka, A. Eriksson, and M. Morooka. The MEFISTO and WPT Electric Field Sensors of the Plasma Wave Investigation on the BepiColombo Mio spacecraft. *Space Science Reviews*, pages 132–216, 2020. URL https://doi.org/10.1007/s11214-020-00760-0. (Cited on pages 5, 69 and 72.)

Y. Kasaba, H. Kojima, M. Moncuquet, J. Wahlund, S. Yagitani, F. Sahraoui, P. Henri, T. Karlsson, Y. Kasahara, A. Kumamoto, K. Ishisaka, K. Issautier, G. Wattieaux, T. Imachi, S. Matsuda, J. Lichtenberger, and H. Usui. Plasma Wave Investigation (PWI) aboard BepiColombo Mio on the trip to the first measurement of electric fields, electromagnetic waves, and radio waves around Mercury. *Space Science Reviews*, 216(65), 2020. URL https://doi.org/10.1007/s11214-020-00692-9. (Cited on pages 5, 60, 72, 73 and 77.)

H. R. Kaufman, J. J. Cuomo, and J. M. E. Harper. Technology and applications of broad-beam ion sources used in sputtering. *Journal of Vacuum Science and Technology*, 21(3):725–736, 1982. URL https://doi.org/10.1116/1.571819. (Cited on page 27.)

V. Korepanov, F. Dudkin, O. Melnik, and K. Pajunpää. Small satellites EMC study. *Advances in Space Research*, 28(1):221–225, 2001. URL https://doi.org/10.1016/S0273-1177(01)00347-7. (Cited on page 7.)

N. A. Krall and A. W. Trivelpiece. Principles of plasma physics. *American Journal of Physics*, 41(12): 1380–1381, 1973. URL https://doi.org/10.1119/1.1987587. (Cited on pages 10, 24 and 40.)

H. A. Kramers. Wellenmechanik und halbzahlige quantisierung. *Zeitschrift für Physik*, 39:828–840, 1926. URL https://doi.org/10.1007/BF01451751. (Cited on pages 10 and 58.)

V. Krasnoselskikh, A. Voshchepynets, and M. Maksimovic. On the efficiency of the linear-mode conversion for generation of solar type III radio bursts. *The Astrophysical Journal*, 879(1):51, 2019. URL https://doi.org/10.3847/1538-4357/ab22bf. (Cited on page 10.)

S. T. Lai. *Fundamentals of spacecraft charging*. Princeton University Press, Princeton, 2012. ISBN 9781400839094. URL https://doi.org/10.1515/9781400839094. (Cited on pages 7, 50, 71 and 163.)

J. G. Luhmann. The inner magnetosheath of Venus: An analogue for Earth? *Journal of Geophysical Research: Space Physics*, 100(A7):12035–12045, 1995. URL https://doi.org/10.1029/94JA02862. (Cited on page 33.)

J. G. Luhmann and L. H. Brace. Near-Mars space. *Reviews of Geophysics*, 29(2):121–140, 1991. URL https://doi.org/10.1029/91RG00066. (Cited on page 33.)

G. G. Managadze. *Time of flight mass spectrometer*. United States Patent: 4611118, 1986. (Cited on page 2.)

A. Mangeney, F. Califano, C. Cavazzoni, and P. Travnicek. A numerical scheme for the integration of the Vlasov-Maxwell system of equations. *Journal of Computational Physics*, 179, 2002. URL https://doi.org/10.1006/jcph.2002.7071. (Cited on page 19.)

R. Marchand, J. K. Burchill, and D. J. Knudsen. Modelling electrostatic sheath effects on Swarm Electric Field Instrument measurements. *Space Science Reviews*, 156(1-4):73–87, 2010. URL https://doi.org/10.1007/s11214-010-9735-y. (Cited on pages 8, 50, 59 and 71.)

N. Meyer-Vernet. *Basics of the Solar Wind*. Cambridge Atmospheric and Space Science Series. Cambridge University Press, 2007. URL https://doi.org/10.1017/CBO9780511535765. (Cited on page 33.)

N. Meyer-Vernet and C. Perche. Tool kit for antennae and thermal noise near the plasma frequency. *Journal of Geophysical Research: Space Physics*, 94(A3):2405–2415, 1989. URL https://doi.org/10.1029/JA094iA03p02405. (Cited on page 3.)

N. Meyer-Vernet, K. Issautier, and M. Moncuquet. Quasi-thermal noise spectroscopy: The art and the practice. *Journal of Geophysical Research: Space Physics*, 122(8):7925–7945, 2017. URL https://doi.org/10.1002/2017JA024449. (Cited on page 3.)

M. Moncuquet, N. Meyer-Vernet, K. Issautier, M. Pulupa, J. Bonnell, S. Bale, T. Dudok de Wit, K. Goetz, L. Griton, P. Harvey, R. Macdowall, M. Maksimovic, and D. Malaspina. First in situ measurements of electron density and temperature from quasi-thermal noise spectroscopy with Parker Solar Probe/FIELDS. *The Astrophysical Journal Supplement*, 246(2):44, 2020. URL https://doi.org/10.3847/1538-4365/ab5a84. (Cited on page 3.)

X. Morel, M. Berthomier, and J.-J. Berthelier. Electrostatic analyzer with a 3-D instantaneous field of view for fast measurements of plasma distribution functions in space. *Journal of Geophysical Research: Space Physics*, 122(3):3397–3410, 2017. URL https://doi.org/10.1002/2016JA023596. (Cited on page 3.)

B. Mortara. *Manual: Galileo: from the lab to the sky*. doi: http://dx.doi.org/10.2760/893128. European Union. JRC96392, 2015. (Cited on page 2.)

H. M. Mott-Smith and I. Langmuir. The theory of collectors in gaseous discharges. *Phys. Rev.*, 28: 727–763, 1926. URL https://doi.org/10.1103/PhysRev.28.727. (Cited on page 3.)

E. Möbius, P. Bochsler, A. G. Ghielmetti, and D. C. Hamilton. High mass resolution isochronous time-of-flight spectrograph for three-dimensional space plasma measurements. *Review of Scientific Instruments*, 61(11):3609–3612, 1990. URL https://doi.org/10.1063/1.1141580. (Cited on page 2.)

T. Neilsen, C. Weston, C. Fish, and B. Bingham. Dice: challenges of spinning cubesats. In *Space Dynamics Lab Publications*, page Paper 97, 2014. URL https://digitalcommons.usu.edu/sdl_pubs/97. (Cited on page 7.)

E. Odelstad, G. Stenberg-Wieser, M. Wieser, A. I. Eriksson, H. Nilsson, and F. L. Johansson. Measurements of the electrostatic potential of Rosetta at comet 67P. *Monthly Notices of the Royal Astronomical Society*, 469(Suppl_2):S568–S581, 2017. URL https://doi.org/10.1093/mnras/stx2232. (Cited on page 3.)

E. Odelstad, A. I. Eriksson, F. L. Johansson, E. Vigren, P. Henri, N. Gilet, K. L. Heritier, X. Vallières, M. Rubin, and M. André. Ion velocity and electron temperature inside and around the diamagnetic cavity of comet 67P. *Journal of Geophysical Research: Space Physics*, 123(7):5870–5893, 2018. URL https://doi.org/10.1029/2018JA025542. (Cited on pages 3 and 35.)

T. O'Neil. Collisionless damping of nonlinear plasma oscillations. *The Physics of Fluids*, 8(12):2255–2262, 1965. URL https://doi.org/10.1063/1.1761193. (Cited on pages 9 and 44.)

V. A. Osherovich, R. F. Benson, J. Fainberg, R. G. Stone, and R. J. MacDowall. Sounder stimulated D_n resonances in Jupiter's Io plasma torus. *Journal of Geophysical Research*, 98(E10):18751–18756, 1993. URL https://doi.org/10.1029/93JE01481. (Cited on page 3.)

G. Paschmann and P. W. Daly. Analysis methods for multi-spacecraft data. *ISSI Scientific Reports Series*, 1, 1998. URL https://ui.adsabs.harvard.edu/abs/1998ISSIR...1.....P. (Cited on pages 1, 2, 69 and 161.)

J. J. Podesta. Spatial Landau damping in plasmas with three-dimensional k distributions. *Physics of plasmas*, 12, 2005. URL https://doi.org/10.1063/1.188547. (Cited on pages 16, 20, 21 and 24.)

R. Pottelette and L. R. O. Storey. Active and passive methods for the study of non-equilibrium plasmas using electrostatic waves. *Journal of Plasma Physics*, 25(2):323–350, 1981. URL https://doi.org/10.1017/S0022377800023151. (Cited on pages 5, 14 and 63.)

R. Pottelette, B. Rooy, and V. Fiala. Theory of the mutual impedance of two small dipoles in a warm isotropic plasma. *Journal of Plasma Physics*, 14(2):209–243, 1975. URL https://doi.org/10.1017/S0022377800009533. (Cited on pages 5, 14 and 63.)

R. Pottelette, M. Hamelin, J. M. Illiano, and B. Lembège. Interpretation of the fine structure of electrostatic waves excited in space. *The Physics of Fluids*, 24(8):1517–1526, 1981. URL https://doi.org/10.1063/1.863556. (Cited on page 77.)

V. Pronenko, V. Korepanov, F. Dudkin, and S. Belyayev. Electromagnetic compatibility in very small spacecrafts. pages 1–1. 1st URSI Atlantic Radio Science Conference (URSI AT-RASC), 2015. URL https://doi.org/10.1109/URSI-AT-RASC.2015.7303041. (Cited on page 7.)

M. Pulupa, S. D. Bale, J. W. Bonnell, T. A. Bowen, N. Carruth, K. Goetz, D. Gordon, P. R. Harvey, M. Maksimovic, J. C. Martínez-Oliveros, M. Moncuquet, P. Saint-Hilaire, D. Seitz, and D. Sundkvist. The Solar Probe Plus Radio Frequency Spectrometer: measurement requirements, analog design, and digital signal processing. *Journal of Geophysical Research: Space Physics*, 122(3):2836–2854, 2017. URL https://doi.org/10.1002/2016JA023345. (Cited on page 3.)

J. L. Rauch, P. Henri, J. E. Wahlund, O. Le Duff, O. Sene, F. Colin, D. Lagoutte, N. Gilet, L. Ahlen, J. Bergman, R. Gill, and W. Puccio. Electron density measurement on JUICE mission by mutual impedance technique: MIME instrument as a part of RPWI consortium. In *European Planetary Science Congress*, pages EPSC2017–518, 2017. URL https://ui.adsabs.harvard.edu/abs/2017EPSC...11...518R. (Cited on pages 5, 60, 73 and 77.)

A. Retinò, Y. Khotyaintsev, O. Le Contel, M. F. Marcucci, F. Plaschke, A. Vaivads, V. Angelopoulos, P. Blasi, J. Burch, J. De Keyser, M. Dunlop, L. Dai, J. Eastwood, H. Fu, S. Haaland, M. Hoshino,

A. Johlander, L. Kepko, H. Kucharek, G. Lapenta, B. Lavraud, O. Malandraki, W. Matthaeus, K. McWilliams, A. Petrukovich, J.-L. Pinçon, Y. Saito, L. Sorriso-Valvo, R. Vainio, and R. Wimmer-Schweingruber. Particle energization in space plasmas: towards a multi-point, multi-scale plasma observatory. *Experimental Astronomy*, 2021. URL https://doi.org/10.1007/s10686-021-09797-7. (Cited on page 1.)

K.-U. Riemann. The Bohm criterion and sheath formation. *Journal of Physics D: Applied Physics*, 24 (4):493–518, 1991. URL https://doi.org/10.1088/0022-3727/24/4/001. (Cited on page 52.)

K.-U. Riemann. Plasma and sheath. *Plasma Sources Science and Technology*, 18(1):014006, 2008. URL https://doi.org/10.1088/0963-0252/18/1/014006. (Cited on pages 7 and 163.)

K. Roennmark. Waves in homogeneous, anisotropic multicomponent plasmas (WHAMP), 1982. URL https://ui.adsabs.harvard.edu/abs/1982wham.rept.....R. (Cited on page 24.)

B. Rooy, M. R. Feix, and L. R. O. Storey. Theory of a quadripolar probe for a hot isotropic plasma. *Plasma Physics*, 14(3):275–300, 1972. URL https://doi.org/10.1088/0032-1028/14/3/005. (Cited on pages 14 and 63.)

H. Rothkaehl, N. Andre, U. Auster, V. Della Corte, N. Edberg, M. Galand, P. Henri, J. de Keyser, I. Kolmasova, M. Morawski, H. Nilsson, L. Prech, M. Volwerk, C. Goetz, H. Gunell, B. Lavraud, A. Rotundi, and J. Soucek. Dust, Field and Plasma instrument onboard ESA's Comet Interceptor mission. In *Europlanet Science Congress*, 2021. URL https://hal.archives-ouvertes.fr/hal-03536600. (Cited on pages 5, 35 and 60.)

R. Z. Sagdeev and A. A. Galeev. *Nonlinear Plasma Theory*. Frontiers in physics. W.A. Benjamin, 1969. URL https://ui.adsabs.harvard.edu/abs/1969npt..book.....S. (Cited on page 9.)

B. Sanchez-Cano, M. Lester, F. Leblanc, D. Andrews, and H. Opgenoorth. The M-MATISSE mission: Mars Magnetosphere ATmosphere Ionosphere and Surface SciencE. In *44th COSPAR Scientific Assembly*, 2022. URL https://hal-insu.archives-ouvertes.fr/insu-03772050. (Cited on page 68.)

R. Sandau, K. Brieß, and M. D'Errico. Small satellites for global coverage: potential and limits. *ISPRS Journal of Photogrammetry and Remote Sensing*, 65(6):492–504, 2010. URL https://doi.org/10.1016/j.isprsjprs.2010.09.003. (Cited on page 2.)

J.-A. Sauvaud, A. Fedorov, C. Aoustin, H.-C. Seran, E. Le Comte, M. Petiot, J. Rouzaud, Y. Saito, J. Dandouras, C. Jacquey, P. Louarn, C. Mazelle, and J.-L. Médale. The Mercury Electron Analyzers for the Bepi Colombo mission. *Advances in Space Research*, 46(9):1139–1148, 2010. URL https://doi.org/10.1016/j.asr.2010.05.022. (Cited on page 3.)

S. J. Schwartz, T. Horbury, C. Owen, W. Baumjohann, R. Nakamura, P. Canu, A. Roux, F. Sahraoui, P. Louarn, J.-A. Sauvaud, J.-L. Pinçon, A. Vaivads, M. F. Marcucci, A. Anastasiadis, M. Fujimoto, P. Escoubet, M. Taylor, S. Eckersley, E. Allouis, and M.-C. Perkinson. Cross-scale: multi-scale coupling in space plasmas. *Experimental Astronomy*, 23:1001–1015, 2009. URL https://doi.org/10.1007/s10686-008-9085-x. (Cited on page 69.)

C. Snodgrass and G. H. Jones. The European Space Agency's Comet Interceptor lies in wait. *Nature Communications*, 10(5418), 2019. URL https://doi.org/10.1038/s41467-019-13470-1. (Cited on page 2.)

H. E. Spence. HelioSwarm: unlocking the multiscale mysteries of weakly-collisional magnetized plasma turbulence and ion heating. In *AGU Fall Meeting Abstracts*, volume 2019, pages SH11B–04, 2019. URL https://ui.adsabs.harvard.edu/abs/2019AGUFMSH11B..04S. (Cited on pages 2 and 161.)

L. Storey, L. Aubry, and P. Meyer. Mutual impedance techniques for space plasma measurements. *In Measurement techniques in space plasmas - Fields, Geophysical Monograph Series*, 103:155, 1969. URL https://doi.org/10.1029/GM103p0155. (Cited on pages 3, 5, 13, 14, 63 and 161.)

M. G. G. T. Taylor, N. Altobelli, B. J. Buratti, and M. Choukroun. The Rosetta mission orbiter science overview: the comet phase. *Philosophical Transactions of the Royal Society A: Mathematical, Physical and Engineering Sciences*, 375(2097):20160262, 2017. URL https://doi.org/10.1098/rsta.2016.0262. (Cited on page 3.)

A. Tkachenko, V. Krasnoselskikh, and A. Voshchepynets. Harmonic radio emission in randomly inhomogeneous plasma. *The Astrophysical Journal*, 908(2):126, 2021. URL https://doi.org/10.3847/1538-4357/abd2bd. (Cited on page 45.)

L. Tonks and I. Langmuir. A general theory of the plasma of an arc. *Phys. Rev.*, 34:876–922, 1929. URL https://doi.org/10.1103/PhysRev.34.876. (Cited on pages 7, 50, 71 and 163.)

J. Trotignon, J. Etcheto, and J. Thouvenin. Automatic determination of the electron density measured by the relaxation sounder on board ISEE 1. *Journal of Geophysical Research Space Physics*, 91(A4):4302, 1986. URL https://doi.org/10.1029/JA091iA04p04302. (Cited on page 3.)

J. Trotignon, J. Rauch, P. Décréu, P. Canu, and J. Lemaire. Active and passive plasma wave investigations in the earth's environment: The Cluster/WHISPER experiment. *Advances in Space Research*, 31(5):1449–1454, 2003. URL https://doi.org/10.1016/S0273-1177(02)00959-6. (Cited on pages 3 and 147.)

J. Trotignon, C. Béghin, D. Lagoutte, J. Michau, H. Matsumoto, H. Kojima, K. Hashimoto, Y. Kasaba, L. Blomberg, J. Lebreton, A. Masson, M. Hamelin, and R. Pottelette. Active measurement of the thermal electron density and temperature on the Mercury Magnetospheric Orbiter of the BepiColombo mission. *Advances in Space Research*, 38(4):686–692, 2006. URL https://doi.org/10.1016/j.asr.2006.03.031. (Cited on pages 5 and 37.)

J. Trotignon et al. RPC-MIP: The Mutual Impedance Probe of the Rosetta Plasma Consortium. *Space Science Reviews*, 128:713–728, 2007. (Cited on pages vii, 3, 4, 5, 35, 37, 73 and 161.)

J. G. Trotignon, P. M. E. Décréau, J. L. Rauch, X. Vallières, A. Rochel, S. Kougblénou, G. Lointier, G. Facsko, P. Canu, F. Darrouzet, and A. Masson. The WHISPER relaxation sounder and the Cluster active archive. 2010. (Cited on pages 3 and 147.)

O. L. Vaisberg, L. A. Avanov, A. V. Leibov, V. N. Smirnov, J. Keller, T. Moore, D. Chornay, M. Collier, V. S. Troshin, and V. D. Myagkikh. A panoramic plasma spectrometer: an all-sky camera for charged particles. *Cosmic Research*, 43:373–376, 2005. URL https://doi.org/10.1007/s10604-005-0058-9. (Cited on page 3.)

C. Vallat, T. Roatsch, M. K. Dougherty, A. Coustenis, Y. Kasaba, J.-E. Wahlund, O. Santolik, S. Barabash, G. Cremonese, P. Palumbo, H. Rothkaehl, L. Iess, G. Piccioni, d. Brandt, Pontus, H. Hussmann, Y. Langevin, F. Poulet, J. Plaut, R. Lorente, R. Jaumann, N. Altobelli, L. Fletcher, K. Retherford, E. Bunce, T. Van Hoolst, H. Hoffmann, G. Tobie, I. Mueller-Wodarg, B. Cecconi, A. Accomazzo, P. Wurz, L. Gurvits, F. Tosi, R. Gladstone, C. Erd, G. Cimo, N. Krupp, P. Hartogh, . Olivier Witasse, L. Bruzzone, O. Grasset, Y. Kaspi, A. Masters, T. Cavalie, D. J. Stevenson, A. Boutonnet, C. Munoz Crego, and I. Tanco. JUICE: a european mission to Jupiter and its icy moons. In *42nd COSPAR Scientific Assembly*, volume 42, pages B5.3–31–18, 2018. URL https://ui.adsabs.harvard.edu/abs/2018cosp...42E3492V. (Cited on page 5.)

E. Vigren, M. André, N. J. T. Edberg, I. A. D. Engelhardt, A. I. Eriksson, M. Galand, C. Goetz, P. Henri, K. Héritier, F. L. Johansson, H. Nilsson, E. Odelstad, M. Rubin, G. Stenberg-Wieser, C.-Y. Tzou, and X. Vallières. Effective ion speeds at ∼200–250 km from comet 67P/Churyumov–Gerasimenko near perihelion. *Monthly Notices of the Royal Astronomical Society*, 469(Suppl_2):S142–S148, 2017. URL https://doi.org/10.1093/mnras/stx1472. (Cited on page 3.)

X. Wang, Z. Sternovsky, M. Horanyi, J. Deca, I. Garrick-Bethell, W. M. Farrell, J. Minafra, and L. Bucciantini. Electrostatic Dust Analyzer (EDA) for measuring dust transport on the lunar surface. In *2021 Annual Meeting of the Lunar Exploration Analysis Group*, volume 2635 of *LPI Contributions*, page 5019, 2021. URL https://ui.adsabs.harvard.edu/abs/2021LPICo2635.5019W. (Cited on page 148.)

G. Wattieaux, N. Gilet, P. Henri, X. Vallières, and L. Bucciantini. RPC-MIP observations at comet 67P/Churyumov-Gerasimenko explained by a model including a sheath and two populations of electrons. *A&A*, 630:A41, 2019. URL https://doi.org/10.1051/0004-6361/201834872. (Cited on pages 17, 24, 71, 74, 148 and 165.)

G. Wattieaux, P. Henri, N. Gilet, X. Vallières, and J. Deca. Plasma characterization at comet 67P between 2 and 4 AU from the Sun with the RPC-MIP instrument. *A&A*, 638:A124, 2020. URL https://doi.org/10.1051/0004-6361/202037571. (Cited on pages 16, 17, 24, 50, 57, 63, 71 and 165.)

G. Wentzel. Eine verallgemeinerung der quantenbedingungen für die zwecke der wellenmechanik. *Zeitschrift für Physik*, 38:518–529, 1926. URL https://doi.org/10.1007/BF01397171. (Cited on pages 10 and 58.)

S. T. West, C. White, C. Celestino, S. Philpott, and M. Pankow. Design and testing of deployable carbon fiber booms for cubesat non-Gossamer applications. *56th AIAA/ASCE/AHS/ASC Structures, Structural Dynamics, and Materials Conference*, 2015. URL https://doi.org/10.2514/6.2015-0206. (Cited on pages 7, 69, 71 and 162.)

B. Westcott. Ionospheric reflection processes for long radio-waves—I. *Journal of Atmospheric and Terrestrial Physics*, 24(5):385–399, 1962. URL https://doi.org/10.1016/0021-9169(62)90233-7. (Cited on pages 10 and 59.)

E. Youssef. *ECSS - European Cooperation for Space Standardization*. 1996. URL https://doi.org/10.2514/6.1996-4305. (Cited on pages 7, 70 and 162.)

V. E. Zakharov and V. I. Karpman. On the nonlinear theory of the damping of plasma waves. *Soviet Journal of Experimental and Theoretical Physics*, 16:351, 1963. URL https://ui.adsabs.harvard.edu/abs/1963JETP...16..351Z. (Cited on page 44.)

A. Zaslavsky, M. Maksimovic, and K. Issautier. Le projet CIRCUS. In *Atelier Nano Satellites*, 2013. URL https://hal.archives-ouvertes.fr/hal-03729996. (Cited on page 77.)

Luca BUCCIANTINI

Sondes à impédance mutuelle pour plateformes nanosatellite

Résumé :

Les sondes à impédance mutuelle sont des expériences spatiales de diagnostic utilisées pour mesurer in situ la densité du plasma et la température des électrons. Des nouvelles versions instrumentales de sondes à impédance mutuelle sont actuellement conçues pour s'adapter aux fortes contraintes des nanosatellites. Les nanosatellites sont des petites plateformes à faible coût, qui pourraient faciliter les futures missions scientifiques multipoints. Ils ont cependant de fortes contraintes en termes de masse, volume et puissance. Ces contraintes devraient fortement affecter la conception et les performances des expériences d'impédance mutuelle.
Premièrement, les nanosatellites sont des petites plateformes, susceptibles de ne pouvoir embarquer que de courts appendices. Donc les capteurs électriques d'impédance mutuelle seront déployés proche de la plateforme nanosatellite, qui émet des signaux électromagnétiques perturbant les mesures. Cet impact pourrait être atténué en augmentant l'amplitude d'émission de l'expérience. Mais de fortes émissions peuvent déclencher des interactions non-linéaires dans le plasma qui peuvent à leur tour affecter le diagnostic expérimental.
Deuxièmement, les satellites dans l'espace sont chargés électriquement par des interactions plasma-satellite. Leur charge perturbe le plasma, qui réagit en générant des régions inhomogènes enveloppant le satellite. Cette région, la gaine, est connue pour perturber le diagnostic local du plasma.
Troisièmement, les fortes contraintes de masse et de volume à bord des nanosatellites incitent le partage de capteurs entre différentes expériences. Ce partage permet une réduction du poids des instruments au prix d'une limitation du temps d'occupation des senseurs. Pour mitiger l'effet de cette limitation, les sondes à impédance mutuelle requièrent des mesures plus rapides afin de garantir l'observation d'environnements à évolution rapide.
Dans ce contexte, cette thèse instrumental vise à résoudre les problèmes susmentionnés en étudiant, pour la première fois, l'impact (i) des interactions non-linéaires du plasma, (ii) des inhomogénéités du plasma à petite échelle et (iii) des mesures rapides sur la performance du diagnostic de densité et de température des sondes à impédance mutuelle.
Cette étude est réalisée à la fois numériquement, en utilisant un modèle Vlasov-Poisson 1D-1V cinétique pour simuler les mesures d'impédance mutuelle, et expérimentalement, en utilisant une chambre à plasma pour effectuer des tests d'impédance mutuelle dans les conditions typiques des ionosphères terrestres et planétaires.
Les résultats de cette thèse sont les suivants. (i) L'amplitude maximale d'émission d'impédance mutuelle qui garantit des Rapports Signal-sur-Bruit élevés et des perturbations non-linéaires négligeables du diagnostic d'impédance mutuelle correspond à des émissions associées à des rapports d'énergie électrique sur thermique dans le plasma allant jusqu'à 0.1. (ii) La gaine plasma du satellite ne perturbe pas le diagnostic de densité mais peut avoir un impact significatif sur le diagnostic de température. Par conséquent, les mesures absolues d'impédance mutuelle de la densité du plasma sont insensibles à la charge du satellite. Au contraire, le diagnostic de température nécessite un modèle de gaine. (iii) De nouvelles procédures expérimentales rapides d'impédance mutuelle (appelées modes chirp et multi-spectral) ont été définies, testées et validées en comparant au mode instrumental nominal d'impédance mutuelle. Le mode chirp permet d'effectuer des mesures étant jusqu'à 20 fois plus rapides que la procédure nominale, avec les mêmes performances de diagnostic.
Ces résultats seront utilisés pour la définition des sondes à impédance mutuelle qui seront embarqués sur des futures missions spatiales, notamment celles basées sur des petites plateformes tel que des nanosatellites.

Mots clés : Diagnostic in situ, Plasma Spatiaux, Sondes actives, Sondes à impédance mutuelle, Simulations Vlasov-Poisson, Chambre plasma, Expériences plasma, Intéractions plasma non-linéaires, Gaine plasma, Mésures à haute résolution.

Mutual impedance probes for nanosatellite platforms

Abstract :

Mutual impedance experiments are active in situ diagnostic techniques used to measure the plasma density and electron temperature, based on the electric coupling between two sets of antennas embedded in the space plasma to be diagnosed. Following the current trend of reducing the size of space platforms and instruments, new versions of mutual impedance instruments are currently being designed to fit the strong constraints of nanosatellites. On the one hand, nanosatellites are small low-cost platforms, expected to enhance future multi-point science missions. On the other hand, nanosatellites have strong constraints in terms of mass, volume and power. Such constraints are expected to strongly affect the design and the performance of mutual impedance experiments.
First, nanosatellites are small platforms, likely to embark only short booms. This means that they are likely to deploy mutual impedance electric sensors only at short distances from the satellite platform. The platform emits, in the surrounding environment, electromagnetic signals that are expected to perturb mutual impedance measurements. Such perturbations shall be mitigated by increasing the mutual impedance emission amplitude. But strong emissions could trigger non-linear plasma interactions that might affect the diagnostic performance of the experiment.
Second, satellites in space acquire a floating electric potential as a result of spacecraft-plasma interactions. Such floating potential perturbs the local plasma, that reacts by generating small-scale (of the order of the Debye length) inhomogeneous regions enveloping the satellite platform. These inhomogeneous regions, called plasma sheath, is known to perturb local plasma measurements.
Third, the strong constraints of mass and volume onboard nanosatellites is a strong motivation for different experiments to share the same sensors, whenever possible. While sensor sharing pushes towards lighter payloads, it also limits the sensor occupation time of each experiment. It follows that mutual impedance experiments require faster measurement procedures to ensure the observation of rapidly evolving environments.
In this context, this instrumental PhD work aims to solve the aforementioned issues by investigating, for the first time, the impact of (i) non-linear plasma interactions, (ii) small-scale plasma inhomogeneities and (iii) fast measurements on the performance of plasma density and electron temperature diagnostic performed by mutual impedance experiments.
This investigation is performed both numerically, using a fully kinetic, 1D-1V cartesian Vlasov-Poisson model to simulate mutual impedance measurements, and experimentally, using a plasma chamber to perform mutual impedance tests in typical Earth and planetary ionospheric conditions.
The results of this PhD work are the following. (i) The maximum mutual impedance emission amplitude that ensures strong Signal-to-Noise Ratios and negligible non-linear perturbations of mutual impedance diagnostic performance corresponds to emissions characterized by electric-to-thermal energy ratios in the plasma up to 0.1. (ii) The spacecraft sheath does not perturb the plasma density diagnostic but might significantly impact the electron temperature diagnostic. Therefore, mutual impedance absolute plasma density measurements are immune to spacecraft charging, while the electron temperature diagnostic requires some sheath model to account for the presence of the plasma sheath. (iii) New fast mutual impedance experimental procedures (called chirp and multi-spectral modes) have been defined, tested and validated against the nominal mutual impedance instrumental mode. The chirp mode procedure is found to perform measurements up to 20 times faster than nominal procedures, while maintaining the same diagnostic performance.
These results will be used to design future mutual impedance experiments on future space missions, especially those based on nanosatellite platforms.

Keywords : In situ diagnostic, Space Plasma, Active probes, Mutual impedance experiments, Vlasov-Poisson simulations, Plasma chamber, Plasma experiments, Non-linear plasma interactions, Plasma sheath, High time-resolution measurements

[LPC2E, CNRS, Université d'Orléans, CNES, Orléans, France]